ISBN: 978-605-68918-2-3

NEM 2023

FULL TEXT BOOK

3rd International Natural Science, Engineering and Material Technologies Conference

September 21-23, 2023, Turkish Republic of Northern Cyprus

FOREWORD

It is a pleasure for us to offer you this Book of Abstract for the 3 rd International Natural Science, Engineering and Material Technologies Conference (NEM 2023). Our goal was to create a platform that introduces the newest results on internationally recognized experts to local students and colleagues and simultaneously displays relevant Turkish achievements to the world. The positive feedback of the community encouraged us to proceed and transform a single event into a conference series. Now, NEM 2023 is honored by the presence of over 110 colleagues from various countries. We stayed true to the original NEM 2023 concept and accepted contributions from all fields of materials science and technology to promote multidisciplinary discussions. The focal points of the conference emerged spontaneously from the submitted abstracts: energy applications, advanced materials, electronic and optoelectronic devices, organic electronic materials, chemistry, physics, environmental science, medical science, applied and engineering science, computer simulation of organic structures, biomedical applications and advanced characterization techniques of nanostructured materials. Further fields of interest include e.g. new advanced and functional materials, advanced-functional composites, biomaterials, smart materials, dielectric materials, optical materials, magnetic materials, organic semiconductors, inorganic semiconductors, electronic materials, graphene, and more.

Therefore, we hope that getting first-hand access to so many new results, establishing new connections and enjoying the Turkish Republic of Northern Cyprus ambience will make you feel that your resources were spent well in NEM 2023.

Our warmest thanks go to all invited speakers, authors, and contributors of NEM 2023 for accepting our invitation, visiting Turkish Republic of Northern Cyprus and using NEM 2023 as a medium for communicating your research results.

We hope that you will enjoy the conference and look forward to meeting you again in one of the forthcoming **NEM 2024** event.

Best regards,
Chairmen's of Conference

Assoc. Prof. Burhan COŞKUN **Prof. Dr. HURİYE İCİL**

Editor:

Assoc. Prof. Burhan COŞKUN

Published, September-2023

nem2023.klu.edu.tr

nem@klu.edu.tr

COMMITTEE

HONORARY PRESIDENT

Prof. Dr. Bülent ŞENGÖRÜR (Rector of Kırklareli University)

Prof. Dr. Aykut HOCANIN (Rector of Eastern Mediterranean University)

CONFERENCE PRESIDENT

Prof. Dr. Huriye İCİL (Eastern Mediterranean University)

Assoc. Prof. Burhan COŞKUN (Kırklareli University)

ORGANIZING COMMITTEE

Prof. Dr. Cemile ÖZCAN / Kırklareli University

Prof. Dr. Meryem ÇAMUR DEMİR- Kırklareli University

Prof. Dr. Sermet KOYUNCU / Çanakkale Onsekiz Mart University

Prof. Dr. Serpil AKÖZCAN- Kırklareli University

Assoc. Prof. Dr. Berna AKGENÇ HANEDAR / Kırklareli University

Assoc. Prof. Dr. Emel PELİT / Kırklareli University

Assoc. Prof. Dr. Fatma KURŞUN BAYSAK / Kırklareli University

Assoc. Prof. Dr. H. Hale KARAYER / Kırklareli University

Assoc. Prof. Dr. Mehmet Mümin KOÇ / Kırklareli University

Assoc. Prof. Dr. Mustafa ARSLAN / Kırklareli University

Assoc. Prof. Dr. Nurdan KURNAZ YETİM / Kırklareli University

Dr. Lecturer Selin ÖZDEN / Kırklareli University

Dr. Instructor Ufuk PAKSU / Kırklareli University

Dr. Duygu UZUN / Eastern Mediterranean University

Dr. Meltem DİNLEYİCİ / Eastern Mediterranean University

Dr. Nihat AKKURT / Kırklareli University

Arwa ABOU RAJAB / Eastern Mediterranean University

Doğa KÜKRER / Eastern Mediterranean University

Elif DOĞRU / Eastern Mediterranean University

Pelin KARŞILI / Eastern Mediterranean University

Selin TEMÜRLÜ / Eastern Mediterranean University

Süleyman SOYEL / Eastern Mediterranean University

SCIENTIFIC COMMITTEE

Prof. Dr. Abdel Salam Hamdy MAKHLOUF / University of Texas / UNITED STATES

Prof. Dr. Abdullah G. AL-SEHEMI / King Khalid University / SAUDI ARABIA

Prof. Dr. Ahmed A. ALGHAMDI / King Abdulaziz University / SAUDI ARABIA

Prof. Dr. Ali DİŞLİ / Gazi University / TÜRKİYE

Prof. Dr. Asa H. BARBER / London South Bank University / UNITED KINGDOM

Prof. Dr. Azar AHMADOV / Baku State Gazi University / AZERBAIJAN

Asst. Prof. Bahadır BEKAR / Trakya University / TÜRKİYE

Assoc. Prof. Dr. Bayram ÇETİN / Kırklareli University / TÜRKİYE

Prof. Dr. Burç MISIRLIOĞLU / Sabancı University / TÜRKİYE

Prof. Dr. Canan AKSU CANBAY / Fırat University / TÜRKİYE

Prof. Dr. Chung GWIY-SANG / Ulsan University / KOREA

Prof. Dr. Denis NIKA / Moldova University / MOLDOVA

Prof. Dr. Dilek NARTOP / Düzce University / TÜRKİYE

Prof. Dr. Elias STATHATOS / Tecnological-Educational Institute of Patras / GREECE

Prof. Dr. Elizabeth BLACKBURN / University of Birmingham / UNITED KINGDOM

Asst. Prof. Erdinç KESKİN / Kırklareli University / TÜRKİYE

Asst. Prof. Evren ÇAĞLAER / Kırklareli University / TÜRKİYE

Assoc.Prof. Harun URAN / Kırklareli University / TÜRKİYE

Asst. Prof. İsmail KILIÇ / Kırklareli University / TÜRKİYE

Asst. Prof. Macide CANTÜRK RODOP / Yıldız Technical University / TÜRKİYE

Prof. Dr. Müjdat ÇAĞLAR / Eskişehir Anadolu University / TÜRKİYE

Prof. Dr. Mustafa ERKOVAN / Beykoz University / TÜRKİYE

Assoc. Prof. Mustafa KURBAN / Ahi Evran Gazi University / TÜRKİYE

Prof. Dr. Niyazi ÖZDEMİR / Fırat University / TÜRKİYE

Prof. Dr. Numan AKDOĞAN / Gebze Technical University / TÜRKİYE

Assoc. Prof. Ömer Suat TAŞKIN / Istanbul University / TÜRKİYE

Prof. Dr. Ram K. GUPTA / Pittsburg State University / UNITED STATES

Prof. Dr. Raşit TURAN / Middle East Technical University / TÜRKİYE

Prof. Dr. S. MANSOURI / University of Gabès / TUNUSIA

Asst. Prof. Sena Esen BAYER KESKİN / Kırklareli University / TÜRKİYE

FULL TEXT PRESENTATIONS

3rd International Natural Science, Engineering and Materials Technology Conference

Sep 21-23, 2023, Turkish Republic of Northern Cyprus

OPTIMIZING HYPERPARAMETERS FOR ENHANCING PERFORMANCE IN NATURAL LANGUAGE UNDERSTANDING FOR TURKISH

A. Suncak[1], Ö. Aktaş[2]

[1]*Department of Computer Technologies, Araç Rafet Vergili Vocational Highschool, Kastamonu University, Kastamonu, TÜRKİYE*

[2]*Department of Computer* Engineering*, Faculty of Engineering, Dokuz Eylül University University, İzmir, TÜRKİYE*

E-mail: atillasuncak@kastamonu.edu.tr, ozlem@cs.deu.edu.tr

The field of Natural Language Processing (NLP) has succeeded remarkable progress in deep learning techniques. Deep learning-based approaches have emerged as superior alternatives to rule-based NLP methods and various NLP tasks such as text classification, sentiment analysis, and document clustering. The fact that the performance of a learning model inarguably depends on fine-tuning its hyperparameters, the selection of appropriate hyperparameters affects the capability of the model in learning and extracting meaningful patterns for the input data. Instead of an exhaustive and time consuming techniques such as trial-and-error approach, using the suitable optimization technique provides more ideal solutions and unleash the full potential of the learning model. In this study, the application of hyperparameter optimization techniques such as Bayesian Optimization, Random Search, and Grid Search to improve the performance of a detection model for defective expressions have been focused on. Despite the fact that the use of deep learning models (Long Short-Term Memory [LSTM], Convolutional Neural Network [CNN], and a hybrid model of CNN and LSTM [C-LSTM]) and machine learning classifiers (Support Vector Machine [SVM] and Random Forest [RF]) has yielded acceptable results through a trial-and-error hyperparameter tuning approach, the main goal of this study is to provide the full potential of these models by applying optimization techniques to fine-tune their hyperparameters. Thus, this study will increase model performance beyond the limitations of the trial-and-error method and make a great contribution to advance the field of NLP.

Keywords: Bayesian optimization, Grid search, Hyperparameter optimization, NLP, Random search, Turkish

1. INTRODUCTION

Natural Language Processing (NLP) has made great advances and gained undeniable importance in parallel with deep learning development. It is obvious with the recent studies that deep learning based implementations for NLP problems became prominent in terms of performance in comparison to rule-based NLP techniques. Therefore, it can be clearly said that pre-trained language models have become one of the common practice for NLP solutions such as text classification, document clustering, sentiment analysis, text prediction and etc.

The fact that the performance of a learning model inarguably depends on fine-tuning its hyperparameters, the selection of appropriate hyperparameters affects the capability of the model in learning and extracting meaningful patterns for the input data. Since hyperparameters are the main factors for behavior of the model, adjusting the ideally becomes crucial for researchers. A model whose hyperparameters are ideally tuned can lead to improve the accuracy, better generalization, prevent overfitting, faster convergence and etc [1].

In general, it can be said that there are two options for hyperparameter tuning: trial-and-error method and optimization techniques. A trial-and-error method is the method which the hyperparameters such as activation function, dropout, batch size, optimizer and etc. are empirically adjusted. After a number of trials, the model whose performance in terms of accuracy, precision, recall or f score is chosen as the optimum model. This method is both exhaustive, time consuming and may not guarantee the model to be the ideal one. On the other hand, a hyperparameter optimization technique such as Bayesian Optimization, Random Search and Grid Search can be said to guarantee the most optimum model in comparison to trial-and-error method. Each technique has its own advantages or limitations. These advantages or limitations depend on the input data, the range of a hyperparameter, the number of hyperparameter or the model itself. Yet, instead of an exhaustive and time consuming techniques, using the suitable optimization technique provides more ideal solutions and unleash the full potential of the learning model [6].

In this study, these optimization techniques are proposed to apply on the models, developed by Suncak & Aktaş [2, 3], that detect defective expressions in Turkish sentences. In order to detect defective expressions, the researchers implemented both deep learning models (Long Short-Term Memory [LSTM], Convolutional Neural Network [CNN] and a hybrid model of CNN and LSTM [C-LSTM]) and machine learning classifiers (Vector Machine [SVM] and Random Forest [RF]). The hyperparameters of these model have been adjusted using trial-and-error method and resulted acceptable performances. Even though the results are acceptable, it is not guaranteed that these models perform in full potential due to the technique of hyperparameter optimization. Therefore, the main goal of this study is to apply the optimization techniques for hyperparameter tuning and increase the performances in comparison to trial-and-error tuning.

2. RELATED WORKS

Throughout the literature, it is found out that NLP researchers benefit several hyperparameter optimization techniques in order to implement the most ideal learning model for the purpose of performance increase. As aforementioned before, since trial-and-error method is tiresome and exhaustive, therefore these optimization techniques are highly crucial, however choosing the right technique depends on the model, number and range of hyperparameters, the problem and etc. The study of Asiri et al. [4] discusses hate speech detection and classification out of text data from social media platforms such as Twitter or Facebook. For this reason, they implemented a model that involves NLP techniques of data preprocess, Glove technique for feature extraction and deep learning models of attention-related bidirectional long short-term memory (ABLSTM). In order to tune the hyperparameters, the researchers employed a metaheuristic algorithm, namely Enhanced Seagull Optimization. The study of Aufa et al. [5] proposes the advantages of metaheuristic nature-inspired algorithms such as Swarm Intelligence or Grey Wolf Optimizer rather than common methods such as Random Search, Grid Search or Bayesian Optimization for hyperparameter optimization of LSTM model for the purpose of Language Modelling task. According to the study, metaheuristic algorithms have balanced exploring-exploiting process which makes the optimization more accurate. The study of Yıldız & Tezgider [7] deals with word2vec word representations development by automatically optimizing hyperparameters. As for the hyperparameters; word count, window size, vector size, iteration number and negative sample have been handled. Furthermore, they introduce two optimization techniques of Decisive Approach and Progressive approach due to being faster than Random Search and Grid Search. As a result, they managed to increase the success by 9% in terms of optimization.

3. LANGUAGE MODELS FOR DETECTING DEFECTIVE EXPRESSIONS IN TURKISH SENTENCES

Defective expression is the grammatical term that addresses semantic and morphologic ambiguities in Turkish sentences. The fact that defective expression is a common issue in Turkish education, mass media platforms or in literary texts, this problem is generally handled by linguistic researchers such as making the students write an essay and analysis on them to find how many defective expressions have been written, analyzing newspapers or magazines in order to find defective expressions and etc. [8, 9]. However, these analyses have been performed by the researchers manually, which is time consuming, exhaustive and requires great knowledge and attention.

The studies of Suncak & Aktaş [2, 3] proposed language models for automatic detection of defective expressions. The researchers employed deep learning models of LSTM, CNN and C-LSTM in addition to machine learning classifiers of SVM and RF. The dataset consists of 9710 Turkish sentences, which some of them involves defective expressions, collected from several online sources of education websites and official exam center of Turkey (ÖSYM) in person. After that, each sentence has been labelled under supervision of an expert in terms of involving defective expression. Since that amount of data is insufficient for training a language model, data augmentation has been performed using Turkish Synonym Dictionary [10] and increased the number of sentence up to 29756, seen in Table 1.

Table 1. The number of sentences in dataset before and after data augmentation

	Number of Sentences with Defective Expression	Number of Sentences without Defective Expression	Total
Before Augmentation	4299	5411	9710
After Augmentation	13398	16358	29756

After labelling operation, several NLP operations such as tokenization, punctuation removal, stop-word omitting and normalization have been applied on the sentences as data preparation process. As for the feature extraction, word2vec technique has been applied in order to represent each word as word vectors, namely word embeddings. Finally, learning models are trained by the word embeddings. The flow of the algorithm is depicted in Figure 1.

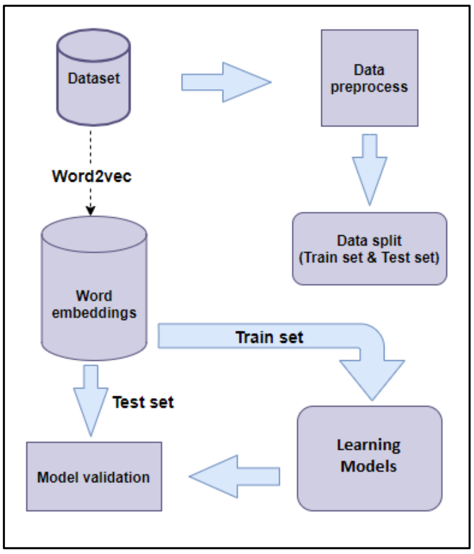

Figure 1. The flow of the algorithm for detecting defective expressions

Hyperparameter tuning of each model have been performed by trial-and-error method. These hyperparameters are listed in Table 2.

Table 2. The hyperparameters and their ranges/samples of each model

Model	Hyperparameters	Range or samples
LSTM	Number of hidden layer	32, 64, 96, 128, 192, 256
	Learning rate	0.01, 0.001, 0.0001
	Activation Function	softmax, sigmoid
	Dropour rate	0.1, 0.3, 0.5
CNN	Filters	64, 128, 256
	Kernel size	2, 3, 4
	Pool size	2, 3, 4
	Number of layers	1, 2, 3
	Learning rate	0.01, 0.001, 0.0001
	Activation Function	softmax, sigmoid
	Dropout rate	0.1, 0.3, 0.5
C-LSTM	CNN Filters	64, 128, 256
	CNN Kernel size	2, 3, 4
	CNN Pool size	2, 3, 4
	LSTM number of hidden layers	32, 64, 96, 128, 192, 256
	Dropout	0.1, 0.3, 0.5
	Learning rate	0.01, 0.001, 0.0001
	Activation Function	softmax, sigmoid
SVM	C	1, 01, 001, 0001
	Kernel	linear, poly, sigmoid
RF	n_estimator	100, 200, 300

Adjusting these hyperparameters with the method of trial-and-error causes huge time-loss and almost impossible to employ the most ideal model since it requires too many hyperparameter combinations. The most accurate performances of each model is depicted in Table 3.

Table 3. Best performances of each model in terms of accuracy metric

Model	Accuracy	Precision	Recall	F1 Score
C-LSTM	0.8854	0.87	0.86	0.87
LSTM	0.8794	0.88	0.89	0.88
CNN	0.8433	0.80	0.88	0.84
RF	0.7812	0.79	0.85	0.81
SVM	0.5850	0.60	0.75	0.66

4. PROPOSED METHODS

In this study, the hyperparameter optimizations of Bayesian optimization, Random search and Grid search techniques are proposed for fine-tuning the learning models to detect defective expressions in Turkish sentences. Each technique has its own strengths and limitations, thus their applications on each model vary in accordance with the aforementioned factors such as number of hyperparameters and their range.

Bayesian optimization is known for being powerful and efficient for tuning parameters due to the fact that its algorithm hinges upon probabilistic modelling and Gaussian process [11, 12]. This technique chooses the most appropriate hyperparameter combination considering the previously observed data and leads to the ideal solution using fewer number of calculations [13, 14].

Random search randomly generates sample of combinations and explores the search space in stochastic manner [15]. Even though it may not guarantee the optimum values due to random discovery of good combinations, it performs efficiently with fewer calculations [16, 17].

Grid search, on the other hand, is a straightforward technique which all combinations are tried exhaustively [18]. Despite being simple and time-consuming, it guarantees the ideal values since every combination of hyperparameter is calculated. However, the most disadvantageous issue is that it is extremely and computationally expensive for the device when the number and range of hyperparameter is high. Furthermore, this situation causes lack of flexibility for the algorithm which results in inefficient performance [19, 20].

5. CONCLUSION

In this optimization plays a significant role for performance maximization and model generalization in NLP. Searching for the most optimum combination of hyperparameters and fine-tuning them not only provide more accurate performances in comparison to trial-and-error method, but also make the model be capable of gathers meaningful patterns and features from text data. Furthermore, an automatic hyperparameter optimization can explore a wide range of combinations and provides the ideal one which enhance the model accuracy and improve convergence speed. In conclusion, with the continuity of advancements in NLP technologies, the power of hyperparameter optimization cannot be ignored. In the future, more advanced optimization algorithms related to NLP tasks will push the boundaries of model performances for their specific domains and lead the researchers focus on providing better solutions in this study area.

REFERENCES

[1] Liu, X., & Wang, C. (2021). An Empirical Study on Hyperparameter Optimization for Fine-Tuning Pre-trained Language Models. arXiv preprint arXiv:2106.09204.

[2] Suncak, A., & Aktaş, Ö. (2021). "A novel approach for detecting defective expressions in Turkish.", Journal of Artificial Intelligence and Data Science (JAIDA), vol.1, 35-40.

[3] Suncak, A. & Aktaş, Ö. (2022). Detecting Defective Expressions in Turkish Sentences Using a Hybrid Deep Learning Method . Dokuz Eylül Üniversitesi Mühendislik Fakültesi Fen ve Mühendislik Dergisi , 24 (72) , 825-834 .

[4] Asiri, Y., Halawani, H. T., Alghamdi, H. M., Abdalaha Hamza, S. H., Abdel-Khalek, S., & Mansour, R. F. (2022). Enhanced Seagull Optimization with Natural Language Processing Based Hate Speech Detection and Classification. Applied Sciences, 12(16), 8000.

[5] Aufa, B. Z., Suyanto, S., & Arifianto, A. (2020, August). Hyperparameter setting of LSTM-based language model using grey wolf optimizer. In 2020 international conference on data science and its applications (ICoDSA) (pp. 1-5). IEEE.

[6] Yogatama, D., & Smith, N. A. (2015). Bayesian optimization of text representations. arXiv preprint arXiv:1503.00693.

[7] Yildiz, B., & Tezgider, M. (2021). Improving word embedding quality with innovative automated approaches to hyperparameters. Concurrency and Computation: Practice and Experience, 33(18), e6091.

[8] Büyükikiz, K.K. (2007). İlköğretim 8. sınıf öğrencilerinin yazılı anlatım becerilerinin söz dizimi ve anlatım bozukluğu açısından değerlendirilmesi. Gazi University, Ankara, Turkey.

[9] Özdem, A. (2012). Çanakkale'deki yerel gazetelerin anlatım bozuklukları açısından incelenmesi. Çanakkale Onsekiz Mart University, Çanakkale, Turkey.

[10] Aktas, Ö., Birant, Ç. C., Aksu, B., & Çebi, Y. 2013. Automated synonym dictionary generation tool for Turkish (ASDICT). Bilig, 65, 47.

[11] Močkus, J. (1975). On Bayesian methods for seeking the extremum. In Optimization Techniques IFIP Technical Conference: Novosibirsk, July 1–7, 1974 (pp. 400-404). Springer Berlin Heidelberg.

[12] Mockus, J., & Mockus, J. (1989). The Bayesian approach to local optimization (pp. 125-156). Springer Netherlands.

[13] Frazier, P. I. (2018). Bayesian optimization. In Recent advances in optimization and modeling of contemporary problems (pp. 255-278). Informs.

[14] Snoek, J., Larochelle, H., & Adams, R. P. (2012). Practical bayesian optimization of machine learning algorithms. Advances in neural information processing systems, 25.

[15] Bergstra, J., & Bengio, Y. (2012). Random search for hyper-parameter optimization. Journal of machine learning research, 13(2).

[16] Andradóttir, S. (2014). A review of random search methods. Handbook of simulation optimization, 277-292.

[17] Andradóttir, S. (2006). An overview of simulation optimization via random search. Handbooks in operations research and management science, 13, 617-631.

[18] Michalski, R. S., Carbonell, J. G., & Mitchell, T. M. (1984). Machine learning an artificial intelligence approach. by Springer-Verlag Berlin Heidelberg New York Tokyo in 1983.

[19] Pontes, F. J., Amorim, G. F., Balestrassi, P. P., Paiva, A. P., & Ferreira, J. R. (2016). Design of experiments and focused grid search for neural network parameter optimization. Neurocomputing, 186, 22-34.

[20] Ensor, K. B., & Glynn, P. W. (1997). Stochastic optimization via grid search. Lectures in Applied Mathematics-American Mathematical Society, 33, 89-100.

EFFECTS OF USING ORANGE FIBER ON TEXTURAL PROPERTIES AND QUALITY PARAMETERS IN MEATBALL PRODUCTION

F.Y. H. Suncak[1], M. Çelik[1]

[1]*Department of Food Engineering, Faculty of Engineering and Architecture, Kastamonu University, Kastamonu, TÜRKİYE*

E-mail: fyhazar@kastamonu.edu.tr

The aim of this research is to use dietary fiber in the production of meatballs extracted from orange pulp, which is the waste of orange juice industry. In addition, it is aimed at increasing the functional properties of the product and providing added value to the industry in terms of waste evaluation. In the study, meatballs were produced using different ratios of orange fiber (0%, 1%, 3%, 5%), which decreased the pH, moisture, fat, diameter reduction and cooking loss values of the meatballs. The TBARS value, which is an indicator of lipid oxidation, showed the highest value in the group with 5% fiber added. In general, sensory analysis parameters of the meatballs were not affected by use of orange fiber. However, it was determined that the textural parameters of the meatballs decreased in general with the increase of fiber ratio.

Keywords: Meatballs, Dietary fiber, Orange fiber, Texture

1. INTRODUCTION

Citrus fruits such as orange, lemon, grapefruit, etc. are the most grown fruits in the world. Most of these fruits are processed in the food industry such as juice or canned. As a result of these processings, a large amount of waste such as shell, seed and pulp is generated. These wastes can be used to produce essential oil, dietary fiber and pigment. One of the effective ways to evaluate these wastes is to produce a natural functional fiber that includes hydrocolloid properties [1]. During industrial processing, a large number of orange by-products are produced, which can be a potential source of dietary fiber [2].

Dietary fibers consist of a heterogeneous mixture of non-starch polysaccharides, including cellulose, hemicellulose, pectin, hydrocolloids, and lignin, which cannot be broken down by enzymes in the gastrointestinal tract. It plays an important role in human nutrition and health. Dietary fiber is classified as soluble dietary fiber (pectin, β-glucan, fructans, and lignin) and insoluble dietary fiber (hemicellulose, cellulose, lignin). It acts as a protective agent against cardiovascular diseases, constipation, colon cancer and diabetes. It has positive effects on improving the digestive process, regulating blood sugar level and bowel movements, and lowering cholesterol [3].

The use of dietary fiber in production changes the textural, rheological, nutritional and sensory properties of food products [4]. Dietary fiber obtained from various plants have various functional properties such as solubility, viscosity, gel forming ability, water binding capacity, oil holding capacity, and mineral and organic molecule binding capacity [5]. Dietary fiber can be used as food additive such as yogurt [6, 7, 8], cake [9,10,11] and bread [12, 13]. It is also included in the production of meat products such as fermented sausage [14] or sausages [15, 16, 17, 18]. Despite being highly nutritious, meat products are pretty deficient in terms of dietary fiber [19]. On the other hand, consumer demand for meat products that do not have adverse health effects such as low-fat and salty foods and even contain health-promoting components is increasing rapidly worldwide [20]. Furthermore, adding dietary fiber to meat products has been suggested in several studies as a way to improve the nutritional and health quality of meat, as well as increase fiber intake among consumers [21,22].

Meat products are categorized as fresh processed meat products, fermented sausages, emulsified meat products, cooked meat products, raw or cooked meat products processed in pieces [23]. Meatball, one of the most consumed meat products worldwide, is a freshly processed meat product [24]. They are among the important foodstuffs in Turkish cuisine. It comes from the Persian word “küfte” and its main material is minced meat. They are produced using various ingredients and cooked with several methods [25,26]. Meatballs, which are used in the ready-made food industry and home-style, have an important place among local products according to different geographical regions of our country [27,26].

In this study, it was aimed to increase the functional properties of the product and to provide added value to the industry in terms of waste evaluation by including dietary fiber in meatball production. For this purpose, different ratios of orange fiber (0%, 1%, 3%, 5%) were used in the production of meatballs. The meatballs obtained at the end of the production were tested in terms of pH, moisture, fat, TBARS, ash, texture profile analysis, sensory and cooking properties.

2. MATERIAL AND METHODS

Orange fiber production

The oranges obtained from the market are washed and made ready to be passed through the juicer. The pulp of the product, which was passed through the juice squeezing device, was also collected in the waste part of the device. The collected orange by-product was placed in a water bath with continuous stirring and heat treated at 90°C for 30 minutes. At the end of the washing and heat treatment phase, it was pressed in order to remove water from the washed product. The pressed product was spread on drying trays and then placed in the drying cabinet at 70°C for 36 hours. After that, a grinder was used to generate powder with a small particle size. The obtained fiber was stored at -18°C until use [28].

Meatball Preparation

In the preparation of meatball dough, 74% beef, 20% meat fat, 5% breadcrumbs, 1% salt and orange fiber (0%, 1%, 3% and 5%) were used. After the meatball dough was kneaded enough, it was formed into round balls with a weight of 40 g for each meatball. Each surface of the meatballs produced was subjected to a 2-minute cooking process at 225 °C. pH, moisture, fat, TBARS, ash, cooking properties (cooking loss, diameter reduction and cooking efficiency), texture profile and sensory analyses were applied on the cooked meatball samples.

Physical and Chemical analyses (pH, Moisture, Fat, Ash)

In order to determine the pH value of the meatball samples, 10 g sample was homogenized with 100 ml distilled water and the pH value was measured using a pH meter. 5 g was taken into drying containers and dried for about 20 hours in a 105 °C oven until it reached a constant weight, and the moisture content was determined by keeping it in a desiccator and weighing. The determination of the amount of oil in the samples was carried out using the Soxhlet method. The ash value, 3 g of sample was weighed and the burning process was continued until a gray-white color was obtained in the ash crucibles brought to 525 °C in the ash oven. The samples taken from the furnace were then cooled in a desiccator and weighed. The results are given as % ash in dry matter [29].

TBARS analysis

2 grams of homogenized meatball samples were taken and 12 ml of TCA solution was added on each. TCA-added samples were homogenized for 15-20 s in ultraturrax and then filtered through Whatman 1 filter paper. 3 ml of the filtrate was taken and transferred to the test tube and 3 ml of TBA (0.02M) solution was mixed. After keeping the test tubes in a boiling water bath for 40 minutes, they were cooled for 5 minutes, then centrifugation process (5 minutes at 2000 g) was applied and the absorbance was measured at 530 nm in a spectrophotometer. TBARS values were calculated using the proper formula. The standard value was obtained from the standard curve formed using TEP (1,1,3,3, tetraethoxypropane). The result is given as mg malondialdehyde/kg [30].

Cooking Properties (Cooking loss, Cooking efficiency and Diameter reduction)

Meatball samples were weighed before cooking, and their weights were measured again after the cooking process was over. For diameter change; the diameter of all samples was measured before cooking, and the diameter reduction was calculated by measuring the diameter again after the cooking process was over.

Texture Profile Analysis (TPA)

TPA was performed using a texture analyser (CT3, Brookfield Engineering Laboratories, USA). Cylindrical sized samples of 2 cm diameter and 1 cm thickness extracted from the meatball samples were analysed at room temperature with two consecutive compression cycles using a 50mm cylindrical probe (TA 25/1000, Brookfield Engineering Laboratories, USA). In the analysis, the pre-test speed was 2.00 mm/s, the test and post-test speed was 1 mm/s, the compression interval was 3 s, and the compression ratio was 50%. From the force-time curves obtained at the end of the analysis, the textural parameters such as hardness, stickiness, cohesiveness, elasticity, chewiness, gumminess and elasticity were calculated.

Sensory Analysis

Hedonic type scale (1-9) was used in the sensory analysis of the cooked meatball samples. The panellists were asked to evaluate the meatball samples between 1-9 points in terms of color, appearance, smell, texture, taste and general acceptability. 1 point was rated as "undesirable" and 9 points as "typically desirable".

3. RESULTS AND DISCUSSION

The effects of orange fiber added meatballs on pH, moisture, fat, TBARS, ash, cooking loss, diameter reduction and cooking efficiency values are given in Table 1. Orange fiber had a significant effect on the pH value of the meatballs. The highest pH value of the meatballs was determined in the control (0%) and 1% fiber groups. While the mean lowest moisture value of meatballs formulated with different ratios of orange fiber was determined in the group containing 5% orange fiber with 54.01%, the highest moisture value was determined in the control group. Peach palm by-product was used in meatball samples; it was stated that as this by-product addition rate increased, there was a decrease in moisture values [31]. The fat value of meatball samples was affected by the addition of orange fiber. As the orange fiber content increased, the oil value decreased. In a study on the use of dietary fiber obtained from kiwifruit pulp in pork meatballs, the fat content of meatballs decreased significantly (P<0.05) compared to control samples [20]. The TBARS value, which is an indicator of lipid oxidation, has a very crucial effect on the orange fiber of meatballs. Meatballs with 5% orange fiber showed the highest TBARS value. There were statistically differences between the ash contents of the meatballs with the use of orange fiber.

The cooking properties (cooking efficiency, diameter reduction and cooking loss) of the meatball samples were also affected by the addition of orange fiber. These properties are severly important when analysing the quality characteristics of meat products. While the cooking efficiency of the control sample was determined at the lowest level, it gave the highest values for diameter reduction and cooking loss. Cooking efficiency increased proportionally with the orange fiber added to the meatball production. The control group meatballs showed more diameter reduction during cooking compared to the orange fiber added meatball samples. Therefore, control group meatballs showed the highest cooking loss. Thus, the addition of orange fiber improved the cooking loss rate of the meatballs. This result is thought to be due to high moisture and oil loss during cooking. Dietary fibers reduced the cooking loss of meatballs due to their high ability to retain moisture and fat in the matrix. In addition, diameter decreased as the use of orange fiber increased, and the lowest value was determined in meatballs produced using 5% orange fiber.

Table 1.The effects of orange fiber on pH, moisture, fat, TBARS and ash values of meatballs

Orange Fiber (OF)	pH	Moisture (%)	Fat (%)	TBARS (mgMDA/kg)	Ash (%)	Cooking yield (%)	Diameter decrease (%)	Cooking loss (%)
0%	6,04±0,09a	58,49±0,84a	20,18±0,50a	16,97±3,33ab	2,31±0,09ab	72,97±2,99d	18,66±2,17a	27,03±2,99a
1%	5,97±0,04a	56,85±0,83ab	17,19±1,01b	15,10±2,66bc	2,36±0,04a	79,18±4,91c	16,30±2,29b	20,82±4,91b
3%	5,71±0,13b	56,26±0,57b	14,33±0,50c	13,48±1,78c	2,31±0,08ab	81,33±3,80b	14,13±2,90c	18,67±3,80c
5%	5,45±0,14c	54,01±3,08c	12,54±1,14d	17,65±2,33a	2,25±0,08b	86,21±4,49a	9,43±2,31d	13,79±4,49d
Sig.	**	**	**	**	*	**	**	**

**P < 0,01, *P<0,05

a-d: Different letters indicate statistical difference (P < 0.05) in each column.

The effect of orange fiber on the texture profile analysis values is given in Table 2. Texture is one of the most important features of meat products that directly affects consumer preferences. Groups of meatballs containing 5% fiber showed the highest hardness value. Statistically, adhesiveness value was significantly affected by the addition of orange fiber. Resilience gave the highest statistical value in the control group. Cohesiveness, springiness and chewiness values were lower in all fiber groups compared to the control. Gumminess value was found to be lower in all fiber supplemented groups compared to control.

Table 2.The effects of orange fiber on texture parameters

Orange Fiber (OF)	Hardness (N)	Adhesiveness (mj)	Resilience	Cohesiveness	Springiness (mm)	Gumminess (N)	Chewiness (mj)
0%	65,09±17,08b	0,17±0,17b	0,13±0,01a	0,41±0,03a	5,02±024a	27,21±8,74a	136,58±44,27a
1%	58,72±9,07c	0,33±0,23a	0,11±0,01b	0,35±0,05b	4,79±0,35b	20,53±4,08b	98,47±21,37bc
3%	64,94±11,71b	0,16±0,18b	0,10±0,01c	0,34±0,03b	4,55±0,41c	22,29±5,69b	102,61±33,61b
5%	70,83±11,61a	0,27±0,26ab	0,08±0,01d	0,30±0,03c	4,10±0,31d	21,45±5,33b	88,75±26,86c
Sig.	**	*	**	**	**	**	**

**P < 0,01, *P<0,05
a-d: Different letters indicate statistical difference (P < 0.05) in each column.

The effect of orange fiber on the sensory analysis values is given in Table 3. While a very significant effect of taste was determined among the sensory parameters of the meatballs with orange fiber addition, other sensory parameters did not affect it statistically.

Table 3. The effect of orange fiber on the sensory analysis values of meatball

Orange Fiber (OF)	Colour	Appearance	Odour	Texture	Taste	General acceptability
0%	7,27±1,23a	7,33±1,21a	7,23±1,38a	6,87±1,83a	7,03±1,88ab	7,03±1,75a
1%	7,33±1,21a	7,40±1,22a	7,20±1,00a	7,03±1,07a	7,50±0,94a	7,23±0,97a
3%	7,53±1,20a	7,43±1,19a	6,87±1,68a	6,63±1,61a	6,43±1,45bc	6,83±1,32a
5%	6,93±1,86a	6,87±1,66a	6,83±1,58a	6,27±1,62a	6,03±1,67c	6,27±1,55a
Sig.	**NS**	**NS**	**NS**	**NS**	**	**NS**

NS: Not Significant; **P < 0,01
a-c: Different letters indicate statistical difference (P < 0.05) in each column.

4. CONCLUSION

In conclusion, the use of orange fiber as a waste by-product affected the textural and some quality characteristics of the meatballs. The pH, moisture, TBARS and fat values of meatballs were the lowest in the groups with 5% fiber added. It is thought that the reduction of cooking losses will contribute to the industry economically. In addition, sensory parameters had an effect only on the taste parameter of meatballs in terms of consumer preference. In the textural parameters, there was a general decrease with the use of fiber.

REFERENCES

[1] Su, D., Zhu, X., Wang, Y., Li, D., & Wang, L., Effect of high-pressure homogenization on rheological properties of citrus fiber. LWT, 127, 109366, 2020.

[2] Liu, Y., Wang, L., Liu, F., & Pan, S., Effect of grinding methods on structural, physicochemical, and functional properties of insoluble dietary fiber from orange peel. International Journal of Polymer Science, 2016.

[3] Pathania, S., & Kaur, N., Utilization of fruits and vegetable by-products for isolation of dietary fibres and its potential application as functional ingredients. Bioactive Carbohydrates and Dietary Fibre, 27, 100295, 2022.

[4] Sharma, S. K., Bansal, S., Mangal, M., Dixit, A. K., Gupta, R. K., & Mangal, A. K., Utilization of food processing by-products as dietary, functional, and novel fibre: A review. Critical Reviews in Food Science and Nutrition, 56(10), 1647–1661, 2016.

[5] Biswas, A. K., Kumar, V., Bhosle, S., Sahoo, J., & Chatli, M. K., Dietary fibers as functional ingredients in meat products and their role in human health. International Journal of Livestock Production, 2(4), 45-54, 2011.

[6] Hoppert, K., Zahn, S., Jänecke, L., Mai, R., Hoffmann, S., & Rohm, H., Consumer acceptance of regular and reduced-sugar yogurt enriched with different types of dietary fiber. International Dairy Journal, 28(1), 1-7, 2013.

[7] Dong, R., Liao, W., Xie, J., Chen, Y., Peng, G., Xie, J., ... & Yu, Q., Enrichment of yogurt with carrot soluble dietary fiber prepared by three physical modified treatments: Microstructure, rheology and storage stability. Innovative Food Science & Emerging Technologies, 75, 102901, 2022.

[8] Fan, X., Shi, Z., Xu, J., Li, C., Li, X., Jiang, X., ... & Pan, D., Characterization of the effects of binary probiotics and wolfberry dietary fiber on the quality of yogurt. Food Chemistry, 406, 135020, 2023.

[9] Masoodi, F. A., Sharma, B., & Chauhan, G. S., Use of apple pomace as a source of dietary fiber in cakes. Plant Foods for Human Nutrition, 57, 121-128, 2002.

[10] Al-Sayed, H. M., & Ahmed, A. R., Utilization of watermelon rinds and sharlyn melon peels as a natural source of dietary fiber and antioxidants in cake. Annals of Agricultural Sciences, 58(1), 83-95, 2013.

[11] Jeddou, K. B., Bouaziz, F., Zouari-Ellouzi, S., Chaari, F., Ellouz-Chaabouni, S., Ellouz-Ghorbel, R., & Nouri-Ellouz, O., Improvement of texture and sensory properties of cakes by addition of potato peel powder with high level of dietary fiber and protein. Food chemistry, 217, 668-677. 2017.

[12] Xu, J., Li, Y., Zhao, Y., Wang, D., & Wang, W., Influence of antioxidant dietary fiber on dough properties and bread qualities: A review. Journal of Functional Foods, 80, 104434, 2021

[13] Toma, R. B., Orr, P. H., D'appolonia, B., Dlntzis, F. R., & Tabekhia, M. M., Physical and chemical properties of potato peel as a source of dietary fiber in bread. Journal of Food Science, 44(5), 1403-1407, 1979.

[15] Fernández-Ginés, J. M., Fernández-López, J., Sayas-Barberá, E., Sendra, E., & Perez-Alvarez, J. A., Lemon albedo as a new source of dietary fiber: Application to bologna sausages. Meat science, 67(1), 7-13., 2004.

[16] Huang, S. C., Tsai, Y. F., & Chen, C. M., Effects of wheat fiber, oat fiber, and inulin on sensory and physico-chemical properties of Chinese-style sausages. Asian-Australasian Journal of Animal Sciences, 24(6), 875-880, 2011.

[17] Choi, M. S., Choi, Y. S., Kim, H. W., Hwang, K. E., Song, D. H., n Lee, S. Y., & Kim, C. J., Effects of replacing pork back fat with brewer's spent grain dietary fiber on quality characteristics of reduced-fat chicken sausages. Korean journal for food science of animal resources, 34(2), 158, 2014.

[18] Ham, Y.K., Hwang, K. E., Song, D.H., Kim, Y. J., Shin, D.J., Kim, K.I., ... & Kim, C.J., Lotus (Nelumbo nucifera) rhizome as an antioxidant dietary fiber in cooked sausage: effects on physicochemical and sensory characteristics. Korean journal for food science of animal resources, 37(2), 219, 2017.

[19] Das, A. K., Nanda, P. K., Madane, P., Biswas, S., Das, A., Zhang, W., & Lorenzo, J. M., A comprehensive review on antioxidant dietary fibre enriched meat-based functional foods. Trends in Food Science & Technology, 99, 323-336, 2020.

[20] Zhang, W., Xiao, S., Samaraweera, H., Lee, E. J., & Ahn, D. U., Improving functional value of meat products. Meat science, 86(1), 15-31, 2010.

[21] Kehlet, U., Pagter, M., Aaslyng, M. D., & Raben, A., Meatballs with 3% and 6% dietary fibre from rye bran or pea fibre-Effects on sensory quality and subjective appetite sensations. Meat science, 125, 66-75, 2017.

[22] Talukder, S., Effect of dietary fiber on properties and acceptance of meat products: a review. Critical reviews in food science and nutrition, 55(7), 1005-1011, 2015.

[23] Gökalp, H.Y., Kaya, M., Tülek, Y. ve Zorba, Ö., Et Ürünleri İşleme Mühendisliği. (5. Baskı). Atatürk Üniversitesi, Ziraat Fakültesi, Yay. No: 70, Erzurum. 468, 2004.

[24] Morsy, M. K., Mekawi, E., & Elsabagh, R., Impact of pomegranate peel nanoparticles on quality attributes of meatballs during refrigerated storage. LWT, 89, 489-495, 2018.

[25] Keçeci, S., Sığır eti köftelerinin bazı fizikokimyasal, tekstürel ve mikrobiyolojik özellikleri üzerine farklı düzeylerde dondurarak kurutulmuş çeşitli sebze turşusu tozlarının etkilerinin belirlenmesi. Yüksek Lisans Tezi, Selçuk Üniversitesi Fen Bilimleri Enstitüsü.Konya, 2018.

[26] Özabravci, A., Tekirdağ köftesi üretiminde bezelye proteini ve lifinin kullanım olanaklarının araştırılması. Yüksek Lisans Tezi, Namık Kemal Üniversitesi Fen Bilimleri Enstitüsü.Tekirdağ, 2019.

[27] Korkmaz, A., & Oz, F., Effect of the use of dry breadcrumb in meatball production on the formation of heterocyclic aromatic amines. British Food Journal 2020.

[28] Fernández-Ginés JM., Fernández-López J., Sayas-Barberá E., Sendra, E. and PérezÁlvarez JA.,. Effect of storage conditions on quality characteristics of Bologna sausages made with citrus fiber. Journal of Food Science, 68(2), 710– 715. 2003

[29] Gökalp, H.Y., Kaya, M., Tülek, Y., Zorba, Ö., Et ve Et ürünlerinde Kalite Kontrolü ve Laboratuvar Uygulama Kılavuzu, Atatürk Üniversitesi Yayınları No:751, Ziraat Fakültesi Yayın No:318, 2001.

[30] Kilic B, Richards MP, Lipid oxidation in poultry döner kebap: Pro-oxidative and antioxidative factors. Journal of Food Science, 68(2): 686-689, doi: 10.1111/j.1365-2621.2003.tb05732.x. 2003.

[31] Echeverria, L., Rigoto, J. D. M., Martinez, A. C., Porciuncula, B. D. A., Scanavacca, J., & Barros, B. C. B., Characterization of lamb burgers with addition of flour from peach palm by-product. *Biosci. j.(Online),* 280-289, 2020.

THERMAL REGULATION OF PVs BY PCM BASED HYBRID SYSTEMS

S. Erdem[1], M. Özdenefe[1]

[1]*Department of Mechanical Engineering, Faculty of Engineering, Eastern Mediterranean University, Famagusta, North Cyprus via Mersin 10, Turkey*

E-mail: sertane1993@gmail.com, murat.ozdenefe@emu.edu.tr

Efficiency of photovoltaic (PV) panels is inversely proportional to the operational temperature of solar cells when the operational temperature is higher than the reference temperature –which generally is 25°C– The current work is an effort to propose a solution to this problem by examining phase change material (PCM) based passive hybrid cooling systems for reducing PV temperatures. Four different hybrid cooling systems which incorporate various melting point PCMs (25°C and 35°C) along with different heat transfer elements (fins and porous medium) were put into test to investigate their cooling effect on PVs. It was found that the system containing low melting point PCM (25°C) and fins had the highest instantaneous cooling capacity, whereas the system containing low melting point PCM (25°C) and porous medium resulted in the highest overall cooling capacity. Moreover, the maximum efficiency increase was found to be 8% which occurred for the low melting point PCM (25°C) and fins configuration.

Keywords: PCM based hybrid cooling systems, PV cooling, Photovoltaics, Thermal regulation, Renewable energy, Efficiency enhancement.

1. INTRODUCTION

The unceasing rise of greenhouse gas emissions primarily due to fossil fuel combustions are considered to be the main reason of climate change. Climate change, as well as the fluctuation in fossil fuel prices, paved the way to develop renewable energy technologies and to implement those technologies in daily applications of energy generation processes. In these days, most common ways to decrease the dependency on fossil fuel in power applications are photovoltaics, solar thermals, wind turbines, nuclear power plants, and geothermal. This shift is crucial to mitigate the impacts of climate crisis and promote sustainable energy solutions [1].

Although PVs are one of the most common technologies to generate electricity, they suffer from low energy conversion rate –as low as 25% of the incident radiation for conventional panels– [2,3]. In addition to this issue, their efficiency drops further when solar cell temperature goes above the reference temperature, which is usually 25°C. According to various studies and manufacturers, PV temperature can go as high as 80°C under high insolation [4–6]. To harvest the maximum energy from the sun via PV panels, temperature regulation of PVs should be done to keep them as cool as possible. Active and passive cooling techniques are currently being used in order to satisfy this need. Active cooling methods use external energy sources to run fans and pumps. On the other hand, passive cooling methods do not use any external energy source [7–9]. Since their low operational and maintenance costs along with low carbon footprint, passive cooling techniques are widely used to cool down the bodies which are used for energy generation [10]. Some of the passive cooling techniques are submerged water cooling, air flow induced by buoyancy, heat sinks, PCMs and evaporative cooling [8,11]. PCMs which are the subject of this work are latent heat storage substances that change phase at certain temperatures. During the phase change, heat is absorbed, and no significant temperature rise occurs. Outside the phase change PCMs behave as sensible heat storage materials and the temperature change occurs proportional to the amount of absorbed heat. [12–14].

The present study is an effort to propose a solution to the aforementioned problem by examining PCM based passive hybrid cooling systems to enhance the efficiency of PVs through an experimental approach. Four different hybrid systems combining two different melting point PCMs (25°C and 35°C) with two different heat transfer elements, fins and porous medium, are produced and tested under laboratory conditions.

2. MATERIAL AND METHODS

Cooling systems were produced by incorporating PCMs with heat transfer elements in aluminum reservoirs which has dimensions of 355×285×40 mm. The fins were made from 2 mm thick aluminum sheets and have dimensions of 250×30 mm. Porous medium on the other hand is composed from perforated aluminum sheets (2 mm thick) with dimensions of 345×280 mm. The porosity of perforated sheets is 48%. Two different paraffin based organic PCMs, with peak melting points of 25°C and 35°C, were poured into the prepared reservoirs which were integrated into the heat transfer elements. The reservoirs were attached to the back of PV panels. The manufacturing process of hybrid systems are illustrated in Figure 1. Four different passive hybrid cooling systems were generated; i- low melting point PCM (25°C) with fins ii- low melting point PCM (25°C) with porous medium, iii- high melting point PCM (35°C) with fins and iv- high melting point PCM (35°C) with porous medium. The configurations of the systems are given in Table 1.

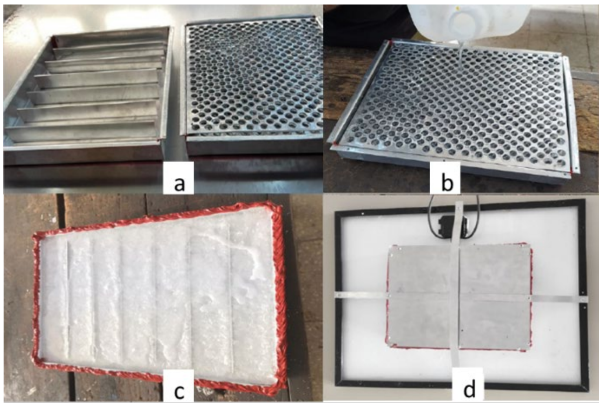

Figure 1: Manufacturing process of hybrid cooling systems. (a) Reservoirs with fins and perforated sheets, (b) PCM addition, (c) hybrid system with solidified PCM (d) hybrid cooling system coupled with PV.

Table 1: Cooling system configurations. (Tick mark indicates presence and cross mark indicates absence of an item).

	PCM Melting Point		**Heat Transfer Element**	
	25°C	35°C	Fin	Porous Medium
Case 1(control case)	×	×	×	×
Case 2	✓	×	✓	×
Case 3	✓	×	×	✓
Case 4	×	✓	✓	×
Case 5	×	✓	×	✓

In order to conduct the experiments, PV panels having 55W of maximum power output were used. K-type, NiCr-Ni thermocouples were employed to measure the temperature of PVs. Three thermocouples were placed on top of the glass cover of the PV panels. The ends of the thermocouples were connected to a data acquisition module which was coupled to a computer. To simulate solar radiation, two 500 W halogen projectors were attached to an arm which was positioned 400 mm above the PV panels. The irradiation of the light source was measured with a pyranometer as 950 W/m^2. Figure 2 illustrates the attached thermocouples to the PV panel and the schematics of the experimental setup. The test duration for each case was 210 minutes. Temperature readings were logged every minute throughout the experiments.

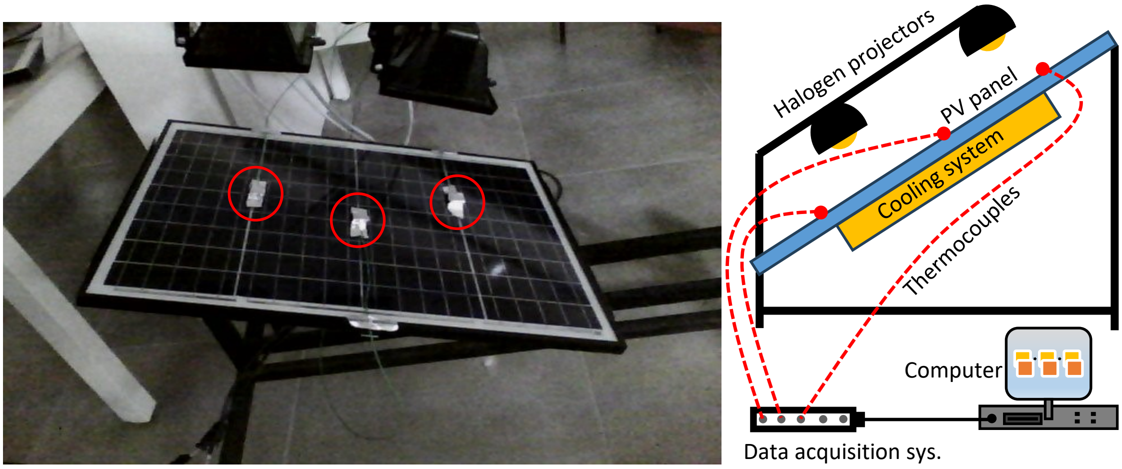

Figure 2: Placement of the thermocouples and schematic experimental setup.

The power output and efficiency of the panels were calculated using equation (1) and equation (2) respectively which are based on the measured instantaneous temperature, irradiation and the reference values of PV panels [2,15].

$$P_{out} = \eta A_{cell} G \tag{1}$$

where P_{out} (W), η (%), A_{cell} (m^2) and G (W/m^2) are power output, efficiency (see equation (2)), solar cell area and irradiation.

$$\eta = \eta_{ref}[1 - \beta_{ref}(T_{PV} - T_{ref})] \tag{2}$$

where η_{ref} (%), β_{ref} (%/°C), T_{PV} (°C) and T_{ref} (°C) are reference efficiency, power decrement rate per unit temperature increase, instantaneous temperature and reference temperature of PV respectively.

3. RESULTS AND DISCUSSION

3.1. PV Panel Temperatures

Temperature curves of respective cases shown Figure 3 reveals that the configurations with fins achieved lower temperatures and have faster melting processes than the configurations with porous medium. It is apparent that all cases except case 5 (PV-35P) experienced temperature reduction compared with the test case during a certain period of time throughout the experiment. As shown in Figure 3, at a room temperature of 18°C, configuration of case 2 (PV-25F) can be said that has the superior cooling performance among all cases since it led the lowest temperature. However, it should be noted that case 3 (PV-25P) keeps the PV cells cooler for a longer time with slightly higher temperature. During the 210-minute experiment, it was found that configurations used in cases 2 and 3 cooled the PV cells on average by 7.2°C and 7.8°C, respectively. In terms of the instantaneous maximum temperature difference, low melting point PCM with fins (case 2) cooled the PV by 17.6°C, while low melting point PCM with porous medium (case 3) cooled it by 17°C. On the other hand, configurations employed in cases 4 and 5 increased the cell temperatures. During the experiment, the average increase in PV temperatures compared to the control case was 0.9°C for case 4 and 6.3°C for case 5.

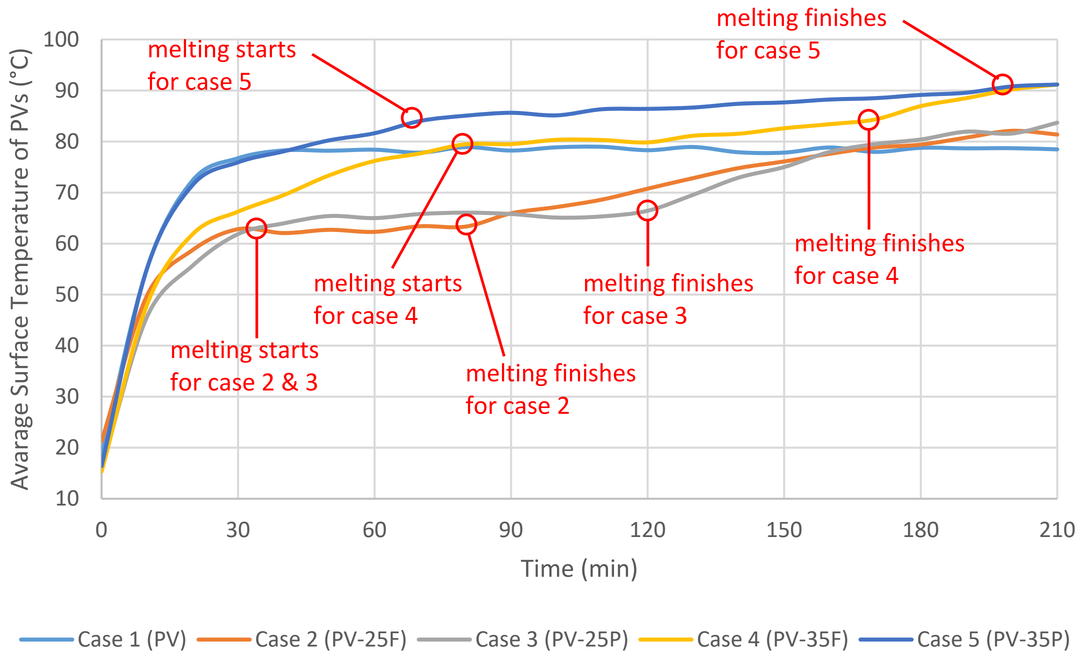

Figure 3: Variation of PV temperatures during the experiment.

Considering the melting point of the PCMs, it is clear that configurations with a lower melting point cool down the PVs more effectively. However, it must be noted that the ambient temperature affects the melting trend of PCMs. With a high melting point PCM, the PVs must reach higher temperatures to supply enough energy to melt the PCM, as the PVs are the only heat source. The low melting point PCMs are therefore more appropriate for thermal regulation of PVs in cooler environments.

3.2. Power output and efficiency

The power output and the efficiency of the panels with different cooling systems were evaluated by Equation 1 and Equation 2 respectively. Power output and the efficiency are function of reference efficiency (25%), power decrement rate per unit temperature increase (-0.38%/°C), reference temperature (25°C) and solar cell area of the PV panels (0.22 m^2) as well as irradiation (950 W/m^2) and the instantaneous temperature of the panels. All the parameters except the instantaneous temperature of the panels are constant during the experiment.

The power output results are given in Figure 4, whereas the efficiencies are given in Figure 5. It is clear from Figure 4 and Figure 5 that the power and efficiency of the PVs degrade as time proceeds because temperature of the PVs increases. It is apparent in the figures that all cases except case 5 (PV-35P), had higher power output and efficiency than the test case (case 1 which is PV without any cooling system) during a certain period throughout the experiment. Case 2 (PV-25F) and case 3 (PV-25P) maintained higher power output and efficiency than the test case for about two and a half hours, whereas case 4 (PV-35F) maintained higher power output and efficiency than the test case for about one hour. In contrast, case 5 (PV-35P) had lower power output and efficiency than the test case throughout the experiment. It is obvious that case 2 (PV-25F) and case 3 (PV-25P) are better options since they enabled higher power output and efficiency than case 4 (PV-35F), case 5 (PV-35P) and the test case. Although case 2 (PV-25F) achieved higher instantaneous power output and instantaneous efficiency than case 3 (PV-25P), case 3 maintained higher power output and efficiency longer than case 2.

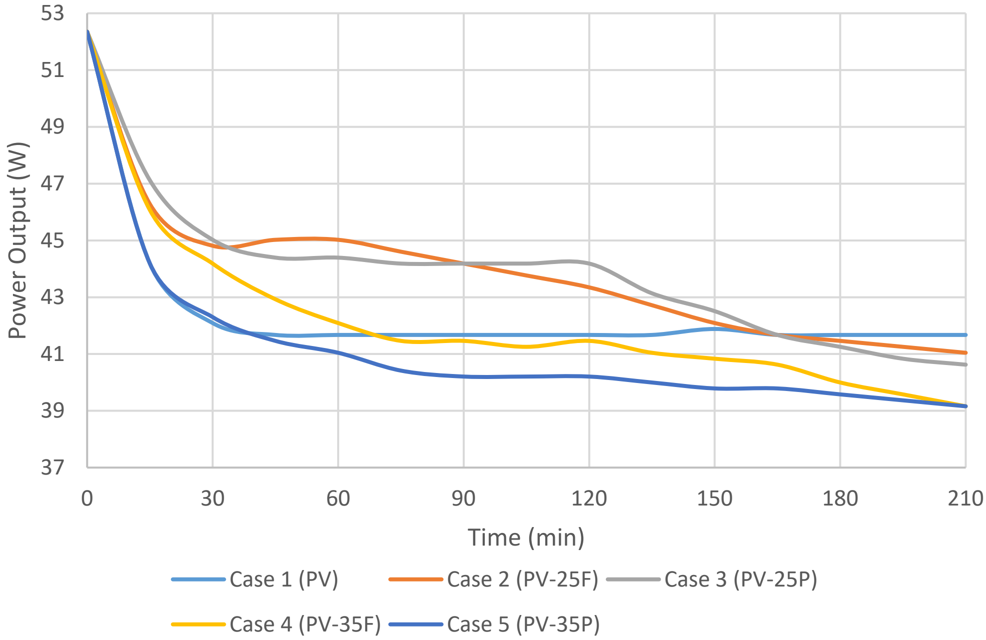

Figure 4: Variation of power output of PVs during the experiments.

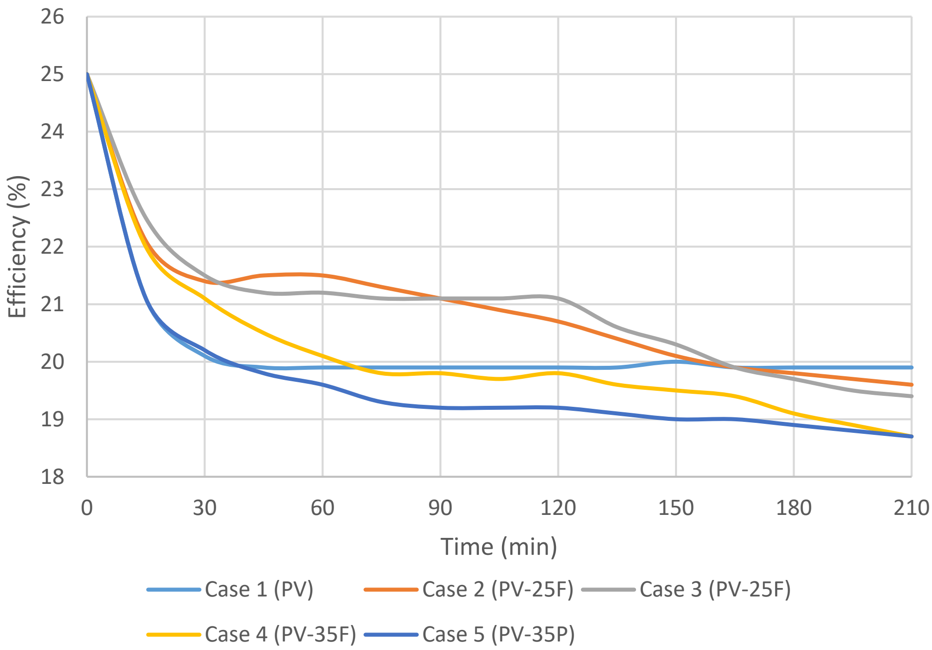

Figure 5: Variation of panel efficiencies during experiments.

Table 2 presents the enhancement of the efficiency in percentage for each case compared to the test case. It can be seen in the table that case 2 (PV-25F) and case 3 (PV-25P) performed alike by increasing the efficiency of the PVs 3.3% on average over the period of the experiment (210 minutes). It is also seen that case 2 (PV-25F) increased the efficiency as much as 8%, whereas maximum increase for case 3 (PV-25P) occurs as 7% at the early stages of the experiment. After about two and a half hours there were no increase in the efficiency. For case 4 (PV-35F) and 5 (PV-35P) on the other hand PVs efficiency reduced by 0.7% and 3% respectively on average over the period of the experiment. At the early stages of the experiment (in first hour) case 4 (PV-35F) led to an increase in efficiency, as much as 5%, however, this was not maintained during the later periods. Case 5 (PV-35P) on the other hand experienced no increase in the efficiency at all during the entire experiment duration. This is expected since case 5 (PV-35P)did not cause temperature reduction of the PV panel (see Figure 3).

Table 3: Theoretical efficiency increments with respect to the test case.

Time (min)	**Case 2 (%)**	**Case 3 (%)**	**Case 4 (%)**	**Case 5 (%)**
0	0	0	0	0
15	4.7	6.6	4.3	0
30	6.5	7	5	0.5
45	8	6.5	3	-0.5
60	8	6.5	1	-1.5
75	7	6	-0.5	-3
90	6	6	-0.5	-3.5
105	5	6	-1	-3.5
120	4	6	-0.5	-3.5
135	2.5	3.5	-1.5	-4
150	0.5	1.5	-2.5	-5
165	0	0	-2.5	-4.5
180	-0.5	-1	-4	-5
195	-1	-2	-5	-5.5
210	-1.5	-2.5	-6	-6
Average	3.3	3.3	-0.7	-3

4. CONCLUSION

In this study, four different hybrid cooling systems having PCMs with two different melting points and heat transfer elements are tested with PV panels having maximum power output of 55W. The hybrid cooling systems are i- case 2: low melting point PCM (25°C) with fins ii- case 3: low melting point PCM (25°C) with porous medium, iii- case 4: high melting point PCM (35°C) with fins and iv- case 5: high melting point PCM (35°C) with porous medium. The tests are performed under laboratory conditions with an average room temperature of 18°C under 950W/m^2 of irradiation. At the end of the tests, it has been found that:

- The highest instantaneous temperature drop with respect to test case is achieved by case 2 with 17.6°C.
- The lowest average temperature throughout the experiment is achieved by case 3 with 67.74°C.
- Porous medium elongated the melting duration of PCMs more than 40% compared to fins.
- Configurations used in cases 2 and 3 increased the efficiencies as much as 8% and 7% respectively.
- Using low melting point PCMs for cooler environmental conditions is more useful for thermal regulation, power output and efficiency improvement.

ACKNOWLEDGMENTS

This study was supported by Eastern Mediterranean University under project number: BAPC-02-22-04.

REFERENCES

[1] Zhang Q, Agbossou A, Feng Z, Cosnier M. Solar micro-energy harvesting based on thermoelectric and latent heat effects. Part II: Experimental analysis. Sensors and Actuators, A: Physical 2010;163:277–83. https://doi.org/10.1016/j.sna.2010.06.026.

[2] Kant K, Shukla A, Sharma A, Biwole PH. Thermal response of poly-crystalline silicon photovoltaic panels: Numerical simulation and experimental study. Solar Energy 2016;134:147–55. https://doi.org/10.1016/j.solener.2016.05.002.

[3] Ma T, Yang H, Zhang Y, Lu L, Wang X. Using phase change materials in photovoltaic systems for thermal regulation and electrical efficiency improvement: A review and outlook. Renewable and Sustainable Energy Reviews 2015;43:1273–84. https://doi.org/10.1016/j.rser.2014.12.003.

[4] LG Energy. At what temperatures do the solar panels perform at their best? n.d. www.lgenergy.com.au/faq/solar-power-explained/at-what-temperatures-do-the-solar-panels-perform-at-their-best (accessed December 1, 2021).

[5] Boston Solar. How do temperature and shade affect solar panel efficiency? 2019. https://www.bostonsolar.us/solar-blog-resource-center/blog/how-do-temperature-and-shade-affect-solar-panel-efficiency/ (accessed December 1, 2021).

[6] Mazer JA. Solar cells. An introduction to crystalline photovoltaic technology. 1st ed. 1997.

[7] Hasanuzzaman M, Malek ABMA, Islam MM, Pandey AK, Rahim NA. Global advancement of cooling technologies for PV systems: A review. Solar Energy 2016;137:25–45. https://doi.org/10.1016/j.solener.2016.07.010.

[8] Chandrasekar M, Rajkumar S, Valavan D. A review on the thermal regulation techniques for non integrated flat PV modules mounted on building top. Energy and Buildings 2015;86:692–7. https://doi.org/10.1016/j.enbuild.2014.10.071.

[9] Kant K, Shukla A, Sharma A, Biwole PH. Heat transfer studies of photovoltaic panel coupled with phase change material. Solar Energy 2016;140:151–61. https://doi.org/10.1016/j.solener.2016.11.006.

[10] Hendricks JHC, van Sark WGJHM. Annual performance enhancement of building integrated photovoltaic modules by applying phase change materials. Progress in Photovoltaics: Research and Applications 2013;21:620–30. https://doi.org/10.1002/pip.1240.

[11] Kant K, Shukla A, Sharma A, Biwole PH. Heat transfer studies of photovoltaic panel coupled with phase change material. Solar Energy 2016;140:151–61. https://doi.org/10.1016/j.solener.2016.11.006.

[12] Ismail KAR, Henríquez JR. Numerical and experimental study of spherical capsules packed bed latent heat storage system. Applied Thermal Engineering 2002;22:1705–16. https://doi.org/10.1016/S1359-4311(02)00080-7.

[13] Zalba B, Marín JM, Cabeza LF, Mehling H. Review on thermal energy storage with phase change: materials, heat transfer analysis and applications. Applied Thermal Engineering 2003;23:251–83. https://doi.org/10.1016/S1359-4311(02)00192-8.

[14] Arkar C, Medved S. Influence of accuracy of thermal property data of a phase change material on the result of a numerical model of a packed bed latent heat storage with spheres. Thermochimica Acta 2005;438:192–201. https://doi.org/10.1016/j.tca.2005.08.032.

[15] Evans DL, Florschuetz LW. Cost studies on terrestrial photovoltaic power systems with sunlight concentration. Solar Energy 1977;19:255–62. https://doi.org/10.1016/0038-092X(77)90068-8.

INVESTIGATION OF HEATSINK DESIGN PARAMETERS IN AN INDUCTION HOB BY USING DOE AND CFD METHODS

Ayberk Salim MAYIL[1], Ergin KAPLAN[2]

[1]Haier Europe Research and Development Center, Eskisehir, TÜRKİYE
[21]Haier Europe Research and Development Center, Eskisehir, TÜRKİYE

E-mail: ayberk.mayil@haier-europe.com

Induction hobs have gained significant popularity as a modern and efficient alternative to conventional gas and electric hobs. The technology behind induction cooking involves the use of electromagnetic fields to heat the cooking vessel directly, as opposed to traditional methods that rely on thermal conduction. This direct transfer of heat not only promises faster and more precise cooking, but also offers potential advantages in terms of energy efficiency and safety. Induction hobs includes electronic system inside of it. For creates the electromagnetic fields via coils, high current is needed from the electronic system. During this period, electronic components reach high temperature. For sustainable usage of hobs, electronic components need to be cooled by ventilation system. One of the important components of ventilation system is heatsink. With the increasing demand for smaller, faster, and more powerful electronic devices, the efficient management of heat dissipation has become a critical challenge. Heatsinks, commonly used in electronic cooling systems, play a vital role in dissipating excess heat generated by electronic components to maintain optimal operating temperatures. The design and performance of heatsinks are crucial factors in ensuring the reliability and longevity of electronic devices. In this paper, aluminium finned heatsink design has been investigated. Electronic components are settled on finned heatsink and they inserted in a simplified induction hob. For the heatsink design, design of experiment is applied by changing number of fins, fin space and fin thickness of heatsink. DOE is created by using Minitab program. For saving tooling time and experimental set-up, CFD method is used to simulate each heatsink design. CFD method is validated with the theoretical heatsink problem. For the CFD method, FloEFD program is used. Results show the effect of each design change on IGBT (Insulated Gate Bi-Polar Transistor) surface temperature which connected to heatsink.

Keywords: Induction Hob, Heatsink, DOE, CFD, FloEFD

1. INTRODUCTION

There is increasingly demand for usage of the Induction hobs ought to advantage of inductions hobs when they are compared with gas and vitro-ceramic hobs. Electromagnetic field is used to heat cooking pan as opposed to conventional cooking methods. They utilize a process called magnetic induction to generate heat directly within the cookware placed on top of them. Induction hobs consist of a flat surface made from a non-magnetic material, typically glass-ceramic, and underneath this surface are copper coils. When an electric current flow through these coils, it creates a fluctuating magnetic field. When a ferromagnetic material, such as iron or steel, is placed on the surface of the induction hob, the magnetic field induces electrical currents within the cookware. These currents, known as "eddy currents," flow in a circular pattern due to the resistance of the material. According to Lenz's law, these eddy currents create their own magnetic field that opposes the changing magnetic field produced by the induction hob. As a result, the cookware experiences resistance to the flow of these eddy currents, and this resistance generates heat within the cookware itself. This heat is then transferred to the food or liquid within the cookware, allowing for efficient and precise cooking. The heat is generated directly within the cookware, rather than the hob surface, which is why induction hobs are known for their fast heat-up times and precise temperature control. It is important to note that induction hobs require the use of cookware that is compatible with induction cooking. This means the cookware must have a magnetic bottom, such as cast iron or stainless steel, to effectively interact with the magnetic field and induce the necessary eddy currents for heating [1-2].

In the literature, there are several studies related to examination of induction hobs. Kawakami et al. studied for the visualizing the temperature and flow patterns on induction and gas hobs by using CFD method. They showed the heat distribution differences between induction and gas hobs by simulating the convection [3]. Kranjc et al. investigated the induction heating process by using numerical and experimental methods [4]. They showed the induction heating of steel workpiece with temperature-depend and independent analyses and they developed thermographic data by using experimental method. Induction hobs include high technology electronic system inside of it so that during the operation of induction hobs, heat dissipations rise from the electronic components. For sustainable and safe usage of induction hobs, well-designed ventilation system is inevitable. Ventilation system is comprised of the fan and heatsink in base. There are several studied for the heatsink design in the literature. Teertstra et al. studied for developing analytical model to obtain the average heat transfer rate in forced convection -cooled in slotted fin heatsinks [5]. They investigated heatsink design parameters. Gupta et al. investigated the heat transfer and flow performance of the heatsink in forced convection by experimentally [6]. They aimed to enhance the heat transfer in plate fin heatsink with dimples and protrusions. Literature shows the there are several methods to increase the heat transfer of heatsink by investigate the effect of design parameters on natural-forced convection, radiation and conduction.

In this study, aluminium finned heatsink design has been investigated by numerical method. For the numerical method FloEFD package CFD program is used. For the sequential analysis, DOE study is developed by using Minitab program. Results showed effect of the design parameters of heatsink on IGBT surface temperature during induction hob working cycle.

2. MATERIAL AND METHODS

In this paper, finned heatsink design parameters are investigated by numerically to obtain well-designed ventilation system of induction hobs for providing the safe usage of them. As a first stage, CFD method is validated by using example of heatsink theoretical calculations [7]. After validation step, a series of sequential analyses are developed with the DOE method by using Minitab program. Based on DOE study, all analyses are applied on FloEFD package CFD program. For the governing equations it uses finite volume method. As a turbulence solution, it uses k-ε model with damping functions [8-9]. For the mesh point of view, FloEFD is using cartesian mesh. It operates the Van Driest's universal profiles and "Two Scale wall functions" approach to describe the turbulent boundary layer [10-11]. To obtain space discretization, the axis oriented rectangular grid is used far from a geometry boundary. Near the geometry boundary Cartesian cut cells approach is used. In computational fluid dynamics, the control volume is divided into a numerical solution grid, and the conservation equations are discretized into algebraic equation systems. Conversation equations are given below. Equation 1 and Equation 2 show the continuity and momentum equations below.

$$\frac{\partial \rho}{\partial t} + \nabla.\left(\rho \vec{V}\right) = 0 \quad (1)$$

$$\rho \frac{D\vec{V}}{Dt} = \rho \vec{g} - \nabla p + \mu \nabla^2 \vec{V} \quad (2)$$

In Equation 1, ρ is fluid density, t is fluid time, $\vec{}$ is velocity component. In the Equation 2, u, v and w are the velocity components of cartesian coordinates. Navier-Stokes equation is shown in Equation 2 above. Left side of the equilibrium represents product of mass and acceleration. Right side of equilibrium represents sum of the forces effected on fluid. First term of right side is gravity force, second term is pressure gradient and third term is internal extension forces. In addition, FloEFD uses the CAD interface for developing the model. Figure 1 shows the heatsink model, created by CAD interface, below.

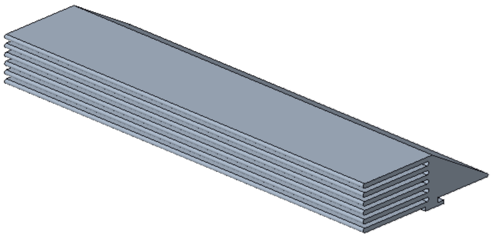

Figure 1. Finned heatsink CAD model

As shown in Figure 1, evaluated heatsink has the fins which provides increment of surface area. Thanks to high surface area, air can more interact with the heatsink. Equation 3 shows the convective heat transfer rate through heatsink below.

$$\dot{Q} = h \; x \; A_s \; x \; \Delta T \tag{3}$$

In Equation 3, h is the mean convective heat transfer coefficient, A is the surface area and T means temperature differences between surface and fluid. The mass flow rate of air is shown in Equation 4 below.

$$\dot{m} = \rho \; x \; A \; x \; V \tag{4}$$

In equation 4, ρ is the fluid density, V is the fluid velocity. The total height of the heatsink accepted as a constant value. With the constant heatsink height, fin thickness and number of fins are evaluated. For the DOE study, there are 2 factors and 2 levels. But for the number of fins, center point is added. In Figure 2, analysis list is shown below.

StdOrder	RunOrder	CenterPt	Blocks	Fin Number	Fin Thickness
4	1	1	1	6	1.9
1	2	1	1	4	1.3
2	3	1	1	6	1.3
5	4	0	1	5	1.6
3	5	1	1	4	1.9

Figure 2. DOE Study

Ventilation system of induction hobs include fan and heatsink. Apart from ventilation system, electronic board are settled in base box. Between the base box and coils, there could be a separator. On top of the hobs, glasses are settled. In this study, focus is ventilation system so for decreasing mesh load of simulation, simplified model is used as shown in Figure 3 below.

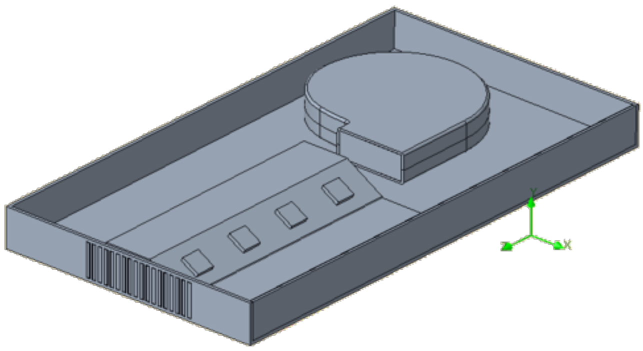

Figure 3. Simplified CFD Model

In Figure 3, simplified CFD model is shown. Base box is plastic, fan, heatsinks are settled in base box. Material of heatsink is Al. On Al, IGBTs are assembled. IGBTs have the 8W heat dissipation for each. Total mesh number of the model 2.8 million. With the mesh independent study, it could be used less mesh number. In Figure 4, meshed model is shown. For simplifying the CFD study, inlet air flow velocity is used for the fan blowing. Rotational effect of the fan effect is neglected for this investigation.

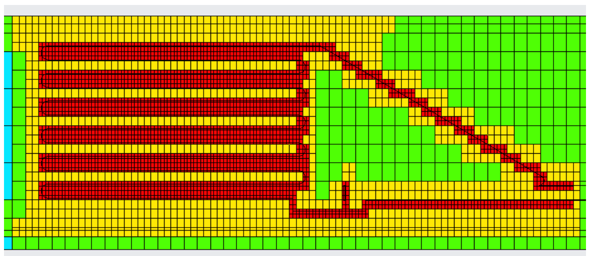

Figure 4. Meshed Model

In this numerical investigation, ventilation system of induction hob is evaluated by numerically. Key factor is specified as a heatsink design. Height and length of the heatsink have been considered as a constant. Number of fins and fin thickness have been evaluated during the design of experiment. After the CFD method validation with theoretical calculations, new model is created and analysed according to DOE study. Results are evaluated with the post-process method and graphical analysis.

3. RESULTS AND DISCUSSION

In this numerical investigation, simplified hob model is created by using CAD program. This study is based on ventilation design parameters of induction hobs. Ventilation system includes, air suction area for the fan inlet, fan, heatsink and outlet on the tray. IGBTs are connected to heatsink for the cooling effect. Firstly, validation study is applied. Theoretical calculations belong to Yunus Çengel "Heat and Mass Transfer" book [7] is given below.

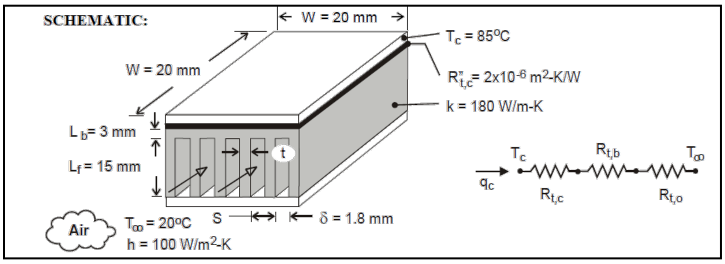

Figure 5. Theoretical Calculation – Yunus Cengel "Heat & Mass Transfer

As shown in Figure 5, example of heatsink study is solved and based on this solution CFD model is created as shown in Figure 6 below.

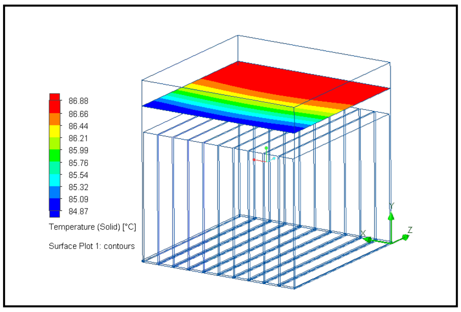

Figure 6. Reference Heatsink Study

METHOD	Heat Transfer Rate [W]	Heat Source Temperature [°C]	Heat Transfer Coefficient [W/m^{2}K]
THEORITICAL	32	85	100
CFD	31.20	86.20	101.96

Figure 7. Theoretical & CFD Comparison

As shown in Figure 7 above, as a maximum rate is 2%, CFD method is validated. Based on this results, simplified hob model is analysed according to DOE study. Post-process results are shown in Figure 8 below.

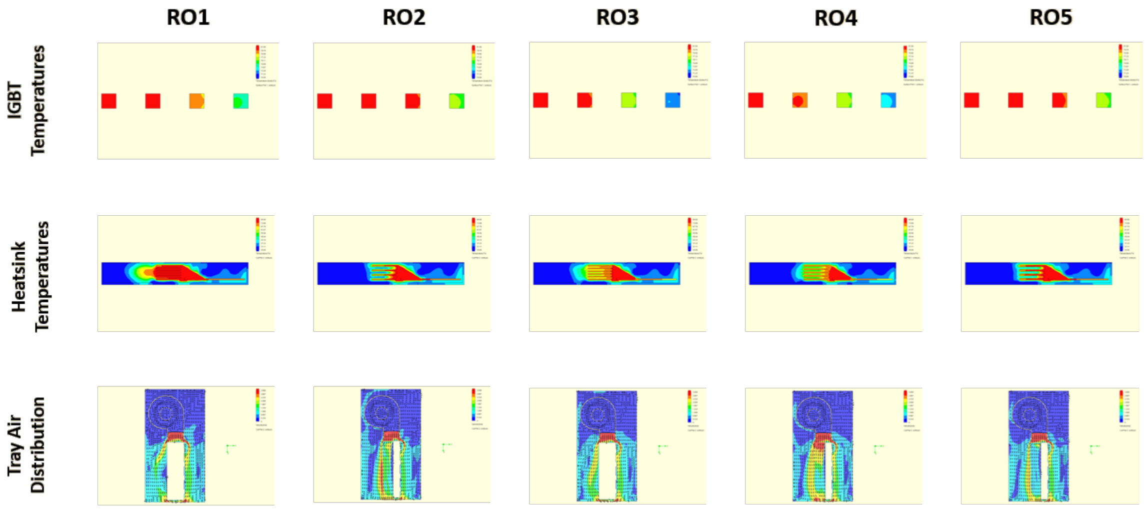

Figure 8. CFD Post-Process results

Figure 8 shows the results of the CFD studies. RO represents Run Order sequence. IGBT temperatures represents, surface temperature of the last IGBT which most far away from the fan. Temperature scale is between 70 °C - 81°C. Heatsink temperatures represents the middle vertical section view of model to see the heatsink temperature differences. Temperature scale is between 25 °C - 80°C. Try air distribution represents the air velocity distribution through horizontal section view of tray. Velocity scale is between 0 m/s – 3 m/s. For deeply results analysis Minitab program is used. By using Minitab tools, DOE results are analysed. The main effect and two ways interaction results are shown in Figure 9 below with the Pareto chart.

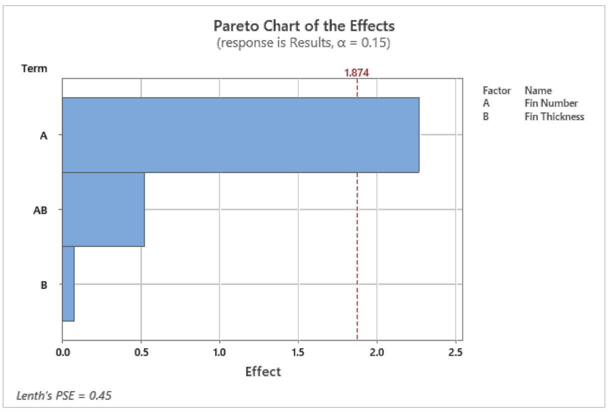

Figure 9. Pareto chart for the one effect & two ways interactions

Based on the Figure 9, the most effective parameter is number of fins then, second one is interaction of the fin number & fin thickness. With the confidence level is 85%, only one effect is important which is number of fins. Also, for all Ros, surface temperature of the last IGBT are close to each other's as shown in Figure 10 below.

Fin Number	Fin Thickness	RESULTS [C]
6	1.9	81.54
4	1.3	83.73
6	1.3	80.94
5	1.6	80.58
4	1.9	83.28

Figure 10. 4th IGBT Surface temperatures for all analyses

Additionally, box plot analysis shows the results and best configuration as shown in Figure 11 below.

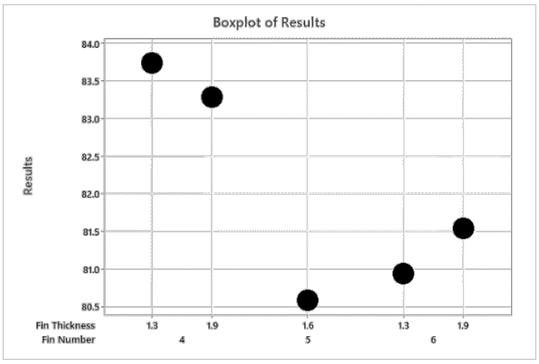

Figure 11. Boxplot of 5 analyses

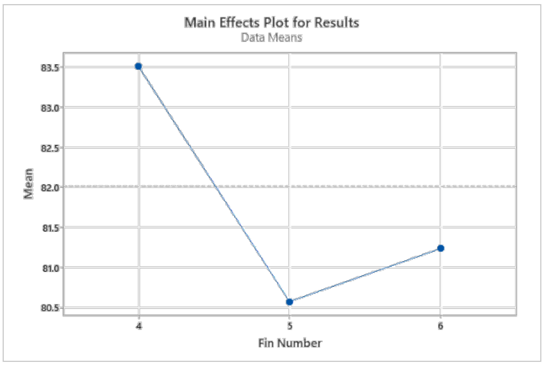

Figure 12. Main effect plot

Figure 12 shows the fin number effect on IGBT surface temperature. According to main effect plot of fin number, 5 fins results are best ones for the IGBT surface temperature point of view.

4. CONCLUSION

In this investigation, heatsink design parameters are evaluated by numerical method. After the validation step, 5 different analyses are applied on FloEFD package CFD program which uses the "Finite Volume Methods" for the solution. Based on the results, Run Order 4 has the lowest IGBT surface temperatures. Run Order 4 configuration has the 5 fin numbers with the 1.6mm fin thickness. But, when all IGBT temperatures are evaluated, there are not such a big difference between results so that during the design, for the two parameters ,fin numbers which 4, 5 and 6 and fin thickness 1.3mm, 1.6mm and 1.9mm, special experimental study is not needed. Ought to this paper, some experimental studies are eliminated. Material and labour cost is gained by eliminating some experimental process.

ACKNOWLEDGMENTS

This study was supported by Haier Europe Cooking Research and Development Center in Eskisehir / Turkey.

REFERENCES

[1] Cabeza-Gil, I., Calvo, B., Grasa, J., Franco, C., Llorente, S., & Martínez, M. A. (2020). Thermal analysis of a cooking pan with a power control induction system. Applied Thermal Engineering, 180, 115789.

[2] Elduque, D., Javierre, C., Pina, C., Martínez, E., & Jiménez, E. (2014). Life cycle assessment of a domestic induction hob: electronic boards. Journal of cleaner production, 76, 74-84.

[3] Kawakami, H., Llave, Y., Fukuoka, M., & Sakai, N. (2013). CFD analysis of the convection flow in the pan during induction heating and gas range heating. Journal of Food Engineering, 116(3), 726-736.

[4] Kranjc, M., Zupanic, A., Miklavcic, D., & Jarm, T. (2010). Numerical analysis and thermographic investigation of induction heating. International Journal of Heat and Mass Transfer, 53(17-18), 3585-3591.

[5] Teertstra, P., Culham, J. R., & Yovanovich, M. M. (1999, November). Analytical modeling of forced convection in slotted plate fin heatsinks. In ASME International Mechanical Engineering Congress and Exposition (Vol. 26669, pp. 3-11). American Society of Mechanical Engineers.

[6] Gupta, A., Kumar, M., & Patil, A. K. (2019). Enhanced heat transfer in plate fin heatsink with dimples and protrusions. Heat and Mass Transfer, 55(8), 2247-2260.

[7] Cengel, Y. A. (2000). Heat and mass transfer.

[8] Lam, C. K. G., & Bremhorst, K. (1981). A modified form of the k-ε model for predicting wall turbulence.

[9] T. V. Trebunskikh, A. V. Ivanov and G. E. Dumnov, “FloEFD simulation of micro-turbine engine,” Mentor Graphics Moscow, Russia. [Online]. Available: http://cadflo.com/fileadmin/user_upload/Trebunskikh__FloEFD_simulation_of_micro-turbine_engine.pdf

[10] Amirabedin, E., Anık, T., & Karaduman, A. Feasibility of Using CFD Analysis for Improving the Gas Hobs Performance In terms of Efficiency and Emissions.

[11] Kalitzin, G., & Iaccarino, G. (2002). Turbulence modeling in an immersed-boundary RANS method. CTR Annual Briefs, 415-426.

FREQUENCY DEPENDENCE OF ELECTRIC CHARACTERISTICS OF POLYMER BASED MPS DEVICE

A. Büyükbaş-Uluşan[1] and A. Tataroğlu[1]

[1]Department of Physics, Faculty of Science, Gazı University, Ankara, TÜRKİYE

E-mail: aysel.buyukbas@gmail.com

In this paper, CuO–Cu_2O–PVA polymer composite was deposited on on p-Si wafer using spin coating technique. To investigate electric characteristics of Au/polymer/p-Si (MPS) device, the admittance (Y) and impedance (Z) measurements were used. The admittance was made a frequency ranging from 10 kHz to 1 MHz. Then, for each frequency the electric parameters such as V_D, N_A and Φ_B were obtained from special plots which is C^{-2}-V plots. Furthermore, the impedance spectroscopy was carried in between 10 Hz-1 MHz and at 0.1, 0.2 and 0.3 V applied dc biases. By using the impedance measurements, other device parameters such as R_p, C_p and R_s were obtained.

Keywords: MPS device, Frequency dependent, Equivalent circuits model, Impedance properties, Cole-Cole plots

1. INTRODUCTION

Metal-semiconductor (MS) is one of the most extensively semiconductor. Metal-polymer-semiconductor (MPS) structure is formed using polymer/organic films as an interlayer between metal and semiconductor [1-5]. The films can form easily on a variety of substrates. Polymers are used instead of the traditional insulating interfacial layers, especially because they are easy to manufacture.

Polymers such as polyvinyl alcohol (PVA) and polyvinyl-pyrrolidone (PVP) are one of organic materials used as electrical insulation in electrical applications. Polymers are also used in many electronic applications, including batteries, sensors and semiconductor devices [6]. Polymers have low conductivity and dielectric permittivity. Therefore, to improve the electrical properties, different metals or other additives are added to polymers. Especially, PVA polymer has numerous advantages such as low cost, very low toxicity and easy production. Polymer films will be prepared by utilizing different techniques, which are called drop-coating, ink printing, electrospinning, dip-coating, spin coating and spraying.

The admittance measurements ($Y=G+i\omega C$) are carried out at a wide voltage and frequency range [7]. Impedance ($Z=1/Y$) is the response of basic electronic components/devices such as transistor, capacitor, resistor and diode used in electronic circuits to an applied potential. These components are built on a semiconductor substrate and are connected to create an electrical circuit. The electrical parameters of the device are analyzed using complex impedance spectroscopy.

The present article aims to determine the electric parameters, including diffusion potential, acceptor concentration, barrier height, parallel resistor, parallel capacitor and series resistance of Au/CuO–Cu_2O–PVA/p-Si (MPS) device by using two different methods including admittance and impedance measurements. Moreover, the effect of frequency on these measurements were studied.

2. MATERIAL AND METHODS

The preparation of CuO-Cu_2O-PVA polymer composite material is similar to the one given in [8]. In this study, the film was prepared on p-Si wafer. The admittance of the Au/polymer/p-Si (MPS) device was measured utilizing HP 4192A LF Impedance Analyzer. Furthermore, the impedance was measured utilizing Solartron SI1260 Impedance Analyzer and Solartron 1296 Dielectric Interface.

3. RESULTS AND DISCUSSION

Admittance measurements

Figures 1 and 2 demonstrate capacitance-voltage (C-V) and conductance-voltage (G/ω-V) curves with the applied forward and reverse biases for various frequencies, respectively. It is clear that the C and G are a function of frequency. The value of C and G/ω decreases as the frequency rises. This result has shown us the presence of interface traps [1],[3],[8-10]. Moreover, while the measured capacitance does not change with the gate voltage at the negative voltages, it decreases at the positive voltages.

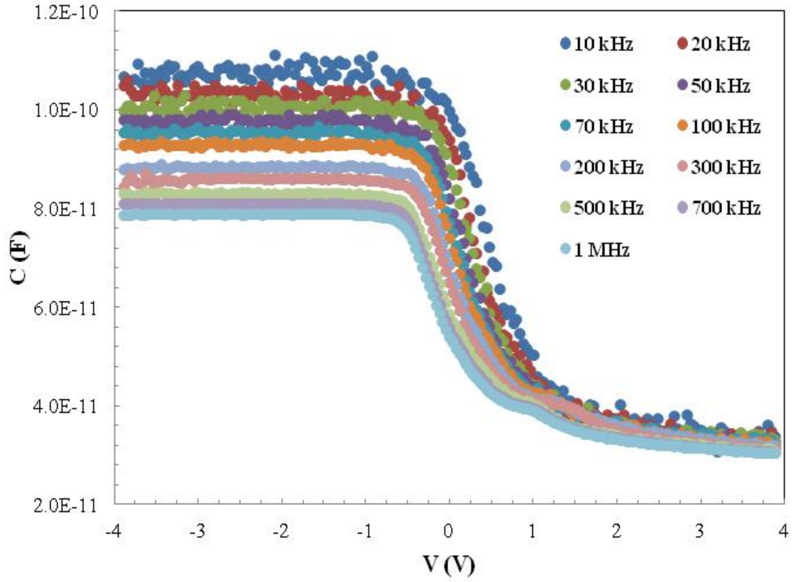

Figure 1. C-V curves.

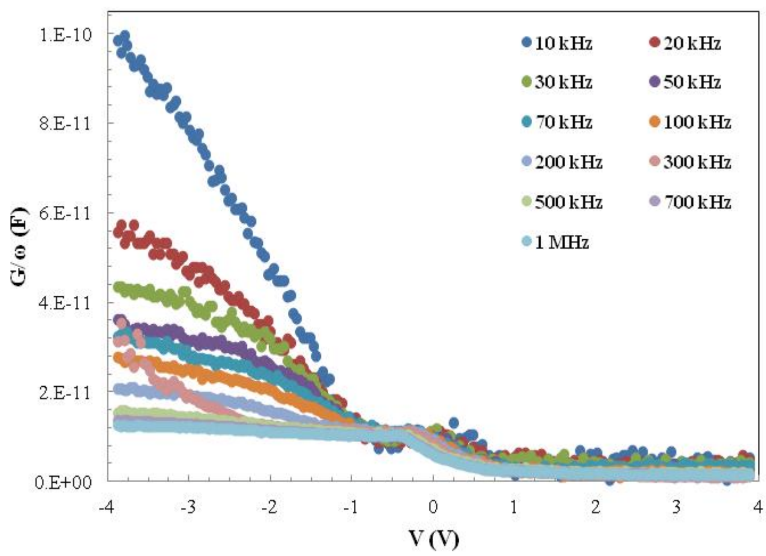

Figure 2. G/ω-V curves.

To calculate some basic parameters which are intercept voltage (V_o), diffusion potential (V_D), acceptor concentration (N_A), barrier height (Φ_B) and depletion layer width (W_D), C^{-2} versus V characteristics were used. Figure 3 illustrates C^{-2}-V curves. These plots indicate a straight line at positive voltage region.

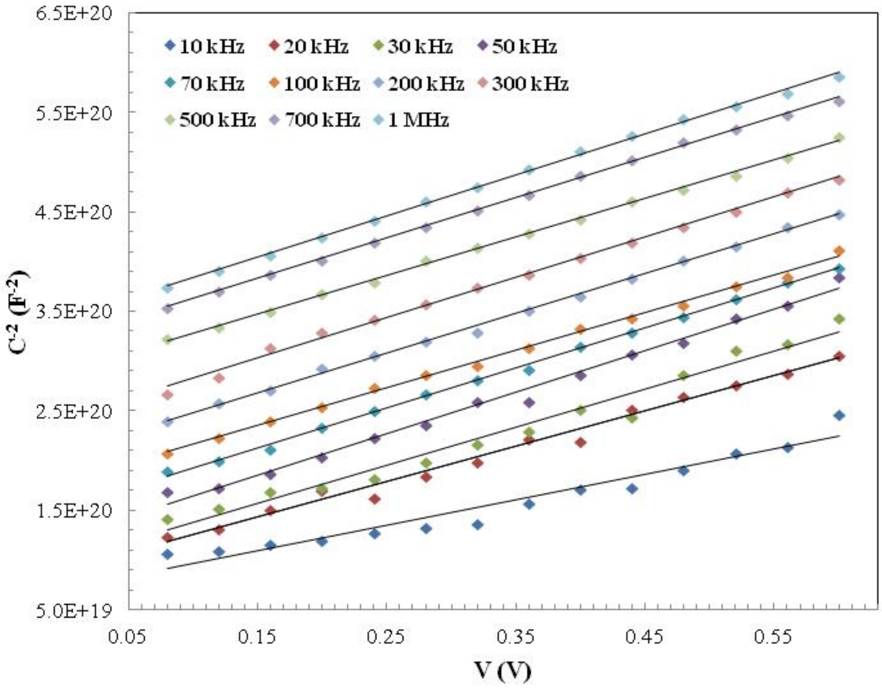

Figure 3. C^{-2}-V curves.

The depletion layer capacitance can be written as follows [1],[11],

$$C^{-2} = 2\,(V_o + V_R)/(q\varepsilon_s\varepsilon_o A^2 N_A) \tag{1}$$

$$\tan\theta = d(C^{-2})/dV_R = 2/(q\varepsilon_s\varepsilon_o A^2 N_D) \tag{2}$$

Here, V_D ($=V_0 + kT/q$) and $N_A = 2/(q\varepsilon_s\varepsilon_0 A^2 slope)$ values are derived from the linear part of C^{-2}-V curve where the intercept and slope are V_D and N_A, respectively. The x-intercept of the plot is V_0. Besides, Φ_B and W_D value can be determined from the following equations. This technique is reliable in estimating barrier height.

$$\Phi_B = V_D + \frac{kT}{q}Ln\left(\frac{N_V}{N_A}\right) - \Delta\Phi_B = V_D + E_F - \Delta\Phi_B \tag{3}$$

$$\Delta\Phi_B = \left[\frac{qE_m}{4\pi\varepsilon_s\varepsilon_0}\right]^{1/2} \qquad E_m = \left[\frac{2qN_AV_0}{\varepsilon_s\varepsilon_0}\right]^{1/2} \qquad W_D = \sqrt{\frac{2\varepsilon_s\varepsilon_0V_D}{qN_A}} \tag{4}$$

Table 1 tabulated the V_0, V_D, N_A, Φ_B and W_D value for numerous frequencies at room temperature. While the increment at the frequency increases value of Φ_B, N_A value decreases due to the existence of interface states [8-9]. The increase in barrier height with decreasing dopant concentration is due to the effect of interface states.

Table 1. The calculated various parameters of the MPS structure.

F(Hz)	V_0(V)	V_D(eV)	N_A(cm^{-3})	Φ_B (eV)	W_D (cm)
10000	0.246	0.272	$4.73x10^{13}$	0.586	$2.75x10^{-4}$
20000	0.249	0.274	$3.40x10^{13}$	0.597	$3.26x10^{-4}$
30000	0.242	0.268	$3.13x10^{13}$	0.593	$3.36x10^{-4}$
50000	0.290	0.316	$2.88x10^{13}$	0.642	$3.80x10^{-4}$
70000	0.379	0.405	$2.99x10^{13}$	0.730	$4.22x10^{-4}$
100000	0.473	0.498	$3.19x10^{13}$	0.822	$4.53x10^{-4}$
200000	0.520	0.546	$3.01x10^{13}$	0.871	$4.88x10^{-4}$
300000	0.595	0.621	$2.97x10^{13}$	0.946	$5.24x10^{-4}$
500000	0.747	0.773	$3.11x10^{13}$	1.096	$5.72x10^{-4}$
700000	0.793	0.818	$2.96x10^{13}$	1.143	$6.03x10^{-4}$
1000000	0.832	0.857	$2.92x10^{13}$	1.182	$6.21x10^{-4}$

Impedance measurements

Impedance spectroscopy (IS) is one of techniques used to characterize the electrical behavior of a device. In this technique, the impedance measurements are performed in a large frequency range. The electronic device can be symbolized by a parallel RC circuit given in Figure 4. Here, R_p, C_p and R_s represent the parallel resistance, parallel capacitor and series resistance, respectively.

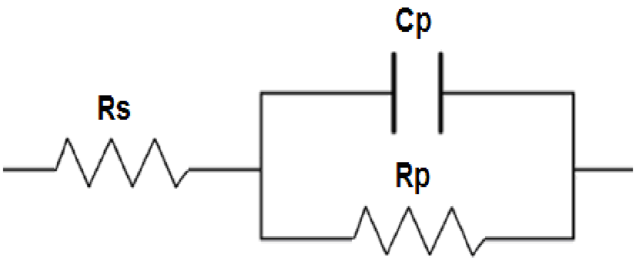

Figure 4. Equivalent circuit of MPS structure.

In general, the complex impedance (Z*) of the equivalent circuit is written as [12-14],

$$Z^* = ReZ + ImZ = Z' + iZ'' = R_s + \frac{R_p}{1+i\omega R_p C_p} \tag{5}$$

The real (Z') and imaginary (Z") parts of the Z* are given as follows,

$$ReZ = Z' = \left[R_s + \frac{R_p}{1+(\omega R_p C_p)^2}\right] \tag{6}$$

$$-ImZ = Z'' = \left[\frac{\omega R_p^2 C_p}{1+(\omega R_p C_p)^2}\right] \tag{7}$$

The variations of ReZ and ImZ of Z* with frequency at 0.1, 0.2 and 0.3 V dc biases were given in Figure 5(a) and (b). ReZ and ImZ values increase with decrease in applied dc biases. The change with the frequency of these plots is different from each other. The values of ReZ firstly remain constant, and then decrease rapidly with increasing frequency. Firstly, the ImZ value increases as the frequency rises and give a peak, and then decrease with further increment. So, as seen in Fig. 5(b), a peak is observed for the whole ImZ vs f plots [12-13], [15-16].

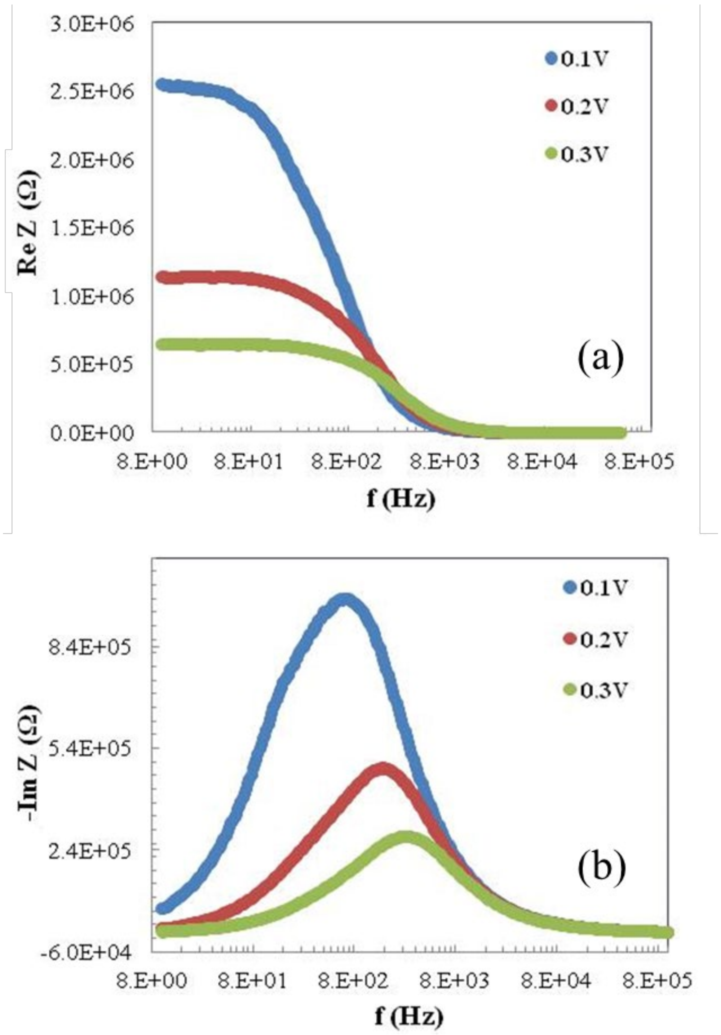

Figure 5. (a) ReZ-f and (b) ImZ-f curves.

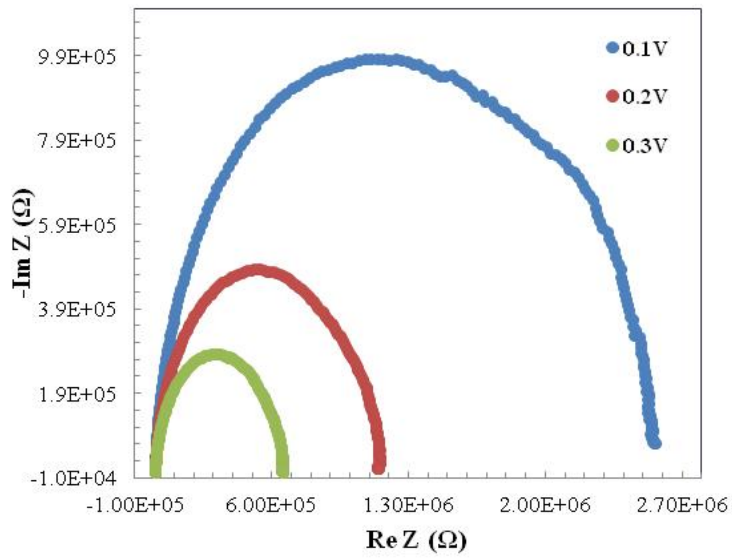

Figure 6. Cole-Cole plots.

In addition, the Cole-Cole plots (-Im Z versus Re Z) at various applied dc biases are illustrated in Figure 6. These plots are shown a single semicircle in each dc biases. The radius ad size of the semicircles increases with decreasing dc biases. Consequently, the MPS structure may be modeled with the equivalent circuit given in Figure 4.

The fitting parameters which are determined with utilizing fitting the single semicircles are shown in Table 2. C_p value remains almost constant with the change of the dc bias voltage. R_p value decreases rapidly with an increase in the dc bias voltage. This decrease is result of the increase in the amount of charge carriers injected into the device with the bias increment [16-17].

Table 2. The calculated values of R_s, R_p and C_p for the device

Voltage (V)	**R_s (Ω)**	**C_p ×10^{-11} (F)**	**R_p ×10^{+5} (Ω)**
0.1	102.4	8.15	21.0
0.2	111.2	8.17	10.3
0.3	144.5	8.31	6.06

The current transport mechanism of the MPS were analyzed using impedance spectroscopy. The dependence of R_p on V voltage was investigated. The voltage-dependent R_p is given by $R_p \propto V^{-m}$. The m represents the conductivity of major charge carriers in the device. m > 1 and m = 1 should be for the space charge limited current (SCLC) theory with exponential trap distribution and trap free, respectively. Figure 7 presents plot of log R_p vs log V curve of the device. The R_p decreases linearly. From the slope of this curve, the m value was found to be 1.12. This result is shown the conductance of the charge carriers follows the SCLC [18-19].

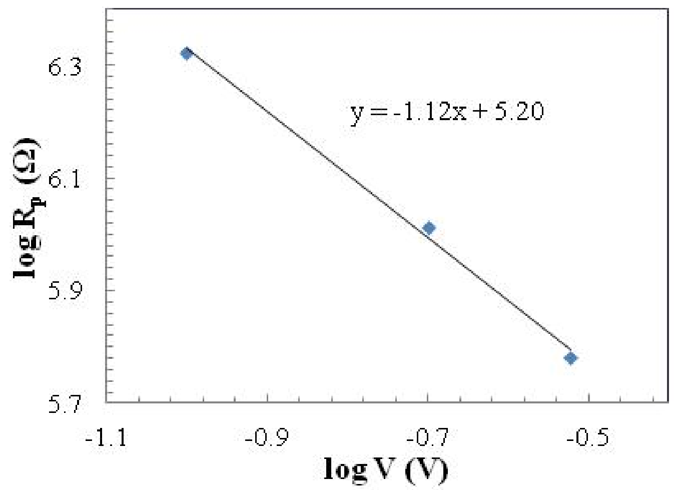

Figure 7. Log R_p-log V curve.

4. CONCLUSION

Electrical properties of Au/polymer/p-Si (MPS) device were studied in this research by utilizing the admittance and impedance spectroscopy methods. The admittance measurements were occurred the C-V and G/ω-V measurements. From the C^{-2}-V characteristics, the V_D, N_A, Φ_B, and W_D value are found as 0.272 eV, 4.73×10^{13} cm^{-3}, 0.586 eV, 9.78×10^{13} $cm^{-2}eV^{-1}$, 2.75×10^{-4} cm at 10 kHz and 0.857 eV, 2.92×10^{13} cm^{-3}, 1.182 eV, 1.58×10^{14} $cm^{-2}eV^{-1}$, 6.21×10^{-4} cm at 1 MHz, respectively. In addition, the impedance measurements were modeled by equivalent electrical circuit. The Cole-Cole plots were used to obtain other parameters, including as R_p, C_p, and R_s. The value of R_p decreases while C_p remains almost constant with the change of the dc biases. In addition, the variation of R_p with applied dc biases indicated that the transport mechanism of the MPS device was SCLC.

REFERENCES

[1] Sze S M, 1981. Physics of Semiconductor Devices, Wiley.

[2] Rhoderick E H, Williams R H, 1988. Metal-Semiconductor Contacts, Oxford University Press, Oxford.

[3] Nicollian E H, Brews J R, 1982. MOS Physics and Technology, Wiley,

[4] Nicollian E H, Goetzberger A, 1965. *Appl. Phys. Lett*., 7, 216.

[5] Chybicki M, 1977. Electrical Properties of Metal–Polymer–Metal (MPM) and Metal–Polymer–Silicon (MPS) Structures with Thin Polymer Films, *Phys. Status Solidi,* (A) 39:271-279.

[6] Hashim Abbass A, 2010. Polymer Thin Films, In Tech.

[7] Tataroğlu A , Altındal Ş, Azizian-Kalandaragh Y, 2020. C-V-f and G/ω-V-f characteristics of Au/(In_2O_3-PVP)/n-Si (MPS) structure. Physica B: Condensed Matter, 582: 411996.

[8] Buyukbas Ulusan A, Tataroğlu A, Azizian-Kalandaragh Y, Altındal Ş, 2018. On the conduction mechanisms of Au/(Cu_2O-CuO–PVA)/n-Si (MPS) Schottky barrier diodes (SBDs) using current–voltage–temperature (I-V-T) characteristics. *J Mater Sci: Mater Electron*, 29: 159-170.

[9] Tanrıkulu H, Tataroglu A, Tanrıkulu E, Buyukbas Ulusan A, 2018. Electrical characterization of MIS diode prepared by magnetron sputtering. *IJPAP*, 56.

[10] Ata D, Altindal Yeriskin S, Tataroglu A, Balbasi M, 2022. Analysis of admittance measurements of Al/Gr-PVA/p-Si (MPS) structure. *J. Phys. Chem. Solids*, 169: 110861.

[11] Tataroglu A, Buyukbas Ulusan A, Altındal Ş, Azizian-Kalandaragh Y, 2021. A Compare Study On Electrical Properties of MS Diodes With And Without Cofe2o4-Pvp Interlayer, *J. Inorg. Organomet. Polym. Mater*., 31:1668–1675.

[12] Tecimer H, Tan S O, Altındal Ş, 2018. Frequency-dependent admittance analysis of the Metal–Semiconductor Structure with an interlayer of Zn-doped organic polymer nanocomposites. *IEEE Transactions on Electron Devices*, 65: 231-236.

[13] Buyukbas A, Tataroğlu A, Balbaşı M, 2014. Analysis of Electrical Characteristics of Metal-Oxide-Semiconductor Capacitor by Impedance Spectroscopy. *J. Nanoelectron. Optoelectron.*, 9: 515-519.

[14] Liu Y, Liu A, Hu Z, Liu W, Qiao F, 2012. Impedance Spectroscopy Studies On Cupc/N-Si Hybrid Solar Cell, *J. Phys. Chem. Solids,* 73:626–629.

[15] Lvovich V F, 2012. Impedance Spectroscopy, Wiley.

[16] Trad H, Rouis A, Davenas J, Majdoub M, 2014. Optical and electrical properties of bi-layers organic devices*. Eur. Phys. J. Appl. Phys*., 68: 10103.

[17] Bi-Xin L, Jiang-Shan C, Yong-Biao Z, Dong-Ge M, 2011. Frequency-Dependent Electrical Transport Properties of 4, 4', 4''-Tri(*N*-carbazolyl)-Triphenylamine Investigated by Impedance Spectroscopy. *Chin. Phys. Lett*., 28: 057201.

[18] Ramar M, Rawat S S, Srivastava R, Suman C K, 2017. AC Impedance Spectroscopy Studies of PtPc Doped Alq3 Thin Film. *Recent Trends in Materials Science and Applications*, 383-390.

[19] Campbell A J, Bradley D D C, Lidzey D G, 1997. Space-charge limited conduction with traps in poly(phenylene vinylene) light emitting diodes, *J. Appl. Phys*.82: 6326.

AN *IN-SILICO* APPROACH TO IDENTIFY POTENTIAL NATURAL COMPOUNDS AS PESTICIDES AGAINST TOMATO MOSAIC VIRUS

N. Gürbüz Çolak[1], *A. Hürriyet Bozdağ*[2]

[1]*Department of Molecular Biology and Genetics, Faculty of Science, İzmir Institute of Technology, İzmir, TÜRKİYE*
[2]*Department of Biotechnology, Enza Zaden Agriculture R&D, Antalya TÜRKİYE*

E-mail: nergizgurbuz@iyte.edu.tr

Tomato plant (*Solanum lycopersicum* L.) is a globally valuable crop. However, it is susceptible to *Tomato Mosaic Virus* (ToMV), which causes a destructive disease that results in significant losses. ToMV belongs to the Tobamovirus genus which can infect a wide range of hosts. ToMV is mainly spread through contaminated seeds or tools as well as through contact with infected plants or materials used by farmers. To manage this disease, infected plants should be excluded, certified virus-free seeds or seedlings should be used, and ToMV-resistant plant cultivars should be selected, because there is no pesticide against the disease. Natural compounds have been explored as pesticides to reduce harm to humans. Molecular docking, an *in-silico* technique that allows the identification of the most favorable binding mode of a ligand to a protein with a predetermined three-dimensional structure, plays a crucial role in computer-aided drug design in medicine and as well as in agriculture. In this study, more than 3000 natural compounds in the MPD3 database were scanned using AutoDock Vina. The aim was to determine their potential binding affinity to the viral helicase enzyme (PDB ID:3vkw), which plays a role in viral RNA replication in ToMV. A threshold of -9.0 kcal/mol binding energy was used for the assessment. Candidates were filtered based on binding energies and ADME properties according to Lipinski's rule of five using the DruLiTo software. Finally, the ProTox II online server was used to evaluate toxicity. There are three natural compounds, namely Newbouldiaquinone A, withanolide F, and heraclenol, that bind to the helicase with a binding affinity of -9.2 kcal/mol, -9.0 kcal/mol, and -9.0 kcal/mol, respectively. These compounds were in accordance with Lipinski's rule of 5, and showed no signs of toxicity. Therefore, they can be utilized to manage tomato mosaic disease.

Keywords *Solanum lycopersicum*, Tomato Mosaic Virus, Pesticide, Natural compounds, Molecular Docking

1. INTRODUCTION

Tomato (*Solanum lycopersicum* L.) is a vegetable that belongs to the Solanaceae family and is widely cultivated all over the world. In 2021, the global production of tomatoes reached 189 million tons, making it the most produced vegetable [1]. In addition to their economic significance, tomatoes are also essential because of their bioactive substances and nutritional properties. Additionally, it can be consumed fresh or processed into soup, sauce, paste, or powder concentrate [2].

The decline in the quality and yield of tomatoes is attributed to the impact of various pathogens and diseases, including *Tomato Mosaic Virus* (ToMV), which is a member of the Tobamovirus genus. ToMV is known to cause a destructive disease in tomatoes, termed tomato mosaic disease, which spreads through contaminated seeds or tools, such as scissors and clothing, as well as contact with infected plants or materials. Seed transmission is a major contributor to the spread of the disease because contaminated seeds can lead to infection during transplantation. To control the disease, farmers should remove infected plants, use certified virus-free seeds or seedlings, and select ToMV-resistant plant cultivars, because there are no pesticides available to combat the disease. ToMV is a global issue, as it has been reported in almost all regions where tomato production occurs. Although ToMV does not generally cause plant death, it can lead to severe symptoms such as inhibition of shoot and root growth, as well as various symptoms on fruits and leaves, ultimately resulting in reduced yield and significant economic losses.

Pests, including viruses, can cause a significant loss in crop yield. The Food and Agriculture Organization (FAO) recently reported that pesticide usage annually causes up to a 40% loss in total crop production worldwide. These losses have serious economic consequences. Although chemical pesticides are effective in controlling plant pathogens, they also have adverse effects on agricultural fields, water resources, and the environment. Moreover, they are harmful to humans [7]. Chemical pesticides not only reduce the diversity of microorganisms in the soil, but also have negative effects on the environment and are toxic to humans [8]. Researchers are currently exploring natural compounds as pesticides to mitigate the harmful effects of chemical pesticides. Unlike chemical pesticides, natural compounds offer environmentally friendly, sustainable, target-specific, inexpensive, and safer alternatives [9]. It is challenging to evaluate the biological activity of the vast number of secondary metabolites produced by plants, which exceeds 100,000. However, molecular docking is a computational technique that enables the determination of the most favorable binding mode of a ligand to a protein with a predetermined three-dimensional structure based on binding energies. Therefore, this technique is useful for the identification of potential candidates.

In the current study, the potential antiviral properties of natural compounds stored in the MPD3 database were examined for their potential to interact with the helicase enzyme of the virus. Following a rigorous screening process, a set of candidates were selected based on multiple criteria. Natural pesticides with the potential to combat mosaic tomato viruses were identified.

2. MATERIAL AND METHODS

Molecular docking was used to determine the binding energies of the natural compounds in this study. A total of 3,150 natural compounds were obtained as .mol files from the MPD3 database and the binding energies of these compounds to the ToMV helicase enzyme were determined using Autodock vina in PyRx virtual screening software. The ligand files were then converted to .pdbqt format after energy minimization and the helicase enzyme (PDB ID:3vkw) was downloaded in .pdb file format from the "RCSB Protein Data Bank" and was used as a rigid molecule. Protein preparation was carried out in "BIOVIA Discovery Studio 2021" software by removing hetero and water molecules, adding hydrogen atoms and then converted to .pdbqt file. Docking studies were performed using PyRx is virtual screening software with a grid box set to cover the active site of the protein. In filtering according to the binding energy, the threshold was taken as -9 kcal/mol.

After filtering the candidates based on their absorption, distribution, metabolism, and excretion (ADME) properties, which helped determine the drug-likeness of the compounds according to Lipinski's Rule of Five (Ro5) using DruLiTo software, the physiochemical properties of the candidates were calculated, including their molecular weight (MW), molar refractivity, logarithm of partition coefficient (LogP), number of hydrogen bond acceptors (HBA), and number of hydrogen bond donors (HBD). To evaluate the toxicity of the candidates *in-silico*, the ProTox II online server was used, and conical smile files of the compounds were employed. The oral toxicity, organ toxicity (hepatotoxicity), mutagenicity, carcinogenicity, cytotoxicity, and immunotoxicity of the selected candidates were evaluated.

3. RESULTS AND DISCUSSION

In the present study, the helicase enzyme of Tomato Mosaic Virus was targeted to identify pesticide candidates derived from natural compounds. This is because helicases are ubiquitously present in the genomes of all living organisms and play a crucial role in gene replication, including viral replication, by unwinding nucleic acid duplexes [12]. To identify potential candidates, a molecular docking technique was employed with a binding energy threshold of -9 kcal/mol. The results of the first filtration, based on these binding energies, are presented in Table 1. A total of 31 out of 3,150 natural compounds bound to the viral helicase enzyme with a binding energy of -9 kcal/mol or lower.

Table 1. Candidates after the first filtration based on binding energies.

Compound Name	**Binding Energies (kcal/mol)**
Styraxlignolide B	-10,3
Physalin H	-9,9
Quercetin-3-O-alpha-D-arabinopyranoside	-9,6
Cassiamin A	-9,6
Reynoutrin	-9,5
8-hydroxymanzamine A	-9,5
6-hydroxymanzamine A	-9,5
Ozturkoside A	-9,5
Myricetin 3-galactoside	-9,5
Limonin	-9,4
Oriciacridone F	-9,4
5,7,4'-Trihydroxyflavanone 7-O-arabinosylglucoside	-9,4
Chaetoglobosin U	-9,4
Jujuboside B	-9,4
Cytoglobosin E	-9,3
Chaetoglobosin F	-9,3
Nigrasin B	-9,3
Ozturkoside B	-9,3
Caryophyllene oxide	-9,3
Desmodol	-9,3
Daphneside	-9,2
Oboflavanone B	-9,2
Nigrolineaxanthone I	-9,2
Newbouldiaquinone A	-9,2
Neocandenatone	-9,1
Chaetoglobosin R	-9,1
Withanolide F	-9,1
Heraclenol	-9
Hypericin	-9
Withanolide E	-9
Avicularin	-9

The second filtering process was conducted based on the ADME properties, considering Lipinski's Rule of Five (Ro5). Ro5 is used to determine the oral bioavailability and membrane permeability of a compound. Molecular descriptors are incorporated into this rule. Therefore, the candidate's molecular weight must be less than 500 Da, its LogP (hydrophobicity) must be less than 5, the number of hydrogen bond donors must be less than 5, and the number of hydrogen bond acceptors must be less than 10. Candidates that comply with these criteria were deemed to have acceptable solubility and cell permeability. Although Ro5 is designed for drugs, these rules can also be applied to agrichemicals such as pesticides [13].

Table 2. Candidates meeting Lipinski's rule of five.

Compound Name	MW	LogP	HBA	HBD
Caryophyllene oxide	220.18	4.607	1	0
Withanolide F	470.27	2.448	6	3
Withanolide E	486.26	1.363	7	3
Nigrolineaxanthone I	392.13	3.115	6	2
Nigrasin B	454.16	1.893	8	4
Newbouldiaquinone A	410.08	1 .92	6	1
Limonin	470.19	1.565	8	0
Heraclenol	304.09	0.833	6	2
Desmodol	366.11	2.832	6	3

A risk assessment is a critical aspect of pesticide development. In this study, *in-silico* toxicity analysis was conducted to evaluate the potential adverse effects of the identified pesticide candidates on human health. The oral toxicity assay was performed to determine acute toxicity, whereas the hepatotoxicity assay was used to evaluate whether the compounds would cause liver failure. A carcinogenicity assay was conducted to determine whether the compounds would trigger tumor formation, and an immunotoxicity assay was used to evaluate whether they would have adverse effects on the immune system. Additionally, a mutagenicity assay was performed to determine whether the compounds caused DNA and cell damage. The cytotoxicity of the candidates was evaluated to determine whether they would cause a deficit [14]. The toxicity profiles of the candidate pesticides are presented in Table 3.

Table 3. Toxicity assessment of the candidates

Compound Name	Oral Toxicity	Hepatoxicity	Carcinognity	Immunotoxicity	Mutagenity	Cytotoxicty
Caryophyllene oxide						
Withanolide F						
Withanolide E						
Nigrolineaxanthone I						
Nigrasin B						
Newbouldiaquinone A						
Limonin						
Heraclenol						
Desmodol						

*Color code; green: non-toxic, yellow: acceptable, red: toxic

*Candidates after filtration were written in red.

4. CONCLUSION

Although tomato mosaic virus (ToMV) inflicts significant economic losses, current control measures are limited. To date, no specific pesticides have been developed to eradicate this disease. Nevertheless, environmental and public health must be considered when managing this disease. Therefore, if future pesticides are to be developed to combat ToMV, natural compounds should be prioritized. In this study, potential natural compounds that may be effective against ToMV were identified using *in-silico* analysis. Additionally, the study found that natural compounds targeting the helicase enzyme of the virus have not been previously reported in the literature. Thus, this study serves as a pioneer for future research.

ACKNOWLEDGMENTS

This study was executed by Enza Zaden Agriculture and the İzmir Institute of Technology corporation.

REFERENCES

[1] FAOSTAT Agricultural Production Statistics 2000–2021, in FAOSTAT Analytical Brief 60.

[2] Gerszberg, A., Hnatuszko-Konka, K., Kowalczyk, T., K. Kononowicz, A.K., Tomato (*Solanum lycopersicum* L.) in the Service of Biotechnology, Plant Cell, Tissue and Organ Culture, 120, 881–902 2015.

[3] Bhandari, D., Status of Host Resistance Against Selected Viral Diseases of Tomato Crops, Research Journal of Agricultural Science, 6, 7–13, 2018

[4] Aseel, D.G., Rashad, Y.M., Hammad, S.M., Arbuscular Mycorrhizal Fungi Trigger Transcriptional Expression of Flavonoid and Chlorogenic Acid Biosynthetic Pathways Genes in Tomato against *Tomato Mosaic Virus*, Scientific Reports, 9, 9692, 2019.

[5] Ishibashi, K., Kubota, K., Kano, A., Ishikawa, M., Tobamoviruses: Old and New Threats to Tomato Cultivation, Journal of General Plant Pathology, 2023.

[6] CABI (2021), *Tomato Mosaic Virus* (Tomato Mosaic), CABI Compend.

[7] Khursheed, A., Rather, M.A., Jain, V., Wani, A.R., Rasool, S., Nazir, R., Malik, N.A., Majid, S.A., Plant Based Natural Products as Potential Ecofriendly and Safer Biopesticides: A comprehensive Overview of Their Advantages Over Conventional Pesticides, Limitations and Regulatory Aspects, Microbial Pathogenesis, 173, 105854, 2022.

[8] Farooq, M.A., Arif, M.J., Gogi, M.D., Nawaz, A., Atta, B., Comparative Efficacy of Different Pesticide Residue Mitigation Modules in Mango, American Journal of Biomedical Science and Research, 4, 214–219, 2019.

[9] Borges, S., Alkassab, A. T., Collison, E., Hinarejos, S., Jones, B., McVey, E., Roessink, I., Steeger, T., Sultan, M., Wassenberg, J., Overview of the Testing and Assessment of Effects of Microbial Pesticides on Bees: Strengths, Challenges and Perspectives, Apidologie, 52, 1256–1277, 2021.

[10] Verma, N., Shukla, S., Impact of Various Factors Responsible for Fluctuation in Plant Secondary Metabolites, Journal of Applied Research on Medicinal and Aromatic Plants, 2, 105–113, 2015.

[11] Muhammed, M.T., Aki-Yalcin, E., Molecular Docking: Principles, Advances, and Its Applications in Drug Discovery, Letters in Drug Design & Discovery, 1-16, 2022.

[12] Nishikiori, M., Sugiyama, S., Xiang, H., Niiyama, M., Ishibashi, K., Inoue, T., Ishikawa, M., Matsumura, H., Katoh, E., Crystal Structure of the Superfamily 1 Helicase from *Tomato Mosaic Virus*, Journal of Virology, 86, 7565-7576, 2012.

[13] Avram, S., Funar-Timofei, S., Borota, A., Chennamaneni, S.R., Manchala, A.K., Muresan, S., Quantitative Estimation of Pesticide-Likeness for Agrochemical Discovery, Journal of Cheminformatics, 6, 42, 2014.

[14] Banerjee, P., Eckert, A.O., Schrey, A.K., Preissner, R., ProTox-II: A Webserver for the Prediction of Toxicity of Chemicals, Nucleic Acids Research, 46(W1), W257-W263, 2018.

SIMULATION OF BUILDING VENTILATED CONCRETE-SLAB IN COMSOL

S. Razavi[1], M. Özdenefe [1]

[1]Department of Mechanical Engineering, Faculty of Engineering, Eastern Mediterranean University, North Cyprus

E-mail: s.razavi@emu.edu.tr, murat.ozdenefe@emu.edu.tr

This work evaluates the distribution of temperature in standard concrete slab building roofs and compares it to that of ventilated concrete slabs in regions with high diurnal temperature ranges (DTR) during the summertime. The overall contribution of incorporated hollow-core slabs to minimizing the need for air-conditioning-cooling was simulated in a finite element code software, COMSOL Multiphysics 6.0. The models represent a thermal network of heat transfers via convection–conduction between the air at the outside and inside of the room, through the hollow slab, and across the building wall components. The simulation results show that the ventilated concrete slab decreased the room's ceiling temperature by up to 1°C along with an additional 9% increase in the total heat flux through the ceiling, leading to further cooling of the structure as compared to the standard concrete system. It is also observed that the thermal bridge effect is reduced with the incorporated ventilated slab due to the effect of dynamic air passing through the hollow cylinders further increasing the thermal resistance of the structure compared to a traditional one-piece solid roof.

Keywords: Heat transfer, ventilated concrete slab, COMSOL Multiphysics, thermal bridge effect

1. INTRODUCTION

Global warming is a continuing concern [1]. The Global Buildings Climate Tracker [2] reported that the share of CO_2 emission from buildings and construction sector had increased by 1%, risen to a peak of 37% (13.77 gigatons) of the global total CO_2 in 2020, compared to the preceding year [3]. To achieve the Paris Agreement therefore, buildings emissions must almost completely be reduced to zero by 2050 [4]. This seems a challenging task particularly in tropical, subtropical, Mediterranean, and arid regions, where maintaining thermal comfort conditions for people inside the buildings can seem unfeasible without the use of air conditioning systems during the summer.

There is a growing body of literature that recognizes decarbonizing the power supply through renewable sources and increased use of zero-carbon cooling technologies as the most widely adopted approach towards mitigating climate change and carbon upfront impacts from building operations [5]. In this context, natural ventilation techniques through the roof, which is the main section of the building archetype exposed to high intensity solar radiation, has shown to offer promising solutions in reducing the cooling-hours burden that is on the HVAC (heating, ventilation, and condition) systems during summer. In particular, it is reported that ventilated slab systems can be effective to reduce the daytime cooling demand for several types of buildings [6].

This paper, therefore, attempts to investigate the influence of ventilated slabs roof, as a passive cooling strategy, in reducing average surface temperatures of the ceiling – hence, indoor air temperature – and compare that to the case of a traditional solid concrete roof structure. The study also sets out to evaluate the positive influence of incorporated VS roof in lowering the energy consumption of the building which can potentially be counteracted by the negative effect of Thermal Bridging phenomenon at building junctions and corners.

2. MATERIAL AND METHODS

Designing building envelope configurations and optimizations through numerical approach simulations provides viable and cost-effective approaches to calculating the required energy conservation in different building archetypes. The computer software used in this work were EnergyPlus, which is a widely used multi-module energy-related building simulation software, in conjunction with COMSOL Multiphysics, which is a coupled multi-physics solver and finite element analysis (FEA) simulation software.

The data were generated by EnergyPlus, which employs DOE-2 convection model and TARP algorithm to predict the respective outside and inside surface convection heat transfer coefficients (W/m^2-K). Consequently, the predicted T and h values for each building envelope structure (i.e., internal and external wall surfaces, roof, and the ceiling) were used as inputs into COMSOL for simulating surface temperatures and heat transfer performance (i.e., positive or negative heat fluxes). The raw data were based on the weather datasets collected over a period of ten year, although only a 30-days (month June) average temperature dataset was used here for COMSOL simulation (by weather observation stations). Also, due to unavailability of the weather data file for the actual location of the building in the city of Famagusta, Larnaca Airport's data file (35 km SW of Famagusta) was used in EnergyPlus software.

2.1. BUILDING MODEL ENVELOPE

Figure 1 illustrates a perspective view of the generated virtual zone building model in EnergyPlus. This geometry can be divided into four main zones, namely, a) an open space office zone, b) 1st floor north zone, c) 1st floor south zone, and d) ground floor zone. Ground floor zone is a single zone comprising spaces that exist on the ground floor, whereas 1st floor north and south zones involve the halls, toilets, and archive rooms on the first floor. The open space office zone on the other hand contains the open space office on the first floor.

Among these four zones, only a corner section of the building on the second floor was modeled in COMSOL, as shown in Figure 1(a), assuming that the ventilated slab run all the way to the end of the roof. Thus, the FE-model includes two side walls that are facing east–west, and the third connecting wall in-between is facing towards north. The total floor area of the modeled section was 24 m^2 with a ceiling heigh of 3.59 m.

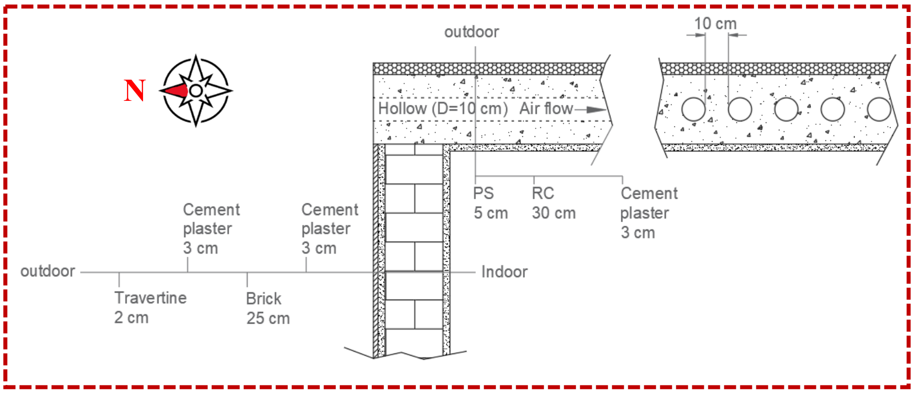

(a)

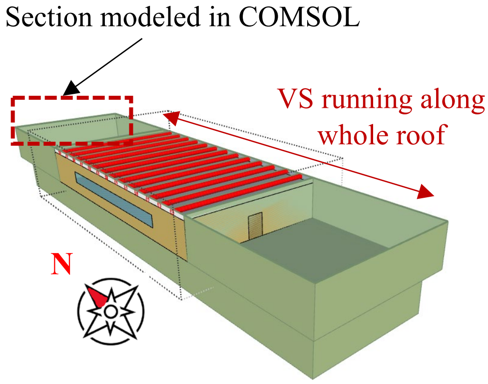

(b)

Figure 1. Building envelope model generated by EnergyPlus. (a) A cross-sectional schematic, and (b) a 3D view of the building zones.

Based on their functionalities, the constituent materials shown in Figure 1(a) can be grouped into two main types: insulation-rendering/cladding, and two load-bearing structural group components. The former group comprises travertine cladding, external and internal cement plaster layers, and outdoor polystyrene (PS) insulation layer; the latter group consists of the two most widely utilized traditional construction materials in Cyprus architypes, which are perforated clay bricks and reinforced concrete (RC). Table 3 summarizes the predicted parameters extracted from the energy simulation and load analysis program EnergyPlus to be used in COMSOL. Based on these data (T and h), the next step was to develop FE-models in COMSOL to simulate temperature distribution and thermal bridging effects (Table 1 and Table 2).

Table 1. Input parameters for temperature distributions simulation in COMSOL.

Types	Solid Slab (SS)				Ventilated Slab (VS)			
Parameters	T_i	T_o	h_i	h_o	T_i	T_o	h_i	h_o
West wall	29.13	25.37	0.85	5.71	27.99	25.24	0.599	5.703
East wall	28.80	38.74	1.12	6.19	27.65	38.62	0.850	6.191
North wall	25.29	26.97	0.627	5.69	25.26	26.97	0.63	5.69
Roof	–	43.84	–	7.29	–	43.68	–	7.28
Ceiling	29.59	–	0.431	–	26.99	–	1.5	–

Table 2. Input parameters for thermal bridge effects simulation in COMSOL.

Types	Solid Slab (SS)				Ventilated Slab (VS)			
Parameters	T_i	T_o	h_i	h_o	T_i	T_o	h_i	h_o
West wall	29.89	23.37	0.996	4.3	28.85	23.25	1.1	4.28
East wall	29.37	25.23	0.77	4.34	28.33	25.11	0.78	4.32
North wall	26.03	22.75	0.74	4.18	26	22.74	0.75	4.18
Roof	–	21.2	–	4.65	–	20.98	–	4.67
Ceiling	29.7	–	0.47	–	27.39	–	1.4	–

Table 3. Typical mechanical and thermal properties of the material used in COMSOL models.

Materials	Travertine	Cement plaster	Brick	Polystyrene	RC
Density (kg/m^3)	2600	2000	700	23	2400
Thickness (cm)	2	3	25	5	30
Thermal conductivity (W/m.K)	2.3	1.4	0.4	0.035	2.2
Heat capacity at constant pressure (J/kg.K)	840	650	840	1470	840

2.1. SIMULATIONS

Four FE-models (Figure 2) and two analyzing scenarios (Table 4) were defined in COMSOL according to the geometrical features in Figure 1(a). The logic behind selecting two different scenarios was based on the occupants' working hours within the office building, which were assumed to be from 08:00am to 17:00pm, during which a mechanical ac system is most likely running actively. Thus, in the first scenario, where the temperature distribution effects are evaluated for both VS and SS systems, only a specific time of the day is considered, which happened to be at 08:00 am when the building be started to be occupied.

In the second scenario, on the other hand, where the thermal bridging effects are compared, a valid conclusion can be made only if the simulation is performed over a continuous timeline, to allow for the heat exchange rate phenomenon (i.e., thermal bridging) to take place over a period of time between cooled slabs (cooled by the air flown inside overnight) and warm air inside of the room. In this case, unoccupied hours between 00:00 to 08:00 am were filtered out from the EnergyPlus output file and averaged over a one-month period (as inputs to the heat flux boundary conditions in COMSOL). To distinguish better between these FE-models with respect to their simulation conditions, hereafter, they will be referred to by their acronyms as **VS$_1$**, **SS$_1$**, **VS$_2$**, and **SS$_2$**.

Table 4. Four models developed for two analysis scenarios.

Analysis Types	Model Types	
	Ventilated Slab (VS)	Solid Slab (SS)
	Averaged over one month period at/between:	
Scenario 1: Temperature distribution	(**VS$_1$**) 08:00am	(**SS$_1$**) 08:00am
Scenario 2: Thermal bridging	(**VS$_2$**) 00:00 – 08:00am	(**SS$_2$**) 00:00 – 08:00am

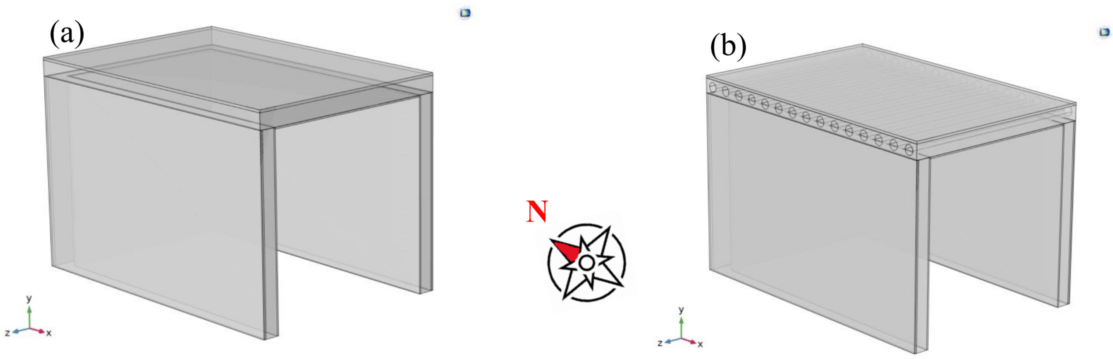

Figure 2. COMSOL models of (a) a solid slab concrete, and (b) a ventilated slab roof.

3. RESULTS AND DISCUSSION

COMSOL Multiphysics 6.0 was used to simulate four FE-models (described in Table 4). The model is an office building with a size of 5.67 m by 3.34 m by 3.62 m (height). The aim was to study and compare the effectiveness of the incorporated VS system in reducing the overall building's energy consumption and occupant thermal comfort through convective heat transfer function from a warmer indoor air medium towards a cooler hollow slab ceiling component. Figure 3 shows the simulation results of all FE-models developed so far, in terms of temperature distribution differences (at 08:00am) between VS$_1$ and SS$_1$ systems, and heat flux (thermal bridging) through roof in models VS$_2$ and SS$_2$, over an eight-hour averaged period between (00:00 to 08:00am).

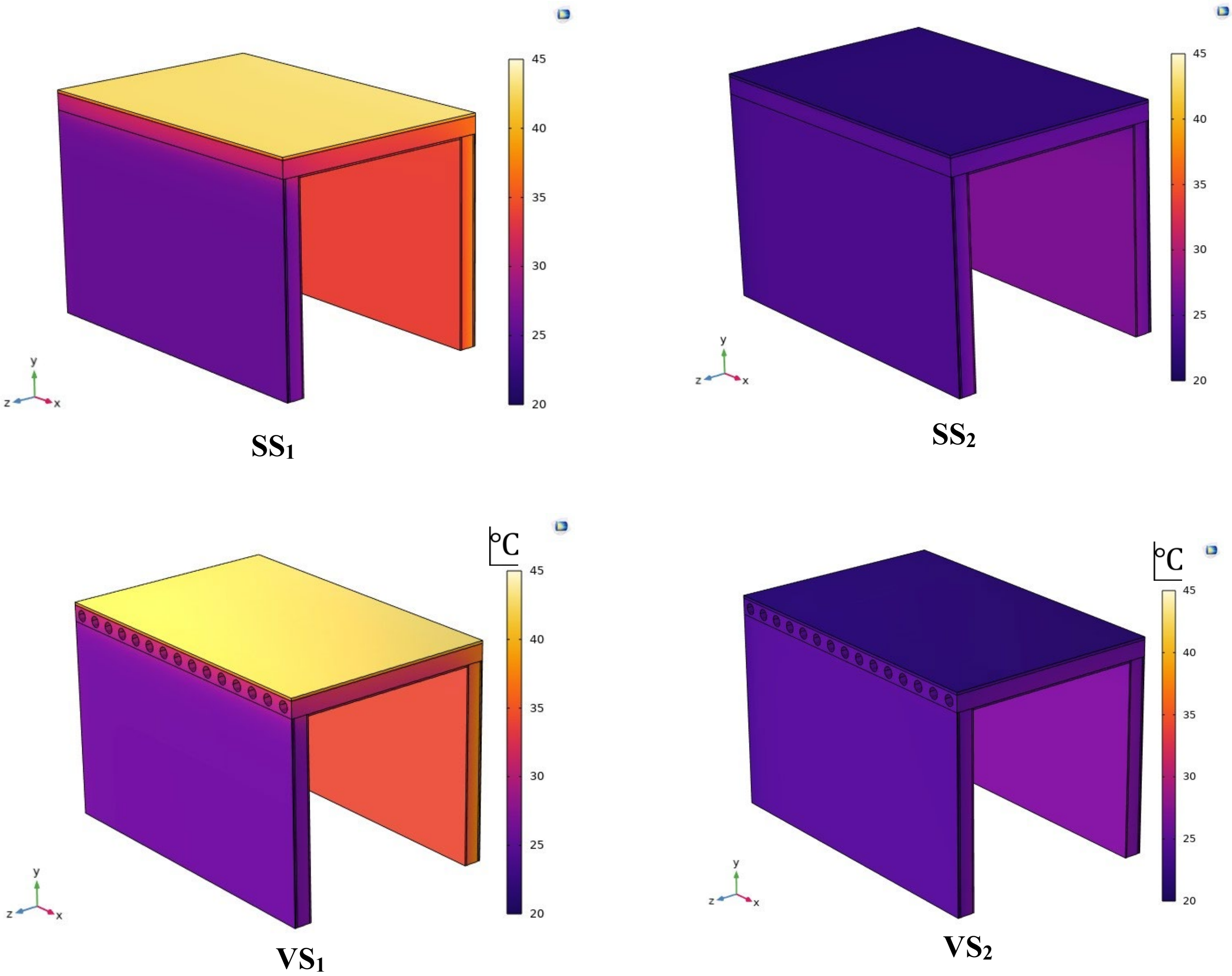

Figure 3. Simulation results for a) temperature distribution effects in SS_1: Solid-Slab roof and VS_1: Ventilated-Slab roof; thermal bridge effects in SS_2: Solid-Slab roof and VS_2: Ventilated-Slab roof models.

Accordingly, the maximum and minimum surface temperatures for all cases are recorded and tabulated in Table 5. It is worth mentioning that the external surface temperatures are excluded here from the results in Table 5. The corresponding graphical results are also shown in Figure 4.

Table 5. Simulation results for the max and min inside surface temperatures.

Types	Minimum Surface Temperature (°C)				Maximum Surface Temperature (°C)			
	West Wall	East Wall	North Wall	Ceiling	West Wall	East Wall	North Wall	Ceiling
SS_1	26.76	31.55	26.12	30.16	30.89	34.94	33.69	34.94
VS_1	26.17	30.98	26.23	29.42	30.02	34.22	32.87	34.22
SS_2	24.12	24.47	22.75	24.05	26.47	26.93	24.1	25.57
VS_2	24.17	24.5	24.07	24.17	26.06	26.45	24.94	25.64

Table 6. Simulation results for max and min heat fluxes between inside surfaces and ambient air.

Types	Minimum Heat Flux (W/m^2)				Maximum Heat Flux (W/m^2)			
	West Wall	East Wall	North Wall	Ceiling	West Wall	East Wall	North Wall	Ceiling
SS_1	-1.49	-6.93	-38.21	-8.35	2.04	-3.1	4.36	-3.29
VS_1	-1.21	-5.58	-4.79	-10.85	1.09	-2.86	-0.61	-3.64
SS_2	3.41	1.88	-5.62	2.29	5.74	3.79	-0.02	4.15
VS_2	3.08	1.48	0.79	2.45	5.16	3.02	1.45	4.5

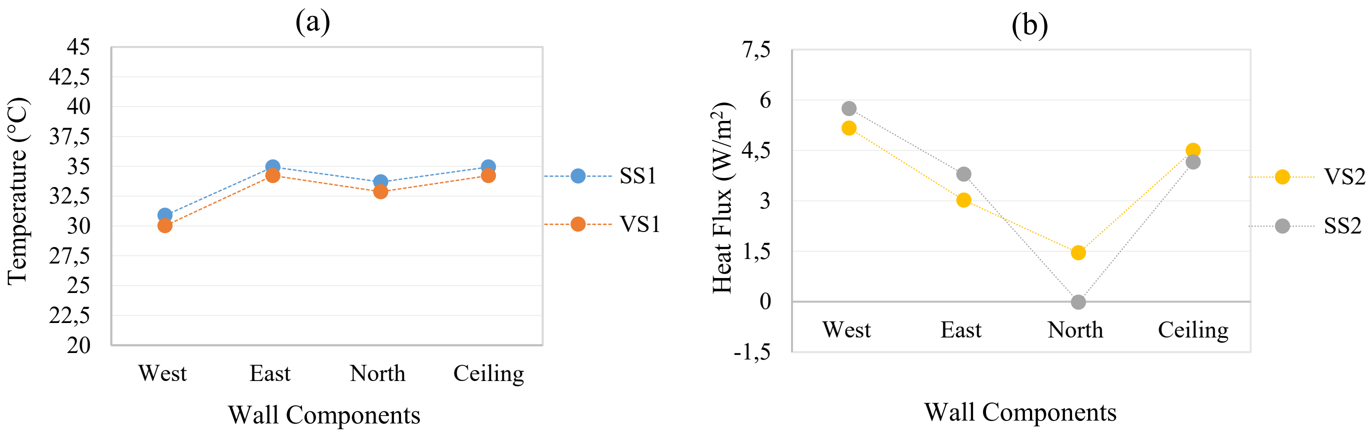

Figure 4. Indoor surface temperatures in (a), and heat flux through roof in (b) for both solid and ventilated slab systems.

As it can be seen from Figure 4, the maximum surface temperature appears to be on the inside surfaces of both east wall and ceiling components for SS_1 (Solid-Slab) roof, having a similar value of 34.94°C on both components. This is while the lowest maximum surface temperature on the opposite wall (west wall) is about

30.89°C. This lower temperature of the latter was to some extent expected, since the former components are directly exposed to the radiation heat from sun at 08:00.

Furthermore, the remaining other two components, i.e., ceiling and north wall, have surface temperatures of around 34.94°C and 33.69°C, respectively, which makes it safe to conclude that the indoor mean air temperature would be somewhere around 33.61°C. This in the case of VS_1 system, however, is lower; around 32.81°C, which further supports the original concept of using VS system as a passive cooling strategy for reducing indoor air temperature and improving the thermal comfort of the occupants (a difference of about 0.8°C). Surprisingly, a similar temperature drop (0.71°C) at ceiling temperatures was achieved for the VS_1 roof with respect to the SS_1 system (Table 5).

The yellow and grey colored curves in Figure 4(b) represent heat flux through the ventilated as well as a solid roof for an average period of eight hours between 00:00 to 08:00. Looking at these two curves for ceiling components in VS_2 and SS_2, it is clear that the ventilated roof has a higher positive heat flux value. A positive heat flux means that heat is flowing from the atmosphere to the surface. This higher heat flux is around 8% more, implying that more heat from indoor air (atmosphere) is being transferred to the surface of the cooled VS_2 ceiling. Interestingly, the correlation between average surface temperature and heat flux magnitude is interesting because a reduction of 0.8°C in average room temperature shows to be in agreement with increased convective heat flux observed for the VS_1 system in Figure 4(b).

Figure 5 illustrates approximate locations where the thermal bridging phenomenon will be prone to occur the most. This result is somewhat counterintuitive, since the effect is usually maximum at the junctions or joints when the insulation layer is interrupted by a more conductive material [7]. Here, a heat flux reduction from approx. 11.97 W/m^2 to 4.5 W/m^2 has been observed for the respective cases of conventional SS_2 and ventilated VS_2 roof. This can be explained by the fact that dynamic air is actively present in the hollow cores, thus, further facilitating convective heat transmission through the slab. This result is in a good agreement with those obtained elsewhere in [8].

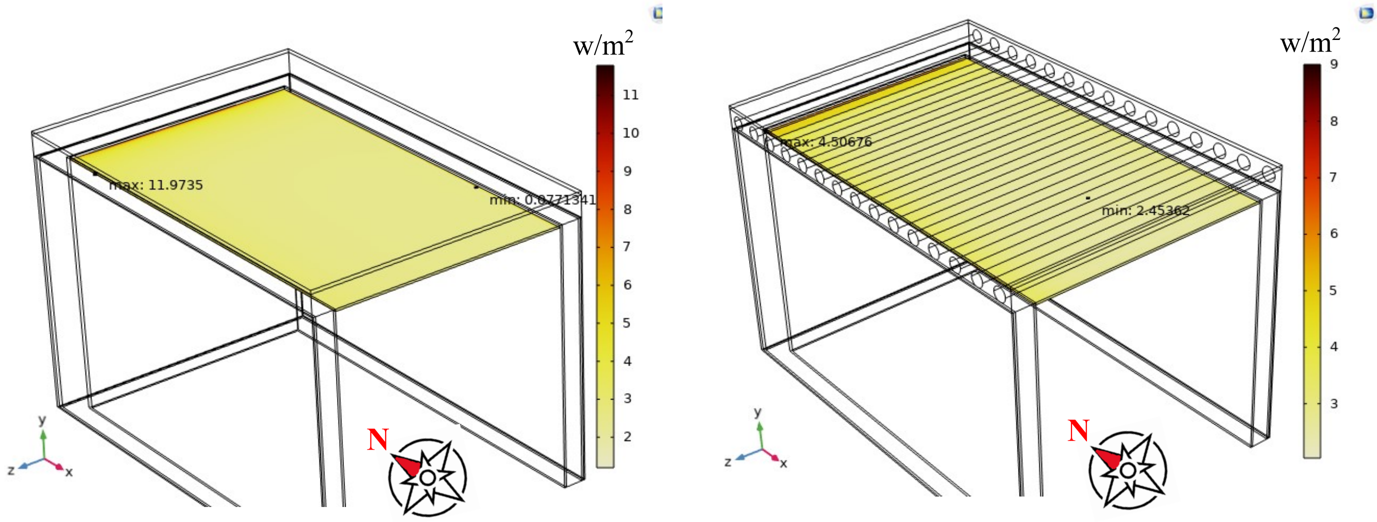

Figure 5. A closed-up view of the junction at which maximum heat flux occurs (thermal bridging).

4. CONCLUSION

This study sets out to predict the effectiveness of using ventilated slab (VS) roof as opposed to traditional solid concrete roof used in arid, tropical, or Mediterranean regions. It was shown that VS that can reduce the building's cooling energy requirements by reducing the surface temperature of the ceiling that is in contact with the indoor air; as well as through increasing convective heat flux by means of dynamic air passing continuously through the hollow slabs. In this investigation, by the help of a numerical simulation software, it was possible to demonstrate that ventilated slab roof archetype can promise a passive cooling functionality when used in conjunction with modern mechanical ac systems so as to reduce cooling loads on these systems.

The simulation results suggested that for an office building of size of 5.67 m by 3.34 m by 3.62 m (height), 15 equally spaced 10-cm diameter hollow cylinders can reduce the mean indoor air temperature of the room by up to 1 °C due to increased convection heat transfer, which in this case was approx. 9% reaching 4.5 W/m^2. This result agrees well with the previous results obtained in [8].

Furthermore, one surprising variable that was found to be significantly associated with the heat flux result was a relative reduction in the thermal bridge effect in ventilated roof (by almost 60 per cent). This relationship may partially be explained by the fact that the structurally uniform longitudinal cylinders in the ceiling acted as a once-piece insulation layer helping to trap local energy to flow towards least thermal resistance path (i.e. junctions and joints due to material discontinuity).

Another reason may be explained by the fact that the thermal conductivity of a solid concrete slab is much higher than ventilated concrete slab – it is worth mentioning that the air thermal conductivity is several times lower than that of concrete. As a result, it is very likely that a ventilated slab can act as a secondary insulation layer hindering easy accumulation of all heat source bundles to reach across the ceiling to the junctions or intersections at which the thermal bridging phenomenon is most likely to occur.

5. REFERENCES

[1] C. Delmastro, "Is cooling the future of heating?," 13 December 2020. [Online]. Available: https://www.iea.org/commentaries/is-cooling-the-future-of-heating. [Accessed 18 September 2023].

[2] UN, United Nation Environment Programme, 2021 Global Status Report for Buildings and Construction: Towards a Zero-emission, Efficient and Resilient Buildings and Construction Sector, Nairobi: Global Alliance for Buildings and Construction, 2021.

[3] European Commission (2021c), "Energy performance of buildings directive," European Commission, 2021. [Online]. Available: https://ec.europa.eu/energy/topics/energy-efficiency/energy-efficient-buildings/energy-performance-buildings-directive_en. [Accessed 17 Septermber 2023].

[4] F. Birol, "World Energy Investment 2021," June 2021. [Online]. Available: https://www.iea.org/reports/world-energy-investment-2021. [Accessed 17 September 2023].

[5] W. Yuxing and W. Chunyu, "Design optimization of office building envelope based on quantum genetic algorithm for energy conservation," *Journal of Building Engineering,* vol. 35, 2021.

[6] M. Özdenefe, S. A. Mousavi and U. Atikol, "Ventilated slabs: Energy consumption mitigation and thermal comfort augmentation," *IOP Conference Series: Materials Science and Engineering,* vol. 609, no. 7, p. 6, 2019.

[7] L. Whale, "Thermal Bridging Guide," Zero Carbon Hub, London, 2016.

[8] V. Kumar, "This is because dynamic air is prevalent in the ventilation and there of a ventilated cool roof with air gap as a thermal barrier," *Springer: Environment, Development and Sustainability,* vol. 25, no. https://doi.org/10.1007/s10668-022-02184-y, p. 14, 2022.

RANKING OF RISKS IN CONSTRUCTION INDUSTRY ACCORDING TO THEIR INDEX VALUES: EXPLORATORY RESEARCH IN CYPRUS

O. Kırılmaz

Department of Industrial Engineering, Faculty of Engineering, Eastern Mediterranean University, Gazimağusa, KKTC

E-mail: oguzhan.kirilmaz@emu.edu.tr

With the increase in the human population, the construction industry continues to grow all over the world. Construction projects generally consist of wide range of complex activities. All those activities must be scheduled and managed carefully and professionally in order to complete the project on the promised time. Because of this growth, complexity and the precedency relationship between activities, the risks faced in the sector are also increasing and risk management has become vital in construction sector. The aim of this research paper is to analyse the risks that affect the turnkey time of the construction projects and to rank the analysed risks according to their significance level. For this purpose, the risks are identified through literature review and interviews with the project managers of seven large-scale construction companies operating in Northern Cyprus. Then, the probabilities of occurrences and the effects of these risks are assessed, and a risk index is created for each identified risk by using probability-impact (P-I) model. Afterwards, the risks are ranked in order of significance according to the index values. Finally, results are discussed, and some risk mitigation measures are proposed.

Keywords: Construction Industry, Risk Management, Cyprus

1. INTRODUCTION

Construction projects generally consist of wide range of complex activities. All those activities beginning from the designing of a technical project to closing up of the project must be scheduled and managed carefully and professionally in order to complete the project on the promised time. Precedence relationship is high and critical in construction activities. Moreover, the variety of materials and equipment increases, new architectural designs emerge, and supply chains of this industry lengthened over time. As a result of these properties of and the advancements in construction industry, the variety, impact, and probability of occurrence of risks in this sector have also increased. Hence, risk management has gained considerable importance in order to prevent the undesirable consequences.

As the human population in the world increases, the growth in the construction industry also increases. Global construction work done will grow over US$4.2 trillion over the next 15 years—from US$9.7 trillion in 2022 to US$13.9 trillion by 2037 [1]. Inside this growth, civil engineering is on track to be the fastest growing segment of the construction market over 2023, as governments around the world continue to champion major infrastructure investment (Figure-1) [2].

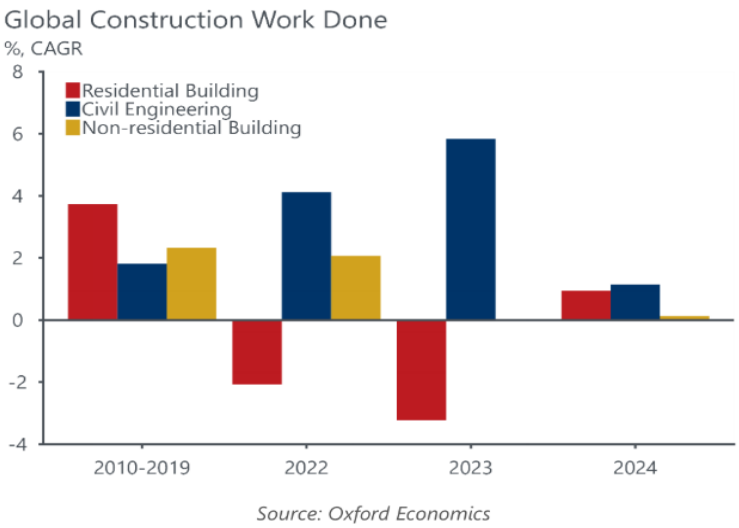

Figure-1: Global construction growth percentage by segment

In parallel with the world's trend, construction industry in Cyprus has also grown exponentially in recent years. That is especially because of the foreign investors who have been moving to and living in Cyprus. These foreign investors are mainly Ukrainians, Russians, Iranians, Israeli and, English. This demand explosion in recent years increases the number of projects in Cyprus. There are several large-scale national construction companies that form the majority of all projects in the whole northern part of the Island. There are also regional, middle to small scale emerging national companies. All those large to small scale companies have limited construction resources such as workforce, equipment, supplier because of being on an island. For all these reasons, their supply chains and construction activities may be affected from internal and external risks slightly more than their peers.

Berruguete B. states that larger values are at risk for companies. Construction costs are soaring because of the higher prices for energy and raw materials. Replacement is costing more and taking longer. Materials can also often be unavailable due to logistics, shipping and supply-chain bottlenecks. The result is that any property damage and business interruption losses are now likely to be significantly higher than before Covid-19. Business interruption/supply chain disruption and natural catastrophes rank as the top risks for the construction and engineering sector, followed by the energy crisis as a new entrant at #3, according to Allianz Risk Barometer respondents in the construction sector [3]

In his construction risk literature review, Taroun A. points out that risk analysis in construction industry has its roots since the development of the Program Evaluation and Review Technique (PERT) in the 1950s for tackling uncertainty in project duration. In the 1980s, risk began to be perceived as a project attribute and Risk Management (RM) became a well-established project management function. During the 1990s researchers investigated different theories to account for the special nature of construction risk, and after the beginning of the new millennium risk assessment flourished as a hot research topic [4].

The impact of a risk on a construction project can be on four different performance measures: cost, quality, safety and time or schedule. It is clear that a risk may affect only one of these measures or all of them simultaneously. In this study, the impact of risk is investigated only on schedule, in other words, time measure. Both private and public construction projects have time schedule. The customers/owners of the projects are promised to take their residents, homes, offices, schools or any kind of facilities in the planned time. When the turnkey time of the project is delayed, the company will lose money because every contract includes compensation payment to the customer for every delayed day/week/month of the project. Another negative consequence of delay will be the loss of reputation. This effect is also very severe in this competitive era. Losing of customer may be worse than losing of money in a single project because bad reputation will prevent other prospective customers to trade with the company. Time delay will also negatively affect the performance of the company because a construction company generally uses same equipment and materials in its other projects simultaneously or sequentially. Therefore, if a risk causes a delay of the schedule, this may affect the other projects performances as well.

2. METHODOLOGY

The risk management process generally consists of three stages: risk identification, risk evaluation and risk mitigation [5], [6], [7]. In literature, some scientists separate the risk evaluation phase into two phases: risk measurement and risk assessment. All the assessments in risk management are based on the prediction of an unknown future. It should be monitored, revised and updated all the time because it is a dynamic process. Therefore, risk monitoring and control phase has also been included in the SCRM process recently [8].

Risk Identification: Risk identification is the first and the most important stage of the risk management. Registered risks in literature, historical records of companies, opinions and experiences of workers and experts, internet sites created for this phase can all be used to identify the risks [9].

Although most of the risks are common for all industrial sectors, there are some risks peculiar to specific sectors. For the construction industry, risks can be financial, contractual, operational, and environmental and can be caused by both internal and external sources. Common risks include safety hazards that lead to worker accidents and injuries, managing change orders, incomplete drawings and poorly defined scope, unknown site conditions, poorly written contracts, unexpected increases in material costs, labor shortages, damage or theft to equipment and tools, natural disasters, issues with subcontractors and suppliers, availability of building materials, poor project management [10].

Risk Measurement: There are two criteria used for the risk measurement; the probability and the impact of a risky event. Expected impact, which is the product of probability and impact, is referred to as the risk measurement.

A probability distribution function or occurrence frequency of a risky event is used to find the value of probability. In order to use probability functions, we must have historical data on that event first. The type of distribution function must be identified by fitting tests. Then, the parameters of the distribution function must be calculated, and the probability of a risky event can be found. Although the probability values found by this method are more reliable and accurate, it is difficult to find the type of distribution function due to lack of required data. In this situation, the likelihood of an event can be used. Likelihood is related to the frequency of occurrence of an event. This method is more practical than and might be as accurate as the other method when experts evaluate the risky event meticulously [8].

The second component of the risk measurement is the impact of a risky event. It is very difficult to estimate and compute the impact in advance because a disruption in any part of the SC usually affects other parts as well. Risk impact is usually expressed in terms of cost but performance loss, physical loss, psychological loss, social loss, time loss etc. are also other types of impacts [11].

As mentioned earlier, expected impact is the product of impact and probability of a risky event. The probability-impact matrix is a useful tool to visualise and define the expected impacts and is widely used in literature. 5 or 10 level Likert Scale can be used to categorise both impact and likelihood of the events (Table 1). A risky event which is unlikely but has a high impact has an index of 8 out of 25. Both the likelihood and impact index of a risky event increase as we move towards the lower right of the matrix.

Table-1: Probability-Impact Matrix

			IMPACT				
			Very Low	Low	Medium	High	Very High
			1	2	3	4	5
LIKELYHOOD	Very Unlikely	1	1	2	3	4	5
	Unlikely	2	2	4	6	8	10
	Medium	3	3	6	9	12	15
	Likely	4	4	8	12	16	20
	Very Likely	5	5	10	15	20	25

Risk Evaluation: Risk evaluation is the process of comparing the results of risk analysis with risk criteria to determine whether the risk is acceptable or tolerable. Risk criteria are based on organisational objectives and can be derived from standards, laws, policies and other requirements [12]. It is impossible and unreasonable to prevent and mitigate all risks. At the end of the risk evaluation phase, a risk owner can select one of the four different strategies: avoid risk, reduce the probability and/or impact of risk, accept the occurrence of risk and prepare contingency plans [13]. Selection of the strategy mainly depends on the trade-off between the expected impact and the cost associated with the implementation of the selected strategy.

Risk Mitigation: Risk mitigation makes use of the data collected in the previous stage to address potential risks with the right countermeasures. This includes classic mitigation strategies which are implemented before the risky event and contingency plans implemented after the risky event [14]. Kleindorfer and Saad argue that prevention is better than a cure, requiring risk managers to act fast and treat urgent risks first [6].

Risk mitigation strategies can be classified into two groups: reactive and proactive. In a reactive approach, no action is taken before the occurrence of a risky event, but it is implemented to mitigate the impact and/or probability after it occurs. In these kinds of strategies, there is no plan to reduce the risk probability. Although there are plans to reduce the impact, they are implemented after the occurrence of the risky event. In a proactive approach, plans are implemented to mitigate the risks before they occur. This approach may include the execution of plans either to decrease the probability or to reduce the impact of the risky event in advance [8].

3. RESEARCH IN CYPRUS CONSTRUCTION INDUSTRY

In addition to all the peculiarities to construction industry mentioned in the previous section, Cyprus has also additional features regarding construction activities. The head of Cyprus Turkish Building Contractors Association states that construction industry is the leverage for the economy because it supports more than 250 sub-sectors, provides a significant employment opportunity, ensures foreign currency input to the economy by attracting foreign investors to the country, and makes a significant contribution to the state with its taxes [15]. However, there are some negative sides of being in Cyprus for construction companies. First, it is relatively difficult to supply goods to an island because transportation modes are limited. Second, in house production is also significantly scarce and most of the equipment and materials are heavily dependent on import. Third, it is relatively hard to find skilful and qualified builder's labourer. These properties give rise extra importance to construction risk management in Cyprus.

According to the Cyprus Turkish Building Contractors Association Databank, number of construction projects increased gradually from 2014 to 2018 and then decreased until 2021. That fall is due to the Covid-19 pandemic like in everywhere. Finally, after the recovery from pandemic, it has begun to increase again as can be seen in Figure-2.

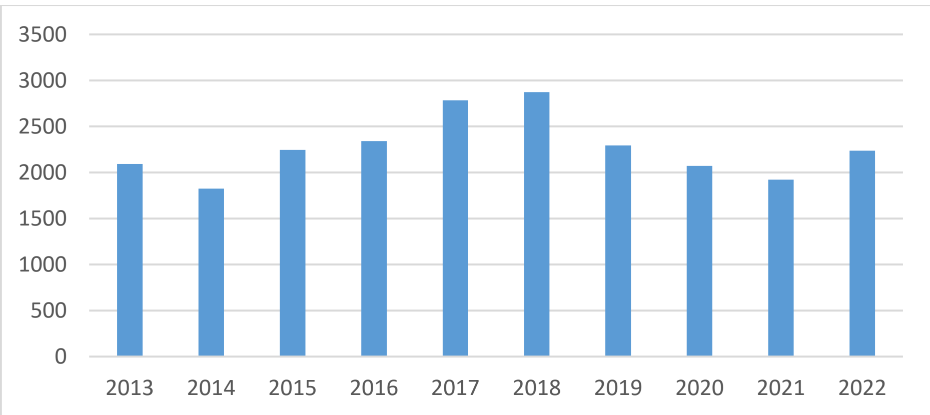

Figure-2: Number of construction projects submitted yearly to Cyprus Turkish Building Contractors Association

In order to identify and measure the risks, four large-scale and nationwide, two medium-scale and, one small-scale regional company are selected. Managers/project managers of these companies are interviewed, and a questionnaire is applied to them. The information about the companies and the interviewees are presented in Table-2.

Table-2: Information about the companies and the interviewees

	COMPANY						
	A	B	C	D	E	F	G
Company Size	Large Scale	Small Scale	Medium Scale	Large Scale	Medium Scale	Large Scale	Large Scale
Position of the Interviewee	Project Manager	Manager	Manager	Project Manager	Architect& Manager	Architect& Manager	Project Manager
Experience of the Interviewee	12 years	7 years	14 years	19 years	5 years	5 years	11 years

First, literature review is performed in the risk identification phase of the study. Identified risks from literature are presented in Table-3.

Table-3: Identified risks from literature.

• Supplier inadequacy	• Strike/lockout etc.
• Workforce insufficiency	• Financial problems of the company
• Workforce incapability	• Currency rate fluctuations
• Technical inadequacy (equipment, material etc.)	• Political instability (election restrictions, setbacks etc.)
• Adverse weather conditions (hot weather, heavy rain etc.)	• Customer related risks (out-of-project requests, late notification of requests, payment delays etc.)
• Logistics challenges (other than supplier incapability)	• Pandemic (some resources categorize pandemic as natural disaster while others not)
• Governmental regulations	• Natural Disasters

After literature review, all these risks are discussed and reviewed by the managers/project managers of the above-mentioned companies. They all agree on the identified risks and one of the project managers has added “Municipality’s Non-functionality (inadequacy)” risk as his experience. So, this risk is also included in the questionnaire to be evaluated by the interviewees.

In the second phase, Likert Scale of likelihood and impact values are discussed and determined by the interviewees. The values in Table-1 are generic and should be modified according to the features of specific industries. Thus, the modified likelihood and impact values peculiar to construction industry in Cyprus are presented in Table-4.

Table-4: Likelihood of occurrence categorization for construction sector risks

				IMPACT				
				Negligible	Minor	Moderate	Severe	Catastrophic
				Delay of project for less than 1 month	Delay of project for 1 to 3 months	Delay of project for 3 to 6 months	Delay of project for 6 to 12 months	Delay of project for 1 year and more
				1	2	3	4	5
LIKELYHOOD	Rare	Once in every 2 years and up	1	1	2	3	4	5
	Seldom	Once in a year	2	2	4	6	8	10
	Sometimes	Once in 6 months	3	3	6	9	12	15
	Often	1-2 times a quarter	4	4	8	12	16	20
	Usually	At least 1-2 times a month	5	5	10	15	20	25

As mentioned in previous sections, only the impact of risks on turnkey time or schedule of construction projects are taken into consideration.

Measurement of each risk is performed by assessing the likelihood and impact of it via interviewing with and applying the questionnaire in Appendix-1 to seven managers/project managers. Then the index of each risk is calculated by multiplying the likelihood index and impact index for each interviewee. In order to determine the final index of each risk, average of all company experts is used.

Since no natural disaster has happened in Cyprus for centuries, the interviewees assess the probability of this risk as 'Rare' (1) but they say that they are unable to assess the impact of it because they have no experience or historical data about this risk. Hence, no measurement is made for 'natural disaster' risk in this study.

The means of all risk's likelihood indexes (blue bars) and impact indexes (orange bars) are presented in Figure-3.

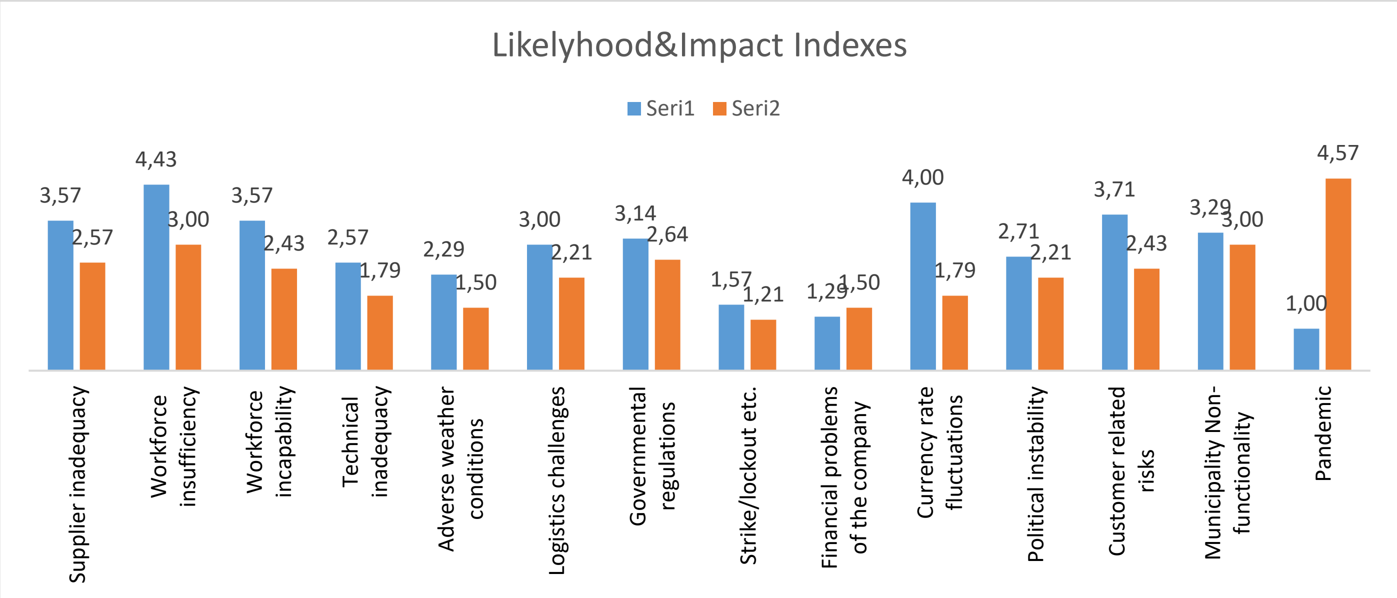

Figure-3: The means of risk likelihood indexes (blue bars) and risk impact indexes (orange bars)

According to the results, "workforce insufficiency" risk has the highest likelihood with the index of 4.43 followed by "currency rate fluctuations" risk with that of 4.00. "Pandemic" risk has the highest impact with the index of 4.57 followed by "municipality non-functionality" risk and "workforce insufficiency" risk with the index of 3.00.

The means of all the risk's indexes are presented from highest to lowest in Figure-4.

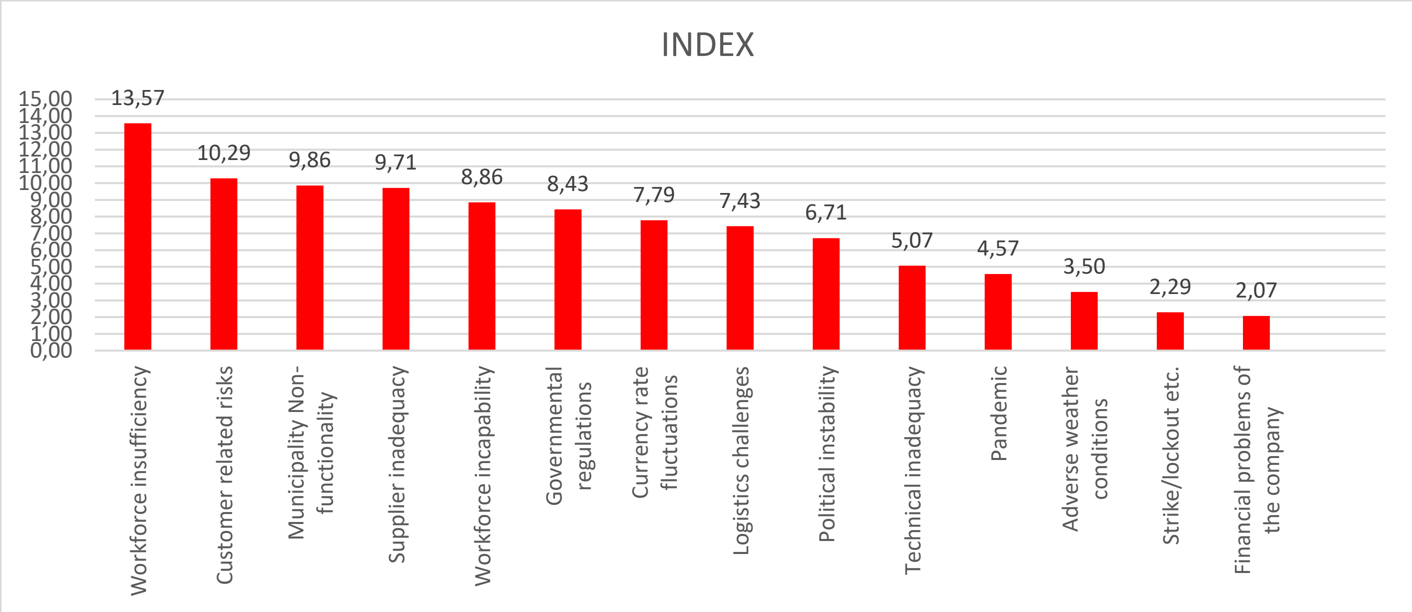

Figure-4: The means of risk indexes

According to the results, workforce insufficiency risk has the highest index value of 13.57 followed by customer related risks with that of 10.29 and municipality non-functionality risk with 9.86.

4. CONCLUSION AND SUGGESTIONS

When the results of the research are analysed, workforce insufficiency risk is the most critical one. There are some underlying reasons for this risk. Construction workers are mainly from Türkiye and they frequently go to their countries for many reasons. Additionally, 06 February 2023 earthquake in Türkiye has affected construction workforce negatively in Cyprus and this impact is evaluated as workforce insufficiency by the interviewees in this study. That is because the construction workers went to Türkiye after the earthquake to work for the recovery projects and also to help their relatives because the workers in Cyprus are mainly from the disaster area.

Customer related risk is the second critical one. Construction companies let their customers customise their houses. When customers inform the company about their requests late or make high degree of customisation, this results the delay of project schedule. Payment problems of the customers also causes delay of the project.

In terms of supplier inadequacy and logistics challenges, there happened a problem in iron supply and rise in iron prices in Cyprus temporarily at the beginning of Ukraine-Russia war. Prices went up because of the uncertainty and demand increase. Companies tried to mitigate supply risk by keeping iron inventory.

Construction companies in Cyprus should focus their resources to the high index-level risks identified in this study in order to mitigate the impact and probability of them. Mitigation strategies for the critical risks can be investigated for further research.

REFERENCES

[1] Fearnley, N., Robinson, G., Leonard, J., Global Construction Futures, Oxford Economics Limited, London, 2023.

[2] Fearnley, N., Key Construction Themes 2023 Revisited, Oxford Economics Limited, London, 2023.

[3] Berruguete, B., Allianz Global Corporat & Specialty, AGCS News&Insights, Civil Engineering, 2023.

[4] Taroun, A., Towards a better modelling and assessment of construction risk: Insights from a literature review, *International Journal of Project Management,* no. 32, pp. 101-115, 2014.

[5] Wagner, S.M., Bode, C., Dominant Risks and Risk Management Practices in Supply Chains, *Supply Chain Risk: A Handbook of Assessment, Management and Performance*, New York, Springer, 2009, pp. 271-290.

[6] Kleindorfer, P.R., Saad, G.H., Managing disruption risks in supply chains., *Prod. Oper. Manag.,* no. 14, p. 53–68, 2005.

[7] Tang, C.S., Perspectives in supply chain risk management., *Int. J. Prod. Econ.,* no. 103, p. 451–488, 2006.

[8] Kırılmaz O., Erol S., A proactive approach to supply chain risk management: Shifting orders among suppliers to mitigate the supply side risks, *Journal of Purchasing & Supply Management,* no. 23, pp. 54-65, 2017.

[9] Jereb, A., Cvahte, T., Rosi, B., Mastering supply chain risks, *Serb. J. Manag.,* no. 7, pp. 271-285, 2012.

[10] Jones, K., Construction Risk Management: Identifying and Managing Project Risks, Construction Risk Management | ConstructConnect, https://www.constructconnect.com/blog/identifying-managing-construction-project-risks, 2020.

[11] Harland, C., Brenchley, R., Walker, H., Risk in supply networks, *J. Purch. Supply Manag. ,* no. 9, pp. 51-62, 2003.

[12] *ISO Guide 73, Risk Management Vocabulary,* 2009.

[13] Baird, I.S., Thomas, H., Toward a contingency model of strategic risk taking, *Acad. Manag. Rev.,* no. 10, pp. 230-243, 2008.

[14] Kern, D., Moser, R., Hartmann, E., Moder, M., Supply risk management: Model development and empirical analysis, *Int. J. Phys. Distrib. Logist. Manag.,* no. 42, p. 60–82, 2012.

[15] Gürcafer, C., Cyprus Turkish Building Contractors Association Databank Brochure, www.ktimb.org, Cyprus, 2017.

COVID-19 IMPACTS ON THE EDUCATION OF MECHATRONIC ENGINEERING IN EASTERN MEDITERRANEAN UNIVERSITY

O. Shekoofa, Q.Zeeshan, M.Ozdenefe, A.Gazioğlu

Department of Mechanical Engineering, Eastern Mediterranean University, Magusa, TRNC

E-mail: omid.shekoofa@emu.edu.tr

The pandemic has had a significant impact on university education, especially on engineering disciplines that rely heavily on practical education. This research examines the effects of Covid-19 on the Mechatronics Engineering curriculum, which requires a multidisciplinary approach and relies heavily on laboratory and workshop activities. The curriculum of EMU University's Mechatronics Engineering program served as a case study. The courses were categorized as area core, university core, faculty core, area elective and university elective courses, and different weights were assigned to each group. The weights were different based on their utilization of workshops, laboratories, and tutorial activities and the year of entry for each group of students. Based on these factors, an index was proposed to evaluate the students' susceptibility to pandemic conditions and its impact on subsequent courses until graduation. The influence of the pandemic on the curriculum of students entering in 2016 up to students entering in 2022, were explored. The results showed that most negative influence happened to the non-regular students of 2019-2020, while the most severe impact on laboratory activities was observed for the non-regular students of 2018-2019. The results of this study can help identify potential weaknesses in graduates during this period and inform curriculum strengthening based on lessons learned from the pandemic.

Keywords: Covid-19, Education, Mechatronic Engineering, Curriculum

1. INTRODUCTION

Higher education is one of the many sectors that has been affected by the emergence of the Covid-19 pandemic [1]. Restrictions have been set to prevent the spread of the virus by the governments of various countries across the globe, including Turkish Republic of Northern Cyprus (TRNC). The restrictions set by the TRNC government started with the lockdown order that was implemented on 14th of March 2020 [2]. Hence, this resulted in face-to-face education in educational institutions to be put on hold and to commence on online platforms.

The present study aims to investigate the impact of Covid-19 on Mechatronics Engineering majors in the Eastern Mediterranean University (EMU), as the delivery of the engineering courses provided by the educational institutions had to be adjusted swiftly [3] which has caused an impact on the learning effectiveness of the courses. The quick adjustments made by EMU delivering engineering courses included transitioning from traditional in-class lectures to online classes, carrying out the practical aspects of the engineering curriculums such as lab activities and workshops virtually, and assessing the students on only online platforms in replacement of in-class exams or presentations of projects in person.

Some studies show that the quick transition from traditional teaching methods to online courses have resulted in student dissatisfaction [4, 5]. This could be due to many reasons such as the technical and financial issues the students might have faced such as the lack of access to hardware and internet [6], mental health struggles such as increased stress and depression due to isolation [7,8], poor studying habits of the students that made it difficult for them to set a healthy studying environment at home, and having issues with adapting from traditional learning methods to online learning. Mechatronics Engineering students take several courses from different departments such as computer, electrical and mechanical engineering throughout the duration of their studies. While some of their courses focus more on theory such as mathematics, their other courses are more practical-work oriented. The effect of the pandemic on the mechatronics majors in EMU considering their major as a whole, and each course in their curriculum individually is investigated in the present study.

2. MATERIAL AND METHODS

In this study, the curriculum of the Mechatronics Engineering program at the EMU University has been considered as the main source of the required data and information about the mechatronic courses, their numbers of lecture, laboratory and tutorial credits, and the semester which each course is offered in the mechanical engineering department of EMU. Table 1 shows the first two semesters of this curriculum.

Table 1. The EMU Mechatronic Engineering Curriculum (only two semesters are shown)

Semester	Ref Code	Course Code	Full Course Title	Course Category	Credit				Prerequisites	ECTS
					Lec	Lab	Tut	Total		
1	2A710	MENG104	Engineering Graphics	AC	2	3	0	3		8
1	2A711	EENG112	Introduction to Programming	UC	4	1	0	4		8
1	2A712	ENGL191	Communication in English - I	UC	3	1	0	3		5
1	2A713	MATH151	Calculus – I	FC	4	0	1	4		6
1	2A714	PHYS101	Physics – I	FC	4	1	0	4		6
1	2A715	MATH163	Discrete Mathematics	AC	3	0	1	3		5
			1st Semester Total Credits					21/21		
2	2A720	MECT190	Introduction to Mechatronics Engineering	FC	1	0	1	1		3
2	2A721	CHEM101	General Chemistry	AC	4	0	1	4		6
2	2A722	ENGL192	Communication in English - II	UC	3	1	0	3	ENGL191	4
2	2A723	MATH152	Calculus – II	FC	4	0	1	4	MATH151	6
2	2A724	PHYS102	Physics – II	FC	4	1	0	4	PHYS101	6
2	2A725	TUSL181/ HIST280	Communication in Turkish*/ History of Turkish Reforms**	UC	2	0	0	2		2
			2nd Semester Total Credits					18/39		

In this program, each student is required to take 44 courses, equivalent to 146 academic credits, consisting of 141 lecture credits, 35 laboratory/workshop credits, and 14 tutorial credits. Due to Covid-19 pandemic, which began in the spring term of 2019-2020 and lasted until the end of the spring term of 2021-22 in TRNC, all students who enrolled in this program from 2016 to 2022 have been affected at various levels.

According to Figure 1, and for the sake of simplicity, all the students in each year have been categorized into only two groups: Regular (fall semester admission) and non-Regular (spring semester admission). We ignored other cases such as transfer students, part-time students and so on in our study.

It is also assumed that in the first two semesters, i.e. spring 2019-2020 and fall 2020-2021, Covid-19 influence was high (because of the wide quarantines and sudden move to full online education system), in the two following semesters, i.e. spring 2020-2021 and fall 2021-2022, the influence was medium (due to adopting the online teaching system and using mixed online and face-to-face education methods), and the last semester of the Covid period, i.e. spring 2021-2022, the influence was low (due to removing most of the restrictions and getting back to normal condition gradually). We also consider a kind of indirect influence of the Covid-19 condition on the rest of the program until the graduation of each student who entered after Spring 2018-2019. Later in this section it is shown how we quantify the different levels of influence on different courses (refer to Table 4).

Covid-19 Period								S 19-20	F 20-21	S 20-21	F 21-22	S 21-22							
Students Entry Year																			
Regular 2016-2017	F 16-17	S 16-17	F 17-18	S 17-18	F 18-19	S 18-19	F 19-20	S 19-20											
Non-Regular 2016-2017		S 16-17	F 17-18	S 17-18	F 18-19	S 18-19	F 19-20	S 19-20	F 20-21										
Regular 2017-2018			F 17-18	S 17-18	F 18-19	S 18-19	F 19-20	S 19-20	F 20-21	S 20-21									
Non-Regular 2017-2018				S 17-18	F 18-19	S 18-19	F 19-20	S 19-20	F 20-21	S 20-21	F 21-22								
Regular 2018-2019					F 18-19	S 18-19	F 19-20	S 19-20	F 20-21	S 20-21	F 21-22	S 21-22							
Non-Regular 2018-2019						S 18-19	F 19-20	S 19-20	F 20-21	S 20-21	F 21-22	S 21-22	F 22-23						
Regular 2019-2020							F 19-20	S 19-20	F 20-21	S 20-21	F 21-22	S 21-22	F 22-23	S 22-23					
Non-Regular 2019-2020								S 19-20	F 20-21	S 20-21	F 21-22	S 21-22	F 22-23	S 22-23	F 23-24				
Regular 2020-2021									F 20-21	S 20-21	F 21-22	S 21-22	F 22-23	S 22-23	F 23-24	S 23-24			
Non-Regular 2020-2021										S 20-21	F 21-22	S 21-22	F 22-23	S 22-23	F 23-24	S 23-24	F 24-25		
Regular 2021-2022											F 21-22	S 21-22	F 22-23	S 22-23	F 23-24	S 23-24	F 24-25	S 24-25	
Non-Regular 2021-2022												S 21-22	F 22-23	S 22-23	F 23-24	S 23-24	F 24-25	S 24-25	F 25-26

High influence
Medium influence
Low influence
Indirect influence

Figure 1. The coincidence of Covid-19 outbreaks with the education program of different groups of students entered from 2016 to 2021

To assess the influence of the Covid-19 pandemic and the resulting constraints, such as social distancing and conducting online classes and meetings, on the quality of education in this field a simple approach has been proposed for quantifying the degree of influence. For this purpose, a parameter called the "Course Influence Index" has been introduced for each mechatronic course. This index is determined by considering several parameters, including:

a) Total number of credits for the whole program and each group of credit types
b) The weight of each credit types:
    a. Lecture
    b. Laboratory/workshop
    c. Tutorial
c) The weight of each course type:
    a. AC (area core course)
    b. UC (university core course)
    c. FC (faculty core course)
    d. AE (area elective course), and
    e. UE (university elective course)
d) Form and severity of the influence
    a. Direct
        i. High
        ii. Medium
        iii. Low
    b. Indirect

The first parameter is defined based on the number of Lecture, Laboratory/Workshop, and Tutorial credits, which is presented for each course in the full version of Table (1) which is accessible at [9]. The total number of these three types of credits are shown in Table 2.

Table 2. Total number of three types of credits

Credit Type	Total Credits
Lecture	141
Laboratory	35
Tutorial	14
Overall (Lecture+ Laboratory+ Tutorial)	146

For each course, according to Table (3), the weight of each Lecture credit is assumed to be 1, the weight of each laboratory/Workshop credit is 1.5, and the weight of each tutorial credit is 0.75.

Table 3. The weight of each credit types

Credit Type	Weight
Lecture	1
Laboratory	1.5
Tutorial	0.75

Moreover, we have considered different weights for various course types. Table 4 presents these weights for four influence scenarios as described earlier. We assigned the highest weight for faculty courses, and lowest weight for the university elective courses. In addition, we halved the weights of all courses for the medium influence scenario with respect to high influence scenario, and the low influence scenario weights were halved respect to the medium scenario weights and so on.

Table 4. The weight of each course types under different influence scenarios

Course Type	High Influence	Medium Influence	Low Influence	Indirect Influence
AC (Area Core)	0.6	0.3	0.15	0.075
UC (University Core)	0.4	0.2	0.1	0.05
FC (Faculty Core)	1	0.5	0.25	0.125
AE (Area Elective)	0.8	0.4	0.2	0.1
UE (University Elective)	0.2	0.1	0.05	0.025

Taking these factors into account, an index was defined to determine the influence of Covid-19 on each course during the pandemic, under different influence scenarios, as follow:

*Course Influrence Index = Influence level *Course Type*(Lecture credits + Lab credits + Tutorial credits)*

We used this formula to determine the influence index for each semester and the whole program of mechatronic students in different entry years, to analyse the level of negative impacts of Covid-19 pandemic on the teaching quality.

3. RESULTS AND DISCUSSION

Based on the assumptions made in the previous section, various results can be obtained from this investigation. Firstly, the influence indexes of Covid-19 for each course, each semester, and the whole program are determined and shown in Table 5.

Table 5. The calculated influence index for each and all courses

Full Course Title	Course Index	Full Course Title	Course Index	Full Course Title	Course Index	Full Course Title	Course Index
Engineering Graphics	3.9	Mechanical Workshop Practice	3.3	Mechatronics Components and instrumentation	2.7	Industrial Training	7.5
Introduction to Programming	2.2	Materials Science	2.7	Fundamentals of Thermodynamics	2.7	Introduction To Capstone Design	1.75
Communication in English - I	1.8	Electrical Circuits	3.3	Manufacturing Technology	3.3	Area Elective-I***	4.4
Calculus – I	4.75	Algorithms and Data Structures	3.3	Mechanical Vibrations	3.3	Area Elective-II ***	3.8
Physics – I	5.5	Engineering Mechanics	2.25	Introduction to Digital Logic Design	3.3	Fundamentals of Engineering Economy	1.8
Discrete Mathematics	2.25	Ordinary Differential Equations and Linear Algebra	2.85	5th Semester Total Credits	15.3	Probability & Statistical Methods	4.5
1st Semester Courses Index	20.4	3th Semester Courses Index	17.7	Machine Elements	2.25	7th Semester Total Credits	23.75
Introduction to Mechatronics Engineering	1.75	Electronics	3.3	Computer Aided Engineering Design	3.9	Capstone Team Project	7
General Chemistry	2.85	Strength of Materials	3.3	Control Systems-I	3.3	Introduction to Robotics	2.85
Communication in English - II	1.8	University Elective I (IENG355- Engineering Ethics)	0.6	Microprocessors-I	3.3	Area Elective-III***	5
Calculus – II	4.75	Signals and Systems	3.3	Numerical Methods for Engineers	2.25	University Elective II (Non-skill based)	0.75
Physics – II	5.5	Communication Skills	3	6th Semester Total Credits	15	University Elective III (Non-skill based)	0.9
Communication in Turkish*/	0.8	4th Semester Courses Index	13.5			8th Semester Total Credits	16.5
History of Turkish Reforms**	0.8						
2nd Semester Courses Index	18.25					**All Courses Index**	**140.4**

Considering this index for the offered courses during each semester coinciding with pandemic period, one can establish a metric for the impact of Covid-19 on the performance of students in each semester and throughout their entire period of study. For this purpose, and by considering the type of courses affected by Covid-19 for each group of the entry years from 2016 to 2022, the diagram of Figure 2 can be resulted. This diagram shows that the non-regular students of 2019-2020 have been most affected by the Covid-19 restrictions.

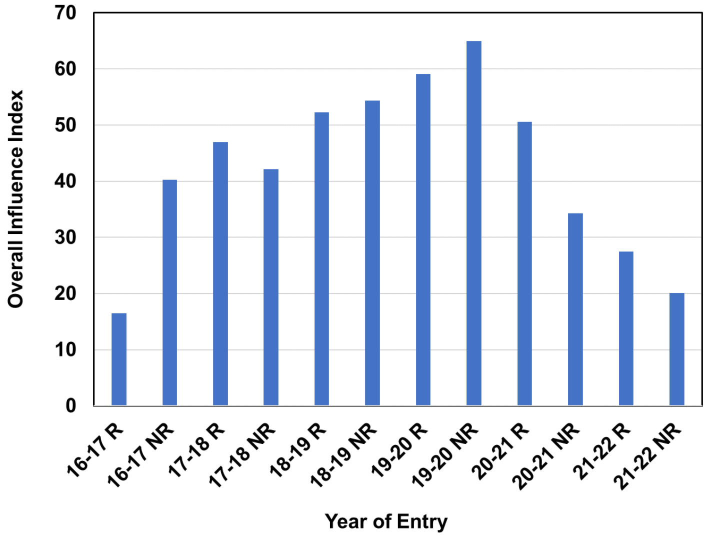

Figure 2. Overall influence index for different entry years

Figure 3 shows the effects of the coronavirus pandemic on the number of affected courses and credits in the curriculum of regular and non-regular students from 2016 to 2022. As indicated on the graphs, in the spring 2019-2020 academic semester more than 22 courses and 70 credits, which represent 50% and 48% of the total courses and credits, respectively, were affected which are the highest evaluated influence levels.

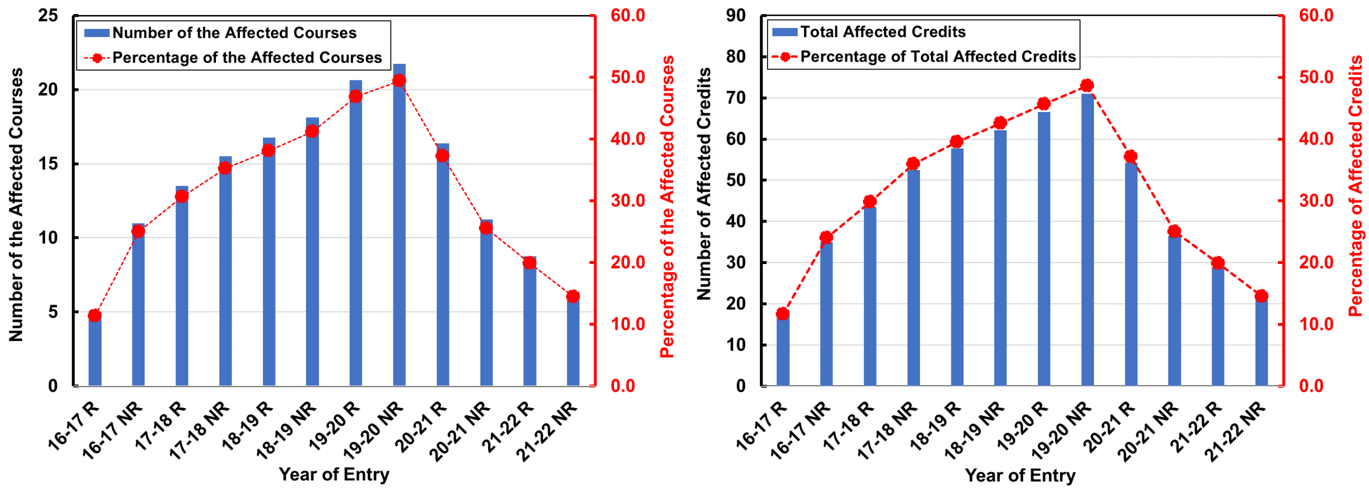

Figure 3. The number of courses (left) and number of credits (right) influenced by Covid-19 in different entry yeas

In the next step, we considered the number of laboratory/workshop credits due to the Covid-19 restrictions. According to the graph of Figure 4, non-regular students of 2018-2019 were subjected more than other groups, by more than 14 lab credits influenced by Covid-19.

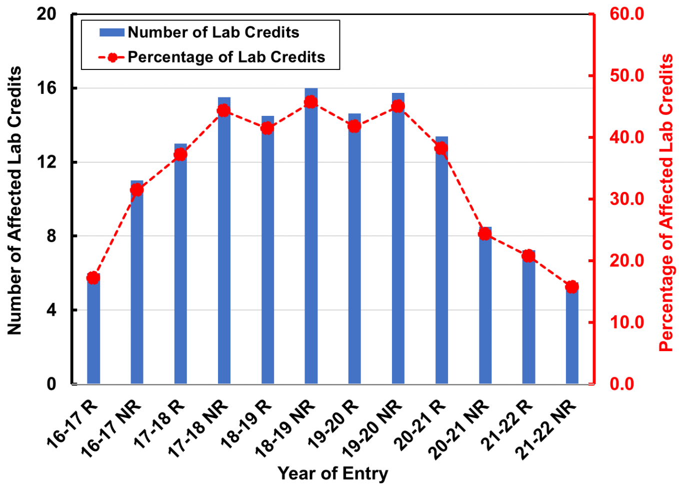

Figure 4. The number of laboratory credits affected by Covid-19 in different entry years.

4. CONCLUSION

This study was carried out to quantitively evaluate the influence of Covid-19 on the teaching of mechatronic engineering program in the mechanical engineering department of EMU. We used the mechatronic curriculum to determine the number of courses and credits for each group of students which faced with the Covid-19 pandemic. We proposed a metric to measure the negative influences of Covid-19 quarantine and restrictions on teaching different courses at different semesters. According to the results, the most severe influence of Covid-19 was observed for the non-regular students of 2019-2020, while the non-regular students of 2018-2019 were suffered more in their laboratory and/or workshop activities. It was also noticed that the indirect negative influences of Covid-19 may last up to fall semester of 2025-2026.

REFERENCES

[1] Treve, M. (2021) 'What COVID-19 has introduced into education: Challenges Facing Higher Education Institutions (heis)', Higher Education Pedagogies, 6(1), pp. 212–227. doi:10.1080/23752696.2021.1951616.

[2] 'Mental health, loneliness and social support during COVID-19 pandemic among International University students in North Cyprus' (2022) Cyprus Turkish Journal of Psychiatry & Psychology, 4(3). doi:10.35365/ctjpp.22.3.01.

[3] Shekh-Abed, A. and Barakat, N. (2021) 'Transition of engineering education during the COVID-19 pandemic', 2021 World Engineering Education Forum/Global Engineering Deans Council (WEEF/GEDC) [Preprint]. doi:10.1109/weef/gedc53299.2021.9657167.

[4] Al-Balas, M. et al. (2020) 'Distance learning in clinical medical education amid COVID-19 pandemic in Jordan: Current situation, challenges, and perspectives', BMC Medical Education, 20(1). doi:10.1186/s12909-020-02257-4.

[5] Alnusairat, S., Al Maani, D. and Al-Jokhadar, A. (2020) 'Architecture students' satisfaction with and perceptions of online design studios during COVID-19 lockdown: The case of jordan universities', Archnet-IJAR: International Journal of Architectural Research, 15(1), pp. 219–236. doi:10.1108/arch-09-2020-0195.

[6] Hosen, M. et al. (2022) 'The impact of covid-19 on Tertiary educational institutions and students in Bangladesh', Heliyon, 8(1). doi:10.1016/j.heliyon.2022.e08806.

[7] Aslan, I., Ochnik, D. and Çınar, O. (2020) 'Exploring perceived stress among students in Turkey during the COVID-19 pandemic', International Journal of Environmental Research and Public Health, 17(23), p. 8961. doi:10.3390/ijerph17238961.

[8] Baltà-Salvador, R. et al. (2021) 'Academic and emotional effects of online learning during the COVID-19 pandemic on engineering students', Education and Information Technologies, 26(6), pp. 7407–7434. doi:10.1007/s10639-021-10593-1.

[9] Mechatronics Engineering Undergraduate Program (B.S., 4 Years), available at the web address: https://www.emu.edu.tr/en/programs/mechatronics-engineering-undergraduate-program/897?tab=curriculum

ECONOMIC VIABILITY AND COST BENEFIT ANALYSIS OF THE DESIGN AND MANUFACTURING OF SMART SPEED BUMPS

I. Musili, B. Ozarin, O. Shekoofa[1]

Department of Mechanical Engineering, Eastern Mediterranean University, Famagusta, TRNC

E-mail: omid.shekoofa@emu.edu.tr

We conducted a systematic survey of financial sensibility and the savings made by generating power using smart speed bumps. The proposed smart speed bumps use rollers that rotate a DC generator to produce usable energy. The smart bump produces electrical energy and serves traffic management purposes. The study has multiple objectives. The first one is to evaluate the financial feasibility of the smart bump in urban and suburban settings. There is need to analyse the traffic volumes in order to factor in the optimum installation locations. The project has a potential of producing a minimum of about 5,000 kW annually that's worth 20,000TL in the TRNC. The return on investment and net present value are obtained from the proposed calculations. It's expected that economic, environmental, and societal benefits will be determined in this research. The potential energy for the system in different settings and different methods of energy generation will also be presented. In conclusion, this study assists in finding a financially feasible way to generate clean energy. This study also offers valuable insights for urban planners, policy makers and investors considering that the method is innovative as well as environmentally friendly.

Keywords: Cost Benefit Analysis**,** Smart Bump, Energy Harvesting, Electricity Price

1. INTRODUCTION

Speed bumpers are commonly used at roads for safety reasons such as decreasing speed of the motor vehicles. Although smart speed bumpers are not implemented that frequently, they are much more efficient and useful than common speed bumpers. With the help of Wireless Power Transfer (WPT) technology, the energy obtained by the smart speed bumper can be transferred to surrounding electrical devices such as CCTVs, road lighting and traffic cameras which reduces energy consumption and emissions since TRNC does not widely use green energy resources to obtain electrical power. Reduced energy consumption means less money spent on to obtain it from different sources. Normal streetlights consume 120-300 Watt in an hour and 1440-3600 Watt per day. There are different concepts to implement speed bump, such as electromagnetic speed bumps, hydraulic speed bumps, piezoelectric speed bumps as well as rack and pinion speed bumps.

Table 1: Comparison between alternative designs for smart bump

SBEHD Mechanism	Sıze And Weıght	Cost Effıcıency	Wear And Tear	Installatıon And Maıntenance	Power Generated	Total
Rack and Pinion	2	2	3	2	3	12
Rollers	3	4	3	3	4	17
Piezoelectric	3	3	2	3	1	13

They all generate energy in different ways and quantities. These systems require a lot of maintenance except the electromagnetic smart bump which is the costliest design to execute. It was opined that the crank-shaft mechanism had balancing issues, and it was prone to mechanical vibration [1]. Magnets used in piezoelectric system can harm the vehicles especially electrical and hybrid vehicles [2]. The shield to prevent this adds extra cost. Rack and pinion system has a big downside. As cars pass by, their energy is immediately exploited for electric generation or if the load is not enough, collected in the potential energy storage and, when enough energy is achieved, used to generate electricity [3]. Among the aforementioned designs, we selected roller mechanism due to some advantages like durability, cost effectiveness, simplicity and efficiency.

Therefore, our smart speed bump utilizes a roller mechanism. The friction force between the tires of the vehicles and the polyurethane rollers produces a rotational motion that directly generates electrical energy. The frictional force therefore directly influences the amount of energy produced. This energy is then transmitted to the DC generator through rotational motion. The gear ratio between the pulley on the roller and the pulley on the DC generator determines the power produced. The ratio is used to amplify the energy that was initially produced. The DC is converted to AC using a sine wave inverter. An Arduino Uno microcontroller is used to monitor and redirect the current to different traffic appliances while the rechargeable battery acts as energy storage and backup. This report displays how these smart speed bumpers are cost friendly and in long term with understanding and researching about financial part of the project.

2. MATERIAL AND METHODS

To make a proper cost analysis, mechanical design of the product must be understood which means understanding possible design problems, limitations, goals and product decomposition. Secondly, cost is determined by making production cost breakdown list.

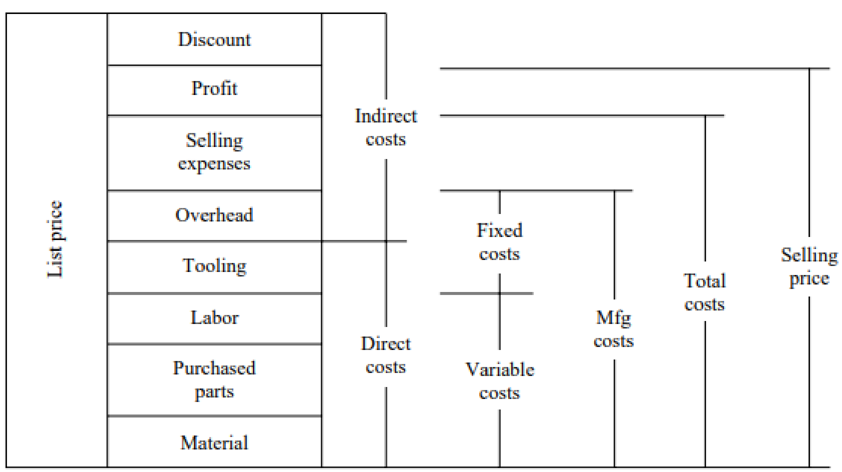

Figure 1: Cost Breakdown List [4]

The material cost table is significant for understanding the finances side of the device in terms of mechanical and electronically. It also displays where to obtain required items which eases to see parts required shipping can be ordered earlier or later. The cost of testing is about 2910 dollars because during this part the subject design is put under harsh conditions. Considering human error, it is better to collect multiple items as a backup. Cost of labour for 1 hour is 4 dollars in

Table 2: Cost to Lifespan of the device with and without maintenance

Name	Quantity	Material	Cost (per piece)($)	Maintenance Cost (per piece) ($)	Lifespan with maintenance (years)	Lifespan without maintenance (years)
Polyurethane Roller	1-3	Polyurethane	9.65	2000 – 2700	5-30	5
380 v DC generator	1	Various	245	2600 – 8800	2.5 -11.5	3
Upscale inverter	1	Various	103	300 – 1000	2-25	6
Arduinonano 33BLE*	2	Various	20.20	30 – 80	2-30	30
Miscellaneous	1	Various	60	70 – 200	3.5-7	3

Turkish Republic of Northern Cyprus which is much lower than cost of materials and testing. Cost of shipping could be lower, if it required upscale inverter could be found cheaper locally, however, it costs less to buy from outside with added shipping costs. It makes about 5,101 dollars all costs included. Figure 2 down below depicts the block diagram.

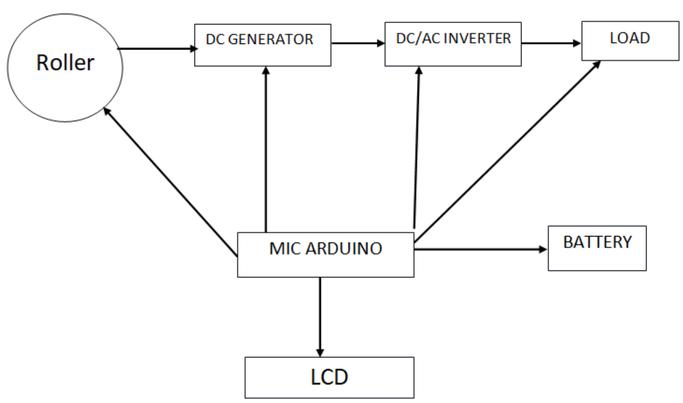

Figure 2. The block diagram of the smart speed bump

Figure 3 shows system breakdown of smart speed bumper using roller mechanism. Mechanical and electrical parts are shown individually. And Figure 4 displays the flowchart of the smart speed bumper mechanism.

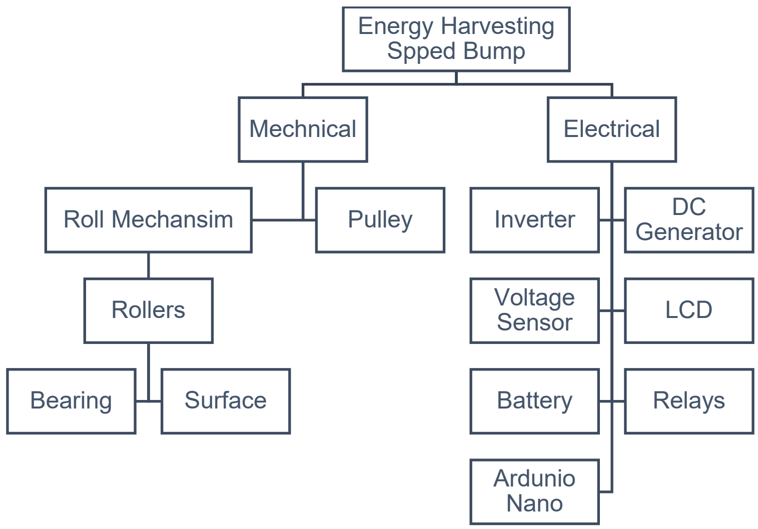

Figure 3: Breakdown of the proposed roller smart speed bump design

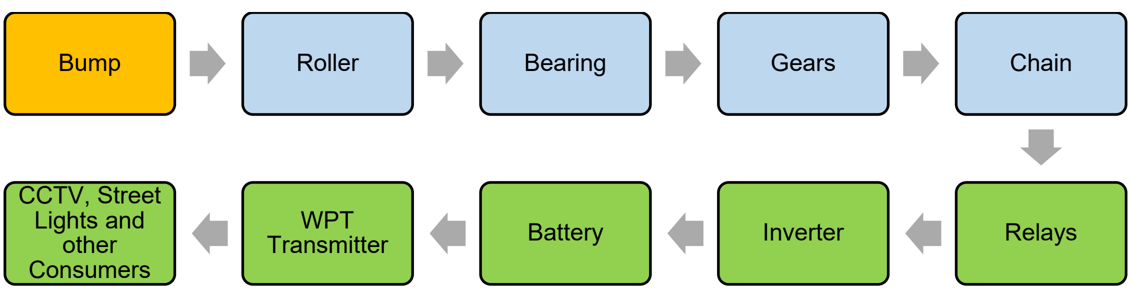

Figure 4: The flow process of the operation of the smart speed bump system

2.1 Lifespan and Maintenance

Wear and tear occurs over time in any system due to a variety of factors, and regular maintenance is vital to increase the longevity of a system. Therefore, we must consider such issues in our design of the speed bump systems and cost analysis.

2.2 Polyurethane Rollers

Polyurethane acts as a damper and a spring since it absorbs lots of shock and returns to the same position making it highly effective in reducing wear and tear from constant impact and environmental exposure. The material is light and easily installed therefore cutting costs even further. This material is highly durable and reliable therefore it can serve the roads for a very long time before any maintenance is required. It is resistant to harsh weather conditions all the while being environmentally friendly.

2.3 Upscale Inverter

This device doesn't need a lot of checkups or maintenance, but this is mainly dependent on its location. Drier areas can harness the strength and reliability of the upscale inverter while wetter areas may not enjoy this advantage. Batteries are used to store the power produced therefore the upscale inverter in its functionality. This further reduces the need for more regular maintenance checks.

2.4 DC Generator

Takes energy from a direct current and transforms this into mechanical energy. It is important to find the life cycle of the smart speed bump to truly determine the economic viability of this project. The most expensive part of the design to maintain will be the DC generator. Several companies seem to shy away [5] from it due to the high maintenance costs but it is advantageous during the transitional stages of some projects. However, this information is dependent on the type of DC generatorin use. The inverter increases the lifespan and efficiency of this system. However, the inverter market price is high with a low maintenance cost.

In order to reduce the overall time and money spent on the DC generator, routine checks are done. During these checks, the brushes be changed, checking the winding insulation using a megohmmeter and machining the commutators in place [6].

2.5 Arduino Uno

The Arduino is extremely durable making its cost quite effective. It can last up to 30 years in optimal temperatures. In extremely hot areas, it may run from 2-5 years, while it could be useful for up to more than 20 years in cooler environments. It's mentioned that approximately for every +10^{0}C the lifespan is halved [13]

2.6 System display

The system display consists of the low-cost materials in this experiment. A voltage sensor to monitor the working system closely and an LCD display. These items work for over 3 years and cost very little. They're therefore easily replaceable in case of malfunctions.

3. RESULTS AND DISCUSSION

The energy generated increments as load of the vehicle passing over the smart sped bumper increases. As a result, it is particularly effective since vehicles reduce their speed when traveling over the speed bump and speed bumps should be kept in areas with frequent traffic to ensure constant energy storage and therefore production.

Table 3. The electricity tariff rates in TRNC[12]

Energy consumption (kWh)	Price (TL)
0 – 250	0.98
251 – 500	2.70
501-750	2.95
751 – 1000	3.25
1001	4

3.1 Output Energy Calculation

When a vehicle passes over the bump, it causes rollers to move which is kinetic energy. Figure 5 shows a typical recorded average number of vehicles daily for a year passing over a central traffic which can be considered as the base of our calculations [11]. The system turns this kinetic energy into electrical energy by the help of inverter. This energy then distributed within the system. The total power output will help determine the value of building the smart bump by including the values of the tariffs in TRNC.

$$\mathbf{Ffr} = \mathrm{Fd} \times \mu \tag{1}$$

$$\mathbf{Ffr} = [\frac{\boldsymbol{\tau e}}{\boldsymbol{rr}} \times \mathrm{ng} \times \mathrm{no}] \times \boldsymbol{\mu} \tag{2}$$

$$\mathbf{Ffr} = [\frac{\boldsymbol{\tau e}}{\boldsymbol{rr}} \times \mathrm{ng} \times \mathrm{no}] \times \boldsymbol{\mu} \tag{3}$$

$$\mathbf{Ffr} * \mathbf{rr} = \mathrm{J}r\theta''r + \mathrm{C}r\theta'r \tag{4}$$

$$[\tau e \times \mathrm{ng} \times \mathrm{no} \times \mu] = \mathrm{J}r\theta''r + \mathrm{C}r\theta'r \tag{5}$$

Where the F_f, is the friction force, F_d is the driving force from vehicle wheels, $\boldsymbol{\tau_e}$ is the engine torque, $\mathbf{r_r}$, is roller radius, and μ is coefficient of friction. Theta is function in time, which will be integrated according to the contact roller arc length.

$$\boldsymbol{Ffr} = \frac{m * g * l}{\sqrt{(\boldsymbol{r^2} - \boldsymbol{l^2})}} = \mathbf{426.49N} \tag{6}$$

, where $\mathbf{F_{fr}}$ is the rolling friction caused by a 1000kg car

$$\mathrm{Work\ (W)} = \mathrm{F} \times \mathrm{d} \tag{7}$$

, where W is the work done (energy generated), F is the force applied in Newtons (N), and d is the distance over which the force is applied in meters (m). From our calculations:

.$\mathbf{F}\mathrm{fr} = 426.49\ \mathrm{Newtons}$

W= 3,351 pounds, M_{car} = 1302kg, M_{wheel} = 325.5kg, Speed = 10km/hr, $\mathrm{Diameter}_{roller}$= 30cm

$$\mathrm{C} = 2\pi r = 2 \times \pi \times (15) = 94.2478 \tag{8}$$

Number of rollers = $\frac{Length\ of\ Speed\ Breaker}{Circumfrence\ of\ roller} = 3.14$, so rollers are required. **(9)**

Min. Energy /year = 0.4 W × 5,000 vehicles/day × 365 days/year = 730,000 joules

Max Energy /year = 1 W × 5,000 vehicles/day × 365 days/year = 1,825,000 joules

W = 426.49 N × 0.5 m = 213.245 Joules

Between 2-5 kilowatts of power can be generated by the hump for every 5,000 vehicles that pass over it.

Minimum power generated per vehicle = 2,000 Watts / 5,000 = 0.4 watts per vehicle

Maximum power generated per vehicle = 5,000 Watts / 5,000 = 1 watt per vehicle

Min. energy generated per vehicle per day = 0.4 Watts × 86,400 seconds = 34,560 joules

Max. energy generated per vehicle per day = 1 Watts × 86,400 seconds = 86,400 joules

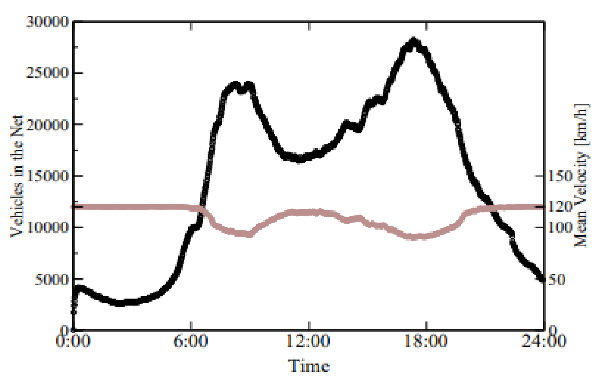

Figure 5: Recorded average number of vehicles daily for a year passing over a central traffic volume [11]

Table 4 shows the total vehicles passing per day and the total energy generated per year.

Table4: Estimated Power Output and Monetary Value of the Power Output Annually

Vehicle passing/year	Generated Power annually (kW)	Electricity Cost in TRNC (TL)
40,000 cars	5,840	23,360
59,000 cars	8,614	34,456
90,000 cars	13,140	520,560

4. CONCLUSION

Keeping this in view, an attempt is made to study about the economic viability and cost benefit analysis of the design and manufacturing of smart speed bumps. The smart speed bumper design is durable and very efficient in long term. It can also transfer wireless power when there is a WPT receiver installed in surrounding CCTVs and lighting. In the future, if any adjustments are required to be made, it would be much easier to renew or change by an up-to-date similar device the required parts by the help of material cost table and manufacturing cost table. To add more, mass production of smart speed bumper costs much cheaper than producing just one piece of product.

REFERENCES

[1] Dara, J. E., Odazie, C. M., Okolie, P. C., &Azaka, A. O. (2020). Design and construction of a double actuated mechanical speed breaker electricity generator. Heliyon, 6(9), e04802. https://doi.org/10.1016/j.heliyon.2020.e04802

[2] Panovko, G. Nerubenko, and A. Shokhin, "Magnetic field shielding in electric vehicles by vibration energy harvesting dampers," Vibroengineering PROCEDIA, vol. 31, pp. 57–61, May 2020, doi: 10.21595/vp.2020.21420

[3] De Fazio, R., De Giorgi, M., Cafagna, D., Del-Valle-Soto, C., & Visconti, P. (2023). Energy harvesting technologies and devices from vehicular transit and natural sources on roads for a sustainable transport: State-of-the-Art analysis and commercial solutions. Energies, 16(7), 3016. doi:10.3390/en16073016

[4] Ullman, D. (2010). Product Evaluation: Design for Cost, Manufacture, Assembly, and Other Measures. The mechanical design process (4th ed., p. 49). McGraw-Hill Science, Engineering& Mathematics.

[5]Idea To Life, A. (2022, October 31). *Prototype vs production: 5 crucial differences in manufacturing*.(https://www.ideatolife.com.au/post/prototype-vs production#:~:text=The%20key%20difference%20between%20prototyping,reduces%20the%20cost%20per%20unit)

[6]Bosch Rexroth plastic round conveyor roller 40mm Dia. X 325mm L, 150N load capacity zinc plated steel, 8mm spindle,. (n.d.). Retrieved from https://uk.rs-online.com/web/p/conveyor-rollers/6657273

[7]RS Components Ltd. (n.d.). 062ed4b0-679b-4f2b-bafc-3b2864baec84. Retrieved from https://uk.rs-online.com/basket?source=web

[8]Pulley. (n.d.). Retrieved from https://www.walmart.com/ip/West-Coast-Paracord-Steel-Double-Wheel-Pulley-with-a-Swivel-Eye-Multiple-Sheave-Height-Pack-Options/218334870

[9]Pollorena, K. (2021, August 27). The importance of DC Generator maintenance. Retrieved from:https://www.gohispeed.com/the-importance-of-dc-motor-maintenance/

[10] Pirisi, A., Grimaccia, F., Mussetta, M., &Zich, R. (2012). Novel speed bumps design and optimization for vehicles' energy recovery in smart cities. Energies, 5(11), 4624-4642. doi:10.3390/en5114624

[11] Sarma, B. S., Jyothi, V., &Sudhir, D. (2014). Design of power generation unit using roller mechanism. IOSR Journal of Electrical and Electronics Engineering, 9(3), 55-60. doi:10.9790/1676-09315560

[12] P**.** Todaria et al**.,** "Design, modeling and test of a novel speed bump energy harvester,"Sensors Smart Struct. Technol. Civil, Mech. Aerosp. Syst. 2015, vol. 9435, p. 943506, 2015,doi: 10.1117/12.2084371.

[13] **P**. Chandra Sekhar, A. Balasubrahmanyam, and K. Rajashaker Reddy, "A study Paperon Power Hump," INTERNATIONAL JOURNAL & MAGAZINE OF ENGINEERING,TECHNOLOGY, MANAGEMENT AND RESEARCH, Jan. 2014.

[14] Wahle, J., &Schreckenberg, M**.** (2001). A multi-agent system for on-line simulations based on real-world traffic data. Proceedings of the 34th Annual Hawaii International Conference on System Sciences. doi:10.1109/hicss.2001.926332

[15] KIBTEK. (2023). Tarrif Rates. KIBRIS TÜRK ELEKTRİK KURUMU. https://www.kibtek.com/

USE OF FECR SLAG IN IRON AND STEEL

Gökhan Başman[1], Tuğçe ÖZCAN[1], Hande ARDIÇOĞLU[1], Erdoğan KARİP[1], Cengiz YASİN[1]

[1]Eti Krom Inc., R&D Center, Elazığ, TÜRKİYE

E-mail: tugce.ozcan@etikrom.com

Eti Krom, which was established as a state-owned enterprise in Elazig in 1936, has been the only high-carbon ferrochrome producer in Turkey since 1976. Joining Yıldırım Holding in 2004 within the scope of privatization, the company increased its production capacity by modernizing 4 arc furnaces to meet the increasing demand for high quality high carbon ferrochrome. Ferrochrome is an alloy containing 50% - 70% chromium and 50% - 30% iron. Ferrochrome produced by reducing chromite ores enriched by extracting from mineral deposits in electric arc-resistance furnaces using coke. High carbon Ferrochrome slag is produced as a waste in the production of high carbon ferrochrome. High carbon ferrochrome slag is mainly composed of MgO, Al_2O_3, and SiO_2. This slag is stored in stock areas.

The main objective of this study is to eliminate the environmental hazard of ferrochrome slag, which is released during ferrochrome production and stored as waste in the fields, to obtain economic returns and to prevent future storage problems.

Keywords: Ferrochrome, Slag, Zero Waste

1. INTRODUCTION

Slag is the material formed as a result of the melting of the products resulting from the interaction of charge components with refractory materials or slag makers during metallurgical processes, or the melting of charge components directly. The composition of the slag consists of oxides, silicates, borates, aluminates and phosphates. Some slags may also contain sulphides and carbides. While the impurities are collected in the formed slag, the metal quality is adjusted in this way. However, in some cases the opposite is true. For example, TiO2, which is used as a dyestuff, is collected in the slag during its production from ilmenite (FeO.TiO2). The effect of slag properties on yield and capacity is significant. For this reason, different types and amounts of slag formers are added from the outside in order to improve the slag properties. Slag builders added to form a fluid slag by interacting with residual minerals are required to have the following properties:

- lower costs,

— low melting temperature,

— low viscosity,

— high fluidity,

— low interaction with refractories, low solubility or immiscibility in metal

— low density to ensure good separation.

Residue minerals are generally siliceous, and silicates in the smelting of lime and magnesia and copper are used as slag builders in iron-steel manufacturing. Lime, fluospar, quartz and iron oxide lower the melting point of the slag and increase its fluidity. In addition to incorporating "slag-metal reactions" and gangue and impurity components, slag also has other important tasks in smelting processes. (1-4)These;

1) To protect the lower liquid metal phase from the effects of the furnace atmosphere and combustion products,

2) In addition to preventing the cooling of the metallic phase, to provide heat transmission from a flame on it to the metal phase,

3) To ensure that the treatment level is kept under control by making special or volume-enhancing additions. Slag formation is generally by endothermic reactions, so as the slag volume increases,

• Requires more heat input and therefore fuel costs increase,

• The amount of metal retained in the slag and consequently metal loss increases,

• Metal yield decreases,

• The rate of heat transfer from the furnace to the molten metal is reduced.

Since one of the functions of fluxes is to make easily melting slag by chemical reaction with unwanted foreign materials, acidic flux is used to remove foreign materials with basic character and basic flux is used to remove foreign materials with acidic character. In general, the melting temperature of the slag, which is formed as a result of the reactions between acidic and basic substances, is lower than the melting temperature of the components that make up the slag. Despite the presence of acidic and basic impurities in many ores, acidic components (such as SiO_2) are more. There are also basic oxides such as CaO+MgO in the ores, but not enough to bind the acidic SiO_2. For this reason, limestone ($CaCO_3$) is used as flux material in the production of raw iron in the blast furnace in order to throw both silica and phosphorus into the slag. Limestone is flux with basic character and dolomite ($MgCO_3.CaCO_3$) is an example of other basic fluxes. An example of acidic fluxes is silica (SiO_2). This flux material is generally used in steel production. Alumina (Al_2O_3) is also rarely used as a flux material. Depending on the conditions, it can act acidic or basic. For example, aluminum silicate in high silica slag forms calcium aluminate compound in high CaO environments (5-6).

The steelmaking process provides an opportunity to change the slag chemistry with external reinforcement slag formers. Although the definition of slag does not make sense to many people, it is a very important concept in the metal industry, the slag and the refractory to be used in the process must be compatible with each other, the appropriate / designed slag is a must for metallurgical processes. The chemical structure of the slag formed during metal production can be made less harmful to refractories by adding various additives. Slag chemistry is the most important element of liquid metalworking processes.

The concepts of acidity and basicity are important in the chemical degradation of refractories by slag. The melting temperature of the slag increases with the increase of slag basicity and %Al_2O_3, %MgO. In this case, MgO with a high melting point increases the slag melting temperature, increasing the adhesion of the slag to the refractory surface (7). This feature, which is a function of the refractory wetting properties of the slag, requires much more detailed studies. Ensuring the adhesion of the process slag, whose composition has been changed, on the refractory working lining is a mechanism that contributes positively to the refractory life.

2. MATERIAL AND METHODS

Some slag is released during ferrochrome production and almost all of it is stored in the stock area. In addition to creating environmental pollution and visual pollution, the slag stored in the open area may fill the stock areas in the future. For this purpose, within the scope of this project, it is aimed to research different usage areas of slag and to create a value-added product.

As a result of literature research (6,7) and interviews with iron and steel companies, it has been seen that dolomite is used with other reinforcements (lime) as a slag builder. The chemical content of dolomite and ferrochrome slag is given in Table 2.

Table 2. Chemical Content of Dolomite and Ferrochrome

	CaO	MgO	SiO2	Al2O3	Fe2O3	Cr2O3
Dolomite(%)	48-50	=	1-2	0,1-3	1	-
Ferrochrome Slag (%) (ECD)	1-1,5	37	35	25	0,5-1	2-3

Experiments were made by sending ferrochrome slag (ECD) to an iron and steel company. The trials were compared with dolomite, which is used as a slag modifier in the iron and steel industry.

The ECD sample was tested in different tonnages to make 8 castings, and a slag sample was taken from each casting and analyzed in the XRF device, and it is shown in Table 3.

6 tons of lime - 2 tons of dolomite in 3 castings,

4 tons of lime in 1 casting - 4 tons of ECD,

5 tons of lime in 2 castings – 3 tons of ECD,

5.5 tons of lime – 2.5 tons of ECD in 2 castings was tested by giving it to the quarry.

Table 3. Arc furnace slag analysis and %P in casting

Trial number	Amount of slag			%Fe2O3	%CaO	%SiO2	%Al2O3	%MgO	Slag basicity
	Lime (kg)	ECD (kg)	Dolomite (kg)						%CaO/SiO2
1	6000		2000	20,9	28,6	18,9	13,4	10,6	1,5
2	6000		2000	30,1	30,1	18,8	14,3	9,7	1,5
3	6000		2000	29,0	29,0	18,9	12,4	9,1	1,5
4	4000	4000		21,2	21,2	22,1	11,3	14,7	0,9
5	5000	3000		22,0	22,0	20,7	11,3	13,2	1,0
6	5500	2500		23,8	23,8	21,3	12,8	11,5	1,1
7	5000	3000		25,3	25,3	24,6	16,6	14,3	1,0
8	5500	2500		25,3	25,3	22,6	15,4	10,7	1,1

As a result of the trials, it was observed that the amount of %CaO decreased, the alkalinity rate in the slag decreased. It was determined that the basicity of slag was below 1.5 in 5 castings in which the tested ECD material was used. It is thought that the %P ratios of the castings have increased since the CaO content is low. In the evaluation of the study with Habaş Demir-Çelik, it was stated that the grain size of the ECD was small and there were problems during feeding into the kiln. In order to reach a more precise conclusion, it is planned that a new ECD trial should be made for use in all shifts for 1 day in an Arc Furnace with an ECD grain size of 10-50 mm.

The slag formation temperatures of the casting trials with ECD and dolomite were determined with the triple phase diagram as shown in Figure 1.

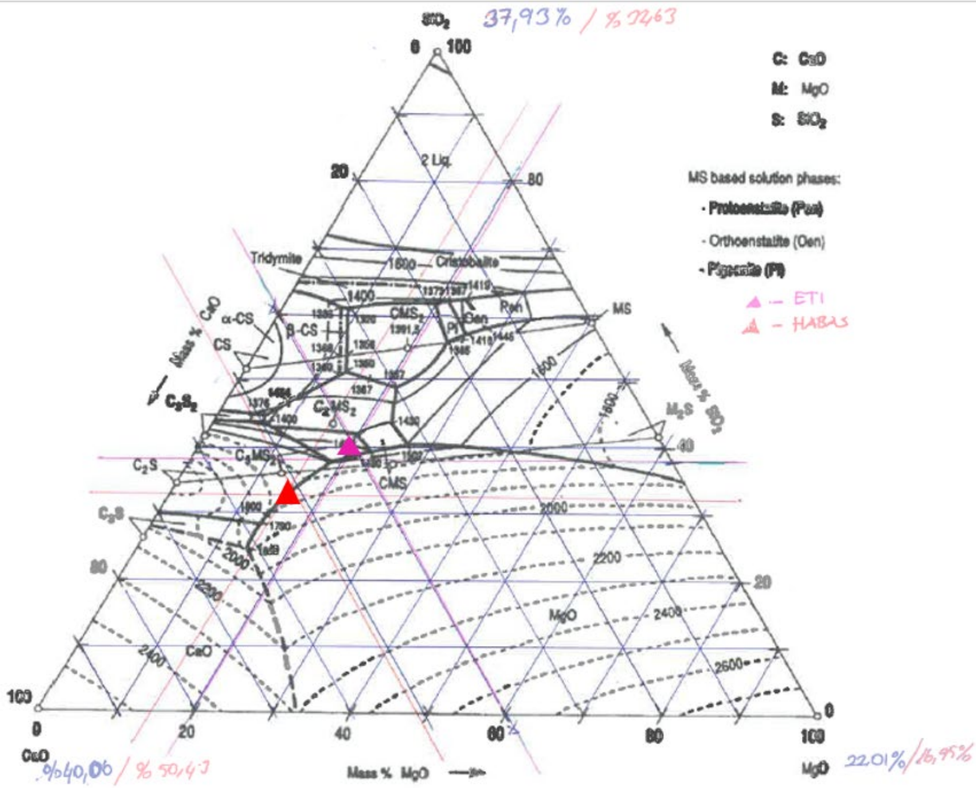

Figure 1. Slag formation temperature of trials using ECD and dolomite

It is important in the iron and steel industry as the CaO/SiO2 ratio affects the basicity of the slag. In addition, Silica (SiO2) increases the viscosity of the slag while decreasing its melting temperature. Since MgO has the feature of protecting the refractory, the formation temperatures of the slag were determined from the CaO-SiO2-MgO triple phase diagram and shown in Figure 1 using ECD. As seen in Figure 1, the use of ECD reduced the temperature of the eutectic point of the slag from 1600 °C to 1450 °C. This not only increased the viscosity of the slag, but also provided energy savings.

3. RESULTS AND DISCUSSION

The main objective of this study is to eliminate the environmental hazard of ferrochrome slag, which is released during ferrochrome production and stored as waste in the fields, to obtain economic returns and to prevent future storage problems. Within the scope of this project, ferrochrome slag started to be sold as a commercial product in the appropriate sector. Sıddıklar Demir A.Ş. In this joint project with the company, it has been observed that ferrochrome slag both regulates the slag in the iron-steel industry and protects the refractory by forming a protective layer on the refractory bricks of the kiln. Within the scope of this project, our current ferrochrome slag sales started in May 2022. The sales amount in May-April is 4289 tons. In the trials conducted with Habaş Demir-Çelik A.Ş within the scope of this project, it has been determined that the use of ECD reduces the slag formation temperature. However, since the ECD grain size affects the kiln regime and causes feeding difficulties, it was deemed appropriate to repeat the experiments by increasing the grain size. Meetings were held with Tosyalı Demir Çelik A.Ş about the slag regulator. Experiments will continue within the scope of this project.

REFERENCES

1- Proctor, D.M., Et al., Physical and Chemical Characteristics of Blast Furnace Basic Oxygen Furnace and Electric Arc Furnace Steel Industry Slags, Environment Science and Technology 34 (8): pp: 1576-1582, 2000.
2- Schroeder, R.L., The Use of Recycled Materials in Highway Construction. Public Roads, 58(2): 32-41, 1994.
3- Ahmed, I., Use of Waste Materials in Highway Construction, Noyes Data Corporation, Park Ridge USA, 1993.
4- Arm, M., Mechanical Properties of Residues As Unbound Road Materials, KTH Land and Water Resources Engineering, Doctorate Thesis, Stockholm, 2003
5- Hill, A.R., Dawson, A.R., Mundy, M., Utilisation of Aggregate Materials in Road Construction and Bulk Fill, Resources Conservation and Recycling 32, 305–320, 2001.
6- ALTAN, E., "Çelikhane Curufu İçerisindeki Hurdaların Değerlendirilmesi", I.Ulusal Demir-Çelik Sempozyumu ve Sergisi, Zonguldak 2001
7- S. BAYCIK, Granule Yüksek Fırın Cürufl arının Karo Sektöründe Kullanılabilirliğinin Araştırılması,Yüksek Lisans Tezi İstanbul Teknik Üniversitesi, 2002 İstanbul, Türkiye

TRIBOLOGICAL EFFECTS OF CHROME, ZIRCONIUM, AND GRAPHITE ON COPPER-BASED COMPOSITES

M. Horlu[1], G. İspirlioğlu Kara[2], C. K. Macit[3], B. Aksakal[4], M. Ayabakan[5]*

[1]Firat University, Faculty of Technology, Department of Mechanical Engineering, Turkey.
[2] Atatürk University, Faculty of Engineering, Department of Mechanical Engineering, Turkey.
[3] Fırat University, Faculty of Engineering, Department of Mechanical Engineering, Turkey.
[4]Firat University, School of Aviation, Aircraft Airframe-Engine Maintenance, Elazig, Turkey.
[5]Aisin Automotive Parts Industry and Trade Inc. 34953, Tuzla, İstanbul

E-mail: mervehorlu@gmail.com

In automotive industry, spot welding and gas arc welding are mainly used as joining methods. A review of the literature shows that Cu has been combined with different materials, but not with a hybrid mixture. In this study, hybrid composites were prepared by adding chromium (Cr), zirconium (Zr), and graphite (Gr) powders to copper (Cu) powder at specific ratios (99%, 98%) with the weight remaining constant at 1%. Cu, Cr, Zr, and Gr powders were mixed in a magnetic stirrer at 800 rpm for 90 minutes. The ready mixtures were homogenized in an ultrasonic mixer. The mixtures were then dried in an oven at 90 °C for 24 hours. The samples were prepared by powder metallurgy methods and were structurally characterized by SEM-EDS and XRD. The produced hybrid composites were subjected to compression, hardness and wear tests. Through wear tests, the weight loss and coefficient of friction values were obtained and were compared to each other. From the analysis, it was found that Cr, Zr and Gr reinforcements improved mechanical properties and wear resistance compared to pure Cu alloy.

Keywords: Hybrid Composites, Powder metallurgy, Zirconium, Graphite, Wear.

1. INTRODUCTION

Welding is the most widely used joining process in the automotive industry. Spot resistance welding is also commonly used that can be adapted to mass production. This method is very fast, it can be done by pressing a button or foot pedal. Therefore, welding labor costs are considerably lower than other methods. On the other hand, machinery and equipment costs are higher than other welding methods. For the spot resistance welding method to be economical, a large number of identical or similar welding processes must be performed. This method is widely used in the automotive and aircraft industries, as well as in the production of metal goods, due to its light weight due to the absence of additional metal, high weld strength, aesthetic appearance, no need for operator skill, and high welding speed [1]. The basic properties such as high electrical conductivity, high room temperature strength, ability to maintain its strength at high temperatures (high-temperature strength), and resistance in tribological properties are sought in coppers to be used in application areas where electrical conductivity is the first request, such as point resistance welding [2].

Today, pure copper is typically utilized in applications requiring high thermal or electrical conductivity, although its alloys (bronzes and brasses) are used in a wide range of industries due to their corrosion and wear resistance [3]. Despite these distinct features, copper's poor strength and hardness have limited its use as a structural material [4,5]. Many studies in the realm of materials have been conducted to overcome these disadvantages. To obtain high-performance Cu-based materials, two processes are commonly used. The first is the alloying pathway, which includes Cu-Cr-Zr, Cu-Cr-Gr, and Cu-Cr alloys, where the predominant strengthening factor is precipitation strengthening induced by intermetallic particles from the aging process. The second way is composite manufacturing, in which reinforcement is provided by particles (carbides, borides, etc.).

Rapidly developing technology requires continuous research in the production of new materials. Composite materials are one of the new material groups. Materials that are combined at the macro level to combine the best properties of two or more materials into a new and single material are called composite materials [8]. Composite materials consist of reinforcing elements and a matrix material that holds them together. The production goal of composite materials is usually to produce materials with high mechanical strength, stiffness, fatigue resistance, wear resistance, and high corrosion resistance, as well as lightweight and aesthetic appearance [9]. The production methods of powder metallurgy are completely different from other metal-forming methods and are similar to the production technology of ceramic parts. In both cases, the process starts with pressing powders into a mold. The formed shape is sintered to obtain the required strength [10]. Some parts may then be calibrated (re-pressing), oil or plastic impregnated, infiltrated with a lower melting point metal or alloy, heat treated, or plated [11].

Cr, Zr, and Gr used as reinforcing elements offer excellent properties such as thermal conductivity, low density, higher fatigue strength, durability, high machinability, durability, wear resistance, dimensional stability, strength-to-weight-dimension ratio performance compared to other alloys [12–15].

There is no information in the literature about the preparation of a copper-based hybrid composite with Cr, Zr, and Gr additives. In this study, hybrid composites were prepared by powder metallurgy method using Cr, Zr, and Gr as reinforcing elements of copper matrix composites. The mechanical and electrical properties of the prepared composite samples were investigated and the metallurgical characterization of the prepared composite was determined.

2. MATERIAL AND METHODS

2.1. Materials Used, Powder Preparation and Production Scheme

Powders with physical properties of 44 (µm) particle size and 99.9% purity were used in the study. Table 1 shows the number of samples used in the composites by weight in the powders produced and the coding and nomenclature of the composites, and the sample preparation scheme is shown in Figure 1. In the preparation of the composites, the matrix material was adjusted to be copper and mixed homogeneously with the reinforcing elements whose weight percentages are given in Table 1. Before the compounding process, the materials in the ratios in Table 1 were weighed on a balance with a sensitivity of 10-4 to fill the 3-gram mold in a particular proportion.

The prepared powders were mixed in a magnetic mixer at 800 rpm for 90 minutes. To obtain a more homogeneous mixture, 40 ml of ethanol was added and subjected to homogenization for 15 minutes at a cycle speed of 20 Mhz. The resulting solution was then dried in an oven at 90 °C for 24 hours without exposure to air. After drying, the mixture was poured into a mold lubricated with zinc stearate ($Zn(C_{18}H_{35}O_2)_2$), and test specimens were prepared in a hydraulic press at a pressure of 35 MPa.

Table 1. Nomenclature of powders and amount of additives by weight

Sample Name	Cu	Cr	Zr	Gr
Cu	%100	-	-	-
Cu-Cr	%99	%1	-	-
Cu-Zr	%99	-	%1	-
Cu-Cr-Zr	%98	%1	%1	-
Cu-Cr-Gr	%98	%1	-	%1
Cu-Zr-Gr	%98	-	%1	%1

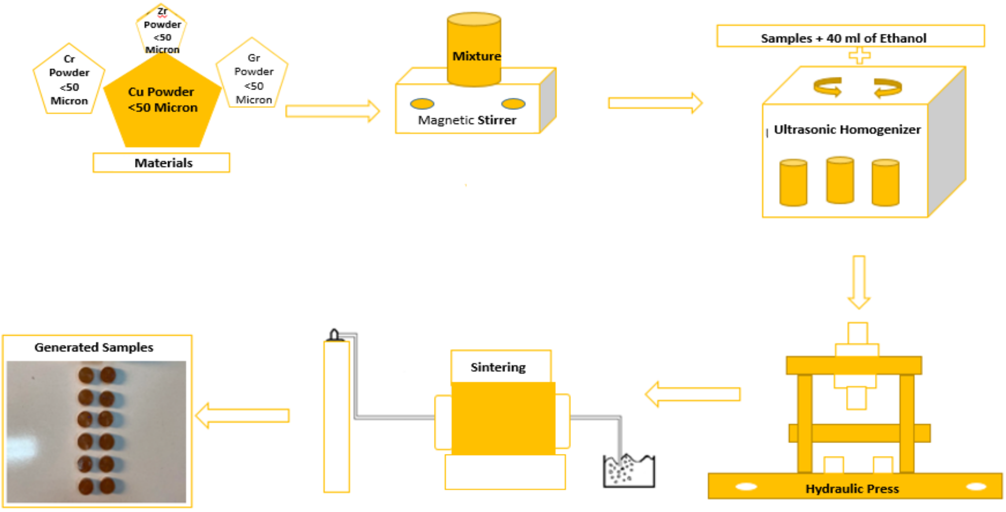

Figure 1. Preparation scheme of copper-based composites

To increase the strength of the specimens, sintering was performed and for this process, they were kept in an argon gas atmosphere at 750°C for 90 minutes and then left to cool on their own. The samples obtained after sintering were bakelitized to examine the microstructure, wear, and hardness of the samples more easily, and then sanding and polishing processes were carried out to examine their tribological properties. Figure 2 shows the samples after bakelite removal and sanding and polishing processes.

a) b) c)

Figure 2. (a) Bakelite taken b) After bakelite c) After polishing

2.2. Microstructure, Hardness, Tribology and Characterization

In the microstructures of the samples, which were produced, pressed, sintered, and prepared for the experiments, the reinforcing element particles distributed in the Cu matrix structure and the homogeneous distribution of the powders were examined by SEM, EDX analysis and the phase identification of the powders by X-ray diffraction (XRD) analysis. In hardness tests, measurements were taken from 5 different points at load values between 1-10,000 g, and the average hardness values of the composites were determined by averaging these values. The average hardness value was found in the Vickers value. Abrasion tests were performed with a pin-on-disk abrasion tester at constant load (10 N), sliding distance (1000 m), and sliding speed (150 rpm).

The weight loss of the composites as a result of abrasion was measured on a balance with a sensitivity value of 10^{-4}. The measured values were recorded and weight loss graphs and coefficient of friction graphs were created for each sample according to the distance. As a result of the wear experiments of the samples, the wear marks that occurred as a result of wear were examined and interpreted in detail in SEM analysis.

3. RESULTS AND DISCUSSION

3.1. XRD Results

XRD diffraction patterns of the composites are shown in Figure 3. XRD analyses showed that each sample retained its characteristic peaks and these characteristic peaks are consistent with literature studies.

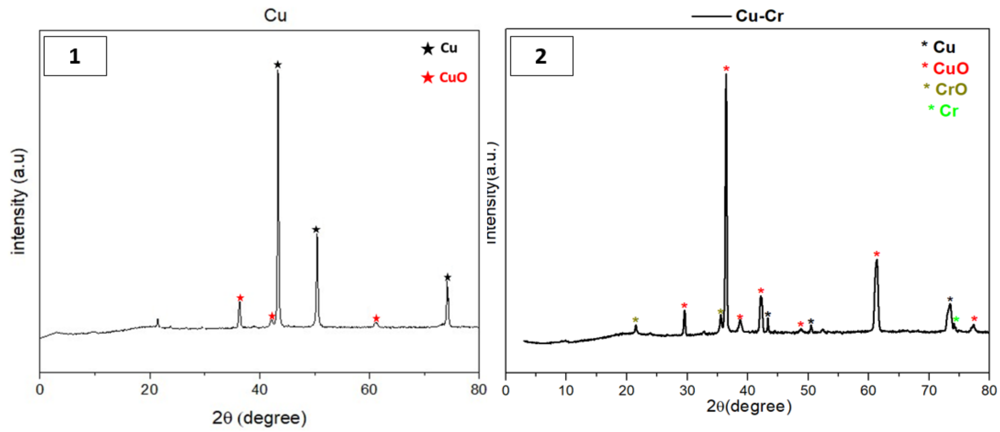

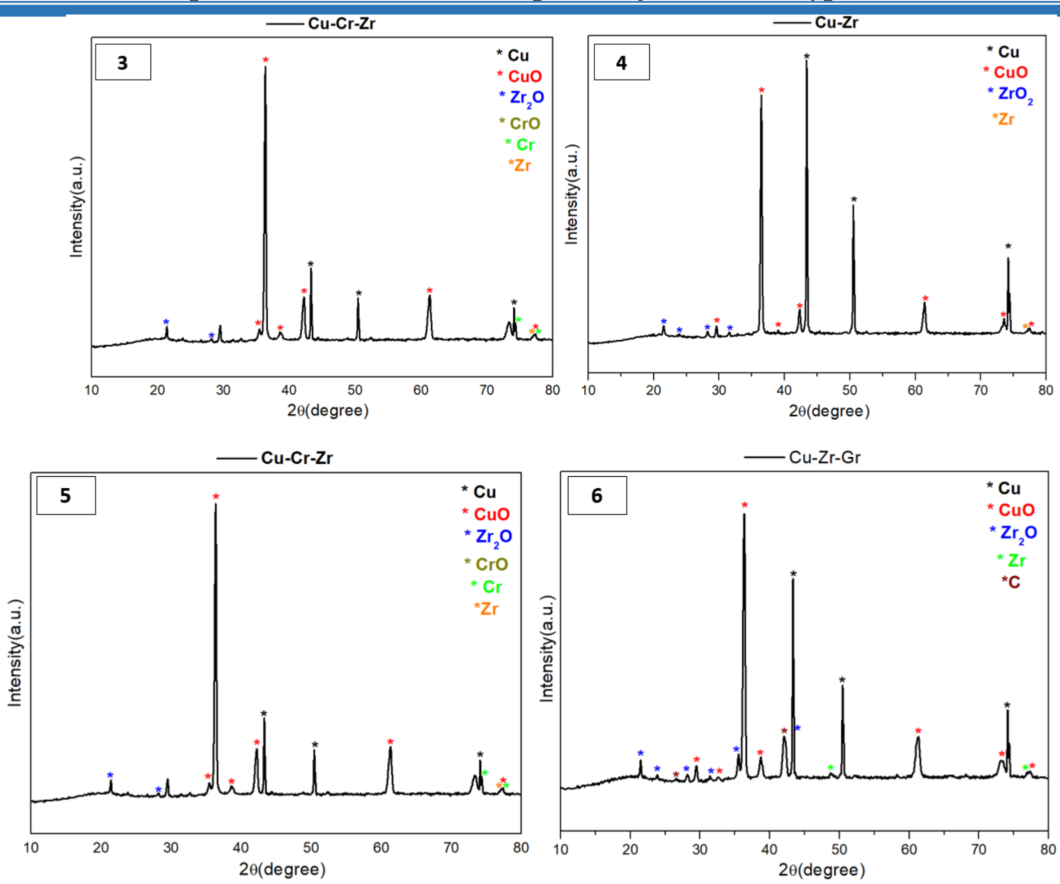

Figure 3. XRD diffraction patterns of the samples

3.2. SEM Images and EDS Analysis

The results of SEM and EDX analysis taken to examine the microstructure of the samples are shown in Figure 4. It is seen that the reinforcement ratios specified in Table 1 are formed together with the matrix material and are homogeneously distributed.

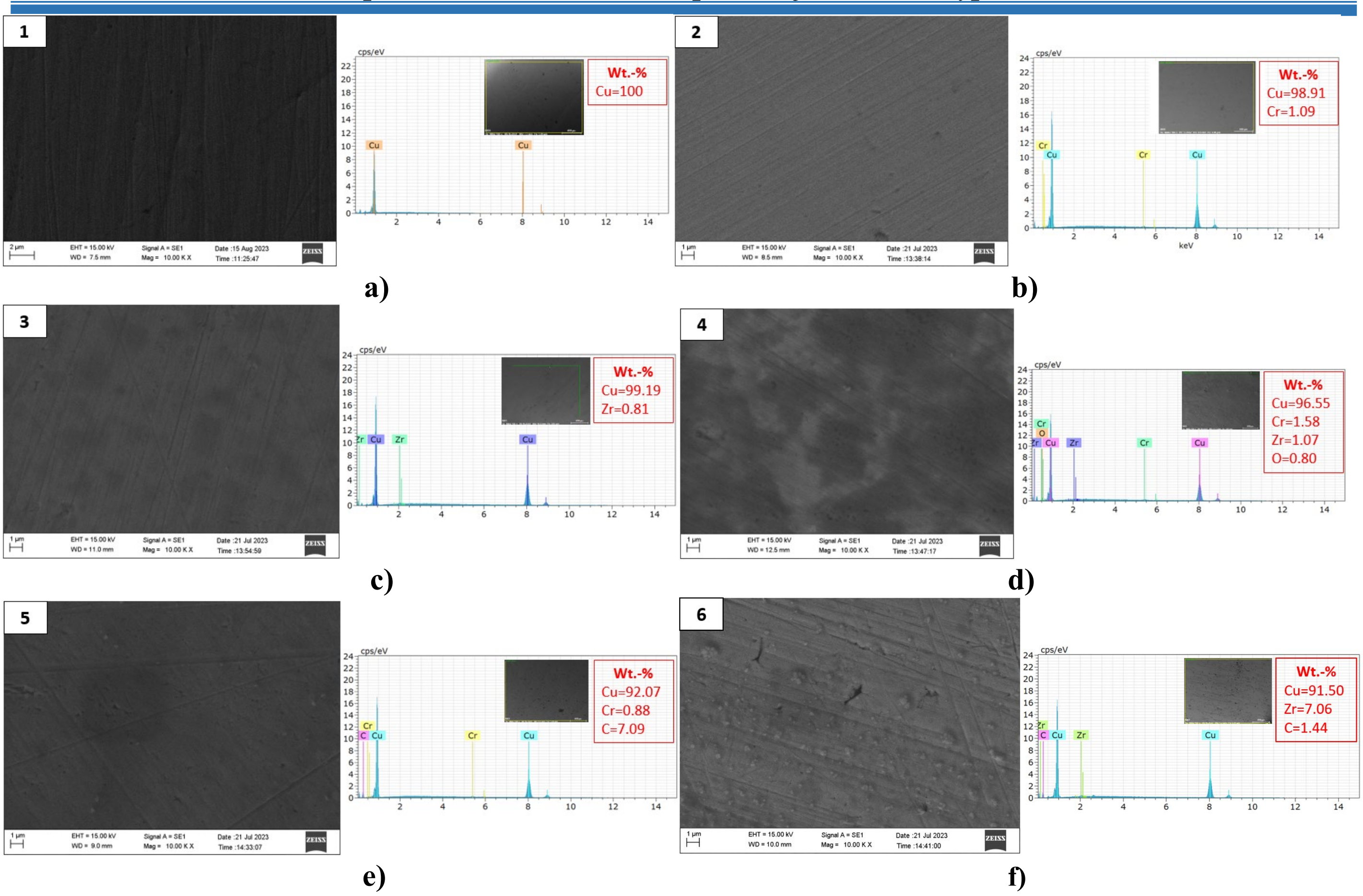

Figure 4. SEM images and EDX results of the samples a) Cu, b) Cu-Cr, c) Cu-Zr, d) Cu-Cr-Zr, e) Cu-Cr-Gr, f) Cu-Zr-Gr

3.3. Hardness and Tribology

Oxide layers were observed on the surfaces of the samples. Sanding and polishing processes were performed again to minimize these oxide layers. When the hardness values of the hybrid composites are examined, the average hardness values taken from 5 different points are shown in Figure 5. The highest hardness value was observed in the Cu-Cr-Gr composite. In the hardness results, much higher hardness results were observed with the addition of reinforcing elements compared to pure copper composites. It is also supported that the addition of Gr, Zr, and Cr positively affects the hardness results when the literature studies are examined [16–19]. The wear weight losses for each sample at a sliding distance of 1000 meters in wear tests are shown in Figure 6. It was observed that Cr, Zr, and Gr increased the wear resistance in wear tests where similar results were obtained to the hardness results.

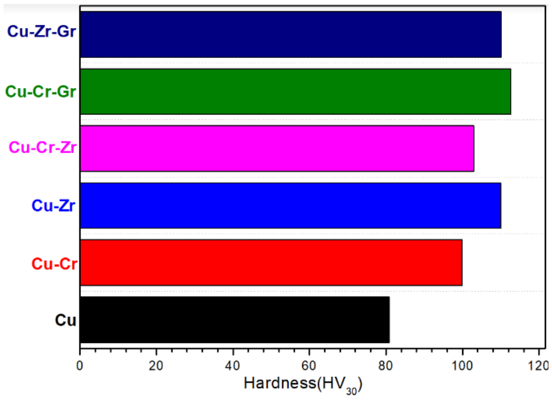

Figure 5. Hardness results

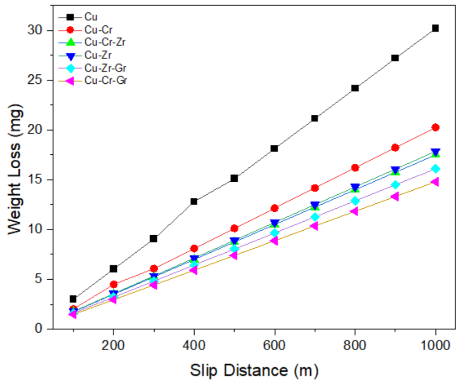

Figure 6. Weight loss values for hybrid composites

Separate samples were prepared for the coefficient of friction values in the composites and the composites were re-worn at a total sliding distance of 1000 meters. The friction coefficient values are shown in Figure 7. The highest coefficient of friction was observed in the Cu composite, while the lowest coefficient of friction value was observed in the Cu-Zr-Gr composite. It was observed that Gr reinforcement decreased the coefficient of friction and increased the wear resistance. When the studies with Cr, Zr, and Gr reinforcements are examined, similar results are reported in the literature studies [16–18].

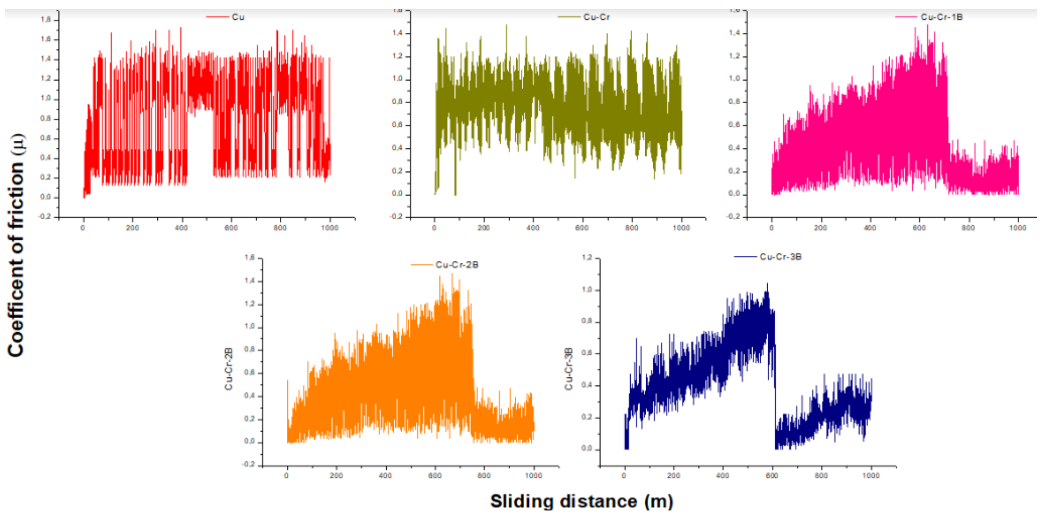

Figure 7. Friction coefficient values as a result of wear

SEM images of the composites after wear are shown in Figure 8. In the wear images, deep cracks and scars were formed after wear on the pure Cu sample. In the Cu sample, the adhesive wear mechanism was observed with the formation of deep craters and deformation of the worn surface. With Cr and Zr doping, Cu-Cr, and Cu-Zr specimens showed decreases in wear scars and depths and increased wear resistance [16–19]. The wear resistance was improved with the doping of Gr particles [17–20]. The best wear resistance was observed in the Cu-Zr-Gr sample.

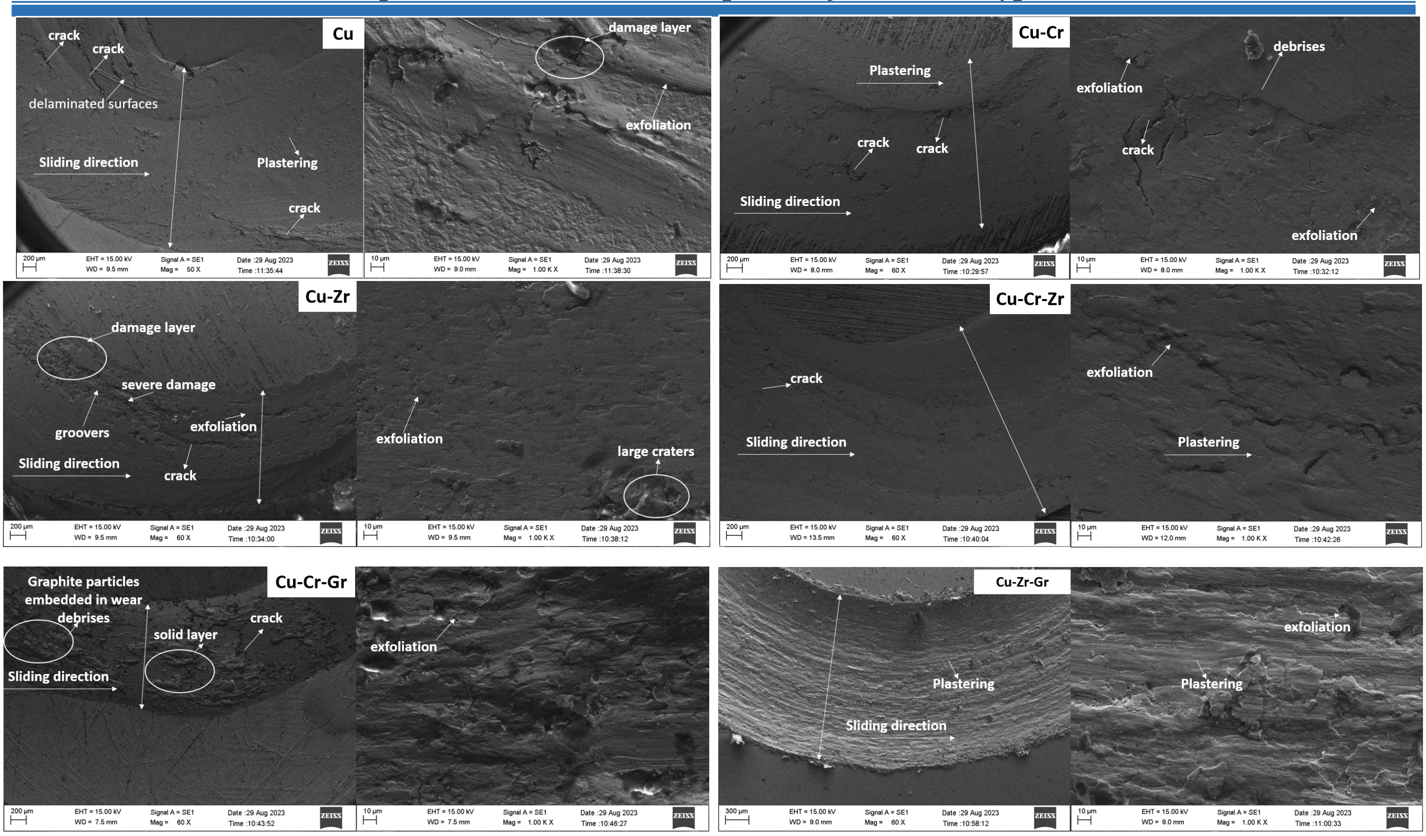

Figure 8. SEM views after wear tests for the composites

4. RESULTS

Different composites (Cu-Cr, Cu-Zr, Cu-Cr-Zr, Cu-Cr-Gr and Cu-Zr-Gr) were produced by powder metallurgy method;

- XRD diffraction patterns show that the matrix material and reinforcements retain their characteristic peaks.
- SEM images and EDS results show that the powders are homogeneously dispersed.
- In the hardness tests applied to the composites, 24% (Cu-Cr), 27% (Cu-Zr), 22% (Cu-Cr-Zr), 28% (Cu-Cr-Gr), and 31% (Cu-Zr-Gr) better results were obtained compared to the pure Cu, respectively. The highest hardness value was observed in the Cu-Zr-Gr composite.
- In the wear test, Cr, Zr, and Gr additives improved the wear resistance and better results were obtained in terms of weight loss in total sliding distance and friction coefficient values.

REFERENCES

[1] C.P. Samal, J.S. y Parihar, D. Chaira, The effect of milling and sintering techniques on mechanical properties of Cu–graphite metal matrix composite prepared by powder metallurgy route, J. Alloys Compd. 569 (2013) 95–101.

[2] G. Manohar, A. Dey, K.M. Pandey, S.R. Maity, Fabrication of metal matrix composites by powder metallurgy: a review, in AIP Conf. Proc., AIP Publishing, 2018.

[3] L. Collini, Copper Alloys: Early Applications and Current Performance-Enhancing Processes, BoD–Books on Demand, 2012.

[4] B. Huang, Y. Hishinuma, H. Noto, T. Muroga, Mechanochemical processing of Cu-Y2O3 alloy by MA-HIP for heat sink materials application, Fusion Eng. Des. 140 (2019) 33–40.
[5] H. Chen, C. Jia, S. Li, Effect of sintering parameters on the microstructure and thermal conductivity of diamond/Cu composites prepared by high pressure and high-temperature infiltration, Int. J. Miner. Metall. Mater. 20 (2013) 180–186.
[6] X. Zhang, Z. Xiao, Z. Xia, S. Han, X. Meng, Y. Zhao, Z. Li, Q. Lei, Microstructure and properties of Cu-TiNi composites prepared by vacuum hot pressing, J. Alloys Compd. 897 (2022) 162729.
[7] T. Han, J. Li, N. Zhao, C. Shi, E. Liu, F. He, L. Ma, Q. Li, C. He, In-situ fabrication of nano-sized TiO2 reinforced Cu matrix composites with well-balanced mechanical properties and electrical conductivity, Powder Technol. 321 (2017) 66–73.
[8] S.E. Susilowati, A. Fudholi, D. Sumardiyanto, Mechanical and microstructural characteristics of Cu–Sn–Zn/Gr metal matrix composites processed by powder metallurgy for bearing materials, Results Eng. 14 (2022) 100377.
[9] S. Akhtar, M. Saad, M.R. Misbah, M.C. Sati, Recent advancements in powder metallurgy: a review, Mater. Today Proc. 5 (2018) 18649–18655.
[10] P.K. Prajapati, D. Chaira, Fabrication and characterization of Cu–B 4 C metal matrix composite by powder metallurgy: Effect of B 4 C on microstructure, mechanical properties and electrical conductivity, Trans. Indian Inst. Met. 72 (2019) 673–684.
[11] M. Meignanamoorthy, M. Ravichandran, Synthesis of metal matrix composites via powder metallurgy route, Mech. Mech. Eng. 22 (2018) 65–75.
[12] L.-P. Lapierre-Boire, C. Blais, S. Pelletier, F. Chagnon, Improvement of the flow of an iron-copper-graphite powder mix through additions of nanoparticles, Powder Technol. 299 (2016) 156–167.
[13] T. Zhimeng, W. Zemin, X. Lei, Z. Libo, H. Zhaohui, L. Jianhua, Thermal and tribological properties of MoS2 doped graphite/copper composites by microwave sintering, J. Mater. Res. Technol. 15 (2021) 6001–6010.
[14] T. Gong, P. Yao, X. Xiong, H. Zhou, Z. Zhang, Y. Xiao, L. Zhao, M. Deng, Microstructure and tribological behavior of interfaces in Cu-SiO2 and Cu-Cr metal matrix composites, J. Alloys Compd. 786 (2019) 975–985.
[15] M. Bhagwat, A. V Ramaswamy, A.K. Tyagi, V. Ramaswamy, Rietveld refinement study of nanocrystalline copper doped zirconia, Mater. Res. Bull. 38 (2003) 1713–1724.
[16] P. Zhang, L. Zhang, D. Wei, P. Wu, J. Cao, C. Shijia, X. Qu, K. Fu, The synergistic effect of Cr and Fe particles on the braking behavior of Cu-based powder metallurgy brake pads, Tribol. Trans. 62 (2019) 1072–1085.
[17] P. Ravindran, K. Manisekar, R. Narayanasamy, P. Narayanasamy, Tribological behavior of powder metallurgy-processed aluminum hybrid composites with the addition of graphite solid lubricant, Ceram. Int. 39 (2013) 1169–1182.
[18] P. Vasanthakumar, K. Sekar, K. Venkatesh, Recent developments in powder metallurgy based aluminum alloy composite for aerospace applications, Mater. Today Proc. 18 (2019) 5400–5409.
[19] H. Zhou, P. Yao, T. Gong, Y. Xiao, Z. Zhang, L. Zhao, K. Fan, M. Deng, Effects of ZrO2 crystal structure on the tribological properties of copper metal matrix composites, Tribol. Int. 138 (2019) 380–391.
[20] N.A.B.N. Zamani, A.K.M.A. Iqbal, D.M. Nuruzzaman, Mechanical and tribological behavior of powder metallurgy processed aluminum–graphite composite, Russ. J. Non-Ferrous Met. 60 (2019) 274–281.

INVESTIGATION of THE MECHANICAL and WEAR PROPERTIES of BORON and CHROMIUM REINFORCED COPPER MATRIX HYBRID COMPOSITES

G. İspirlioğlu Kara[1], M. Horlu[2], C. K. Macit[3], B. Aksakal[4], S. Sezek[1], M. Çelik[5]

[1]Ataturk University, Faculty of Engineering, Department of Mechanical Engineering, Erzurum, Turkey
[2]Firat University, Faculty of Engineering, Department of Mechanical Engineering, Elazig, Turkey
[3] Firat University, Faculty of Engineering, Department of Mechanical Engineering, Turkey
[4] Firat University, School of Aviation, Aircraft Airframe-Engine Maintenance, Elazig, Turkey
[5] Aisin Otomotiv Parça San. Tic. A.Ş., Tuzla, İstanbul

E-mail: gamze.ispirlioglu@atauni.edu.tr

Copper (Cu) and its alloys are widely used in engineering applications such as machinery, electronics, transport, etc. due to its electrical conductivity and chemical stability. However, it exhibits low mechanical and tribological properties, especially when used at high temperatures (600-800^{0}C). One of the most effective ways to increase wear resistance is to produce Cu matrix-reinforced hybrid composites. In this study, hybrid composites were produced by adding chromium (Cr) (1%wt) and boron (B) (1%, 2%, 3%wt) powders (1%, 2%, 3%wt) at certain ratios to pure (99.9%) Cu powder. The samples were prepared with powder metallurgy production parameters. The hybrid composites were produced using a cold press (35MPa) and sintering (750 ^{o}C) under a controlled atmosphere. The produced samples have been characterized by SEM-EDS and XRD analysis, and hardness and wear tests were also performed. According to the results obtained in the study, changes in hardness and wear values with the addition of chromium and boron reinforcement to the copper matrix. While the hardness value of the pure Cu sample was 80 HV, the hardness value increased to 130 HV in the Cu-Cr-3B sample. In the wear tests, it was found that the value of the friction coefficient decreased and the resistance to friction increased with Cr and B additives.

Keywords: Copper, Boron, Chromium, Powder metallurgy, Tribology

1. INTRODUCTION

Copper has attracted great interest in recent years due to its high electrical and thermal conductivity, corrosion resistance, and easy processing [1]. Therefore, Copper (Cu) alloys are widely used in electronic engineering. For example; it is preferred in electrodes for resistance welding, contacts for electrical welding, and heat sink materials [2,3]. Cu and its alloys are also widely used in chemical and automotive industries for many parts such as radiators and pipes, in cooling systems, and in the defence industry [4–6]. However, copper has poor mechanical properties (such as low hardness, low tensile yield strength, and poor creep resistance) at high temperatures, which prevents its use as a structural material [1,7]. Therefore, there is a need to improve the mechanical performance of Cu and Cu alloys that have both good mechanical properties and excellent conductive properties [8]. The best way to increase the mechanical strength of copper is age hardening or the addition of reinforcing elements to the copper matrix. The main challenge in the development of copper matrix composites is to keep the electrical conductivity high while improving the mechanical properties [9,10].

Chromium (Cr) and Boron (B) were used individually as reinforcing elements. Cr-reinforced composites are preferred because chromium is relatively cheap, easily recyclable, increases hardenability, superior tribological properties, and superior refractoriness compared to composites reinforced with different reinforcement categories [11–13]. Boron-reinforced copper matrix composites can have properties such as high stiffness, strength, and thermal stability. Since boron is a corrosion-resistant material, it can increase corrosion resistance when used as a reinforcing material in copper matrix composites [14,15]. Boron has very low solubility in metals at room temperature and has a significant effect on hardenability and transformation characteristics, so it is of great benefit in improving the properties of metals such as high-temperature resistance, high strength, high elasticity, high surface protection, high wear and corrosion resistance, high adhesion and adhesion [16].

When the literature studies are examined, there are studies in which B and Cr powders are added to Cu powder separately. However, it was observed that a hybrid mixture was not made as in this study. In this study, a hybrid blend was made by adding Cr and B in proportions of (1%, 2%, and 3%) by weight to pure Cu powder at a constant rate of 1%. Microstructure (SEM, EDX, and XRD), hardness, and wear tests were performed to characterize the composites

2. MATERIAL AND METHODS

2.1. Materials Used, Preparation of Powders and Production Scheme

The flow chart of the processes carried out in the study is shown in Figure 1 and the naming of the powders and the amount of additives by weight are shown in Table 1.

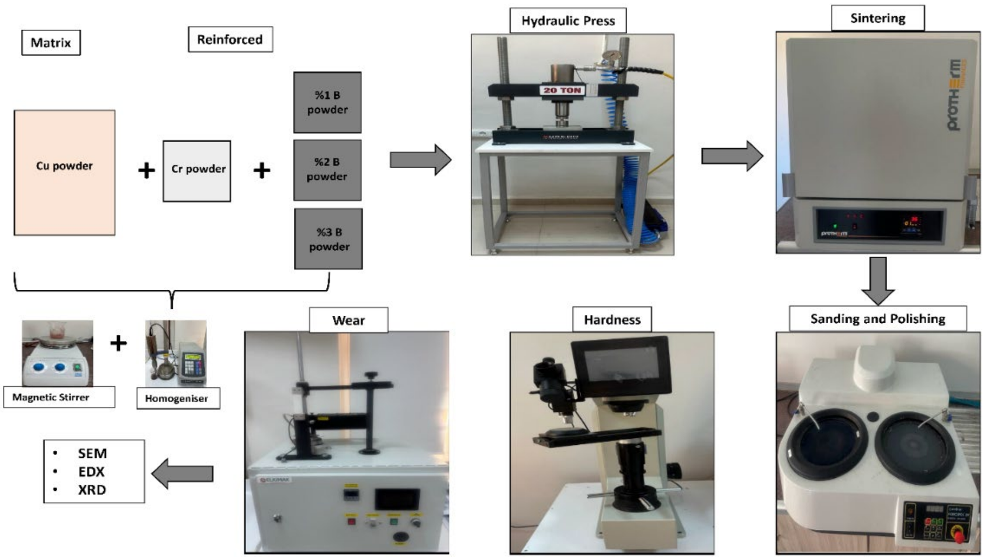

Figure 1. Boron-reinforced Hybrid Composite preparation scheme

Table 1. Hybrid composite groups and amounts of additives by weight

Numune	Cu	Cr	B
Cu	%100	-	-
Cu-Cr	%99	%1	-
Cu-Cr-1B	%98	%1	%1
Cu-Cr-2B	%97	%1	%2
Cu-Cr-3B	%96	%1	%3

The matrix material used in the study is Cu and the reinforcement materials are Cr and B. In the powder preparation process, the reinforcement elements and matrix material were mixed in a magnetic mixer at 700 rpm for 60 minutes. To make the prepared powders more homogenous, they were mixed again in Sonics vibra cell brand ultrasonic homogenizer at a frequency of 20 MHz for 10 minutes. The composite mixtures were cold pressed at a pressure of 35 MPa. Sintering was carried out in an argon gas atmosphere at 750^{0}C for 90 minutes and then allowed to cool. After the samples were baked, they were sanded with 100, 240, 400, 600, 800, 1000, and 1200 mesh SiC sandpaper and then polished with a 3 µm diamond paste.

2.2. Characterization, Tribology and Hardness

The samples were taken to bakelite and sanding and polishing processes were carried out. X-ray diffraction (XRD) analysis of Rigaku RINT-2000 X was performed for phase identification of the prepared samples. Zeiss EVO MA10 brand Scanning Electron Microscope (SEM) and Energy Dispersive Spectrum (EDS) analyses were performed to examine the distribution of reinforcing elements in the microstructure of copper matrix composites.

The samples were bakelite, and sanding and polishing were performed. X-ray diffraction (XRD) analysis of Rigaku RINT-2000 X was performed for phase identification of the prepared samples. Zeiss EVO MA10 brand Scanning Electron Microscope (SEM) and Energy Dispersive Spectrum (EDS) analyses were performed to examine the distribution of reinforcing elements in the microstructure of copper matrix composites.

Abrasion tests were carried out at a sliding distance of 1000 meters and the weight loss of the samples was measured every 100 meters on a precision balance these values were recorded and weight loss graphs were created. To determine the coefficients of friction, each specimen was abraded over a sliding distance of 1000 meters. Friction coefficient values were recorded and friction coefficient graphs were prepared.

In hardness tests, measurements were taken from 7 different points using the ONALKON brand hardness tester, and hardness values were determined by averaging these values.

3. RESULTS AND DISCUSSION

3.1. Microstructure

XRD analyses were performed for the prepared samples (Figure 2). As a result of XRD analyses, it was observed that chromium and boron reinforcing elements were formed in the structure within the copper matrix. XRD analyses showed the formation of copper (Cu), chromium (Cr), boron (B), copper oxide (CuO), and boron chromium (Cr_2B) elements and compounds.

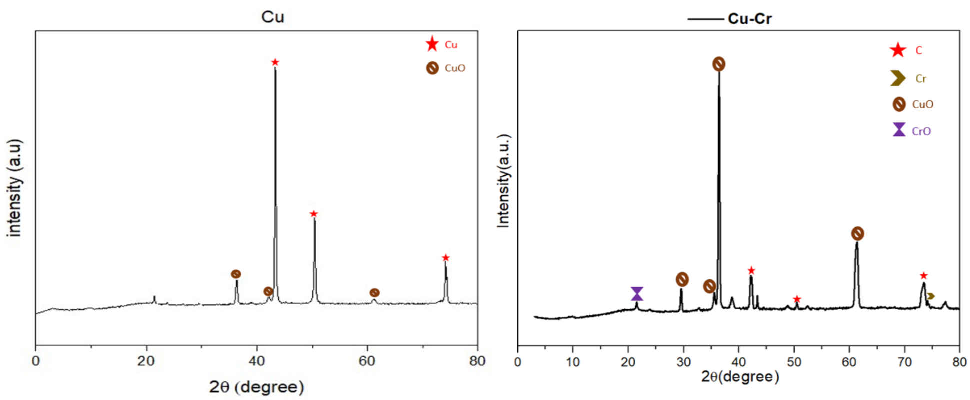

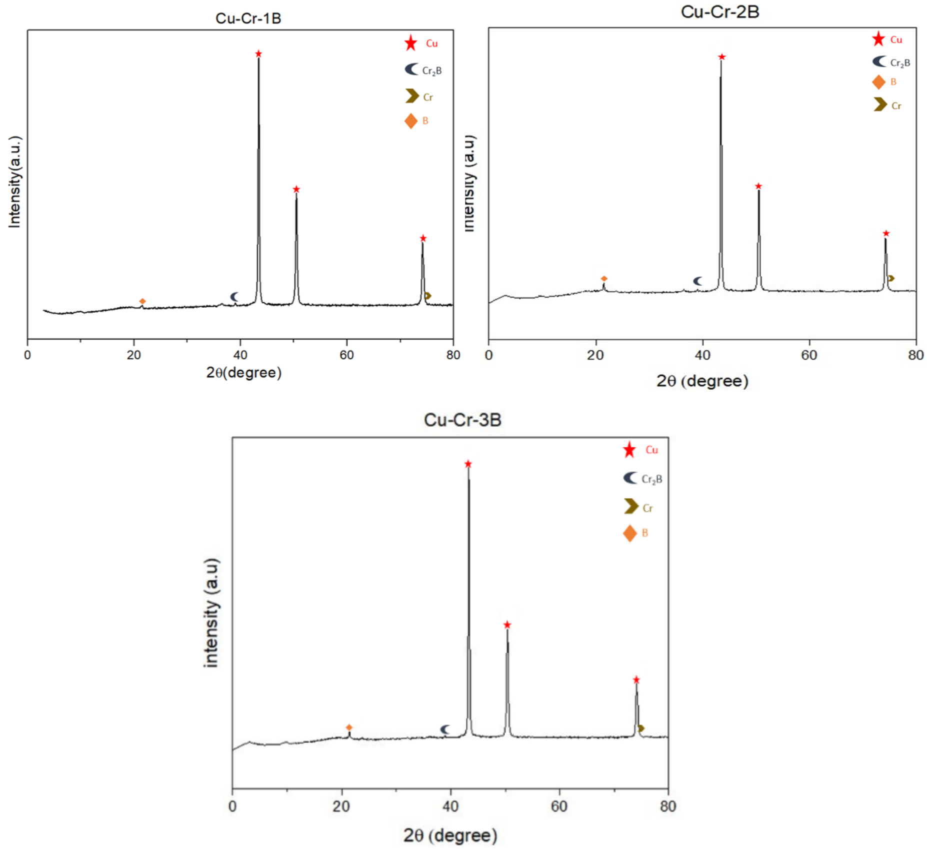

Figure 2. XRD diffraction patterns

SEM and EDS analysis results of copper matrix hybrid composites are shown in Figure 3. SEM results show that Cr and B particles are homogeneously distributed in Cu composites. It was observed that B particles were observed more clearly with the increase of B additives in the composites. EDS analysis results show that Cr and B additives are combined with Cu.

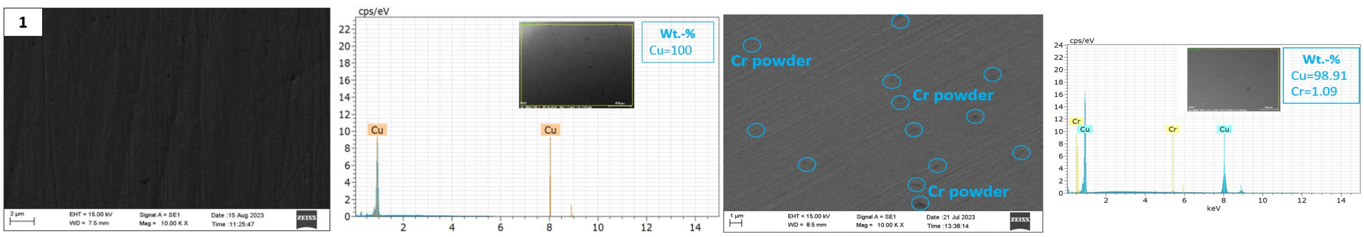

a) b)

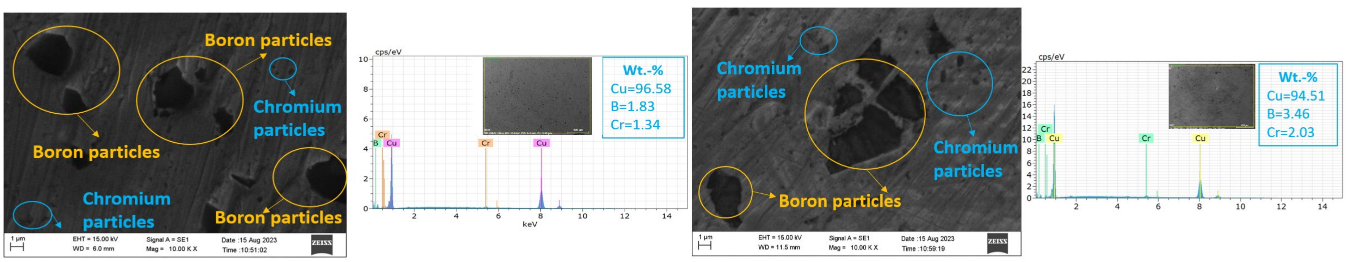

c) d)

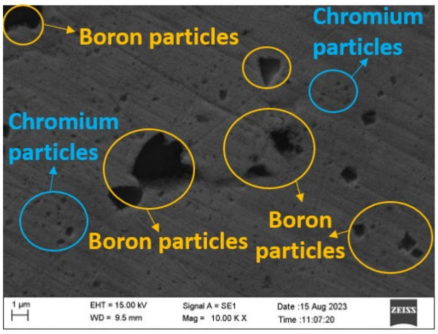

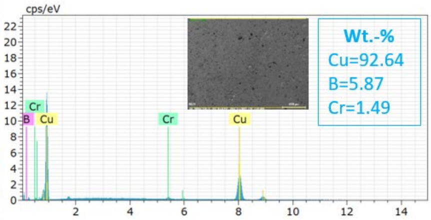

e)

Figure 3. SEM images of composites a) Cu, b) Cu-Cr, c) Cu-Cr-1B, c) Cu-Cr-2B, c) Cu-Cr-3B

3.2. Hardness

The hardness values of the copper matrix composite samples were found in Vickers hardness. In the hardness tests, it was observed that the hardness value of pure Cu value was similar to the literature values [17]. In hardness tests, it was observed that Cr and B additives significantly increased the hardness value of composite samples. It can be seen from the results that, particularly B addition increased the hardness of the composites (Figure 4).

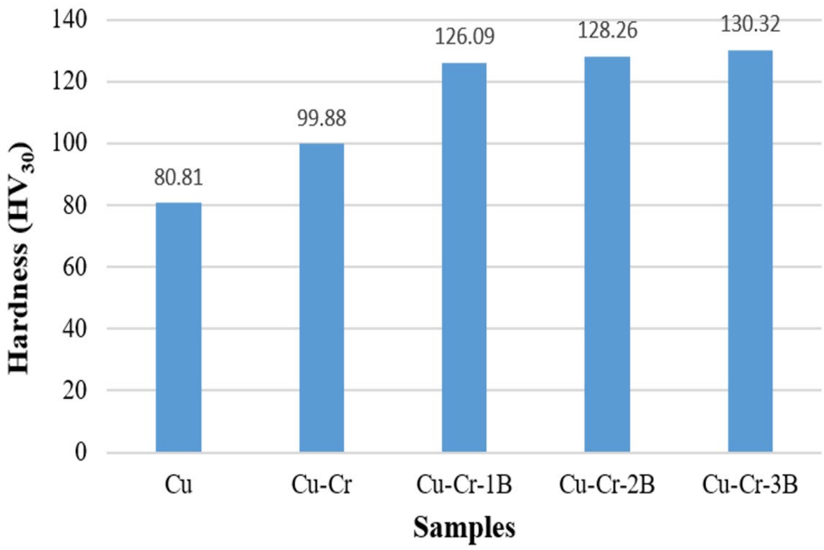

Figure 4. Hardness values

3.3. Wear tests

1000 m sliding distance, the total weight loss results of the composites in the wear tests are shown in Figure 5. It was observed that Cr and B additives decreased the weight loss amounts and the wear resistance on the wear surfaces increased with the increase of B additive.

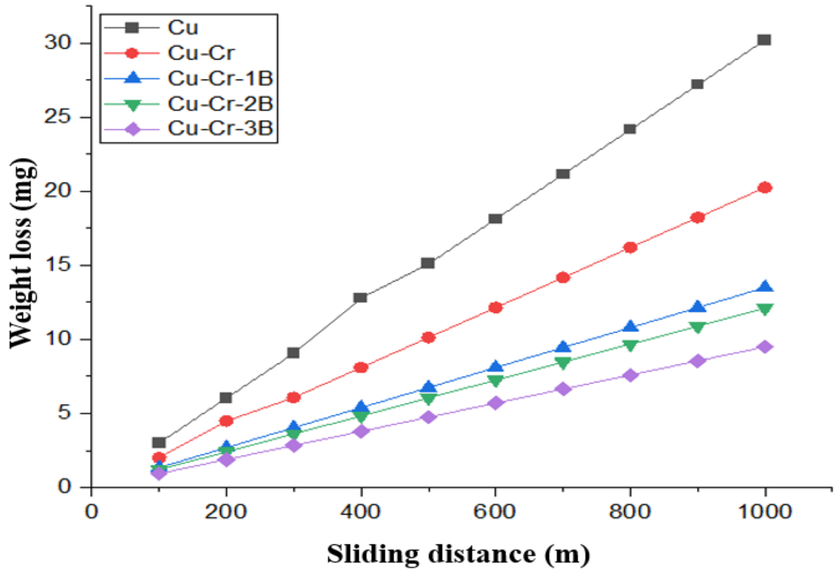

Figure 5. Abrasion weight loss amounts of copper matrix composites

The friction coefficient values of hybrid composites are shown in Figure 6. It is thought that Cr and B additives significantly reduce the coefficient of friction and the increase in B additive reduces the wear resistance by forming a tribo layer on the Cu matrix [15,18].

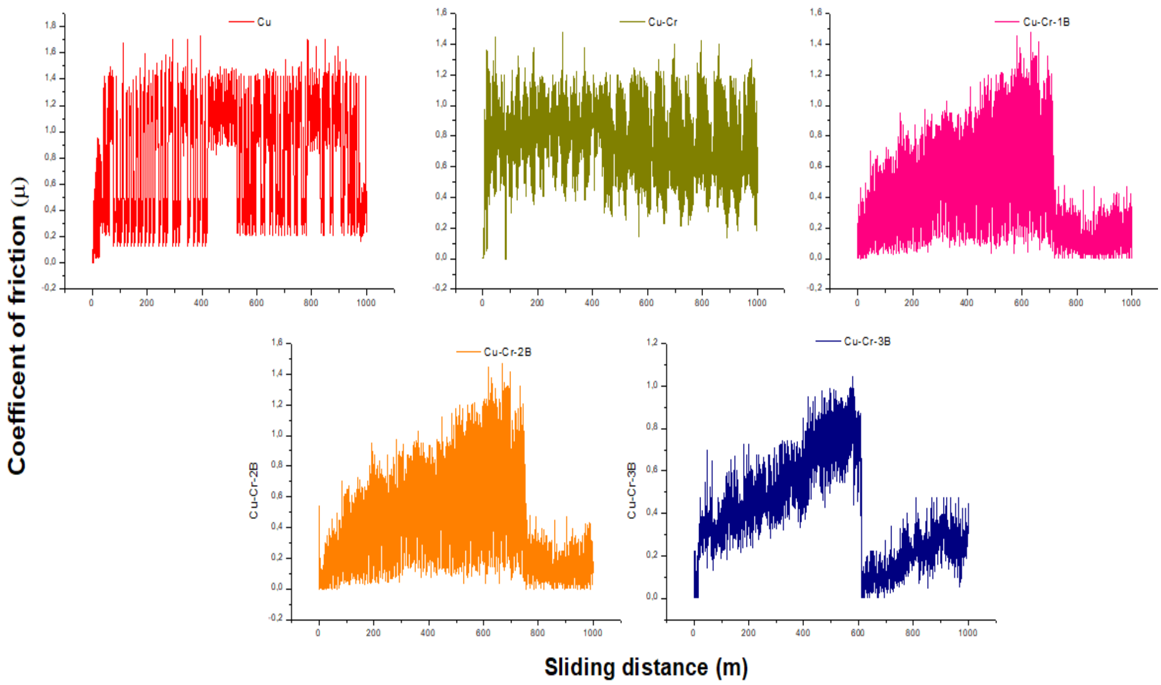

Figure 6. Friction coefficient values of copper matrix composites

SEM images of the wear tests are shown in Figure 7. Deep cracks in pure Cu composite were significantly reduced by Cr and B reinforcement. B particles were seen in SEM images with increasing B reinforcement. It is thought that the main reason for the decrease in the friction coefficient values is the formation of a thin lubricant film on the pin surface of the composites with the increase in the amount of B during shear wear [19]. It was observed that with the increase of boron additive, B particles formed more intensely on the wear surfaces and increased the resistance against abrasion. It was observed that the cracks seen in pure Cu and Cu-Cr samples were not observed on the wear surfaces with boron reinforcement and the samples were less deformed.

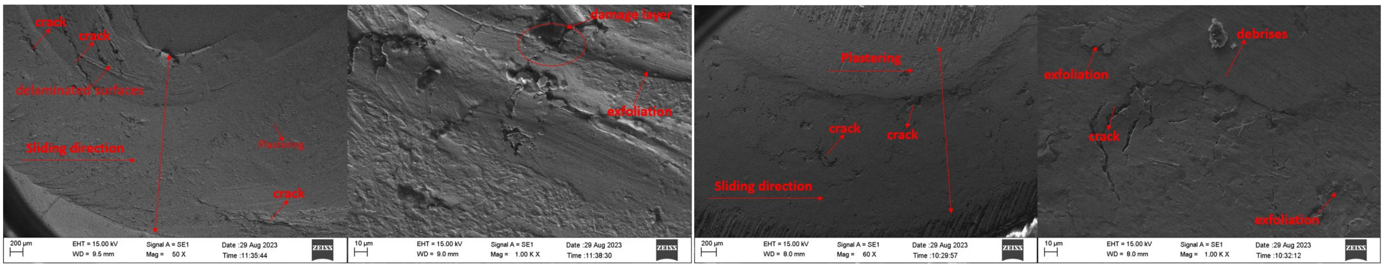

a) b)

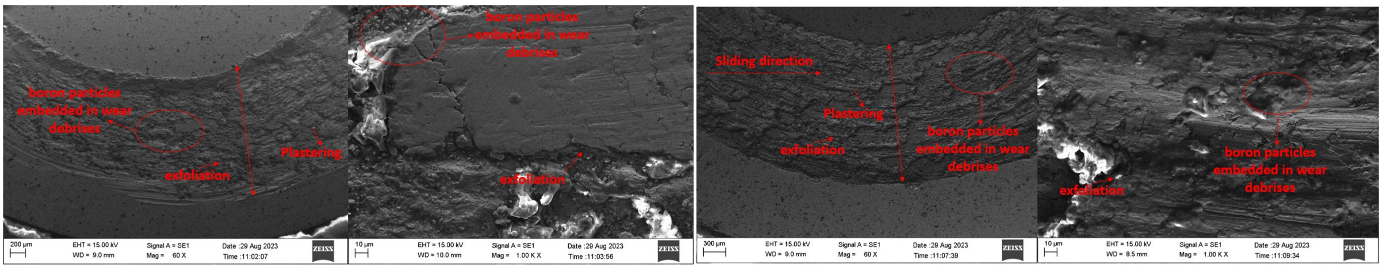

c) d)

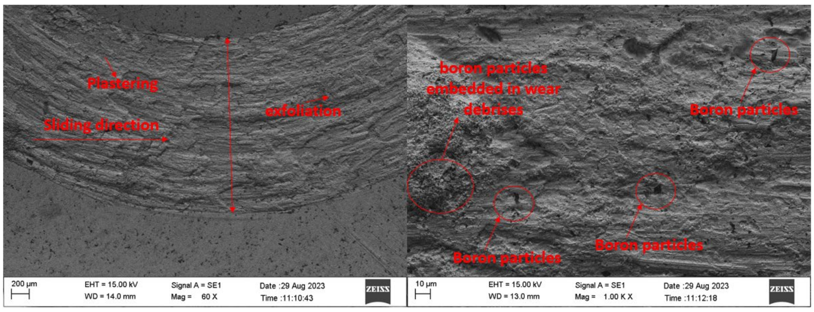

e)

Figure 7. SEM images after wear

4. CONCLUSION

The following results were obtained as a result of microstructure, hardness, wear, and wear tests of the produced Cu-Cr, Cu-Cr-1B, Cu-Cr-2B, and Cu-Cr-3B hybrid composites.

- It was observed that Cr and B additives were homogeneously distributed in the hybrid composite structures obtained.
- It was shown that Cr and B additives significantly increased the hardness value of the composite samples. It is seen that the increase in the amount of B additive further increased the hardness of the composites.
- The addition of Cr and B as reinforcement to the Cu matrix significantly increased the wear resistance.
- In the wear tests, with the increase of B additive, the composites showed a much better wear resistance than pure Cu in weight loss amounts.

REFERENCES

[1] Qin Y, Tian Y, Peng Y, Luo L, Zan X, Xu Q, et al. Research status and development trend of preparation technology of ceramic particle dispersion strengthened copper-matrix composites. J Alloys Compd 2020;848:156475.

[2] Abd-Elwahed MS, Wagih A, Najjar IMR. Correlation between micro/nano-structure, mechanical and tribological properties of copper-zirconia nanocomposites. Ceram Int 2020;46:56–65.

[3] Qin YQ, Wu YC, Huang XM, Wang Y, Cui JW, Hong Y, et al. Effect of heat treatment on conductivity of Cu-1.0 Cr-0.12 Zr alloy. Adv Mater Res 2015;1061:7–12.

[4] Hussain Z, Kit LC. Properties and spot welding behavior of copper–alumina composites through ball milling and mechanical alloying. Mater Des 2008;29:1311–5.

[5] Sheibani S, Heshmati-Manesh S, Ataie A. Structural investigation on nano-crystalline Cu–Cr supersaturated solid solution prepared by mechanical alloying. J Alloys Compd 2010;495:59–62.

[6] Wu JY, Zhou YC, Wang JY. Tribological behavior of Ti2SnC particulate reinforced copper matrix composites. Mater Sci Eng A 2006;422:266–71.

[7] Han L, Liu Z, Yu L, Ma Z, Huang Y, Liu Y, et al. Effect of WC nanoparticles on the thermal stability and mechanical performance of dispersion-reinforced Cu composites. Scr Mater 2023;222:115030.

[8] Huang B, Hishinuma Y, Noto H, Muroga T. Mechanochemical processing of Cu-Y2O3 alloy by MA-HIP for heat sink materials application. Fusion Eng Des 2019;140:33–40.

[9] Gao N, Tiainen T, Ji Y, Laakso L. Control of microstructures and properties of a phosphorus-containing Cu-0.6 Wt.% Cr alloy through precipitation treatment. J Mater Eng Perform 2000;9:623–9.

[10] Qi WX, Tu J-P, Liu F, Yang YZ, Wang NY, Lu HM, et al. Microstructure and tribological behavior of a peak aged Cu–Cr–Zr alloy. Mater Sci Eng A 2003;343:89–96.

[11] Zhang L, Pang X, Gao K, Elias A, Chen W. Mechanical properties of a bi-continuous Cu–Cr3C2 composite. Mater Sci Eng A 2015;623:4–9.

[12] Larsson P, Axén N, Akdogan G, Ekström T, Gordeev S. Wear of chromium carbide-copper composites with continuous phases. Tribol Lett 2004;16:59–64.

[13] Xi S, Zuo K, Li X, Ran G, Zhou J. Study on the solid solubility extension of Mo in Cu by mechanical alloying Cu with amorphous Cr (Mo). Acta Mater 2008;56:6050–60.

[14] Uzunsoy D. Investigation of dry sliding wear properties of boron-doped powder metallurgy 316L stainless steel. Mater Des 2010;31:3896–900.

[15] Hsu C-Y, Yeh J-W, Chen S-K, Shun T-T. Wear resistance and high-temperature compression strength of Fcc CuCoNiCrAl 0.5 Fe alloy with boron addition. Metall Mater Trans A 2004;35:1465–9.

[16] Li J, Gan L, Liu Y, Mateti S, Lei W, Chen Y, et al. Boron nitride nanosheets reinforced waterborne polyurethane coatings for improving corrosion resistance and antifriction properties. Eur Polym J 2018;104:57–63.

[17] Uddin SM, Mahmud T, Wolf C, Glanz C, Kolaric I, Volkmer C, et al. Effect of size and shape of metal particles to improve hardness and electrical properties of carbon nanotube reinforced copper and copper alloy composites. Compos Sci Technol 2010;70:2253–7.

[18] Ma S, Zhang J. Wear resistant high boron cast alloy-A review. Rev Adv Mater Sci 2016;44:54–62.

[19] Zepon G, Nascimento ARC, Kasama AH, Nogueira RP, Kiminami CS, Botta WJ, et al. Design of wear-resistant boron-modified super martensitic stainless steel by spray forming process. Mater Des 2015;83:214–23.

INVESTIGATION of WEAR PROPERTIES of BORON CARBIDE REINFORCED and CHROMIUM REINFORCED COPPER MATRIX COMPOSITES

C. K. Macit[1], M. Horlu[2], G. İspirlioğlu Kara[3], B. Tanyeri[4], B. Aksakal[5], E. Yılmaz[6]*

[1] *Firat University, Faculty of Engineering, Department of Mechanical Engineering, Elazig, Turkey.*
[2]*Firat University, Faculty of Engineering, Department of Mechanical Engineering, Elazig, Turkey.*
[3]*Ataturk University, Faculty of Engineering, Department of Mechanical Engineering, Erzurum, Turkey.*
[4,5] *Firat University, School of Aviation, Aircraft Airframe-Engine Maintenance, Elazig, Turkey.*
[6] *Aisin Otomotiv Parça San. Tic. A.Ş. 34953, Tuzla, İstanbul*

E-mail: macitkursatcevher@gmail.com

In this study, hybrid composites were achieved by adding Boron carbide (B_4C) (1%, 2%, 3%wt) and Cr (1%wt) powders at certain ratios to pure Copper (Cu) powder. When the literature studies are examined, there are studies in which B_4C and Cr powders are added to Cu powder separately. In this study, the tribological effects of the specific properties of two different reinforcing elements on Cu powder was investigated.

Mixing of Cu powder with B_4C and Cr powders was carried out in a grinder at 750 rpm for 75 minutes. The blended powders were then homogenized in 20 ml ethanol (99.9% purity) at a frequency of 20 mHz for another 15 minutes by ultrasonic homogenizer. and the mixed samples were dried in a vacuum oven for 24 hours. The samples were prepared with powder metallurgy methods and microstructure, hardness, and wear tests were performed under dry conditions at constant sliding distance and speed. The weight loss graphs and coefficient of friction values were generated for each composite sample.

As a result of the hardness and wear tests, Cu-Cr-3B_4C was the composite that gave the best results, while the lowest result was seen in the pure Cu composite. A better result of 32% in hardness value and 151% in wear weight loss was obtained for Cu-Cr-3B_4C composite compared to Cu composite. to the current study further reinforcing materials could be used for Cu matrix hybrid composites.

Keywords: Copper, Chromium, Boron carbide, Powder metallurgy, Tribology

1. INTRODUCTION

Copper matrix composites have been widely investigated for their good mechanical and physical properties, and wear resistance, good electrical and thermal conductivity. Therefore, they are considered as potential high-performance materials for use in the fields of electronic packages, coolers, and fuel cell electrodes [1-4]. Although Copper (Cu) possess important properties for various engineering materials used in the automotive, electrical, and electronics sectors, it has limitations in its application areas. The key factor to overcome these limitations is to choose the right reinforcing elements to improve their mechanical and tribological properties [5]. Copper matrix composites are considered to be the most suitable materials that can be used in the industry for the above-mentioned properties and can be used for longer service life.

Cu and its alloys can be produced by a wide range of traditional and advanced forming techniques, including hot and cold forming techniques such as stir casting, die casting, powder metallurgy (PM), pressurized liquid metal leaching, deep drawing, rolling, hot extrusion, etc. Recently, material production with TM has been one of the fastest-developing manufacturing methods. The reason for this is that metal matrix composites are limited to being shaped by conventional methods such as rolling and extrusion due to their crystal lattice structures, making it necessary to carry out studies on shaping these alloys by different methods. The TM production method is a manufacturing method in which mixed metal powders are pressed and shaped in a mold with the shape and dimensions of the part to be produced at room temperature or high temperatures and then sintered at a certain temperature [6-8]. However, in copper-based powder metallurgy processes, single ceramic particles used as friction components do not significantly improve the stability of friction performance due to uneven distribution in the copper matrix and lower bonding interface strength. The use of two or more particles can ensure the complementarity of performance and structure to achieve excellent friction performance at high temperatures. Alloying the metal matrix with strong carbide-forming elements (e.g. boron) has the benefit of improving the interfacial structure of copper [12]. The B_4C particles used as reinforcement in the study are known to be easily oxidized in a high-temperature environment, causing B_2O_3 precipitation [13]. This has the fluidity that can form a good lubricating film to improve the friction performance on the wear surface [9]. Sathiskumar et al. observed the effect of B_4C particles used as reinforcement on the wear mechanism. It was observed that B4C reinforcement on abrasion creates an abrasion resistance [10]. Balalan et al. investigated the effect of B4C content (1.5-6 wt%) on the microstructure of Cu matrix composites and revealed that superior wear resistance occurs with increasing B_4C content. [11]. Chromium (Cr) is another reinforcing element that has been doped into copper matrix materials. Cr-reinforced composites are one step ahead of other alloying elements and are preferred due to their superior refractoriness, increased hardenability, relatively inexpensive, easily recyclable, and superior tribological properties compared to composites reinforced with different reinforcement categories [14].

In this study, new hybrid mixtures were made by adding Cr and B4C at the rates of (1%, 2%, 3%) by weight to pure Cu powder at a constant rate of 1% by weight. When the literature studies were examined, it was seen that Cu powders were not mixed in a hybrid mixture as in this study. Microstructure (SEM, EDX, and XRD), hardness, and wear tests under 10N load in dry conditions were performed to characterize the composites.

2. MATERIAL AND METHODS

2.1. Materials Used, Preparation of Powders and Production Scheme

The powders used in the study were purchased commercially from the company (Nanografi, Ankara, Turkey). The grain size and purity of the powders used are shown in Table 1, the weight of sample used in powders and the nomenclature of the composites are shown in Table 2. The sample preparation scheme is shown in Figure 1. In the compounding of composite materials, powders were first prepared according to the mixing ratios in Table 2. They were mixed in a magnetic mixer at 750 rpm for 75 minutes. After mixing, the mixtures were homogenized in 20 ml ethanol for 20 minutes in an ultrasonic homogenizer. The mixed powders were dried in a vacuum oven at 80 °C for 24 hours. Homogeneous mixing of the powders with close particle sizes was completed. After mixing, the composites were pressed by cold pressing technique at a pressure of 35 MPa. During pressing, the inside of the mold was lubricated with $Zn(C_{18}H_{35}O_2)_2$ (Zinc stearate) to remove the powders more easily in the mold. The sintering process was carried out in argon atmosphere and the time graph is shown in Figure 2.

Table 1. Purity, particle size, and physical properties of the powders used in the study

Material	**Cu**	**Cr**	**B_4C**
Purity (%)	99.9%	%99,9	%99.9
Particle size (µm)	0<Cu<50	0<Cr<50	0< B_4C<50

Table 2. Nomenclature of powders and amount of additives by weight

Sample	**Cu**	**Cr**	**B_4C**
Cu	%100	-	-
Cu-Cr	%99	%1	-
Cu-Cr-1B_4C	%98	%1	%1
Cu-Cr-2B_4C	%97	%1	%2
Cu-Cr-3B_4C	%96	%1	%3

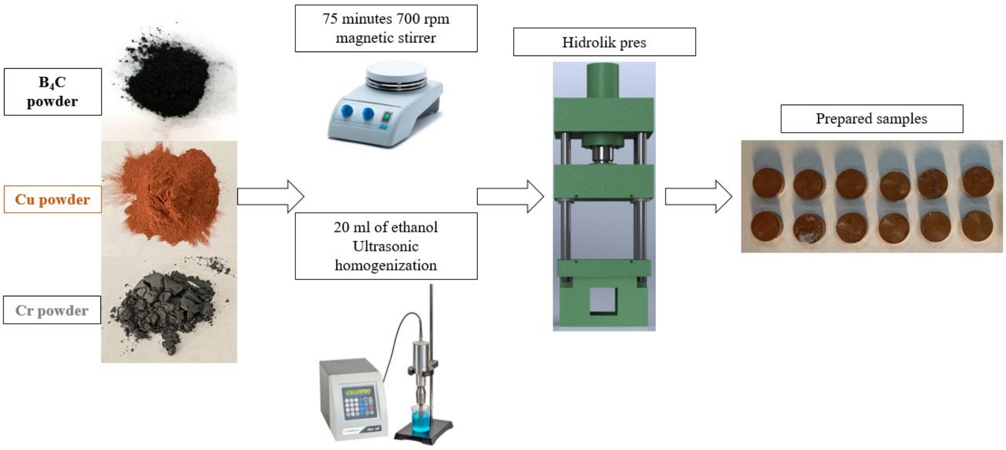

Figure 1. Composite preparation scheme

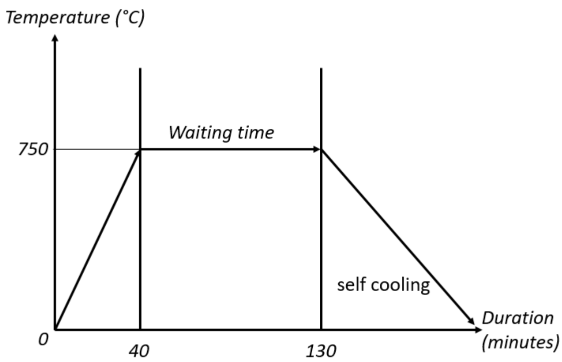

Figure 2. Sintering process

2.2. Characterization

The sintered samples were bakelitized before microstructure and hardness tests were performed. Sanding and polishing were carried out to examine the microstructures of the bakelite samples more clearly. The samples were washed with pure water and alcohol respectively. SEM and EDX (Zeiss EVO MA10) analyses were performed to determine the reinforcing element particles distributed in the Cu matrix structure in the microstructures of the samples and to examine the wear surfaces. For phase identification of the prepared samples, XRD (Rigaku RINT-2000 X) performed at a scanning range of $2\theta = 20$ to 80° and 40 kV/40 mA.

2.3. Tribology and Hardness

In hardness tests, hardness values were determined by averaging the values taken from 3 different points in HV30 at 15 seconds of waiting time. Abrasion tests were carried out with a pin-on-disc abrasion tester under 10 N load, 50 mm/sec sliding speed, and a total sliding distance of 1000 meters under dry abrasion conditions using a steel abrasion pin. At a total sliding distance of 1000 meters, the weight loss of the samples was measured every 100 meters on a weight lab instruments balance with a sensitivity value of 10-4 the measured values were recorded and weight loss graphs were created for each sample according to the distance. For the determination of friction coefficients, which is the other process in abrasion tests, each sample was abraded for a sliding distance of 1000 meters and the friction coefficient values of the composites were recorded in the abrasion tester. The recorded coefficient of friction values were transferred to the computer and coefficient of friction graphs were generated.

3. RESULTS AND DISCUSSION

3.1. Microstructure

XRD analysis was first performed on the samples prepared for microstructure analysis. XRD analyses are shown in Figure 3. As a result of XRD analysis, it was seen that Cr and B_4C reinforcing elements were formed in the Cu matrix structure. XRD analysis showed the formation of copper (Cu), boron (B), boron copper (CuB_{24}), carbon (C), chromium boron carbide (Cr_7BC_4), boron chromium (Cr_2B) and chromium (Cr) compounds and elements.

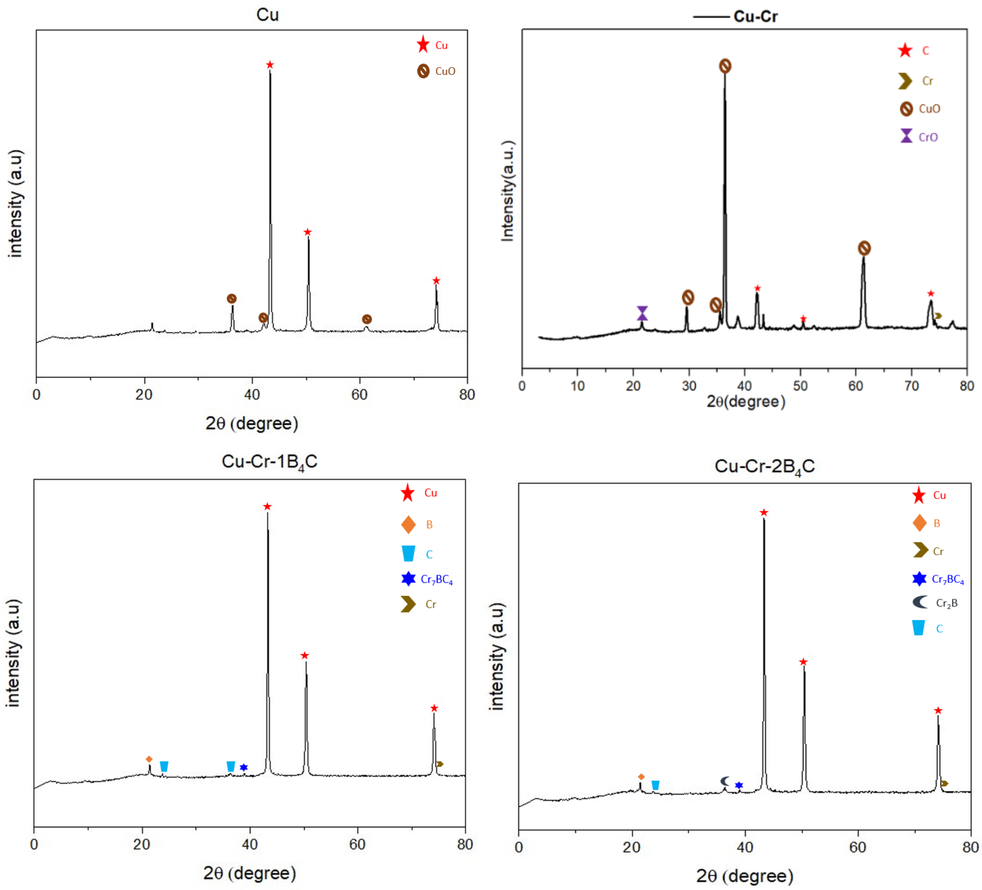

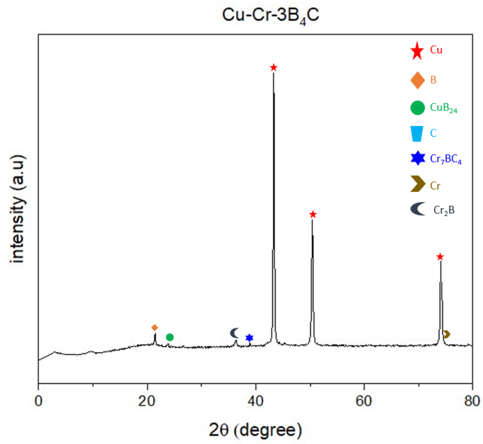

Figure 3. XRD diffraction patterns

SEM images of the composites at 2 different intensities (10.00 K.X.-100 K.X) and EDS analysis results are shown in Figure 4. SEM images and EDX analysis results show that the reinforcing elements are homogeneously distributed on the matrix material.

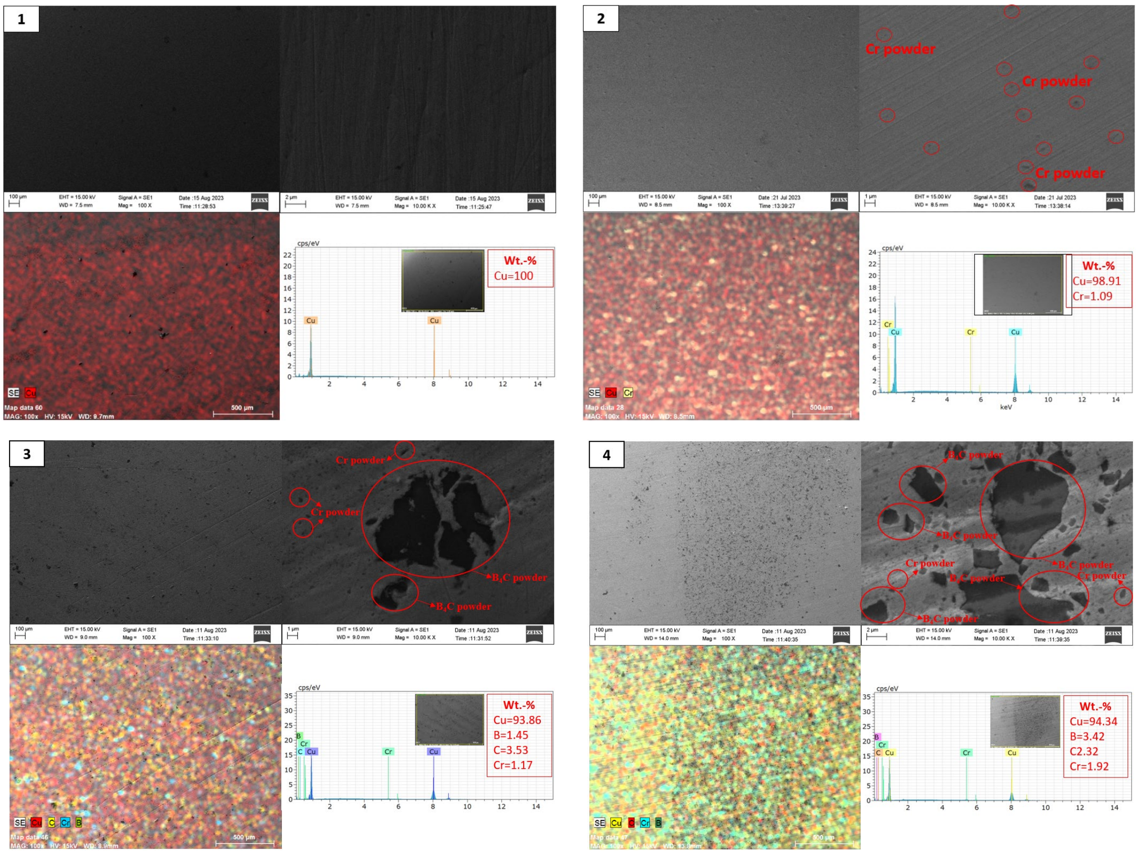

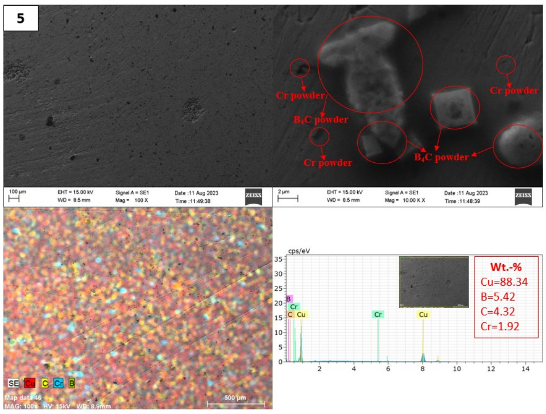

Figure 4. SEM images of the samples

3.2. Hardness

The averages of hardness values taken from 3 different points of the samples are shown in Figure 5. In the hardness results, significant increases were observed in the composites with the increase in the amount of B_4C reinforcement. While the lowest hardness value was obtained in the pure copper composite, the highest hardness value was obtained in the Cu-Cr-3B_4C composite. It is also seen in literature studies that B_4C and Cr reinforcement increases the hardness value in metal matrix composites [11-17].

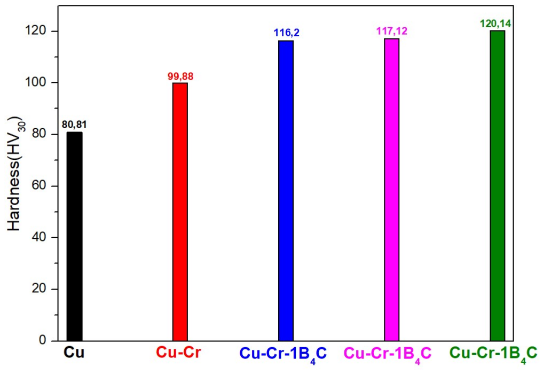

Figure 5. Hardness values

3.3. Tribology

Total wear weight losses under 10 N load are shown in Figure 6. As a result of the wear tests, the highest weight loss value was observed in pure Cu composite, while the lowest weight loss was observed in Cu-Cr-3 B_4C composite. Cr and increasing B_4C additives made the values of the composites superior as well as the hardness results [11-17].

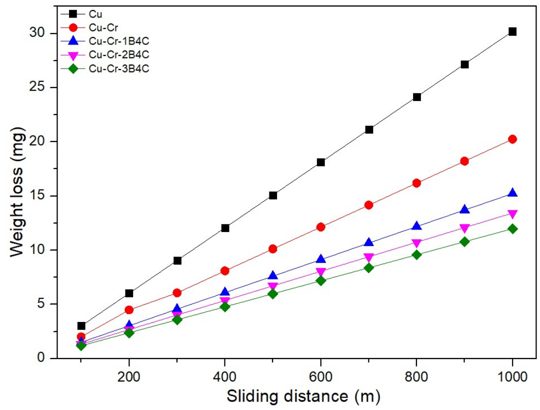

Figure 6. Weight loss as a result of wear

The friction coefficient and average friction coefficient values of the abraded composites at a sliding distance of 1000 meters are shown in Figure 7. In the friction coefficient results, Cr and B_4C additives decreased the friction coefficient value and it was observed that the resistance to friction increased. When the literature studies were examined, it was seen that Cr and B_4C supplementation had a positive effect on the wearing properties [11-17].

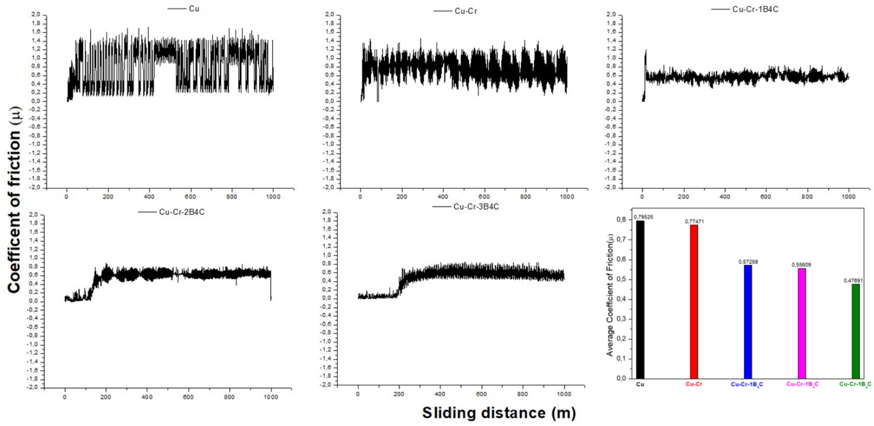

Figure 7. The coefficient of friction values of the samples

The SEM images taken to examine the wear marks on the post-wear composites are shown in Figure 8. In the SEM images, it was observed that deep cracks and scars occurred on the surface of the pure Cu composite after abrasion. With the increase of B_4C reinforcement of the samples whose wear resistance increased with Cr additive, better results were obtained in the depths of the scars on the wear surface. It is thought that the B_4C reinforcement exhibits a resistance that increases the wear between the abrasive tip and the Cu matrix [11-17].

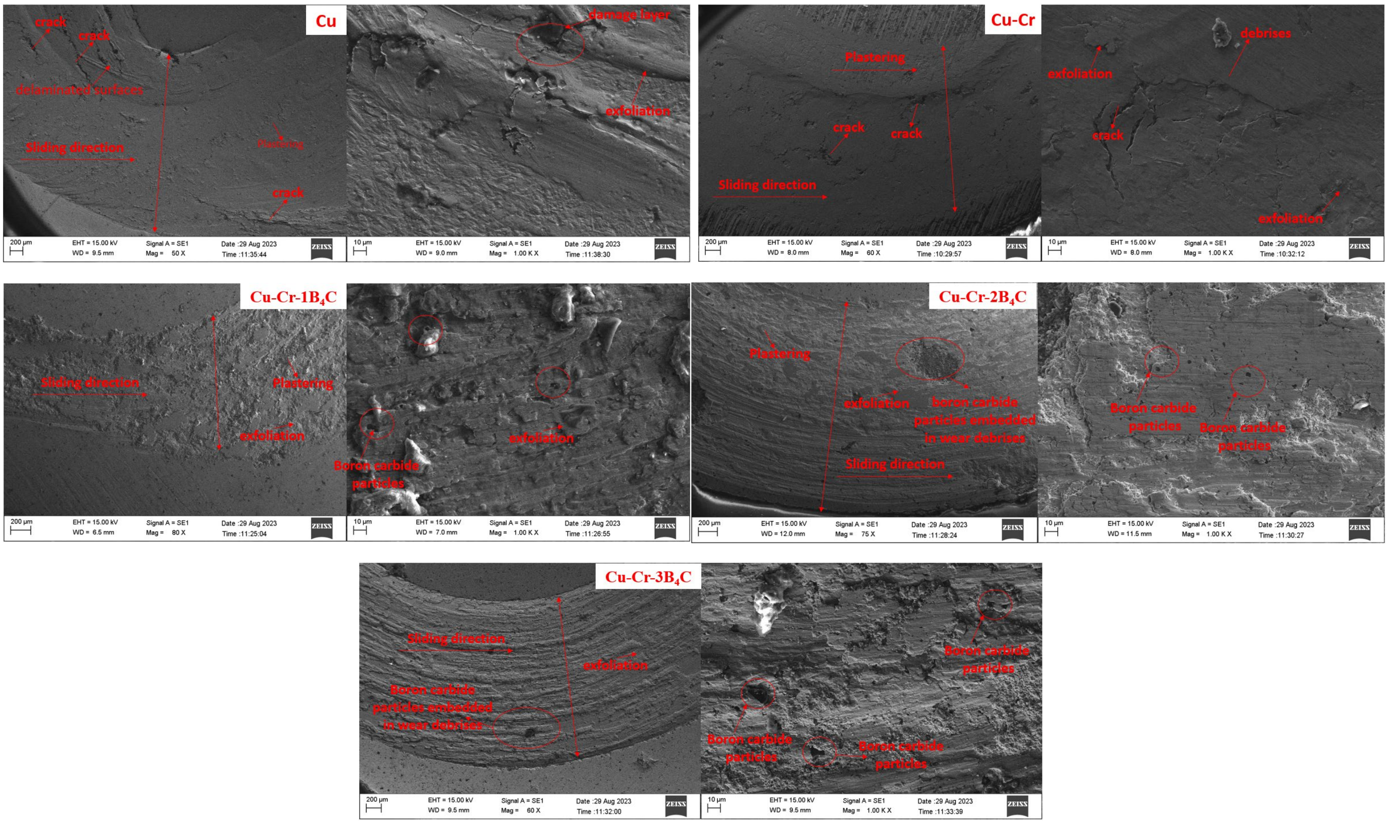

Figure 8. SEM images after wear

4. CONCLUSION

The microstructure, hardness, wear and friction coefficient properties of the produced Cu matrix Cr and B_4C reinforced composites were experimentally investigated. As a result of the experiments the following conclusions can be summarized;

• As a result of structural and morphological analyzes, it was observed that Cu-Cr-B_4C powders preserved their characteristic peaks in XRD analyzes and new compounds were formed among each composition. In the SEM images, it was seen that the reinforcement elements were homogeneously distributed on the matrix structure.

• The hardness values of all the reinforced composites in the study increased significantly compared to the pure Cu composite.

• Cr and B_4C reinforcements increased the wear resistance of the composites. Compared to the pure Cu composite, the Cu-Cr-3B_4C composite achieved the best results, with 151% better overall weight loss and 66.25% better friction coefficient value.

REFERENCES

[1] Q. Liu, X.B. He, S.B. Ren, C. Zhang, T.T. Liu, X.H. Qu Thermophysical properties and microstructure of graphite flake/copper composites processed by electroless copper coating J. Alloys Compd., 587 (2014), pp. 255-259.

[2] S. Tjong Microstructural and mechanical characteristics of in situ metal matrix composites Mater. Sci. Eng. R Rep., 29 (2000), pp. 49-113.

[3] X.S. Jiang, W.X. Liu, J.R. Li, Z.Y. Shao, D.G. Zhu Microstructures and mechanical properties of Cu/Ti3SiC2/C/MWCNTs composites prepared by vacuum hot-pressing sintering J. Alloys Compd., 618 (2015), pp. 700-706

[4] S.J. Yoo, S.H. Han, W.J. Kim A combination of ball milling and high-ratio differential speed rolling for synthesizing carbon nanotube/copper composites Carbon, 61 (2013), pp. 487-500

[5] Thankachan, T.; Prakash, K.S. Microstructural, mechanical and tribological behavior of aluminum nitride reinforced copper surface composites fabricated through friction stir processing route. Mater. Sci. Eng. 2017, 688, 301–308.

[6] Kumar Bhoi, Neeraj, Harpreet Singh, and Saurabh Pratap. "Synthesis and characterization of zinc oxide reinforced aluminum metal matrix composite produced by microwave sintering." Journal of Composite Materials 54.24 (2020): 3625-3636.

[7] Tandon, R., Madan, D.2014." Emerging Applications Using Magnesium Alloy Powders: A Feasibility Study", Springer International Publishing, pp. 21–25.

[8] Burke, P., Kipouros, Y. G., Judge, W. D., Kipouros, G. J.2019." Surprises and Pitfalls in the Development of Magnesium Powder Metallurgy Alloys", in Magnesium and Its Alloys, 1st ed., L. Dobrzanski, M. Bamberger, and G. Totten, Eds. Boca Raton, FL: CRC Press, 2019, pp. 337–373.

[9] D. Zhang, X. He, Y. Liu, et al. The effect of in situ nano-sized particle content on the properties of TiCx/Cu composites[J] J. Mater. Res. Technol., 10 (2021), pp. 453-459,

[10] R. Sathiskumar, N. Murugan, I. Dinaharan, et al. Characterization of boron carbide particulate reinforced in situ copper surface composites synthesized using friction stir processing Mater. characterized., 84 (2013), pp. 16-27

[11] Z. Balalan, F. Gulan Microstructure and mechanical properties of Cu-B4C and CuAl-B4C composites produced by hot pressing[J] Rare Met., 38 (12) (2019), pp. 1169-117

[12] Weber, L. & Tavangar, R. On the influence of active element content on the thermal conductivity and thermal expansion of Cu–X (X = Cr, B) diamond composites. Scripta Materialia 57, 988–991,

[13] S. Islak, D. Kır, S. Buytoz Effect of sintering temperature on electrical and microstructure properties of hot-pressed Cu-TiC composites [J] Sci. Sinter., 46 (1) (2014)

[14] Sreenivasa, R., & Mallur, S. B. (2021). Sliding wear behavior of Cu+ Sn+ Cr composites by Taguchi technique. Journal of Bio-and Tribo-Corrosion, 7, 1-8.

[15] Saravanan, C., Subramanian, K., Anandakrishnan, V., & Sathish, S. (2018). Tribological behavior of AA7075-TiC composites by powder metallurgy. Industrial Lubrication and Tribology, 70(6), 1066-1071.

[16] Canute, X., & Majumder, M. C. (2018). Mechanical and tribological behaviour of stir cast aluminium/boron carbide/fly ash composites. Journal of Engineering Science and Technology, 13(3), 755-777.

[17] Manohar, G., Pandey, K. M., & Maity, S. R. (2021). Characterization of Boron Carbide (B4C) particle reinforced aluminium metal matrix composites fabricated by powder metallurgy techniques–A review. Materials Today: Proceedings, 45, 6882-6888.

DETERMINATION OF DEGRADATION KINETIC PARAMETERS OF PISTACHIO, WALLNUT AND HAZELNUT SHELLS USING THERMO-GRAVIMETRIC ANALYSIS

D.Köksal Öztürk[1], M.Levent[2], K.Gündoğan[3]

[1]Department of Chemical Engineering, Faculty of Engineering,, Usak University, Uşak, TÜRKİYE
[2]Department of Chemical Engineering, Faculty of Engineering,, Usak University, Uşak, TÜRKİYE
[3]Department of Material Science and Nanotechnology Engineering, Faculty of Engineering,, Usak University, Uşak, TÜRKİYE

E-mail: dilan.koksal@gmail.com

This study presents pyrolysis behaviors and solid state kinetic data of hazelnut shell, wallnut shell, and pistachio shell investigated by non-isothermal thermogravimetric analysis (NI-TGA). The samples shaped as powder size and experiments performed in nitrogen athmosphere with four different heating rates of 10 ºC, 15 ºC, 20 ºC, 30 ºC, respectively. Kissinger-Akahiro-Sunose (KAS) method is non-integral free method which is used to calculate Arrhenius equation parameters and to verify reaction mechanisms of pyrolsis process. Effect of heating rate during on decomposition is also studied. According to obtained results, in DTG curves about thermal decomposition process showed weight loss rate changed with increasing heating rate. Mean activation energies of pistachio, wallnut and hazelnut shells were calculated as 140,5793 kJ/mol, 137,4402 kJ/mol and 138,5320 kJ/mol respectively. Kinetic parameters obtained from KAS method is in good agreement and also efficient to description of decomposition mechanism of samples.

Keywords: Pyrolsis, Biomass, Kinetic parameters

1. INTRODUCTION

During the past few decades, conventional fuels has been the main source of worlds energy needed. Although fossil fuels meet a large percentage of energy need today, studies show that their reserves are declining [1]. For this purpose research on alternative energy sources has been rapidly increasing. Biomass is regarded as popular and important renewable clean energy. Biofuels have low nitrogen and sulfur contents, environmental friendly, and large resources such as household waste, agricultural solids, and forestry [2].

Many countries in the world have large biomass potentials. Pistachio, wallnut and hazelnut shells are the most important of these sources with their production amounts per year [3]. These resources generally use as a form of solid waste and there is no any alternative other than direct burning in domestic heating [4].

Plant-derived biomass sources generally consist of cellulose, hemicellulose, and lignin. Biomass has high quality, easier to store and transportable solid, liquid and gaseous fuels compared to existing fuels [5]. Production of biomass fuels, thermochemical process is most effective method for engineering applications. With thermochemical methods, biofuel is converted into valuable hydrocarbons with high efficiency [6].

Thermal decomposition of biomass is complex process consisting of four main steps which are removal of moisture and volatile substances, decomposition of hemicellulose, cellulose and lignin [7]. First step started moisture removal temperature range between 0 ºC to 200 ºC. At the end of this first step, bond breaks and free radicals occured [8]. With release of water, carbon monoxide, carbon dioxide and other carbonyl groups occured [9]. Second step called active pyrolysis region which biomass is lost of mostly its initial weight and solid decomposition occured [10]. In last step, temperature rised up 700 ºC and C-H and C-O bonds are broken [11]. This region defined as passive pyrolsis. Changing temperature range during pyrolysis process affected reaction kinetics, conversion of solid, liquid and gaseous product and their chemical composition [12].

Thermogravimetric analysis is one of the most common techniques to investigate thermal characteristics of materials [13]. Weight change of processed sample and temperature difference between sample and reference are measured and sample is heated at constant heating rate under controlled atmosphere [14]. Weight changes (water release, volatile substance removal) occured material is controlled by thermogravimetry (TG), and temperature changes result from exothermic or endothermic reactions are controlled by differential thermal analysis (DTA) [15]. There are two basic methods, model-based and model-free used for kinetic calculations from non-isothermal TGA data [16]. In current study thermal decomposition of lignocellulosic based biomass was performed using thermogravimetric analyzer. In the light of obtained data and curves from non-isothermal TGA, activation energy of process was calculated by model-free integral method of Kissinger-Akahiro-Sunose (KAS). According to experimental results from kinetic analysis, activation energy values of biomass samples similar with literature such as round robin activation energy calculated from KAS method is 175,6 kj/mol and another study activation energy for wood based biomass was calculated 183,9 kj/mol [17] [18].

The aim of presented work is to approach thermal degradation and solid-state reaction mechanisms of biomass by Thermogravimetric analysis (TGA) with the maximum temperature of 1100 ºC at four different heating rate under nitrogen atmosphere.

2. MATERIAL AND METHODS

2.1 Experimental Method

Pistachio, wallnut and hazelnut shells are obtained as household waste and grinded as powder size before analysis. Experiments were performed in Laboratories of engineering faculty of Usak University. Before experimental study, each time, 10 gr of biomass samples were taken from grinded biomasses sources, and then, these samples are pre-dried at 50 °C for duration of 45 minutes in order to prevent any side reactions within porcelain crucibles. For each experiment sets, samples were weighed between 10 and 12 mg, heated to maximum temperature of 1100 °C at 10 °C, 15 °C, 20 °C and 30 °C heating rates with the presence of nitrogen and aluminum crucible. For each experiment sets, samples were weighed between 10 and 12 mg, heated to maximum temperature of 1100 °C at 10 °C, 15 °C, 20 °C and 30 °C heating rates with the presence of nitrogen and aluminum crucible. Experimental measurements were automatically recorded on the computer.

2.2 Kinetic Analysis

For modelling biomass degradation process there are some approaches used. General emprical model employs kinetics, and Arrhenius expression is used to correlate the solid state data of reaction [7]. On this work model-free intergal method of Kissinger Akashiro Sunose is used to calculate kinetic parameters of active pyrolysis region of biomass samples. The following expressions can be considered for KAS method:

$$ln\left(\frac{\beta}{T^2}\right) = ln\left(\frac{AR}{E_a g(a)}\right) - \frac{E_a}{R}\left(\frac{1}{T}\right) \quad (1)$$

Here, α is the amount of sample, ß denotes heating rate, A is pre-exponantial factor (min^{-1}), E_a is activation energy of reaction (kJmol^{-1}), R is the universal gas constant (JK^{-1} mol^{-1}), and T is the absolute temperature (K). Where, activation energy of samples was derived with different f(a) values between 0.1 and 0.9 are applied to slope of ln (β/T^2) vs (1/T) KAS method at different heating rates.

3. RESULTS AND DISCUSSION

3.1 Thermogravimetric analysis

TG and DTG curves and datas are important to determine the thermal characterization of the materials during the degradation process [20]. TG curve indicate weight loss of the samples depending on the temperature, while the DTG curve shows temperature-dependent maximum weight loss rate obtained by derivative of TG curve [21]. Graphics obtained by Thermogravimetric analysis of pistachio, wallnut and hazelnut shells at four different heating rates (10, 15, 20 and 30 ºC/min) exhibited in the Fig. 1.

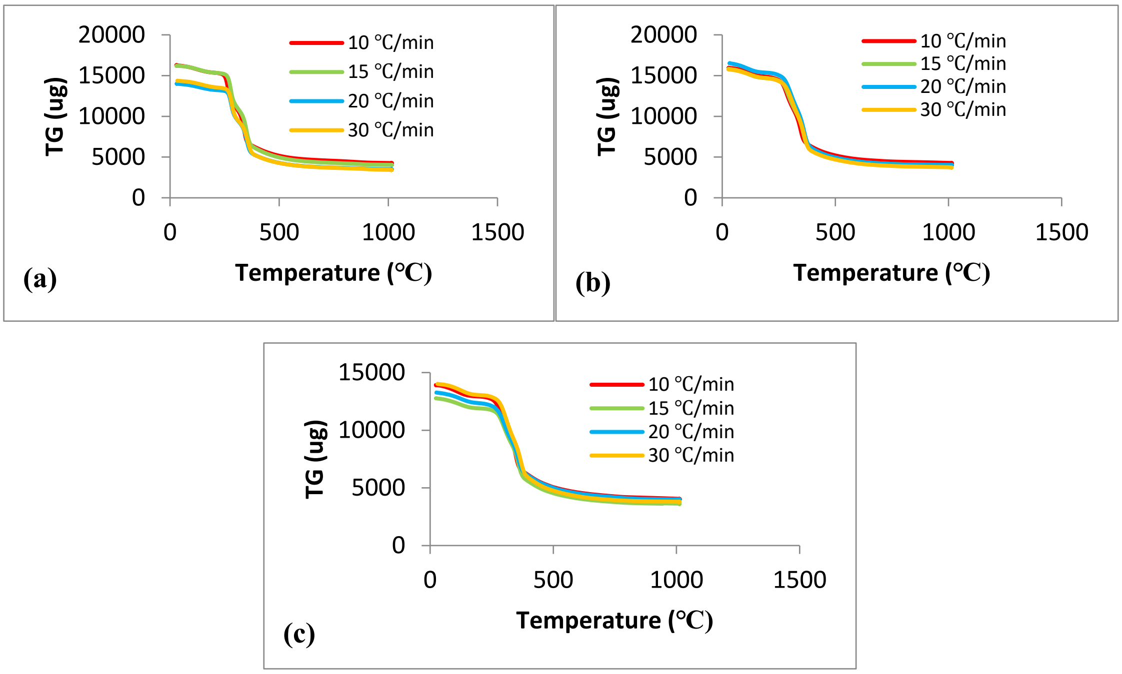

Figure 1. TGA curves of samples. (a) pistachio shell, (b) wallnut shell, (c) hazelnut shell.

On presented TG curves first major weight loss of samples occurred between 250 ºC and 275 ºC as mean at four different heating rates. Largest weight loss, which is clearly seen on curves, was calculated as 50% at 377 ºC temperature for the wallnut shell, 51% at 371 ºC temperature for pistachio shell and 50% at 377 ºC for hazelnut shell at 15 ºC/min heating rate. At 1000 ºC 80% weight loss obtained for all samples and structure of samples completely decomposed.

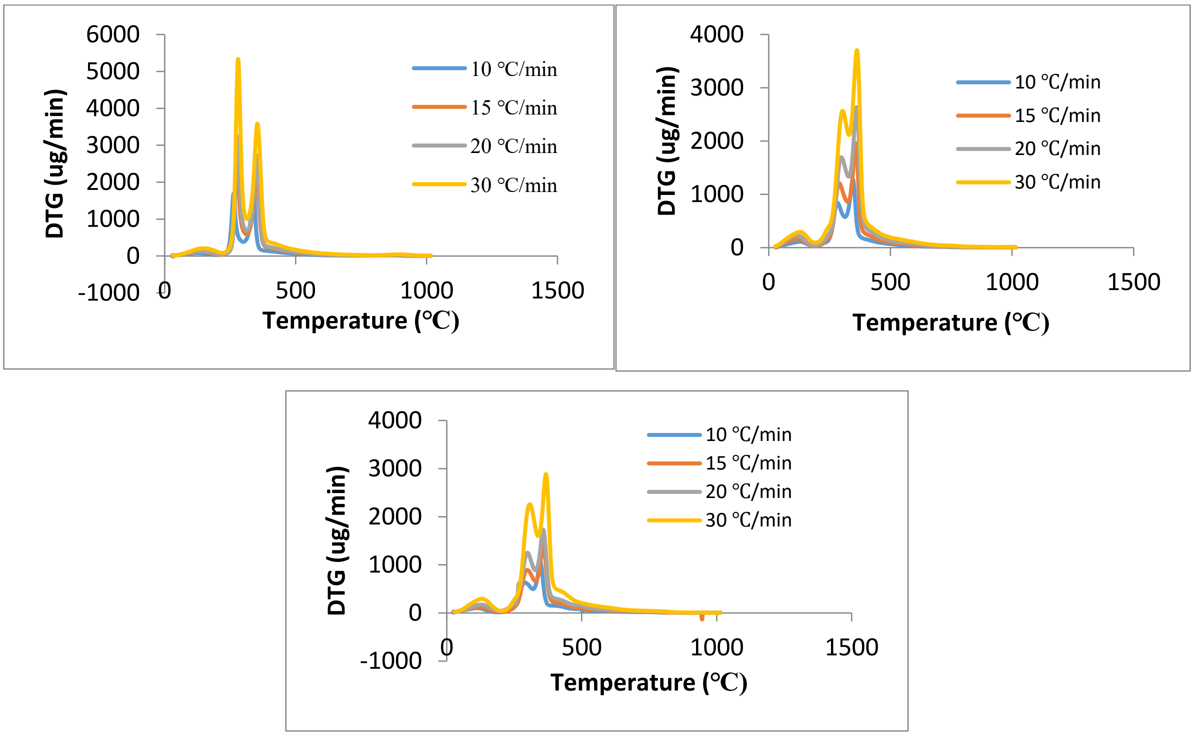

Figure 2. DTG curves of samples. (a) pistachio shell, (b) wallnut shell, (c) hazelnut shell.

DTG curves of biomass samples are illustrated on Fig. 2. and it was clear that degradation process of all samples are taken place in four steps at all heating rates. Distinct peaks are observed especially 2nd step (hemicellulose decomposition) and 3rd step (cellulose decomposition) of degradation (pyrolysis) process between 220 °C and 410 °C temperatures. Second step of pyrolsis process defined as active pyrolysis region where the weight loss and weight loss rate are highest for sample. Weight loss ratio of samples increased proportionally with heating rate. Since, energy loaded into the system per unit time is increased with heating rate, and so on weight loss per unit time is increased proportional with heating rate.

Table 1. Weight loss and oxidation temperatures of samples at active pyrolysis region.

	10 °C/min			15 °C/min			20 °C/min			30 °C/min		
	PS	WS	HS	PS	WS	HS	PS	WS	HS	PS	WS	HS
Ti (°C)	261	267	267	267	270	277	268	277	279	275	279	282
Tf (°C)	360	369	369	369	377	385	371	387	388	375	389	392
Wmax (%)	45	45	45	44	50	44	41,5	51,5	41,5	45	53	45

Table 1 presented weight loss ratios at different heating rates and initial and final temperatures of active pyrolsis region of biomass samples, which is the second step of pyrolysis process. According to the table, all samples lost an average of 45% of their initial weight after moisture content removal during oxidation stage. The increase in the oxidation temperature of the samples with the increase of heating rate is expected. At low heating rates particles will heat up more slowly and heat transfer will occur more efficiently than at high heating rates. With the increase of the heating rate, heat transfer takes place at lower efficiency and the initial and final temperatures of active pyrolysis region achieved higher degrees.

3.2 Kinetic Analysis

The activation energies ($-E_a/R$) for active pyrolsis region (2nd step of the reaction) are obtained by KAS method using Eq.9 from the slope of the plot of ln (β/T^2) versus 1/T and presented on Fig. 3. Conversion range of samples selected from 0,1 to 0,9.Ea and correlation coefficients (R^2) are tabulated in Table 2. Activation energies of active pyrolsis region for each samples given high R^2 correlation.In Fig.3. it was seen clearly points and curves linear and given same slopes. So that E_a values of biomass samples for all conversion range close to each other.

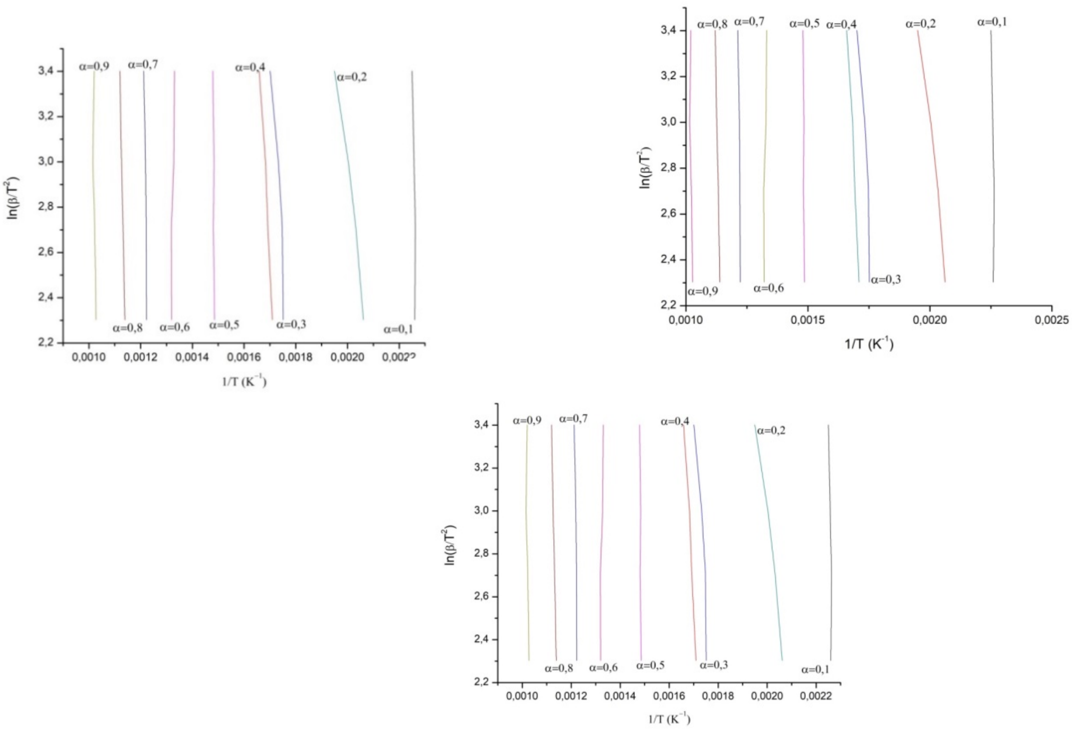

Figure 3 Isothermal conversional and non-isothermal determination of solid-state kinetic parameters obtained by KAS method. (a) pistachio shell, (b) wallnut shell, (c) hazelnut shell.

Table 2 Calculated kinetic datas of biomass samples.

	Conversion rate	Oxidation step lineer equations	R^2 value	Activation energy (kj/mol)
Pistachio shell	0,1	y=-8967x+6,0126	0,9578	77,5968
	0,2	y=-9486x+6,9872	0,9677	78,8666
	0,3	y=-13456x+12,1169	0,9489	120,9654
	0,4	y=-17554x+15,1236	0,9898	145,9439
	0,5	y=-18023x+15,9654	0,9905	154,4552
	0,6	y=-19365x+17,8796	0,9245	161,0006
	0,7	y=-20106x+18,9364	0,9632	169,3002
	0,8	y=-21230x+20,453	0,9770	176,5062
	0,9	y=-22014x+21523	0,9854	179,6987
	Mean value	-	0,9672	140,4785
Walnut shell	0,1	y = -7759x + 6,4698	0,9589	69,8774
	0,2	y = -8555x + 7,6475	0,9707	71,1320
	0,3	y = -11165x + 11,2365	0,9714	101,2566
	0,4	y=-16124x+16,3698	0,9785	134,0549
	0,5	y = -17456x + 17,1236	0,9485	156,2365
	0,6	y=-19226x+18,5641	0,9538	161,9668
	0,7	y = -20456x+19,5675	0,9865	170,0712
	0,8	y = -20989x + 24,5200	0,9954	174,5025
	0,9	y = -21603x + 27,6402	0,9746	179,2698
	Mean value	-	0,9709	135,3741
Hazelnut shell	0,1	y = -8896x + 4,7789	0,9788	75,4556
	0,2	y = -9175x + 5,6547	0,9945	86,2809
	0,3	y = -11755x + 9,9645	0,9906	132,3698
	0,4	y=-16193x + 15,9996	0,9956	144,6286
	0,5	y = -18475x + 16,0456	0,9656	155,2658
	0,6	y = -19162x + 16,7895	0,9566	169,3129
	0,7	y = -20966x+19,9630	0,9745	171,2365
	0,8	y = -22120x + 21,597	0,9682	183,9057
	0,9	y = -22456x + 21,9850	0,9669	185,1236
	Mean value	-	0,9768	144,8421

Table 2 listed activation energy values oxidation step of pistachio shell, wallnut shell and hazelnut shell calculated by the KAS method at conversion ratio range from 0.1 to 0.9. Here, calculated activation energy values for each sample increased proportionally conversion rate. According to table, activation energy of pistachio shell with 0,2 conversion rate is calculated 78,866 kJ/mol, while this value is 176.5062 kJ/mol at 0,8 conversion rate. A similar situation is also reported in wallnut shell and hazelnut shell. Since hemicellulose and cellulose have high thermal stability during the pyrolysis process, it is expected that the activation energy values will increase with the increase in the conversion rate during thermal decomposition. Computed Activation energies for all samples, are increasing with conversions and higher activation energy values are obtained at higher conversions. This means diffusion is effective on degradation reaction. Because of higher activation energy values we may say that degradation chemical reaction at different temperatures is diffusion controlled.

Thermal degradation behaviors during the pyrolysis process were determined with details for all biomass samples. According to experiment results pyrolsis process of biomass sample occured in four steps which is during first step of process, moisture and some volatiles are removed, and then hemicelluse decomposed 2nd step, cellulose decomposed 3rd step and finally lignin decomposed 4th step. After thermal degradation, samples lost approximately %52 of their initial weight at maximum 1000 °C temperature. The effects of heating rate on characteristics of active pyrolysis steps was also investigated. It was determined increased heating rate of process active pyrolsis region temperatures increased proportionally.

4. CONCLUSION

Kinetic parameters of biomass samples decomposition process was determined by KAS method which is the model free integral method. According modelling results, TGA curves and kinetic datas provide helpful information about pyrolsis process behaviour of biomass and kinetic model of biomass and optimization of process conditions also. TGA datas applied on KAS method was given good agreement of solid state reaction mechanisms. Pre-exponential factor and activation energy of each sample was calculated conversion from 0,1 to 0,9 with the help of ln $(\beta/T^2) - (1/T)$ graphics. Since calculation of the kinetic parameters and thermal degradation mechanism for biomass samples were completed with details the important steps for design, optimization of pyrolsis processes were presented.

ACKNOWLEDGMENTS

This research was carried out in Laboratories of Engineering Faculty in Usak University, Turkey. The authors thank the Chemical Engineering and Materials Engineering Departments for providing the Laboratory Facilities during this study. Corresponding author Dilan Köksal Öztürk is a 100/2000 The council of Higher Education (CoHe) PhD Scholar in Fuels and Combustion.

REFERENCES

[1] P. Giudicianni, G. Cardone, R. Ragucci, Cellulose, hemicellulose and lignin slow steam pyrolysis: Thermal decomposition of biomass components mixtures, Journal of Analytical and Applied Pyrolysis 100, 3–222, 2012.

[2] S.A. El-Sayed, M.E. Mostafa, Pyrolysis characteristics and kinetic parameters determination of biomass fuel powders by differential thermal gravimetric analysis (TGA/DTG), Energy Conversion and Management 85, 165–172, 2014.

[3] H. Zhoua, Y. Longa, A. Menga, Q. Li, Y. Zhang, The pyrolysis simulation of five biomass species by hemi-cellulose, cellulose and lignin based on thermogravimetric curves, Thermochimica Acta 566, 36 – 43, 2013.

[4] J.C. Grivel, Thermal decomposition of yttrium(III) propionate and butyrate, Journal of Analytical and Applied Pyrolysis 101, 185–192, 2013.

[5] P. Parthasarathy, K.S. Narayanan, L. Arockiam, Study on kinetic parameters of different biomass samples using thermo-gravimetric analysis, Biomass and Bioenergy 58, 58-66, 2013.

[6] A. Demirbas, Biomass resource facilities and biomass conversion processing for fuels and chemicals, Energy Conversion and Management 42, 1357-1378, 2001.

[7] G. Mishra, T. Bhaskar, Non isothermal model free kinetics for pyrolysis of rice straw, Bioresource Technology 169, 614-621, 2014.

[8] M. Carrier, A. Loppinet-Serani, D. Denux, J. Lasnier, F. Ham-Pichavant, F. Cansell, C. Aymonier, Thermogravimetric analysis as a new method to determine the lignocellulosic composition of biomass, Biomass and bioenergy 35, 298-307, 2011.

[9] A. Agrawal, S. Chakraborty, A kinetic study of pyrolysis and combustion of microalgae Chlorella vulgaris using thermo-gravimetric analysis, Bioresource Technology 128, 72–80, 2013.

[10] L.Burhennea, J. Messmera, T. Aichera, M. Laborie, The effect of the biomass components lignin, cellulose and hemicellulose on TGA and fixed bed pyrolysis, Journal of Analytical and Applied Pyrolysis 101, 177–184, 2013.

[11] A. Chee, R. Bridgid, L. FuiChin, Z. AbbasJawad, K. LingHii, Kinetic Analysis of Rice Husk Pyrolysis Using Kissinger-Akahira-Sunose (KAS) Method, Procedia Engineering, 148, 1247-1251, 2016.

[12] N. Sbirrazzuoli, Determination of pre-exponential factors and of the mathematical functions f(α) or G(α) that describe the reaction mechanism in a model-free way, Thermochimica Acta 564, 59-69, 2013.

[13] A. Marcilla, A.N. García, M.V. Pastor, M. León, A.J. Sánchez, D.M. Gómez, Thermal decomposition of the different particles size fractions of almond shells and olive stones, Thermal behaviour changes due to the milling processes, Thermochimica Acta 564, 24-33, 2013.

[14] P. Parthasarathy, K.S. Narayanan, L. Arockiam, C. Gai, Y. Dong, T. Zhang, The kinetic analysis of the pyrolysis of agricultural residue under non-isothermal conditions, Bioresource Technology 127, 298-305, 2013.

[15] M.A. Lopez-Velazquez, V. Santes, J. Balmaseda, E. Torres-Garcia, Pyrolysis of orange waste: A thermo-kinetic study, Journal of Analytical and Applied Pyrolysis 99, 170-177, 2013.

[16] R.Barzegar, A. Yozgatligil, H. Olgun, A. Atimtay, TGA and kinetic study of different torrefaction conditions of wood biomass under air and oxy-fuel combustion atmospheres, Journal of the Energy Institute 93, 889-898, 2020.

[17] A. Anca-Coucea, C. Tsekosb, S. Retschitzeggerc, F. Zimbardid, A. Funkee, S. Banksf , T.Kraiag, P. Marquesh, R. Scharlera, W. Jongb, N. Kienzl, Biomass pyrolysis TGA assessment with an international round robin, Fuel 276, 118002-118004, 2020.

[18] Z. Chen, Q. Zhu, X. Wang, B. Xiao, S. Liu, Pyrolysis behaviors and kinetic studies on Eucalyptus residues using thermogravimetric analysis, Energy Conversion and Management 105, 251-259, 2015.

[19] A. Domingos, M. Leandro, C. Morais, Kinetic parameters of red pepper waste as biomass to solid biofuel, Bioresource Technology 204, 157-163, 2016.

[20] S. Kim, H. VuLy, J. Kim, J. Choi, H. Woo, Thermogravimetric characteristics and pyrolysis kinetics of Alga Sagarssum sp., Biomass Bioresource Technology 139, 242-248, 2013.

ECAP MOLD DESIGN WITH TWO DIFFERENT EDGE ANGLES AND SIMUFACT ANALYSIS WITH Zn-A-B

S. Sezek[1], G. İspirlioğlu Kara[1], M. H. Akıncı[1], B. Aksakal[2]

[1] Department of Mechanical Engineering, Faculty of Engineering, Ataturk University, Erzurum, Turkey
[2] Aircraft Airframe-Engine Maintenance, School of Aviation, Firat University, Elazig, Turkey

E-mail: ssezek@atauni.edu.tr

Improving the mechanical properties of materials has become one of the most important research topics in materials science today. Regarding biomaterials, the range of materials that can be selected due to biocompatibility is very narrow compared to other sectors. In addition to conventional plastic deformation methods, extreme plastic deformation methods can also be used to improve the mechanical properties of biocompatible materials. Extreme plastic deformation methods have many advantages over conventional plastic deformation methods. With Equal Channel Angular Pressing, an extreme plastic deformation method, it is possible to improve the material's mechanical properties without changing its cross-section. In this study, a mold design was made to investigate how the change of the edge angle, which is one of the most critical parameters of the Equal Channel Angular Pressing (ECAP) process, which produces different results with various parameter changes, causes changes in the mechanical properties of the material. Although there are many parameter comparison studies in the literature, there is no mold design that allows pressing with two different edge angles with a single mold. The mold is designed to be removable, including two pressing ways with 90° and 135° edge angles and 20° corner angles. In addition, to facilitate the application of the process with different pass numbers, a mold design was made to allow the sample to be removed without disturbing the mold. With the Simufact program, the analysis of the zinc alloy biomaterial with an original design of the mold with two edge angles was also performed. The most suitable edge angle was tried to be determined to achieve the best mechanical properties without damaging the sample.

Keywords: Severe Plastic Deformation, Equal Channel Angular Pressing (ECAP), ECAP Die Design

1. INTRODUCTION

Alloys are used in different sectors due to their mechanical properties. For example, Titanium (Ti) and Aluminium (Al) alloys are used in aerospace due to their high strength and low weight, while Copper (Cu) alloys can be used in cold working due to their relatively soft and ductile properties. Since it is not possible to combine properties such as high strength and ductility in a single alloy, research on improving mechanical properties by changing the elemental contents and ratios of alloys has gained momentum [1–4].

Over time, deformation methods that cause changes in the internal structure of the material have been developed to improve the existing properties of materials rather than changing the alloy content and proportions. These traditional plastic forming methods, which are efficient in terms of material shaping, have not been able to provide the desired changes in mechanical properties since they do not directly aim to improve mechanical properties. When traditional plastic forming methods (such as deep drawing, and rolling) were insufficient to improve mechanical properties, extreme plastic deformation (APD) methods came into play. APD methods affect the mechanical properties of the material through microstructure change. This method causes improvements such as strength increase and toughness increase in the material [5,6].

Among the extreme plastic deformation methods, the most remarkable is the Equal Channel Angular Pressing (ECAP). The most important difference of ECAP from other extreme plastic deformation methods is that it can improve mechanical properties without causing any change in the cross-section and volume of the workpiece. This method has been the subject of much recent research. Reducing the grain size of metals and alloys by plastic deformation makes many materials higher strength and more ductile. EKAP is widely used in scientific studies and manufacturing [7–9].

The main reasons for the widespread use of ECAP are its lower cost and higher efficiency compared to other extreme plastic deformation methods. In the ECAP process, mold design is important for reasons such as edge angle, corner angle, and practicality of the process. The mold design should be made with the aim of less deformation on the surface of the sample and easy removal of the sample from the channel. As the interest in the ECAP process has increased, studies have accelerated to make the process more practical and more effective [10,11].

In this study, a mold with the ability to process with two different edge angles was manufactured and the wear resistance, corrosion resistance, and grain size of the Zn-Mg-1Ag alloy used in the human body were examined before the ECAP process. Then, the post-treatment wear and corrosion resistance and grain size of the samples, which were processed with different pressing numbers in Bc and C routes with two different edge angles of 90° and 135°, were investigated. It is aimed to compare these properties of treated and untreated materials. This comparative study, it is aimed to optimize the ECAP process of Zn-Mg-1Ag alloy and to improve the mechanical properties without changing the sample cross-section and accordingly to extend the life of the material in the human body.

2. MATERIAL AND METHODS

2.1. Mold Design

In addition to improving the mechanical properties of the material, the study aims to determine the most accurate edge angle, route, and number of presses since it is an optimization study. To reduce the cost of the mold, a mold design was made that allows two different edge angles to be processed in a single mold. Since the process requires a large number of repetitive pressings, the demountability of the mold and easy removal of the sample were also taken into consideration in the design.

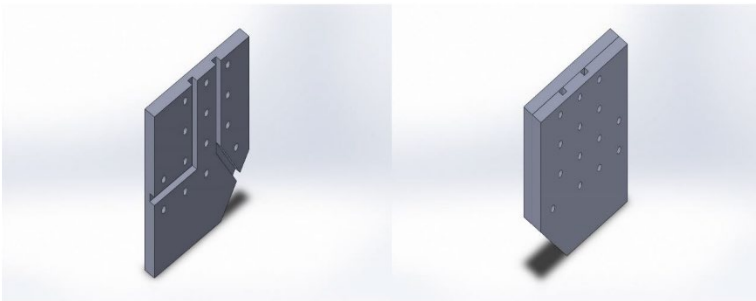

Figure 1. ECAP mold design a) main mold, b) mold assembly

Thanks to the mold design with two different pressing paths with 90° and 135° edge angles, the mold manufacturing cost was halved by designing a single mold (Figure 1a). Screw holes were drilled in the auxiliary mold and the main mold in the direction of the pressing paths. In this way, the two molds can be tightly connected with screws. Thus, when the mold is connected, the sample is prevented from leaking between the two parts of the pressing mold (Figure 1b).

2.2. Punch Design

To be able to press the sample placed in the pressing path, a punch with a square cross-section was designed using dimensions suitable for the channel cross-section (Figure 2). A square piece with a wider cross-section was mounted on the punch for uniform distribution of the load under the hydraulic press.

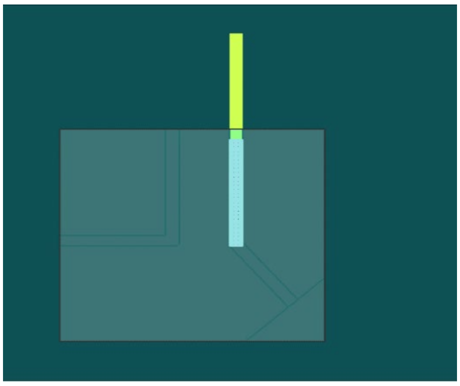

Figure 2. Punch design

2.3. Analyses

The Simufact Forming program was used to verify the process parameters of ECAP. This program can perform finite element analysis of materials subjected to plastic deformation. The molds drawn on Solidworks were transferred to Simufact Froming and the molds were considered rigid. The friction scaling factor was accepted as 0.25. The meshing process was performed as a surface mesh. The element size is 1mm and the number of elements is 8500 (Figure 3).

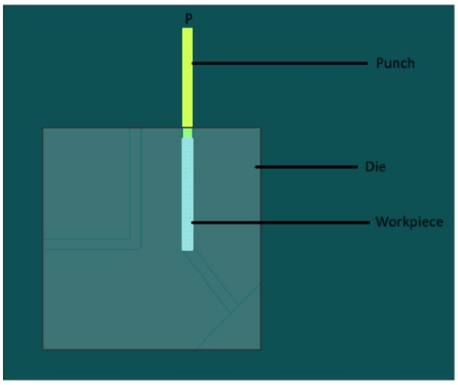

Figure 3. ECAP analysis

In the analyses where two different edge angles were compared, all other parameters were kept constant (Table 1).

Table 1. Analysis Parameters

Edge Angle	Corner Angle	Mould Temperature	Sample Temperature	Pressing Speed
90°	20°	100°C	100°C	2 mm/sn
135°	20°	100°C	100°C	2 mm/sn

2.4. Preparation of Samples

Zinc alloy specimens were manufactured by casting method. The specimens have a 10x10 mm cross-section and 100 mm length. The specimens were sanded with a Metkon brand sanding-polishing device to fit tightly to the pressing path. Since the long length of the specimens would cause the punch to bend under load during pressing, the specimens were cut and their length was reduced to 50 mm, thus increasing the number of specimens (Figure 4).

Figure 4. Sample

2.5. Mould Manufacturing

The mold was produced by the machining method using 4140 steel. The mold consists of two parts, one main part, and one auxiliary part. The dimensions of the mold are 200x200x40 mm (Figure 5).

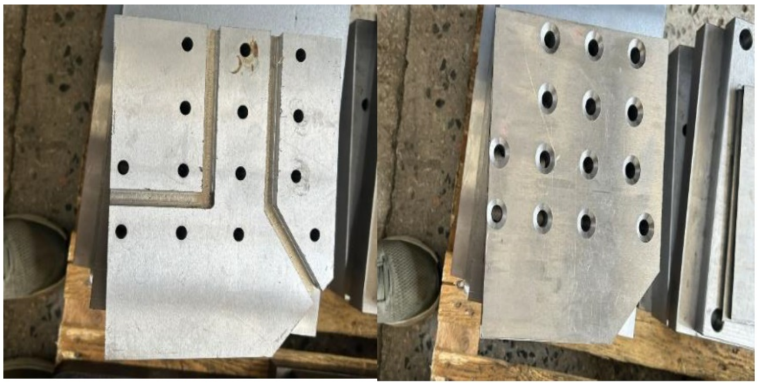

Figure 5. ECAP mold

The mold is manufactured to allow pressing with two edge angles (ϕ), 90° and 135°. Corner angles (Ψ) are 20° for both pressing paths. The fact that the mold has different edge angles provides the opportunity to observe the change in the mechanical properties and grain size of the sample subjected to the EKAP process with different parameters. Samples with 10x10 mm cross-sections and 50 mm lengths can be subjected to the EKAP process with different edge angles, different passes, and different routes.

2.6. Pressing Process

The pressing process was performed with a BESMAK brand Servo Hydraulic Bending Test Machine. The process was performed at room temperature with a pressing speed of 0.1 mm/sec. Mobil brand grease XHP 322 Mine grease lubricant was used to reduce friction in the pressing path and facilitate the passage. After the specimen was placed and the lubricant was applied, the mold was clamped, and pressing was performed. For a 135° edge angle, the process was performed with a pressing pressure of 34 MPa and took an average of 9 minutes for each pass. For both edge angles, 4 passes were performed in the Bc route and 2 passes in the C route (Table 2). Despite the risk of crack formation in the specimens, the 135° edge angle route was processed first (Figure 6).

Table 2. Pressing Parameters

Edge Angle	Corner Angle	Route	Number of Passes	Temperature
90°	20°	Bc	4	20°C
90°	20°	C	2	20°C
Edge Angle	**Corner Angle**	**Route**	**Number of Passes**	**Temperature**
135°	20°	Bc	4	20°C
135°	20°	C	2	20°C

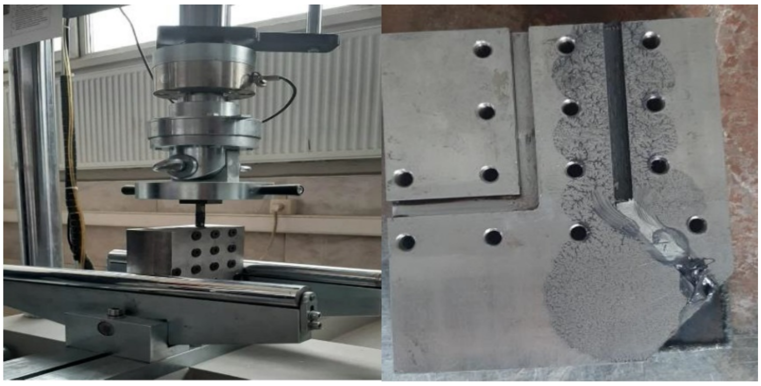

Figure 6. Pressing process

RESULTS

The Zn-Mg-1Ag specimen was analyzed with the Simufact program with molds with 90° and 135° edge angles (ϕ). As a result of 30% feed (30mm), the highest effective plastic strain in the EKAP process with a 90° edge angle was 1.56, while this value was 0.20 at a 135° edge angle, and strain distribution was determined. In this case, with the pressing force applied, the sample did not protrude out of the mold and progressed appropriately in the ECAP channel (Figure 7).

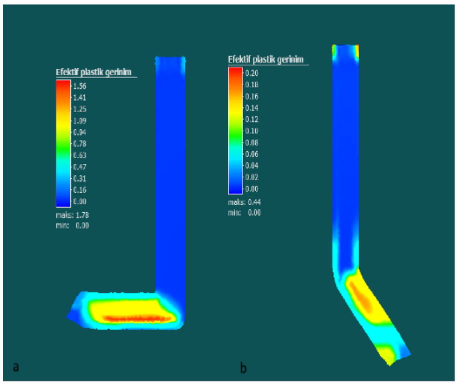

Figure 7. 30% Feeding effective plastic strain a) ϕ=90°, b) ϕ=135°

When the 50% feed result (50mm) is compared with the 30% feed result, it is seen that the effective plastic strain values are very close to each other and the strain value is uniform at all stages of the process (Figure 8).

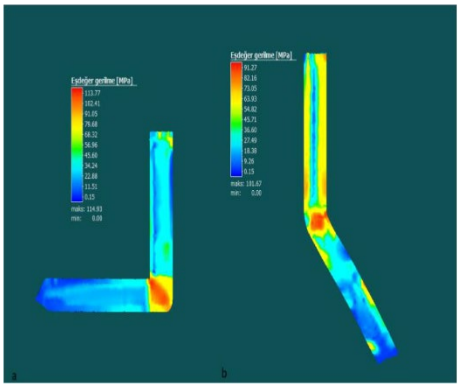

Figure 8. 50% Feed equivalent stress a) ϕ=90°, b) ϕ=135°

As a result of 50% feed (50mm), it was observed that the highest equivalent stress was approximately 114MPa in the EKAP process with a 90° edge angle and 92MPa at a 135° edge angle. It is seen that the highest stresses occur at the exit point of the sample from the EKAP channel in both cases. The difference between the maximum equivalent stress values in the analyses for the two edge angles is approximately 22MPa (Figure 9).

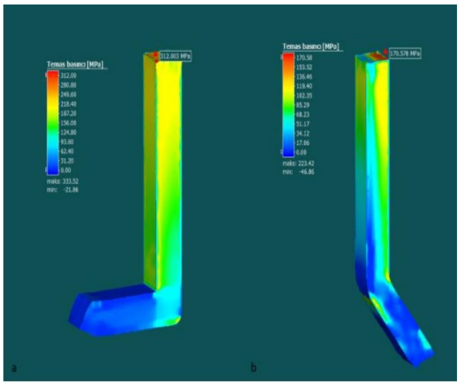

Figure 9. 30% feed contact pressure a) ϕ=90°, b) ϕ=135°

As a result of 30% feed (30mm), it was observed that the highest contact pressure, which was approximately 312 MPa in the EKAP process performed at 90° edge angle, decreased to 255MPa at 70% (70mm) feed, and this value decreased from 170MPa to 141MPa at 135° edge angle. It is seen that the highest contact pressure at the point where the sample contacts the punch at 30% feed occurs at the exit point of the sample from the EKAP channel at 70% feed (Figure 10).

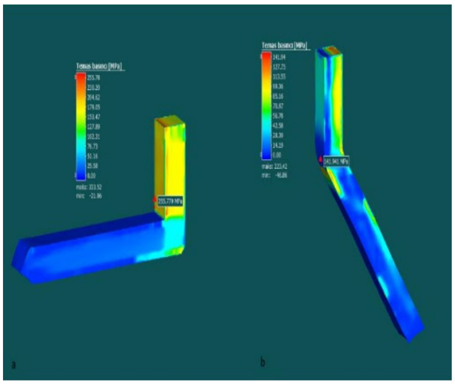

Figure 10. 70% Feed contact pressure a) ϕ=90°, b) ϕ=135°

It is seen that the material flow is parallel and regular with the sample exit direction in the EKAP process with both parameters (Figure 11).

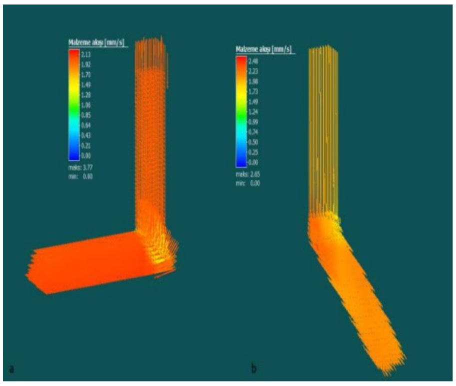

Figure 11. Material flow a) ϕ=90°, b) ϕ=135°

CONCLUSIONS

ECAP FEM analyses showed that the elbow angles and mold tolerances designed in the ECAP FEM analyses could allow the Zn alloy to move freely in the groove. With the applied pressure, the Zn alloy moved without getting stuck on the mold edges.

REFERENCES

[1] Mondolfo LF. Aluminum alloys: structure and properties. Elsevier; 2013.

[2] Ankem S, Margolin H, Greene CA, Neuberger BW, Oberson PG. Mechanical properties of alloys consisting of two ductile phases. Prog Mater Sci 2006;51:632–709.

[3] Saravanan M, Pillai RM, Pai BC, Brahmakumar M, Ravi KR. Equal channel angular pressing of pure aluminum--an analysis. Bull Mater Sci 2006;29.

[4] Qu S, An XH, Yang HJ, Huang CX, Yang G, Zang QS, et al. Microstructural evolution and mechanical properties of Cu–Al alloys subjected to equal channel angular pressing. Acta Mater 2009;57:1586–601.

[5] Swapna D, Rao CS, Radhika S. A review on the deep drawing process. Int J Emerg Res Manag Technol 2018;6:146–9.

[6] Han Y, Liu M, Hu L, Kang X, Lin D, Zhang Y, et al. Deformation twins induced by excessive deformation enhanced the two-way shape memory effect in aged NiTi alloy. Mater Lett 2022;324:132632.

[7] Valiev RZ, Langdon TG. Principles of equal-channel angular pressing as a processing tool for grain

refinement. Prog Mater Sci 2006;51:881–981.

[8] Balasundar I, Rao MS, Raghu T. Equal channel angular pressing die to extrude a variety of materials. Mater Des 2009;30:1050–9.

[9] Gupta A, Chandrasekhar B, Saxena KK. Effect of Equal-channel angular pressing on mechanical properties: An overview. Mater Today Proc 2021;45:5602–7.

[10] Agwa MA, Ali MN, Al-Shorbagy AE. Optimum processing parameters for equal channel angular pressing. Mech Mater 2016;100:1–11.

[11] Djavanroodi F, Ebrahimi M. Effect of die channel angle, friction and back pressure in the equal channel angular pressing using 3D finite element simulation. Mater Sci Eng A 2010;527:1230–5.

ENHANCING ENERGY EFFICIENCY AND REAL-TIME MONITORING IN INDUSTRIAL ENVIRONMENTS THROUGH AN INTEGRATED SOFTWARE SOLUTION: NIGHTWATCH

K. Nikbay Oylum[1], K. Selçuk[1], T. T. Bilgin [2]

[1]Mert Software Electronics, Bursa, TÜRKİYE
[2] Department of Computer Engineering*, Faculty of Engineering and Natural Sciences, Bursa Teknik University, Bursa, TÜRKİYE*

E-mail: kenanselcuk@trex.com.tr

Globally, the demand for energy continues to escalate due to factors such as heating, lighting, transportation, and fuel supply for various devices. In a context where energy has garnered such paramount importance, achieving energy efficiency has necessitated a comprehensive approach encompassing activities related to energy generation, transmission, and consumption.

Any positive or negative developments in the realm of energy significantly impact both human and environmental factors, which constitute the focal points of sustainable development. Consequently, enhancing efficiency in production and consumption phases, rather than mere expansion, is poised to yield positive economic, social, and environmental contributions.

The presented study centers around a software application developed to address these concerns. The application operates within industrial settings and interfaces with energy analyzers, collecting and analyzing data such as energy consumption, instantaneous current, and voltage. This initiative seeks to provide real-time visibility into energy-related operations on factory premises. Additionally, the software's capabilities extend to retrospective data analysis, enabling informed insights for future extrapolations. Furthermore, the integration of energy consumption data from the analyzers into the Manufacturing Execution System (MES) facilitates energy tracking on a per-job basis. The software's dashboard component empowers users to establish customized threshold values for monitored energy parameters. When these thresholds are exceeded or when values deviate from expected levels, the software triggers alerts and notifications via email and other communication channels, ensuring timely dissemination of pertinent information. Consequently, the software allows businesses to evaluate unit costs associated with specific job orders. Additionally, the study aims to establish a correlation between energy consumption data at the job-order level and machine-level energy consumption. This correlation could foster the augmentation of efficient energy utilization, thereby enhancing competitiveness and overall efficacy.

Keywords: Real-time Data Monitoring and Visualization, Data Analytics, Cloud Systems, Energy Tracking and Analysis, Industry 4.0, Intelligent Manufacturing.

1 INTRODUCTION

The need for effective monitoring and analysis of energy consumption in industrial environments has become increasingly important. In the past, energy consumption data was often collected manually, leading to delays in accessing and analyzing the information. However, with the development of energy monitoring and analysis software platforms, businesses now can monitor their energy consumption in real-time and make informed decisions based on the collected data. This paper will demonstrate the importance of energy monitoring and analysis software in industrial environments. Real-time monitoring and analysis of energy consumption is crucial in industrial environments. It allows businesses to track and analyze their energy usage patterns, identify areas of inefficiency, and make adjustments to reduce energy consumption and costs.

One of the key features of energy monitoring and analysis software is real-time monitoring of energy consumption. This software platform collects and analyzes values such as energy consumption, instantaneous current, and voltage from energy analyzer devices used in industrial environments. The collected data is then used to monitor the factory in real-time, providing businesses with insights into their energy usage patterns at any given moment. Furthermore, the software platform allows for retrospective data analysis. This means that the collected data can be analyzed over time to make inferences for the future. For instance, businesses can identify trends in energy consumption and make predictions about future energy needs.

Another important aspect of energy monitoring and analysis software is its integration with other systems. For example, the energy consumption data collected from the energy analyzer can be integrated into the work order/production notifications in the MES system. This integration enables businesses to monitor energy consumption on a work order basis, allowing them to measure the unit costs realized for each work order. Moreover, the software platform includes a control panel or dashboard that provides alarms and notifications when user-defined threshold values for energy consumption are exceeded or lower than expected, alerting relevant personnel through channels such as email. This feature ensures that businesses can take immediate action in response to any anomalies or deviations in energy consumption, helping them optimize their energy usage and minimize costs.

One of the benefits of implementing energy monitoring and analysis software in industrial environments is the potential for increased efficiency and competitiveness.[1]. By monitoring energy consumption on a work order basis, businesses can identify areas of inefficiency and take corrective actions. For example, by analyzing the relationship between work order-based energy consumption data and machine-based energy consumption, businesses can identify machines or processes that are consuming excessive[2] energy and implement measures to optimize their use. Additionally, the software platform allows for the comparison of energy consumption between different work orders or production lines.[3].

This allows businesses to identify best practices and replicate them across the organization, leading to more efficient energy usage and ultimately, increased competitiveness in the market. The integration of energy monitoring and analysis software with other systems, such as the MES system, enables businesses to have a comprehensive view of their energy consumption and make informed decisions based on real-time data [4]. The energy management systems offers many benefits, such as optimizing energy consumption, reducing costs, improving the corporate image of the enterprise, and reducing the negative impact on the environment [5]. Therefore, by implementing an effective energy monitoring and analysis software platform within industrial environments, businesses can not only reduce their overall energy consumption and costs but also improve their environmental sustainability and corporate reputation. Moreover, the integration of energy consumption data into work order and production notifications allows for a more accurate measurement of unit costs. This allows companies to have a more transparent understanding of their energy expenses, enabling them to make data-driven decisions for cost optimization. In this context, monitoring and analyzing energy consumption in industrial environments can play a vital role in achieving energy savings and promoting sustainability. Alerts and notifications provided by the developed control panel further enhance the efficiency of energy management. These notifications ensure that relevant stakeholders are immediately informed when energy values exceed or fall below predefined thresholds [6]. As a result, prompt actions can be taken to address any anomalies or deviations, preventing potential energy waste or inefficiencies.

In today's rapidly changing world, the significance of accurate monitoring and analysis of energy consumption in industrial environments cannot be overstated. Energy efficiency is a crucial factor for the industrial sector, and businesses are increasingly recognizing the importance of implementing effective energy management systems [5]. These systems not only enable businesses to optimize their energy consumption and reduce costs but also improve their corporate image and minimize their negative impact on the environment.

2 MATERIAL AND METHODS

This section outlines the methodology and components employed in this study for enabling real-time data collection from machines, analyzers, and sensors situated within production fields, along with the standardization of data transmission to upper-level modules and systems. The key concepts within the overarching architecture are as follows:

- **Data Collection:** Data retrieval is based on configurations and involves the extraction of data from data sources, notably Modbus TCP gateways. Device identification, encompassing device IP/port and unit ID/slave ID, as well as addresses and data types, plays a crucial role in data collection.
- **Device:** Refers to a physical device or gateway utilized for data retrieval. Presently, the system is configured to interface with Modbus TCP gateways, with plans to accommodate other protocols and standards in the future.
- **Unit**: A logical component residing within a device, presently identified via a Slave ID/Unit ID.
- **Reading Definition:** Signifies a data point characterized by a unique address and data type. Readings for units are defined, and numeric formulas are attached to these readings to facilitate value calculations.
- **Numeric Formulas:** These formulas offer the means to compute actual values from raw reading data. Numeric formulas support basic calculations by employing predefined and optional multipliers and divisors.
- **Alerts:** A mechanism for sending notifications to users predicated on predefined threshold values and trigger conditions. Alerts are defined in relation to a device reading, identified by its name, and the numeric formula attached to the reading definition.
- **Channels:** Channels are used to disseminate alerts. Presently, SMTP Mail and Telegram channels are supported.
- **Sinks:** Sinks are employed to disseminate reading data to message brokers, databases, third-party systems with REST endpoints, and our proprietary trexDCAS. Some sink implementations support the distribution of alerts. Sinks can be configured for integration purposes to transmit device data or alerts.

- **Actor Model:** Data collection and alert chart generation background services are implemented as Actor Models using the Akka.NET framework. All logic is encapsulated within actors, with services utilized by these actors. Communication between actors is achieved through messages and events.
- **Plots:** Device data is visualized using OxyPlot charts within our Windows Desktop application. Additionally, support is provided for embedding PNG charts within alert messages.

Figure 1 provides an overview of the system's general architecture.

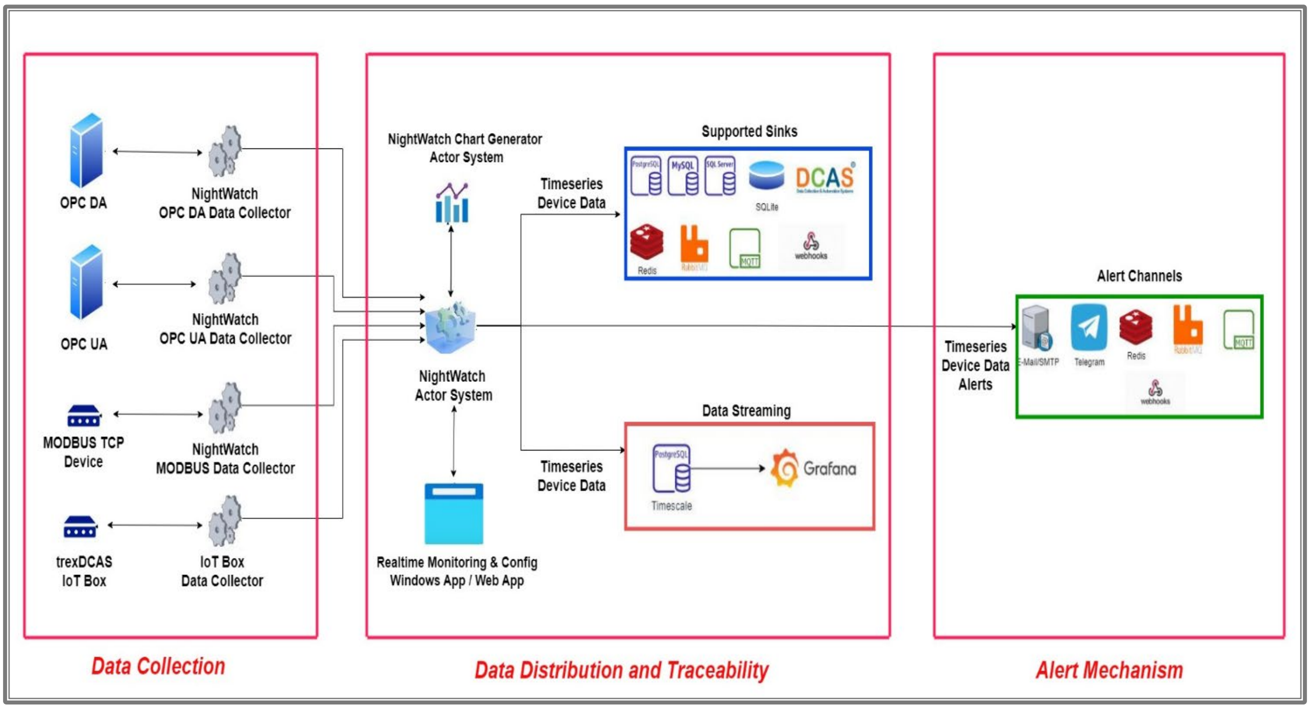

Figure 1. General System Architecture.

The system comprises three primary components, namely, data collection, data distribution and traceability, and the last one is the alert mechanism.

2.1 Data Collection

Developing industrial IoT solutions presents a primary challenge arising from the diversity of machines and sensors used in the field, resulting in difficulties in maintaining a consistent and healthy data flow.The key issues encountered in data collection and the broader challenges they pose can be summarized as follows:

- Disruption of digitization in production fields due to the presence of older machines incapable of generating data.
- Escalation of system complexity and data collection expenses owing to the diversity in machine and sensor brands, models, protocols, and data formats.
- Diminished data quality at the corporate level due to the inability to centrally perform data integration, cleansing, and enrichment processes.

- High costs and prolonged installation and project durations resulting from repetitive efforts at the organizational level. These efforts arise from the need for various systems (MES, ERP, Quality Applications, etc.) to access machine data using distinct frequencies and methods.

The developed system provides support for widely used industrial protocols, including OPC UA, OPC DA, and MODBUS TCP. Furthermore, it offers direct data retrieval capabilities from PLCs such as Siemens, Mitsubishi, Omron, Rockwell, and Allan-Bradley. In addition to these aforementioned protocols and PLCs, the system is also compatible with Mert Software & Electronics' proprietary hardware, known as the trexDCAS IoT Box.

In the Nightwatch platform, raw data collected from machines and sensors can be amalgamated, filtered, and enriched using advanced scripts that can be defined during the configuration phase. This enrichment encompasses a broad spectrum of functions, encompassing not only fundamental mathematical operations but also advanced numerical processes, signal processing, geographical location calculations, conditional expressions, and more.

2.2 Data Distribution and Traceability

The component responsible for transmitting raw or enriched data collected from various machines and sensors to upper-level modules or systems is referred to as the "data distribution" component. The system's data distribution capabilities encompass the following features:

- **Definition of Target Systems:** The system allows for the definition of target systems for data transmission using generalized and standardized configurations.
- **Data Transmission Formats:** It enables the transmission of collected and computed data to target systems in four different standard formats, regardless of the source machines and protocols, based on the intended use.
- **Simultaneous Data Transmission:** The system facilitates simultaneous data transmission to multiple target systems, whether they are of the same type or different types.

The fundamental concept underpinning the data distribution capabilities of the designed system is referred to as a "Sink." Sinks encompass the types of target systems to which data will be sent and the associated settings for these target systems, including addresses, usernames, passwords, and more. In essence, Sinks are the components responsible for enabling data transmission to external systems within the system.

The system utilizes integration sinks for distributing collected or generated data and alarm sinks for distributing alarm data when predefined alarm conditions are met. The platforms to which the system can distribute data using integration sinks include:

- Relational databases (PostgreSQL, Microsoft SQL Server, Oracle, MySQL, MariaDb, and SQLite)
- Message brokers supporting the MQTT protocol (e.g., Mosquitto)
- Message brokers supporting the AMQP protocol (e.g., RabbitMQ)
- Redis
- Systems supporting the OPC UA protocol (e.g., KepWare)
- Custom systems tailored to individuals or customers using the Web Hook mechanism, based on REST
- trexDCAS Energy module
- trexDCAS Operator Panel

Time-series data gathered from the sensors are stored in PostgreSQL, an open-source database management system, for further analysis. This data is subsequently transformed into real-time and historical analysis plots using Grafana [7], allowing for in-depth analysis (Figure 2).

Figure 2. Visualization of the collected data

2.3 Alert Mechanism

The alert mechanism in this system involves real-time processing of data obtained from machines and sensors based on user-defined conditions. It also includes the capability to send alarm notifications through user-defined channels to external systems, email, or instant messaging services when specific alarm conditions are met.

The design principles for the alarm system in this developed system encompass the following aspects:

- **Ease of Alarm Definition:** Alarm conditions should be easily defined.
- **Real-time Processing:** Alarm conditions should operate in real-time on the raw data collected from machines and sensors.
- **Utilization of Calculations:** Alarm conditions should also be capable of operating on real-time calculations performed on data generated from the raw data.
- **Notification Channels:** Notifications should be sent through defined channels when alarm conditions occur.
- **Integration with External Systems:** Alarm information should be distributed to external systems via alarm sinks when alarm conditions are met.
- **Historical Data Distribution:** Historical values of the sensor data that triggered the alarm can be distributed as information and, if desired, in graphical form through channels or sinks.

The alarm detection mechanism of the system is founded on four fundamental concepts:

- **Raw Data:** Real-time data collected from machines or sensors, with unit conversions applied.
- **Generated Data:** Real-time data derived from raw data using either complex or simple calculations supported by scripts integrated into the system.
- **Data Monitoring Windows:** These are created by users and configured concerning time intervals.
- **Alarm Condition Occurrence:** Alarm conditions are defined through configuration and are used to trigger alarms.

The system generates alarms based on these four concepts to notify users of changes in status or conditions, thus offering effective real-time monitoring and alerting capabilities.

When an alarm is detected, the system simultaneously dispatches alarm information and historical data, along with a graph, as a message to one or more configured channels, which can be of different types. The developed system supports channels of the Email and Telegram types, simplifying the configuration and use of alarm notifications through these user-friendly channels.

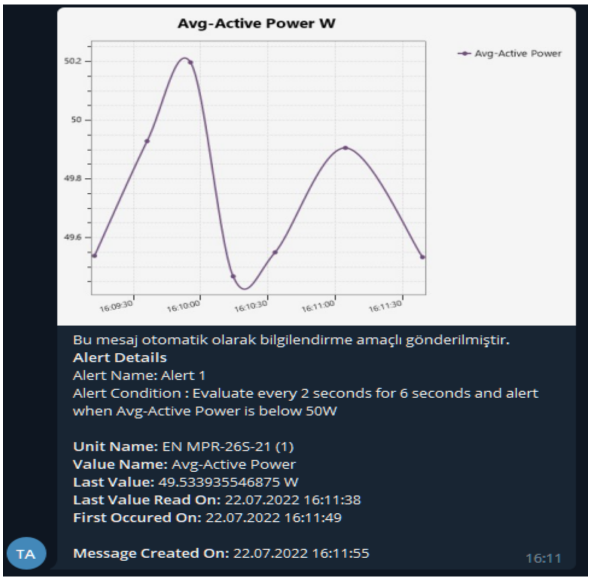

Figure 3. Alert message sent to the Telegram channel

Figure 3 illustrates the structure and content of an alarm message sent to the Telegram channel. For channels not directly supported by the system, such as delivering notifications through messaging platforms like Slack or Microsoft Teams, the system offers the option to utilize pre-existing sinks (e.g., MQTT, RabbitMQ, Redis, etc.). These sinks allow the system to interpret alarm messages in JSON format and forward them to the preferred sink for further transmission to the desired messaging services (see Figure 4).

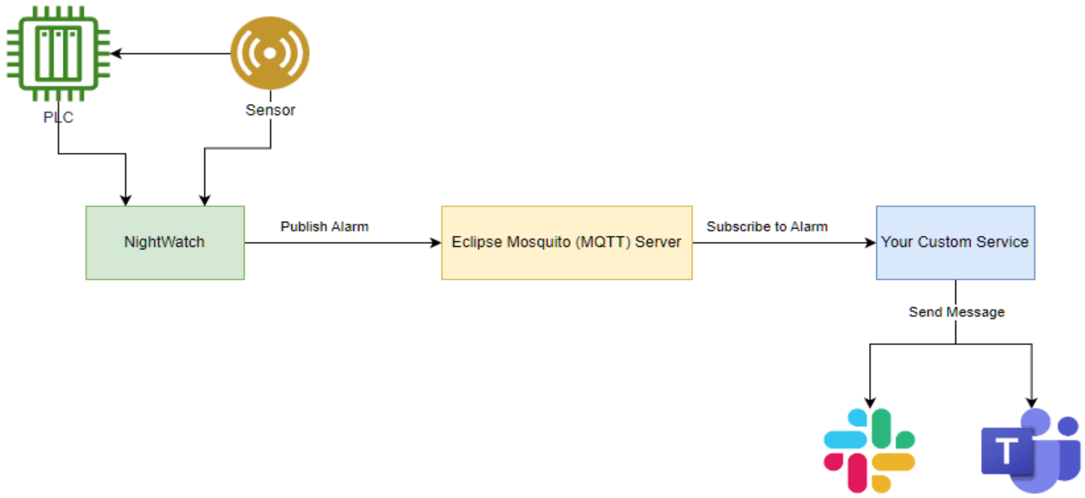

Figure 4. Sample structure for sending alert messages to Slack and Microsoft Teams

3. RESULTS AND DISCUSSION

In this article, the proposed system facilitates the recording of data related to processes that enterprises aim to monitor. Consequently, it enables businesses to measure unit costs on a work order basis and monitor the relationship between work order-based energy consumption data and machine-based energy consumption.

Upon adapting and implementing the developed system in an enterprise focused on monitoring energy losses, notable results have been obtained. When comparing sample machine data for the same number of work orders over a 5-month period, using a 5-minute data collection interval, it becomes evident that energy consumption for the selected machine improved by 36% from the initial reading (71.1 Amperes) to the final reading (45.4 Amperes) due to the actions taken.

4. CONCLUSION

In today's world, where energy and natural resources are limited, monitoring critical issues such as energy, water, and pollution, and swiftly implementing potential improvements, are of paramount importance in leaving a more habitable world for future generations.

Building on this understanding, the system under discussion in the article enables the following processes:

- Energy consumption data collection and monitoring,
- Energy consumption Key Performance Indicator (KPI) calculation and monitoring,
- Process machine data collection and manual data measurement,
- trexDCAS production line energy consumption and anomaly detection machine data collection,

- Machine Overall Equipment Efficiency (OEE)/performance data collection.

As a result, Nightwatch software is a significant endeavor in terms of enabling businesses to monitor overlooked aspects through the system, take necessary actions, and make improvements. Our proposed energy management software architecture will make a positive contribution to an organization's energy management and savings policies.

REFERENCES

[1] B. Sucic, M. Peckaj, Z. Tomsic and J. Uranic. "Systematic approach for improving energy efficiency in industrial facilities, from energy audit to practical implementation – case study production of autoclaved aerated concrete". Jan. 2019.

[2] H. J. Kang, J. Lee and D. H. Lee. "An Integrated Energy Data Analytics Approach for Machine Tools". Jan. 2020.

[3] J. Wang, Y. Huang, Q. Chang and S. Li. "Event-Driven Online Machine State Decision for Energy-Efficient Manufacturing System Based on Digital Twin Using Max-Plus Algebra". Sep. 2019.

[4] M. Linan-Reyes, J. Garrido-Zafra, A. Gil-de-Castro and A. Moreno-Munoz. "Energy Management Expert Assistant, a New Concept". Sep. 2021.

[5] M. T. Rajić, R. Maksimović, P. Milosavljevic and D. M. Pavlović, "Energy Management System Application for Sustainable Development in Wood Industry Enterprises".

[6] N. Zhang, N. Yang and J. Liu. "Optimal Time-of-Use Electricity Price for a Microgrid System Considering Profit of Power Company and Demand Users". Oct. 2021.

[7] Grafana. [Online]. Available: https://grafana.com/. Accessed: [August 2023].

THE IMPROVEMENT OF CORROSION PERFORMANCE OF CoCrW ALLOY WITH BIOACTIVE GLASS COATING

Y. Uzun[1], B. Taş[1], Ş. M. Tüzemen[1], A. Çelik[1]

[1]Department of Mechanical Engineering, Faculty of Engineering, Atatürk University, Erzurum, TÜRKİYE

E-mail: sukrantuzemen@atauni.edu.tr

In the developing world, increasing needs and health problems are constantly on the agenda. Solutions to these problems should support each other and should not cause another problem. In this context, implants and prostheses used to replace a missing or damaged structure in living organisms must show the necessary mechanical, electrochemical and biocompatibility properties together. Although CoCr alloys, which are frequently preferred for their superior mechanical properties in places such as dental implants and hip prostheses, show good corrosion performance, it has been found that they cause the release of Cr ions into the body after a while. In addition, these alloys are also weak in terms of biocompatibility as osseointegration. With the surface engineering approach to such problems, it is known that the desired properties can be gained with a number of surface treatments without destroying the desired mechanical properties of the structure.

In this study, commercial 63S bioactive glass powder was coated on the surface of CoCrW alloy by electrochemical storage using different parameters, then sintered and corrosion behavior in artificial saliva was investigated. As a result of the investigation, necessary morphological and structural analyzes were performed. Based on the analysis, it was observed that coatings with 63S bioactive glass powder improved the corrosion resistance of CoCrW alloy.

Keywords: CoCr alloy, Electrophoretic deposition, Bioactive glass, Corrosion

1. INTRODUCTION

CoCr alloys are biocompatible metallic alloys with high strength and good corrosion resistance due to their high chromium content, heat and abrasion resistant, non-magnetic and biocompatible [1]. With their high modulus of elasticity (E), they reduce the weight of metal substructures in implants by providing strength without the need for heavy cross-sections. While these alloys are widely preferred in orthopedic and dental implants, they are frequently used in dentistry for metal frames, crowns, partial dentures and dental restorations. In addition, thanks to the developing production and material technologies, CoCr alloys have recently been preferred in body joints such as hip, knee, shoulder and stent construction [2].

However, CoCr alloys are very difficult to fabricate due to their high hardness, melting point and less ductility [3]. Additive manufacturing (AM) is used as a good solution to overcome this problem. Additive manufacturing, a laser-driven manufacturing technology, can be broadly divided into three manufacturing methods: selective laser sintering (SLS), laser metal deposition (LMD) and selective laser melting (SLM). Among these methods, SLM uses thermal energy from a laser beam, focused and accurately controlled with the help of computer-aided design (CAD) data, to melt metal powders and add metal powders layer by layer to form a metallic structure. Compared to traditional methods, the SLM technique offers advantages such as low production cost, high product density, high dimensional accuracy, less waste, improved mechanical properties with finer grains due to the rapid melting and high cooling rate of the metal powder, and no casting defects. This manufacturing technique facilitates the production of complex and non-machinable parts for advanced applications in different industries such as medical, automotive, aviation and aerospace. Recently, CoCr alloys produced by SLM have attracted much more attention as they exhibit higher mechanical strength, hardness and biocompatibility properties compared to conventional manufacturing techniques [4-7].

On the other hand, unnecessary release of ions such as Co^{2+}, Cr^{3+} and Cr^{6+} from implants made of CoCr alloys into the body has been shown in some studies to develop hypersensitivity and inflammatory responses at the implant site [4]. For this reason, many studies on the potential risks of applying these alloys in the human body have focused on the corrosion resistance of CoCr alloy implants produced by casting. In these studies, the corrosion resistance of CoCrMo alloys, taking into account their composition, electrolyte solutions and structures, etc., was also investigated in different biological solutions with varying element and additive content, such as urine, joint fluid, serum, saline solution, Hanks and so on. As a result of the studies, it was found that the elemental content used in these alloys has a more significant effect than the electrolyte solutions preferred as corrosive media. Basically, it has been observed that the elemental content of CoCrMo alloys as well as the selected production method have a great influence on microstructures and phases due to different interfacial properties. In terms of corrosion resistance in general, it is another finding that as the stability of the oxide film formed in CoCrMo alloys increases, corrosion resistance increases at the same rate and ion release decreases [6,8,9].

The electrophoretic deposition (EPD) technique is highly attractive for bioactive coatings due to its simplicity, low equipment cost, the ability to deposit on complex forms of base materials at room temperature, as well as the high purity and microstructural homogeneity of the films formed. EPD is technically realized by moving suspended powder particles onto the base material under the influence of an electric field. However, the binding force between the coating and the base material formed as a result of this technique is not high enough. Therefore, after deposition, heat treatments are needed to further densify the coating and strengthen the adhesion [10].

Bioactive coatings on base materials with EPD have been reported in the literature in a few cases, with most research on hydroxyapatite coatings. Base materials coated with hydroxyapatite by EPD usually include materials such as stainless steel, titanium and its alloys, silicon and carbon fiber. The research findings and results of the studies show that a strong adhesion occurs between the base material and hydroxyapatite in EPD hydroxyapatite coated structures. In addition, the corrosion resistance of these structures in simulated body fluid (SBF) was found to increase compared to uncoated samples [11,12]. Only a few studies have been conducted for coating other types of bioactive coatings by EPD technique. Therefore, the aim of this study is to 63S bioactive glass coatings on CoCrW alloy using EPD technique for different durations, followed by sintering to increase adhesion. The study investigated the effect of time factor on the obtained film thickness and electrochemical corrosion resistance. In the study, sintering and suspension concentration conditions were determined as optimum conditions based on other studies in the literature.

2. MATERIAL AND METHODS

The production of CoCrW specimens with dimensions of 10 x 10 x 2 mm^3 by the SLM method was carried out on the CONCEPT LASER MLab Cusing device with CoCrW powders according to ASTM F75. Layer fabrication with fiber laser was carried out in a protective argon atmosphere and using simple straight line scans to melt each layer and the process parameters used for samples production by SLM are listed in Table 1. Then the post-production residues were cleaned with sandpaper. CoCrW alloys generally contain 58.85% Co, 26.30% Cr and 12.62% W, 1.13% Si and 1.1% C by weight.

Table 1. Process parameters for CoCrW samples manufacturing by SLM.

Plane		Contour		Layer Thickness
Scan power	*Scan speed*	*Scan power*	*Scan speed*	
75 W	1000 mm/s	75 W	1000 mm/s	25 µm

For the EPD process, suspension was prepared with 99 ml of distilled water, 1 ml of acetic acid, 0.2 ml of phosphate ester and 66 g/L 63S Bioactive glass® commercial powder (containing 63% SiO_2, 28% CaO, and 9% P_2O_5 by weight) at room temperature. After the suspension was dispersed for 10 minutes, it was stirred for 12 hours on a magnetic stirrer. During the coating, the suspension was stirred continuously at 20 rpm with the help of magnetic stirrer. All EPD experiments were performed at room temperature, graphite was used as the counter electrode and the electrodes were placed with a distance of approximately 2 cm between them. The electrodes were washed with acetone before processing. Cathodic Electrophoretic Deposition (C-EPD) for all samples was performed using GW GPR-30H10D Laboratory DC Power Supply with CoCrW sample as the cathode electrode and graphite as the anode electrode, applying a constant voltage of 3 V for 20 minutes and 3 V for 60 minutes. The schematic representation of the EPD process is given in Figure 1. All samples were then sintered at 800 °C for 1 hour to increase adhesion.

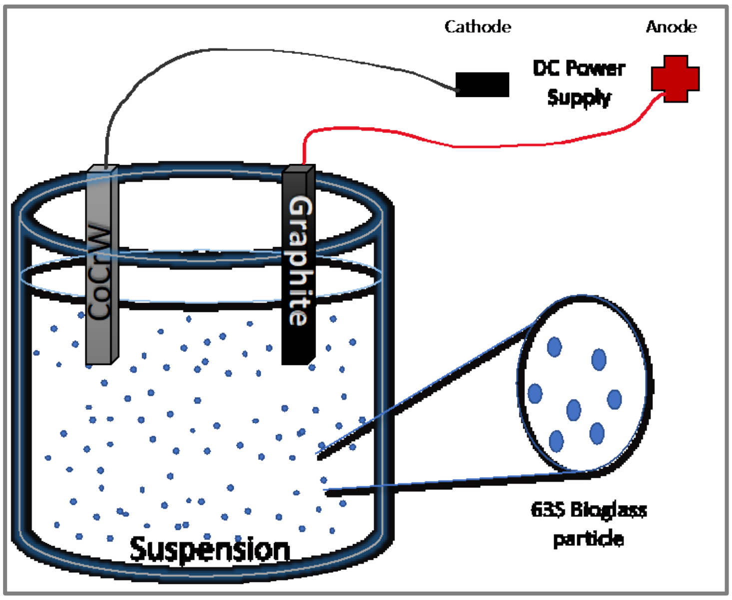

Figure 1. The schematic representation of EPD process for 63S coating on CoCrW alloy.

In order to examine the untreated and coated surfaces of CoCrW samples in a more realistic environment, corrosion tests were carried out in Artificial Saliva (Saliva). The corrosion tests were completed using Gamry G750 Potentiostat/Galvanostat system, firstly by Open Circuit Potential (OCP) and then by Cyclic Polarization. The test setup was constructed using a triple electrode system with untreated and coated samples as the working electrode, graphite rod as the counter electrode and Ag/AgCl as the reference electrode. During the test, the corrosion surface area was set to 1 cm^2 and the time required for the Open Circuit Potential reading was set to 5400 seconds. Cyclic Polarization measurements were performed with a scan rate of 1 mV/s at 0.5 V beyond the Open Circuit Potential values. The Tafel polarization curves obtained from the electrochemical analysis were analyzed in detail.After all these processes, EDS and SEM analysis was performed with SEM (FEI QUANTA-FEG 250) in order to analyse the structural and morphological effects of coating on the samples.

3. RESULTS AND DISCUSSION

When the findings obtained are examined, it is confirmed from the EDS analysis results of the coated samples given in Figure 2 that the coating was carried out correctly with the presence of Si, Ca and P elements, which are the main components of 63S Bioactive glass material. It coincides with the studies conducted in the literature and the findings obtained [13].

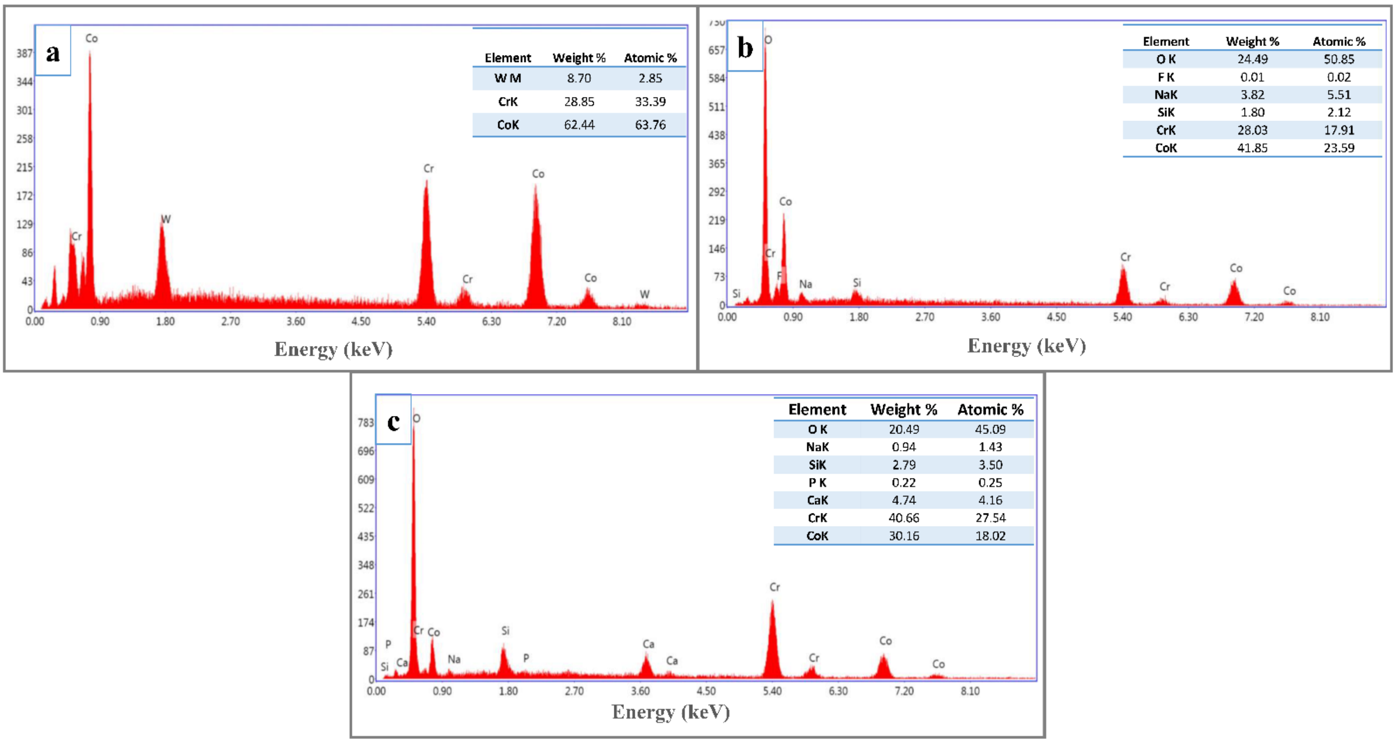

Figure 2. EDS analyses of (a) 3 V - 20 min and (b) 3 V - 60 min 63S Bioactive glass coated CoCrW samples.

In Figure 3, cross-section SEM images of (a) 3 V - 20 min and (b) 3 V - 60 min 63S Bioactive glass coated CoCrW samples are given. The images confirm that the coatings were performed relative to the untreated sample. In addition, it was observed that the coating thickness increased as the coating time increased.

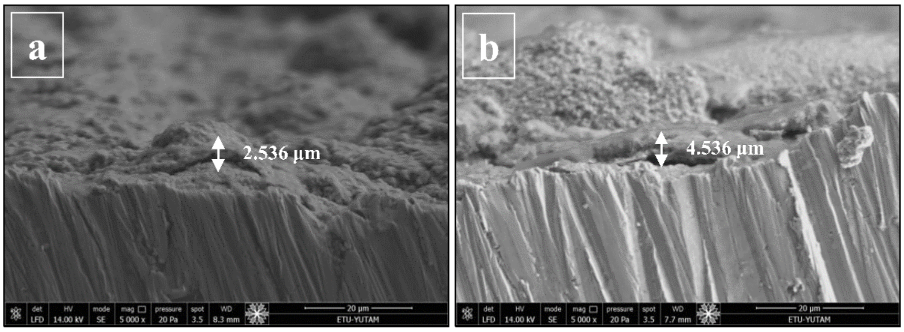

Figure 3. Cross-section SEM images of (a) 3 V - 20 min and (b) 3 V - 60 min 63S Bioactive glass coated CoCrW samples.

In Figure 3, cross-section SEM images of (a) 3 V - 20 min and (b) 3 V - 60 min 63S Bioactive glass coated CoCrW samples are given. The images confirm that the coatings were performed relative to the untreated sample. In addition, it was observed that the coating thickness increased as the coating time increased.

The data obtained as a result of electrochemical measurements show that the open circuit potential shifts to more positive values as the coating time increases. Figure 4 shows the potentiodynamic polarization curves of all samples.

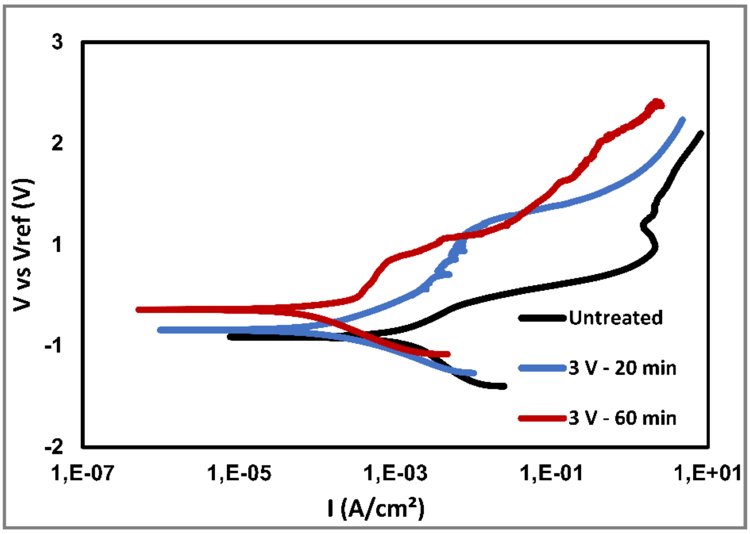

Figure 4. Potentiodynamic polarization curves of untreated, 3 V - 20 min and 3 V - 60 min 63S Bioactive glass coated CoCrW samples.

Table 2 shows the E_{corr} and I_{corr} values obtained as a result of cyclic polarization curves for untreated and 3 V - 20 min, 3 V - 60 min samples. According to the table, E_{corr} values are -4.13 mV for the untreated sample, -3.45 mV for 3 V - 20 min and -1.42 mV for 3 V - 60 min, respectively. According to these values, it was determined that the corrosion resistance increased as the time increased. With the help of these values, mass losses and the formula in equation (1), corrosion rates of the samples were calculated and they are given in Table 2. In the equation (1); I_{corr} represents corrosion current, K represents a constant, EW represents equivalent mass, d represents density and A represents surface area.

$$Corrosion\ Rate = I_{corr} KEW/dA \tag{1}$$

When the corrosion rate values of the untreated and coated specimens are analyzed; it is seen that the untreated specimen has a poor performance in terms of material loss due to corrosion with a corrosion rate of 38.96 mm / year. In coated samples, these values were calculated as 238.1×10^{-3} mm/year for 3 V - 20 min and 188.6×10^{-3} mm/year for 3 V - 60 min, respectively. This proves that the coated specimens show a good performance in terms of corrosion resistance compared to the untreated specimens in terms of corrosion rates. In addition, when the coated samples were evaluated among themselves; the corrosion rate of the sample coated for 60 minutes was lower in terms of corrosion rates, confirming that the corrosion resistance increased due to the increase in coating thickness as the coating time increased.

Table 2. Results of electrochemical measurements of untreated, 3 V - 20 min and 3 V - 60 min 63S Bioactive glass coated CoCrW samples.

Samples	**E_{corr}** ***[mV]***	**I_{corr}** ***[nA]***	**Corrosion Rate** ***[mm/year]***
Untreated	-4.13	92.6	38.96
3 V – 20 min	-3.45	553.0	232.7×10^{-3}
3 V – 60 min	-1.42	118.0	49.74×10^{-3}

4. CONCLUSION

In the scope of the study, in order to increase the adhesion of the coatings, it was determined that the sintering process at 800 ° C temperature and normal atmosphere for 1 hour after treatment with EPD increased the adhesion with oxidation. Corrosion resistance was also improved with increasing coating time. The fact that the experiments were performed in Artificial Saliva fluid shows more optimum results for implants made of CoCrW alloy. Inorganic bioactive glass coatings on such alloys seem to be promising in terms of corrosion resistance in line with the data obtained from the study.

ACKNOWLEDGMENTS

This research has not received any specific grants from funding agencies in the public, commercial, or nonprofit sectors.

REFERENCES

[1] Milošev, I, CoCrMo Alloy for Biomedical Applications, Djokić, S. (Eds.), Biomedical Applications, Modern Aspects of Electrochemistry, 55, 1-72, 2012, Springer, Boston, MA.

[2] Mani, G., Metallic biomaterials: cobalt-chromium alloys, Murphy, W., Black, J., Hastings G. (Eds.), Handb. Biomater. Prop (second ed.), 159-166, 2016, Springer.

[3] Ozel, T., Bartolo, P., Ceretti, E., De Ciurana Gay, J., Rodriguez, C.A., Da Silva, J.V.L., Biomedical devices: design, prototyping and manufacturing, 2017, John Wiley & Sons.

[4] Chen, Q., Thouas, G.A., Metallic implant biomaterials, Mater Sci Eng R Rep, 87, 1-57, 2015.

[5] Takaichi, A., Suyalatu, T., Nakamoto, N., Joko, N., Nomura, Y., Tsutsumi, S., Microstructures and mechanical properties of Co-29Cr-6Mo alloy fabricated by selective laser melting process for dental applications, J Mech Behav Biomed Mater, 21, 67-76, 2013.

[6] Seyedi, M., Zanotto, F., Monticelli, C., Balbo, A., Liverani, E., Fortunato, A., Microstructural characterization and corrosion behaviour of SLM CoCrMo alloy in simulated body fluid, Metall Ital, 110, 45-50, 2018.

[7] Mergulhão, M.V., Podestá, C.E., das Neves, M.D.M., Valuation of mechanical properties and microstructural characterization of ASTM F75 Co-Cr alloy obtained by Selective Laser Melting (SLM) and casting techniques, Mater Sci Forum, 899, 323-328, 2017.

[8] Igual Muñoz, A., Mischler, S., Effect of the environment on wear ranking and corrosion of biomedical CoCrMo alloys, J Mater Sci: Mater Med, 22, 437–450, 2011.

[9] Hodgson, A.W.E., Kurz, S., Virtanen, S., Fervel, V., Olsson, C.O.A., Mischler, S., Passive and transpassive behaviour of CoCrMo in simulated biological solutions, Electrochim Acta, 49, 2167–2178, 2004.

[10] Pishbin, F., Simchi, A., Ryan, M.P., Boccaccini, A.R., Electrophoretic deposition of chitosan/45S5 Bioactive glass® composite coatings for orthopaedic applications, Surface and Coatings Technology, 205, 5260–5268, 2011.

[11] Khanmohammadi, S., Ojaghi-Ilkhchi, M., Farrokhi-Rad, M., Evaluation of Bioactive glass and hydroxyapatite based nanocomposite coatings obtained by electrophoretic deposition, Ceramics International, 46, 26069-26077, 2020.

[12] Khanmohammadi, S., Ojaghi-Ilkhchi, M., Khalil-Allafi, J., Electrophoretic deposition and characterization of Bioactive glass-whisker hydroxyapatite nanocomposite coatings on titanium substrate, Surface and Coatings Technology, 378, 1-13, 2019.

[13] Saji, V.S., Electrophoretic (EPD) coatings for magnesium alloys, Journal of Industrial and Engineering Chemistry, 103, 358-372, 2021.

TOOL LIFE ESTIMATION WITH NOISE LEVEL IN HIGH VOLUME METAL CUTTING

C. Tuncer[1], M.B. Gedikli[1], A. Oral[1,2]

[1] R&D Center, Gesbey Enerji Türbini Kule Üretim San. ve Tic. A.Ş., Bandirma/Balikesir, TÜRKİYE
[2]Department of Mechanical Engineering, Faculty of Engineering, Balikesir University, Balikesir, TÜRKİYE

E-mail: mustafaburak.gedikli@gri.com.es

High-speed and high-volume cutting technology has become an increasingly useful technology in high-volume metal cutting industries such as molding. However, the high intensity noise generated during high-volume, high-speed metal cutting operations can also have adverse effects on the accuracy and quality of the workpiece. While the increase in noise, especially in worn tools, creates an effect that can disrupt the hearing health of employees; efforts to establish a relationship between increased noise and tool life have also gained importance.

In this study, an experimental study was carried out to determine the tool life in a machine developed at the Gesbey R&D Center that performs high-volume edge milling that can create the welding bevel of 30 mm thick plates in single pass. According to ISO 3685, tool life is considered to end when the flank wear value is 300 µm. In the study, machining length and sound pressure levels and flank wear values were measured as tool life criteria when the tool started machining each plate.

In this study, a practical tool life estimation method has been developed for our business by measuring the cutting length and noise levels corresponding to the wear value at which the tool life ends according to ISO 3685.

Keywords: tool wear, metal cutting, tool life

1. INTRODUCTION

With the developing technology in recent years, cutting speeds in machine tools have increased significantly. With increasing cutting speeds, tool costs have become a very important expense item in metal cutting. Cutting technology determines the quality of industrial products and significantly affects production efficiency and processing costs [1].

The main purpose of metal cutting processes is the ability of the cutting tool to remove chips with high performance and desired properties at maximum tool life. It is extremely important to warn the operator before these behaviours are expected from the cutting tool and the tool becomes unusable. Many of the techniques developed for on-line monitoring of tool wear and breakage are not suitable for practical use. In principle, the metal cutting process should not be stopped during the measurement [2].

During machining, the cutting edges of the tools encounter some challenging phenomena such as wear, breakage, chatter vibration and built-up edge. Therefore, monitoring these events is critical to maximize production by selecting the best cutting conditions. Moreover, the application of monitoring technology has an effective impact on improving production safety conditions [3]. However, it's not suitable for mass production. Considering that we are in an industrial environment that does not tolerate idle time, it is clear that direct monitoring methods will not be acceptable for factories [4].

Although there are some signs of tool wear during metal cutting operations, tool wear during machining is often difficult to determine. Therefore, different methods can be used to predict tool wear. These methods can be divided into two main groups as direct and indirect approaches. Direct monitoring of tool wear ensures highly accurate results and disrupts production. Due to the interruption of the process during the manufacturing phase, this process can be applied in laboratory and R&D studies only for the purpose of collecting data rather than production environments.

Some of the methods to indirectly monitor tool wear online are; measurement of the current, cutting forces, vibration, sound pressure and surface roughness values of the machine drawn during cutting [2].

It has been seen that usable results have been obtained from experimental studies conducted for this purpose. Some studies on tool tracking methods are mentioned below.

In the study conducted by Prickett et al. (1999), it was stated that cutting force and vibration analysis is one of the most widely used methods among on-line tool wear monitoring methods. It has also been noted that the relationship between cutting force variation and tool wear is an effective tool condition monitoring strategy. However, it has been evaluated that due to the nature of the process in the milling process, it is limited to reach the result by vibration analysis [5].

In the study conducted by Kemal Yaman, Mustafa Başaltın (2017) for turning operations, the relationship between tool wear and cutting parameters and the sound signals emitted during machining was examined. In the study, it was seen that the sound pressure level increased as the flank wear (VB) increased, it was concluded that there was a strong relationship between tool wear and sound pressure level and that tool wear could be monitored with sound pressure measurements [6].

Karabulut et al. (2018) examined the effects of cutting parameters on surface roughness, sound pressure level and power consumption in the milling process of Hadfield steels. It has been observed that the power consumption and the resulting sound pressure increase with increasing feed rate and cutting depth values [7].

2. MATERIAL AND METHOD

In the bevelling machine developed by Gesbey R&D Center, a welding bevel is created by applying edge milling method onto the edges of the steel plates to be used in the construction of wind turbine towers. A total of 40 minutes including all preparation processes and processing time is defined for the bevelling operation of the plate, the largest of which has dimensions of 13000 x 3000 (mmxmm). This period is the minimum period for the on time delivery of the ordered wind turbine towers and it is absolutely not possible to exceed this period. Bevelling machine is given in Figure 1.

Figure 1. Bevelling machine [8]

Examples of welding bevels to be generated on wind turbine tower sheet metal plate edges are given in Figure 2. Figure 3 shows the specially designed cutting tool created for bevelling. This cutting tool has a total of 63 inserts in 7 rows and can be used for all bevel geometries up to 30 mm thickness for the turbine tower plates.

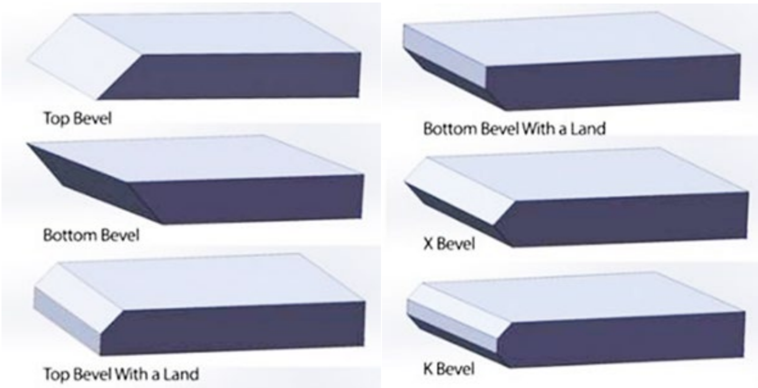

Figure 2. Types of welding bevels used in wind turbine tower construction

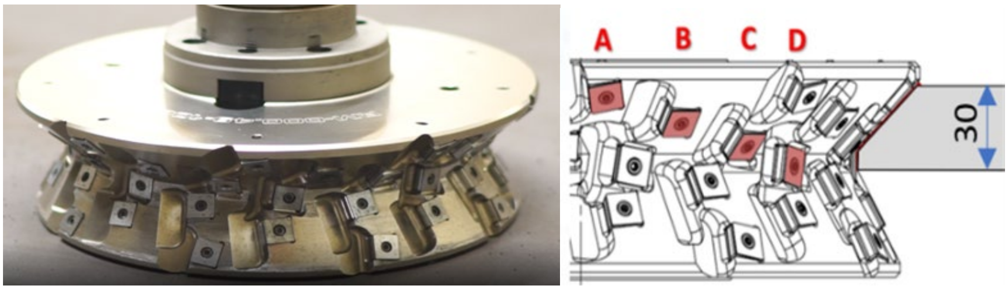

Figure 3. Cutting tool for bevelling process [8]

It has been decided to use an aluminium oxide coated SNHX1406TN08-M12 MP2501 insert seen in Figure 4, as a cutting tool in the bevelling process. The cutting parameters used for the test runs on the test plate are given in Table 1.

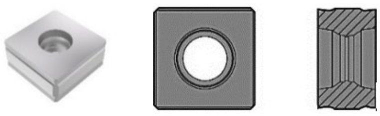

Figure 4: SECO SNHX1406TN0-M12 MP2501 cutting insert [8]

Table 1: Cutting speed and feed rate values used in the experiments

Insert ID	Cutting Speed (m/min)	Feed Rate (mm/min)
A	240	820
B	225	820
C	210	820
D	203	820

In the production of wind turbine towers, first, the welding bevel (Figure 2) is generated in the form appropriate to all edges of the plates cut in the form appropriate to the tower form (Figure 5). The cylindrical form of the tower section is shaped in bending process by passing the plate with bevelled edges, though the bending machine (Figure 6) and the tower section is formed by welding each other of cylindrical formed plates.

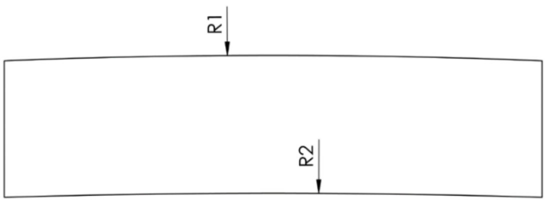

Figure 5. Sheet plate for turbine tower

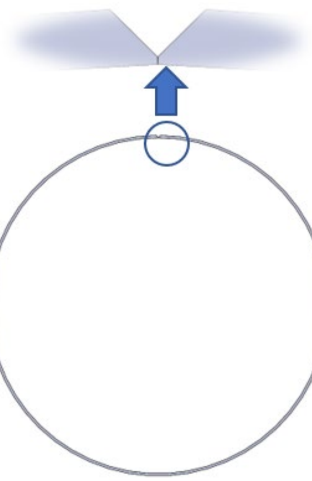

Figure 6. Turbine sheet formed in cylindrical form

The bevelling process must be carried out with a minimum feed rate of 820 mm/min in order to achieve production targets (Table 1). In this study, we focused on 4 of the total 63 inserts that remove chips to create the welding bevels to the 30 mm thickness plates (Figure 3). During this process, it is imperative to set a practical tool life criterion. For this process, the measurement of flank wear on the tool after creating the welding bevel around a plate was found to be impracticable due to the time it takes.

3. RESULTS AND DISCUSSION

In the study, it was evaluated that a relationship could be established between the sound pressure level measurement during chip removal and the flank wear of the cutting tool. Between tool and workpiece during high-volume metal cutting chip removal operations; high vibrations occur due to factors such as cutting parameters and tool wear. Vibration is a typical uneven event in high-speed machining that leads to deterioration of the surface quality of the workpiece and shortening the life of the tools. In cases where the vibration increases excessively, it damages the tool and even the machine tool, negatively affecting the accuracy and stability of the process. The sound pressure level is measured using a non-contact measuring device that is easy to use and reliable [9].

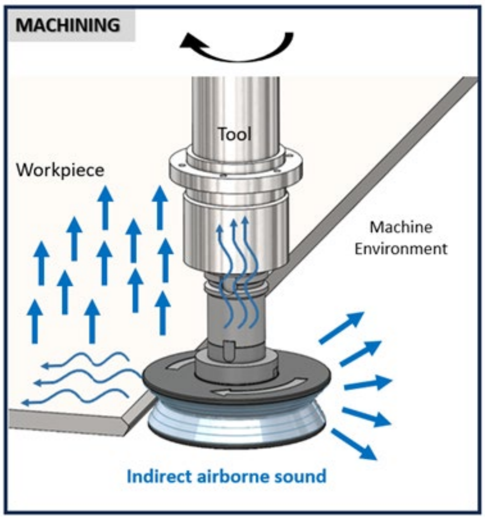

Figure 7. Vibration sources in machining process

According to ISO 3685, tool life is considered to end when the flank wear value is 300 µm. In the study, machining length and sound pressure levels and flank wear values were measured as tool life criteria when the tool finished machining each plate. UNI-T UT353 Mini Sound Meter was used for measurement of sound pressure level.

The edge milling length, measured wear values and noise values at the end of the edge milling process are given in Table 2. The relationship between edge milling of cutting length and flank wear is given in Figure 8 and the relationship between noise and flank wear is given in Figure 9.

Table 2. Flank wear and noise level

Cutting length (m)	Noise (dBA)	Flank wear			
		A	B	C	D
29,7	85,6	0,111	0,107	0,11	0,117
59,5	86,15	0,134	0,135	0,137	0,122
89,1	87,05	0,143	0,151	0,143	0,149
118,9	88,95	0,164	0,156	0,151	0,176
148,7	89,8	0,187	0,163	0,155	0,183
178,4	90,9	0,196	0,168	0,166	0,212
208,14	92,0	0,212	0,178	0,171	0,224
237,88	93,1	0,221	0,205	0,183	0,24
267,62	94,2	0,228	0,207	0,189	0,247
297,36	95,4	0,232	0,228	0,194	0,256
327,1	96,5	0,245	0,233	0,207	0,263
356,84	97,6	0,281	0,248	0,223	0,278

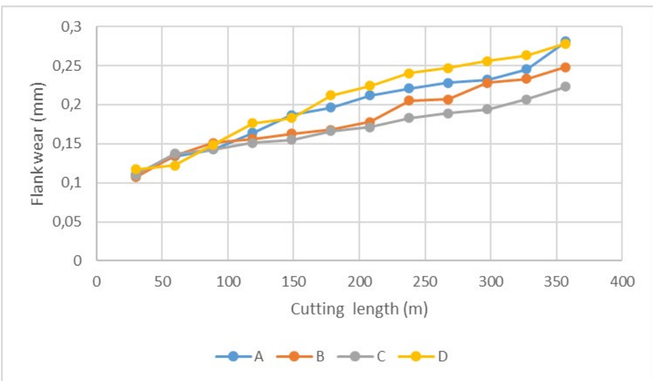

Figure 8. The relationship between flank wear and cutting length

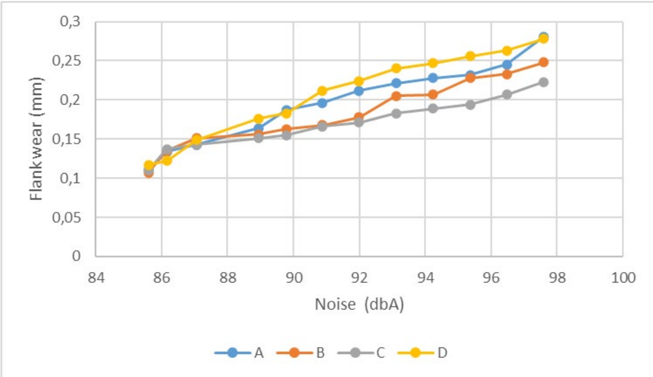

Figure 9. The relationship between flank wear and noise

4. CONCLUSION

In this study, a practical tool life estimation method was developed for the bevelling process applied to 30 mm thick steel plates to be used in wind turbine tower production.

As a result of experimental studies, it has been seen that as the amount of wear on the cutting tool increases, the sound pressure during chip removal increases significantly. With this study, a strong relationship was found between tool wear and noise level during machining of 30 mm thick plates. It has been evaluated as a practical tool life estimation method for the operations to be performed in our company.

The experimental study was carried out during the testing process of the bevelling machine, during the processing of only 30 mm thick plates. Generalization of the study can be achieved by repeating these studies for materials of different thicknesses and different bevelling geometries.

5. REFERENCES

1- Yin, R.; Ke, J.; Mendis, G.; Sutherland, J.W. A cutting parameter-based model for cost and carbon emission optimisation in a NC turning process. Int. J. Comput. Integr. Manuf. 2019, 32, 919–935.

2- Işık,Y., Talaşlı İmalatta On-Line Takım Durumu İzleme Yöntemleri Uludağ Üniversitesi Mühendislik-Mimarlık Fakültesi Dergisi, Cilt 9, Sayı 1, 2004, 82-91

3- Kishawy, H.A.; Hegab, H.; Umer, U.; Mohany, A. Application of acoustic emissions in machining processes: Analysis and critical review. Int. J. Adv. Manuf. Technol. 2018, 98, 1391–1407.

4- Yang, Z.; Yu, Z. Grinding wheel wear monitoring based on wavelet analysis and support vector machine. Int. J. Adv. Manuf. Technol. 2012, 62, 107–121

5- P.W. Prickett, C. Johns, An Overview of approaches to end milling tool monitoring, International Journal of Machine Tools & Manufacture. 39 (1999) 105-122.,

6- Yaman, K., Başaltın, M.: SAE 1030 çelik dövme malzemenin tornalama işleminde kesme parametrelerinin ve takım aşınmasının akustik olarak incelenmesi, Journal of the Faculty of Engineering and Architecture of Gazi University 32:4 (2017) 1077-1088

7- Karabulut Ş., Şahinoğlu A., R260 Çeliklerinin İşlenmesinde Kesme Parametrelerinin Yüzey Pürüzlülüğü, Güç Tüketimi ve Makine Gürültüsü Üzerine Etkileri, Politeknik Dergisi, 2018; 21 (1) : 237-244

8- Tuncer, C., Türköz S, ORAL A., Determination Cutting Parameters for Aggressive-High Performance Chip Removal of The Beveling Machine with Automated Workpiece Determination and Tool Path Generation System, 19th INTERNATIONAL CONFERENCE ON MACHINE DESIGN AND PRODUCTION, 31 August-3 September 202, CAPPADOCIA- TURKIYE

9- Wei, W., Shang, Y., You Peng and Rui Cong Research, Progress of Noise in High-Speed Cutting Machining, Sensors 2022, 22(10), 3851; https://doi.org/10.3390/s22103851

INVESTIGATION OF WEAR RESISTANCE OF ELECTROPHORETİC DEPOSITION ONTO Ti6Al4V ALLOY

Y. Uzun[1], S. Biçer[1], Ş. M. Tüzemen[1], A. Çelik[1]

[1]Department of Mechanical Engineering, Faculty of Engineering, Atatürk University, Erzurum, TÜRKİYE

E-mail: sukrantuzemen@atauni.edu.tr

Ti alloys are one of the most preferred biomaterials in the body due to their superior mechanical properties and biocompatibility. However, it is known that when these alloys are subjected to wear depending on where they are used, ion and particle release from the structure into the body occurs. In order to prevent this, surface treatments are preferred, and other desired properties can be gained without damaging the superior properties of Ti alloys. In this context, within the scope of this study, Ti6Al4V samples produced by selective laser melting (SLM) method were coated with bioactive glass at different concentrations using electrophoretic storage (EPD), a green coating method that does not require heat treatment. Necessary morphological and structural examinations were made before and after the coating. After coating, coated and uncoated samples were subjected to tribology tests in dry medium and in liquid medium using stimulated body fluid (SBF). As a result of the examinations, it was observed that the wear resistance of the coated samples increased in both mediums compared to the uncoated samples.

Keywords: Ti6Al4V, Electrophoretic deposition, Bioglass, Wear

1. INTRODUCTION

Titanium and its alloys are advanced engineering materials that are frequently preferred in the chemistry, space, aviation and energy industries due to their high temperature ranges and strengths. In addition, it is one of the widely preferred metallic biomaterials in orthopedic and dental implants due to its extraordinary deterioration resistance and biocompatibility [1]. It is ensured that the properties of Ti alloys are changed with the structures of the phases. In industrial applications, Ti alloys are different according to the transformations of the phases, and phases close to α+β and β are often the basis in biomaterial production. Ti6Al4V alloys are α+β alloys and are frequently seen in the literature as the material of choice for hip and dental implant production [2,3].

The high production cost of Ti-based parts also limits their usage areas. These alloys can be produced in a variety of ways using casting, forging, powder metallurgy and additive manufacturing techniques. However, since these alloys require machining operations after the casting method, the production of parts with this method causes high costs with material consumption along with machining difficulties. It is possible to produce parts close to the final shape and more cost-effective with additive manufacturing techniques, and it has been determined by some scientific studies that this method is frequently used especially in the production of porous implant materials [4]. Among these techniques, Selective laser melting is a type of additive manufacturing method used to melt metal powders with the help of a laser beam and then stack them layer by layer to directly create metal parts in their final form [5]. Bartolomeu et al. studied the microstructural and tribological behavior of Ti6Al4V biomedical alloy produced by selective laser melting, hot pressing and casting, and concluded that compared to hot pressing and casting, Ti6Al4V alloy produced by SLE has the highest hardness and wear resistance due to the high cooling rate [6].

Due to the passive oxide layer, commercially pure Ti and Ti alloys exhibit high corrosion resistance and, as a disadvantage, poor wear resistance [6,7]. The poor corrosion resistance and the corrosive environments used are known to cause the release of metal particles and ions from these alloys over time. However, Al and V, the main alloying elements of Ti6Al4V, have been reported to cause health problems, including allergic reactions, carcinogens and neurological disorders [8]. Furthermore, metallic artificial implants are biologically inert and can lead to encapsulation by the formation of fibrous tissues, resulting in a weak bond with bone and implant failure. Despite various limitations such as lack of bioactivity and low wear resistance, ceramic coatings such as calcium phosphate compositions may be preferable to reduce failures. In this sense, bioactive glasses have proven clinical success in bone repair applications and have been used in many medical applications since their discovery by [9]. The application of bioactive glass coatings on titanium and its alloys has been reported in the literature by a number of thermochemical methods such as plasma spraying, flame spraying, magnetron sputtering [10]. However, electrophoretic deposition (EPD), an electrochemical deposition method, offers the advantage of producing films on substrates of different forms and shapes and allows to control the mobility of particles in suspension along the applied electric field. Therefore, homogeneous and densely packed films can be obtained by EPD [11].

In this study, 10x10x2 mm3 Ti6Al4V alloys produced by SLE were coated with commercial 45S5 bioactive glass powder by EPD method. Although the coating method and the materials used are found in the literature, there are no detailed investigations on the wear behavior of such structures. Therefore, the coated samples were subjected to XRD and SEM analyses followed by tribology tests in dry and SBF environment. Friction coefficient graphs and wear rate calculations were made and the analysis was completed.

2. MATERIAL AND METHODS

Ti6Al4V samples with dimensions of 10 × 10 × 2 mm^3 were produced from Ti6Al4V powders using the CONCEPT LASER MLab Cusing device with a maximum power of 100W Ytterbium (Yb) fiber laser. Powder sizes were chosen in accordance with ASTM B348. The production parameters were 75 W laser power, 1000 mm/s plane and contour scanning speed and 25 µm layer thickness. The fabrication was carried out entirely in Ar gas environment. The chemical composition of Ti6Al4V alloy is given in Table 1.

Table 1. The chemical compounds of Ti6Al4V (%wt).

	Ti	Al	V	Fe	O	C	N	H
Ti6Al4V	Balance	5.5 - 6.7	3.5 - 4.5	< 0.4	< 0.2	< 0.08	< 0.01	< 0.05

For the EPD process, suspensions were first prepared. One suspension was prepared with 99 ml of distilled water, 1 ml of acetic acid, 0.2 ml of phosphate ester and 0.6 g/L 45S5 Bioglass® (containing 45% SiO_2, 24.5% CaO, 24.5% Na_2O and 6.0% P_2O_5 by weight) commercial powder and the other with 99 ml of distilled water, 1 ml of acetic acid, 0.2 ml of phosphate ester and 1 g/L 45S5 Bioglass® commercial powder. They were stirred with a magnetic stirrer for 3 min before each deposition to avoid precipitation of particles. All EPD experiments were performed at ambient temperature, graphite was used as the counter electrode and the electrodes were placed with a distance of approximately 2 cm between them. The electrodes were washed with acetone before processing. Cathodic Electrophoretic Deposition (C-EPD) for all samples was performed using GW GPR-30H10D Laboratory DC Power Supply with Ti6Al4V sample as the cathode electrode and graphite as the anode electrode, applying a constant voltage of 10 V for 20 minutes. The phases on the surface of the coated samples were determined using the XRD-GNR Explorer instrument operated at 40 kV and 30 mA Cu Kα (λ = 1.789 Å) source diffractometer. Also, the samples were examined by SEM (FEI QUANTA-FEG 250).

Then, tribological effects of the coating process on the samples were investigated by tribometer. The reciprocation wear tests were carried out on a Turkyus PODWT&RWT reciprocating tribo-tester according to ASTM G133-02 by using a 6 mm diameter alumina (Al_2O_3). Wear tests were performed at room temperature (25°C), 50% relative humidity, 8 mm wear track diameter and 2 N normal force for 60 minutes with a total sliding distance of 56.7 m. The Archard equation (k = Q/[W.L]) was used to calculate the amount of wear on each specimen. Friction coefficients were also calculated from the graphs obtained.

3. RESULTS AND DISCUSSION

The XRD patterns of the post-coating and untreated Ti6Al4V samples are given in Figure 1. The presence of CaCO3, $Na_6Ca_3Si_6O_{18}$, and $CaSiO_3$ peaks in the graph confirmed that the 45S5 Bioglass coating was coated on Ti6Al4V samples by EPD treatment [12].

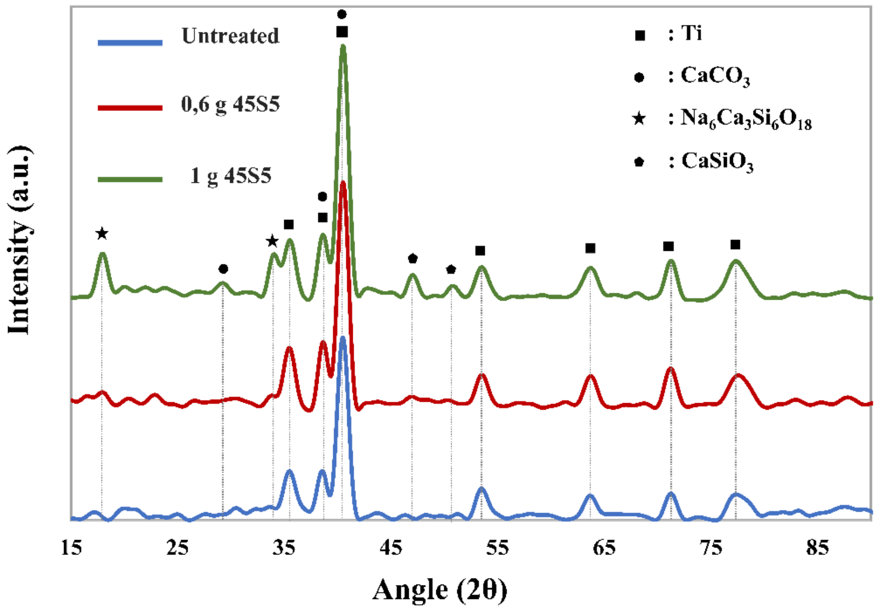

Figure 1. X-Ray diffraction graphs of untreated Ti6Al4V, 45S5 Bioglass coating on Ti6Al4V with 0.6 g and 1 g.

In Figure 2, SEM images of (a) untreated, (b) 0.6 g and (c) 1 g 45S5 Bioglass coated Ti6Al4V samples are given. The images confirm that the coatings were performed relative to the untreated sample. In addition, it was observed that the coating accumulated more on the surface as the concentration of 45S5 Bioglass increased.

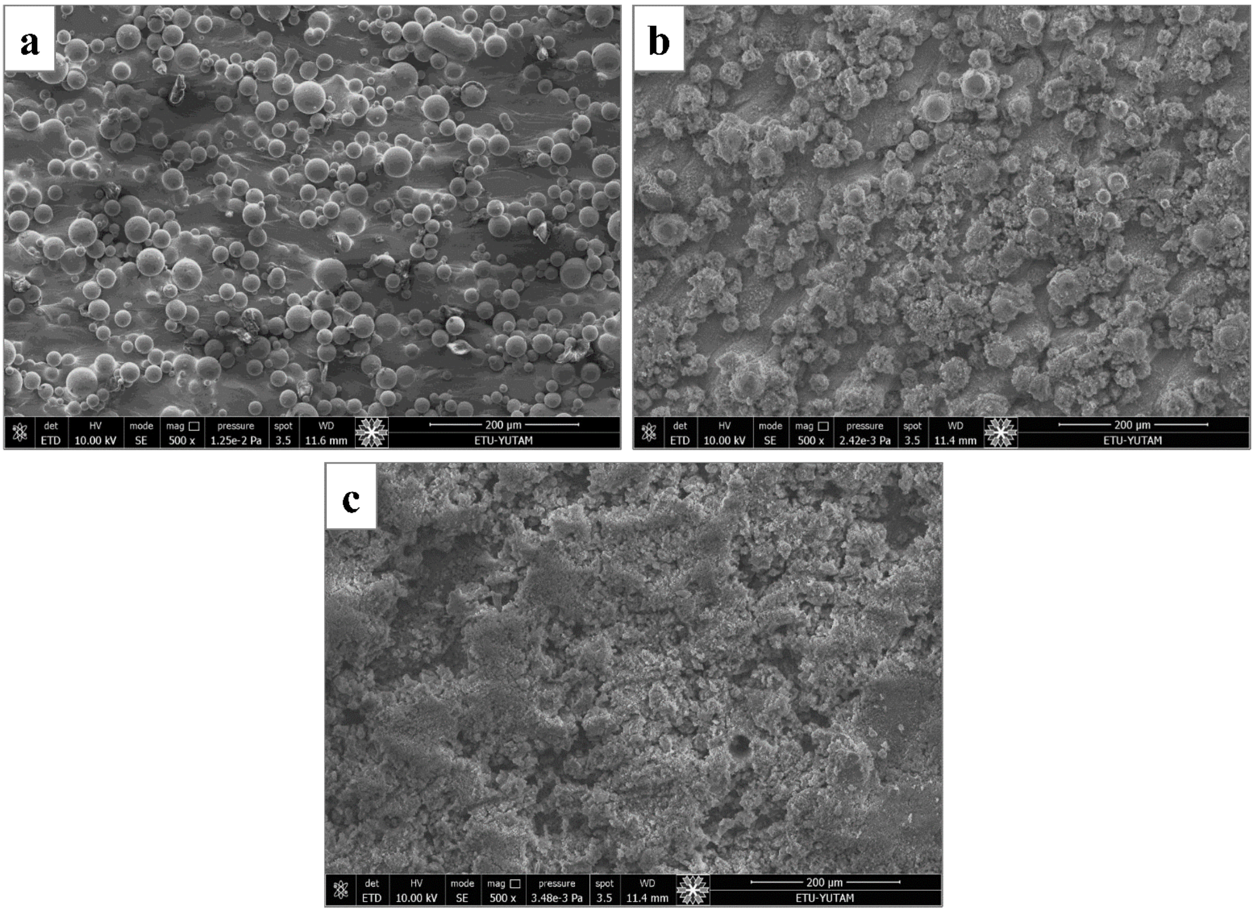

Figure 2. SEM analyses of **(a)** untreated Ti6Al4V, 45S5 Bioglass coating on Ti6Al4V with **(b)** 0.6 g and **(c)** 1 g.

The friction coefficient-time graphs of the untreated and deposited samples at different concentrations are given in Figure 3. The coefficient of friction of the coated samples exhibited a relatively stable behaviour during the wear test, while the coefficient of friction of the untreated samples journaled a fluctuating behaviour in dry and SBF mediums (Figure 3 (a) and (b)). This indicates that the surfaces of the coated samples have less surface roughness than the untreated sample produced with SLM. In Figure 3 (c), the friction coefficient values of all samples are given as a bar graph, depending on the test environments. In the graph, it is seen that the average values decreased in the other samples except 0.6 g of the coating in dry environment. In Figure 3 (d), the wear rate values of the samples are given as a bar graph, again depending on the environments. When the graph is examined, it is seen that the wear rates of the untreated samples are relatively higher than the coated samples in both environments. This confirms that the applied coating creates a self-lubricating effect on the Ti6Al4V surface in a dry and SBF environment. When the studies in the literature were examined, it was seen that both the material used and the method gave results in direct proportion to the data included in the study [10,12].

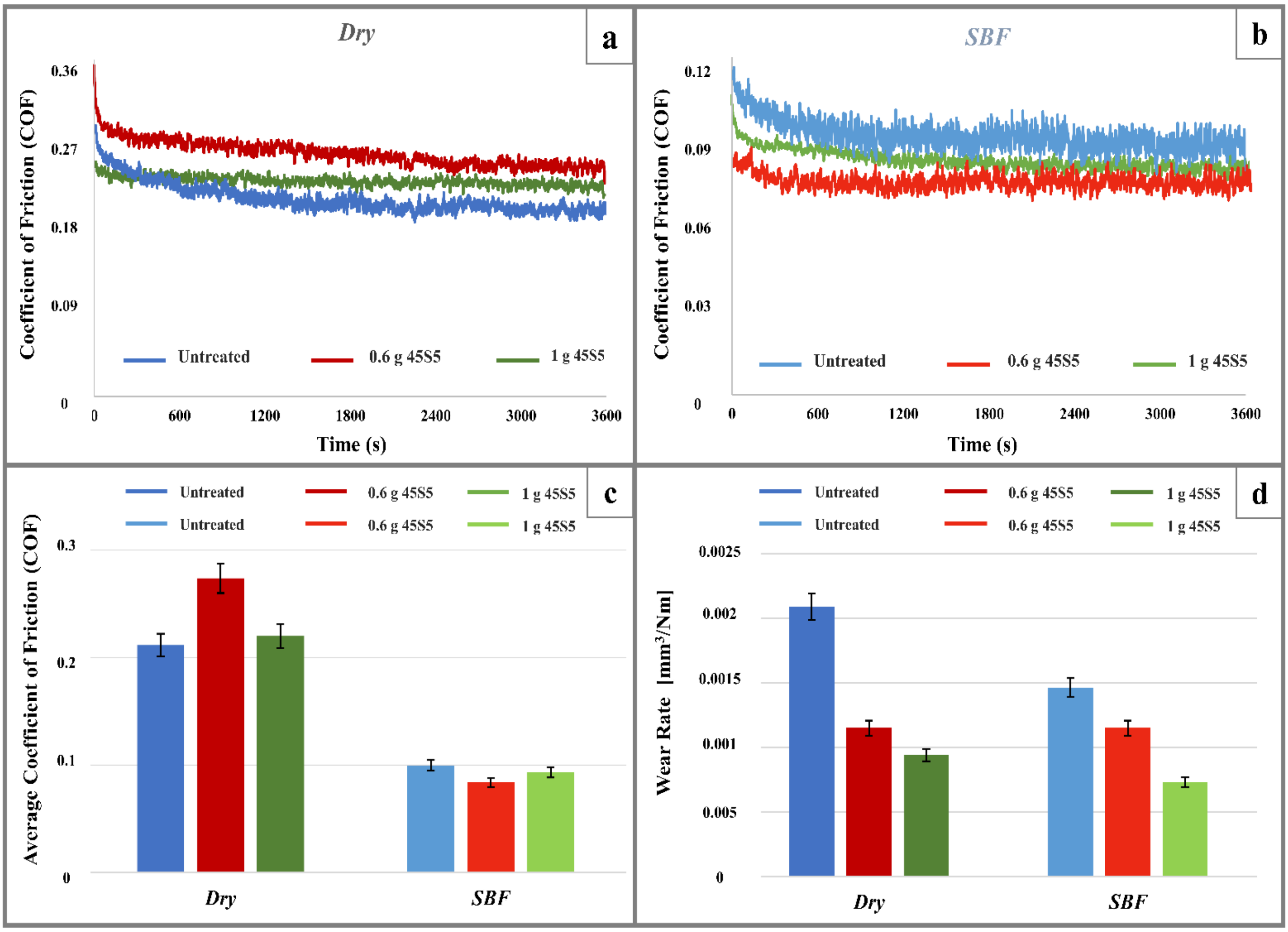

Figure 3. Coefficient of friction-time graph of untreated, 0.6 g and 1 g 45S5 Bioglass coated Ti6Al4V specimens in **(a)** dry conditions, **(b)** SBF conditions, **(c)** average coefficient of friction plot of untreated, 0.6 g and 1 g 45S5 Bioglass coated Ti6Al4V specimens in dry and SBF conditions, **(d)** wear rate plot of untreated, 0.6 g and 1 g 45S5 Bioglass coated Ti6Al4V specimens in dry and SBF conditions.

4. CONCLUSION

The results and analyzes show that 45S5 Bioglass bioactive glass material can be easily produced without any heat treatment to the Ti6Al4V biometallic material surface with the EPD process. It is remarkable that the method is simple, economical and relatively more environmentally friendly. The quality of the coatings made with this method has been examined in terms of wear resistance in this study. When the results of the wear tests in dry and SBF environments were evaluated, it was observed that the coating made increased the bioactive properties of the Ti6Al4V alloy, which is an implant material, while improving the wear properties.

ACKNOWLEDGMENTS

This research has not received any specific grants from funding agencies in the public, commercial, or nonprofit sectors.

REFERENCES

[1] Singh, N., Hameed, P., Ummethala, R., Manivasagam, G., Prashanth K.G., Eckert J., Selective laser manufacturing of Ti-based alloys and composites: impact of process parameters, application trends, and future prospects, Mater Today Adv, 8, 1-37, 2020.

[2] Feng, Q., Duan, B., Jiao, L., Chen, G., Zou, X., Lu, X., Li, C., Microstructure and tensile properties of a multi-alloyed α + β titanium alloy Ti4.5Al10.5V3Fe, Materials Chemistry and Physics, 295, 1-7, 2023.

[3] Murra, L.E., Esquivel, E.V., Quinones, S.A., Gaytan, S.M., Lopez, M.I., Martinez, E.Y., Medina, F., Hernandez, D.H., Martinez, E., Martinez, J.L., Stafford, S.W., Brown, D.K., Hoppe, T., Meyers, W., Lindhe, U., Wicker, R.B., Microstructures and mechanical properties of electron beam-rapid manufactured Ti–6Al–4V biomedical prototypes compared to wrought Ti–6Al–4V, Mater. Charact., 60, 96-105, 2009.

[4] Leban, M.B., Kosec, T., Finšgar, M., Corrosion characterization and ion release in SLM-manufactured and wrought Ti6Al4V alloy in an oral environment, Corrosion Science, 209, 1-15, 2022.

[5] Gao, B., Zhao, H., Peng, L., Sun, Z., A Review of Research Progress in Selective Laser Melting (SLM). Micromachines, 14, 1-17, 2023.

[6] Bartolomeu, F., Buciumeanu, M., Pinto, E., Alves, N., Silva, F.S., Wear behavior of Ti6Al4V biomedical alloys processed by selective laser melting, hot pressing and conventional casting, Transactions of Nonferrous Metals Society of China, 27, 829-838, 2017.

[7] Yetim, A.F., Yıldız, F., Vangölü, S.Y., Alsaran, A., Çelik, A., Several plasma diffusion processes for improving wear properties of Ti6Al4V alloy, Wear, 267, 2179-2185, 2009.

[8] Noronha Oliveira, M., Schunemann, W.V.H., Mathew, M.T., Henriques, B., Magini, R.S., Teughels, W., Souza, J.C.M., Can degradation products released from dental implants affect peri-implant tissues?, J. Periodo Res, 53, 1-11, 2018.

[9] Liu, J., Miao, X., Sol–gel derived bioglass as a coating material for porous alumina scaffolds, Ceramics International, 30, 1781-1785, 2004.

[10] Azzouz, I., Khlifi, K., Faure, J., Dhiflaoui, H., Ben Cheikh Larbi, A., Benhayoune, H., Mechanical behavior and corrosion resistance of sol-gel derived 45S5 bioactive glass coating on Ti6Al4V synthesized by electrophoretic deposition, Journal of the Mechanical Behavior of Biomedical Materials, 134, 1-11, 2022.

[11] Liu, J., Miao, X., Sol–gel derived bioglass as a coating material for porous alumina scaffolds, Ceramics International, 30, 1781-1785, 2004.

[12] Azzouz, I., Faure, J., Khlifi, K., Cheikh Larbi, A., Benhayoune, H., Electrophoretic Deposition of 45S5 Bioglass® Coatings on the Ti6Al4V Prosthetic Alloy with Improved Mechanical Properties, Coatings, 10, 2020.

AN INVESTIGATION ON THE COLOR CHANGE OBSERVED IN FERROCHROME METAL POWDER

Gökhan BAŞMAN[1], Erdoğan KARİP[1], Tuğçe Özcan[1], Cengiz Yaşin[1]

[1] *Yılmaden Holding, Eti Krom Inc., R&D Center, Elazığ, TÜRKİYE*

E-mail: erdogan.karip@etikrom.com

Eti Krom, the world's largest marketable hard lumpy chrome ore producer, is Turkey's only high-carbon ferrochrome producer. Ferrochrome production briefly consists of feeding the raw materials to the furnaces, separating the slag from the metal and preparing the products for sale at the Sandvik crushing-screening plant. Sandvik crushing-screening plant has primary (jaw crusher) and secondary (cone crusher). Powder metal of 0-5 mm size that emerges at the primary (jaw crusher) stage in the crushing-screening plant is called by-pass metal powder. In addition, 0-5 mm ferrochrome metal powder is formed in the secondary crusher. While ferrochrome metal powder is sold, by-pass metal powder is mostly re-laid in metal pools. Although these two products, ferrochrome metal powder and by-pass metal powder, have the same content, the color of the by-pass powder is darker. Raw materials containing Fe_2O_3 are used to color ceramic bodies, glazes and linings. Therefore, ferrochrome metal powders attract attention.

This study was conducted with the aim of operational process improvement. Samples were taken from all stages of the by-pass metal powder from laying in the pool to crushing-screening it. X-ray diffraction (XRD), X-ray fluorescence (XRF) and Scanning Electron Microscope (SEM/EDX) analyses of ferrochrome metal powder and by-pass metal powder were made and the color change between them was analysed. Fe-Cr hematite pigments tend to actually form a brown color. The darker colors of this structure are affected by parameters such as raw material particle size distribution, initial composition, synthesis temperature and time. As a result, it has been observed that the by-pass metal powder, which is continuously laid in the metal pool, is exposed to heat for a long time, causing color darkness. The dissemination of these or similar studies will contribute to the development of projects based on industry-university cooperation.

Keywords: Ferrochrome, By-pass metal powder, Color change

1. INTRODUCTION

Eti Krom, a group company of Yıldırım Holding, is the world's largest producer of high carbon ferrochrome (HCFeCr). Eti Krom, which produces metallurgical (hard part, friable and concentrated) and refractory (hard part and friable) type materials, transforms high-grade chrome ore into high-quality and high-carbon ferrochrome in its factory in Elazığ. Almost all ferrochrome's are produced in electric arc furnaces. Using metallurgical coke, chromium and iron oxides are reduced to metal in electric arc furnaces. Also, some of the silica is reduced. The temperature of the slag is 1700 ºC while the temperature of ferrochrome is 1600 ºC. The melting point of the slag must be higher than the melting point of the metal because the metal is superheated using the liquid portion of the slag. Generally, the optimum melting point is applied as 1680-1720 ºC [1, 2]. The high-carbon ferrochrome obtained by these processes is divided into different sizes (0-5 mm, 5-10 mm, 10-50 mm and 10-100 mm) in the Sandvik crushing-screening plant and turned into a ready-to-sell product. 0-5 mm sized powder metal that emerges at the primary (jaw crusher) stage in the crushing-screening plant is called by-pass metal powder. In addition, 0-5 mm ferrochrome metal powder is formed in the secondary (cone crusher) crusher. While ferrochrome metal powder (0-5 mm) is sold, by-pass metal dust (0-5 mm) is mostly re-laid in metal pools. Although ferrochrome metal powder and by-pass metal powder have the same content, the color of by-pass powder is darker.

Chromium is obtained only from the chromite mineral. Chromite, which is in the form of $Fe_2O_3.Cr_2O_3$ in nature, is calcined and turned into paint in order to be useful in industrial scale [3]. Magnetite in $FeO.Fe_2O_3$ or Fe_3O_4 formula and chromite in $FeO.Cr_2O_3$ formula are black in color. Iron compounds are present more or less in aluminium silicates and other ceramic materials. The number of minerals in which iron is in the form of compounds is very large, and many minerals contain more or less iron. Chromite and magnetite are commonly used ferrous black dyes. Excellent black and grey paints are produced from the simple iron chrome system. The resulting dyes are very stable and defects such as metallic stain, pinhole, eggshell effect are minimal. In addition, lower cost magnetite and chromite raw materials are used instead of commercial pigments. Chromium compounds are known important color sources. The color developed with chromium in most ceramic glaze compositions is the characteristic chrome green [4, 5]. Various studies have been carried out on the coloring properties of different materials and wastes containing chromium [6-15].

This study was carried out for operational process improvement. Samples were taken from all stages of the by-pass metal powder from laying in the pool to crushing and sieving. The color change between ferrochrome metal powder and by-pass metal powder was investigated by XRD, XRF and SEM/EDX analysis. As a result, it has been observed that the by-pass metal powder, which is continuously laid in the metal pool, is exposed to heat for a long time and causes color darkness. The dissemination of these and similar studies will contribute to the development of projects based on industry-university cooperation.

2. MATERIAL AND METHODS

Ferrochrome production consists of feeding the raw material to the furnaces, separating the slag from the metal and preparing the products for sale in the crushing-sieving plant. Powder metal of 0-5 mm size that emerges at the primary (jaw crusher) stage in the crushing-screening plant is called by-pass metal powder. By-pass metal powder is spread over metal pools and used repeatedly. In this study, samples were taken in all process parameters from laying the by-pass powder in the metal pool to the grinding time of 0-5 mm in crushing-screening. Metal pool number 356 was used in experimental studies. In Table 1, the places where the samples were taken, the process steps and sample codes are given.

Table 1. By-pass process steps and sampling areas

Sample Codes	Sampling stages in the ferrochrome production process
Sample 1	By-pass powder laid in the metal pool no. 356
Sample 2	First metal poured into metal pool
Sample 3	Second metal poured into metal pool
Sample 4	By-pass metal obtained in the crushing-screening plant
Sample 5	By-pass powder obtained in the crushing-screening plant
Sample 6	Ferrochrome metal (10-50 mm) obtained in the crushing-screening plant

Photographs of the areas where the samples were obtained are given in Figure 1. The color change between ferrochrome metal powder and by-pass metal powder was investigated by X-ray diffraction (XRD), X-ray fluorescence (XRF) and Scanning Electron Microscope (SEM/EDX) analysis.

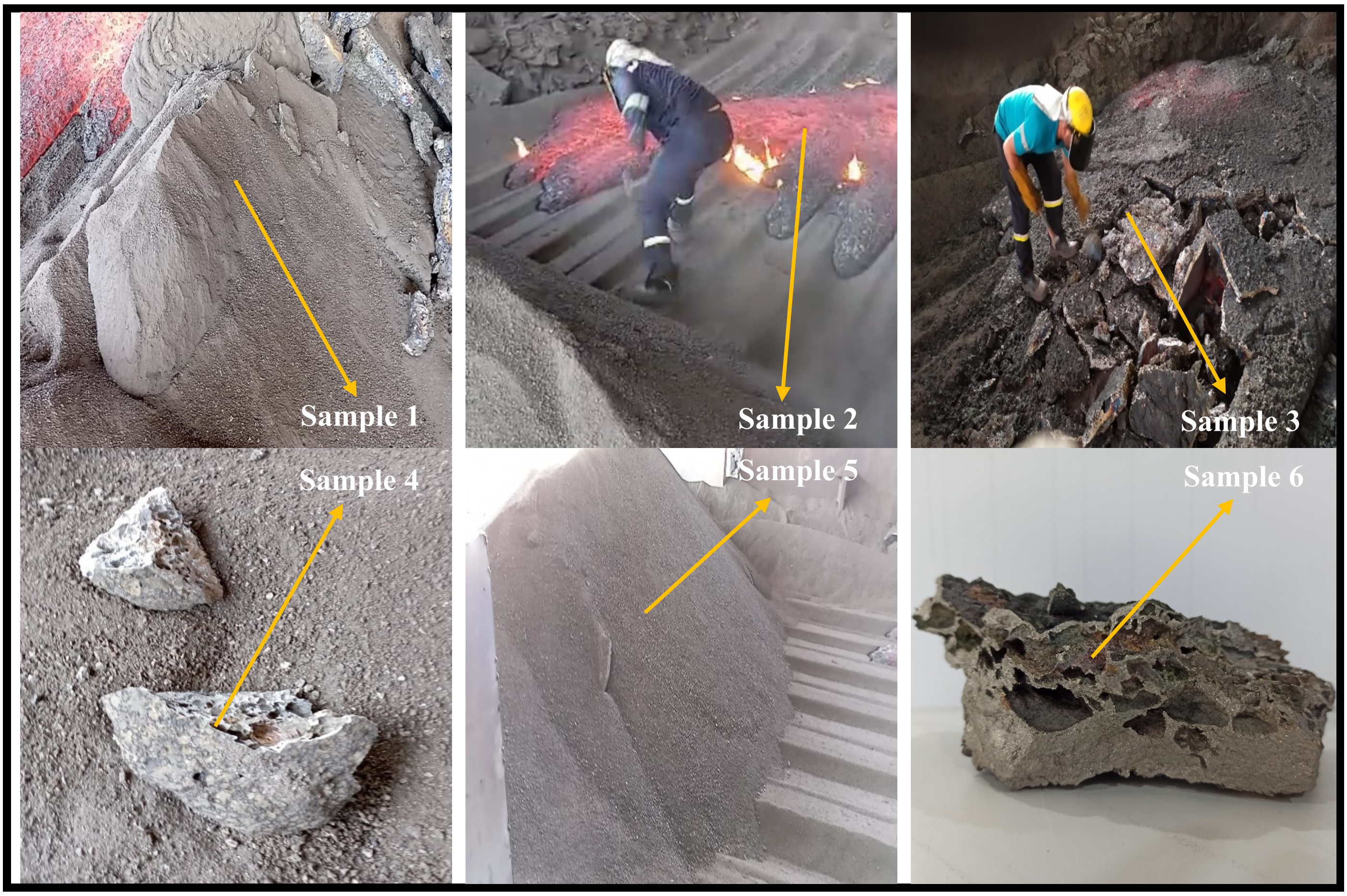

Figure 1. Areas where samples were obtained

3. RESULTS AND DISCUSSION

XRF analyses of the samples were made at MATİL (Material Testing and Innovation Laboratories Inc.). XRF analyses were performed as both elementary analysis and oxide analysis. XRF analysis results are given in Table 2.

Since chromium is a transition metal, it is known that it produces different colors and the characteristic chrome green is obtained in glaze compositions. However, the differences seen in this color change with the influencing temperature. For example, $(Fe\text{-}Cr)_2O_4$ is in the form of hematite and forms black and brown [16, 17]. In addition, if Cr_2O_3, Fe_2O_3, Al_2O_3, NiO, TiO_2 ve MnO are used together, these oxides create varying shades of brown [18-20]. As seen in the XRF analysis, there is a large amount of Cr_2O_3, Fe_2O_3 and Al_2O_3 in the by-pass structure (Table 2). In addition, high temperatures affect the by-pass during the process and the waiting time of the by-pass also changes. For this reason, the color structure of the by-pass material is formed in darker tones.

Table 2. XRF analysis results of samples

Sample 1	**Oxide Analysis**	**Cr_2O_3**	**Fe_2O_3**	**SiO_2**	**MgO**	**Al_2O_3**	**CaO**	**NiO**	**Na_2O**	**V_2O_5**	**SO_3**
		65.15	20.42	6.37	3.21	2.29	1.30	0.29	0.22	0.20	0.12
	Elementary Analysis	**Cr**	**Fe**	**Si**	**Mg**	**Al**	**Ca**	**Ni**	**Na**	**V**	
		66.40	22.97	3.93	2.50	1.59	1.27	0.38	0.21	0.16	
Sample 2	**Oxide Analysis**	**Cr_2O_3**	**Fe_2O_3**	**SiO_2**	**MgO**	**Al_2O_3**	**CaO**	**NiO**	**Na_2O**	**V_2O_5**	**SO_3**
		76.90	19.59	1.62	0.28	0.43	0.38	0.19	---	0.23	---
	Elementary Analysis	**Cr**	**Fe**	**Si**	**Mg**	**Al**	**Ca**	**Ni**	**Na**	**V**	
		76.05	21.30	0.98	0.21	0.29	0.36	0.24	---	0.18	
Sample 3	**Oxide Analysis**	**Cr_2O_3**	**Fe_2O_3**	**SiO_2**	**MgO**	**Al_2O_3**	**CaO**	**NiO**	**Na_2O**	**V_2O_5**	**SO_3**
		79.79	18.83	0.51	---	---	---	0.18	---	0.24	---
	Elementary Analysis	**Cr**	**Fe**	**Si**	**Mg**	**Al**	**Ca**	**Ni**	**Na**	**V**	
		78.48	20.35	0.30	---	---	---	0.22	---	0.19	
Sample 4	**Oxide Analysis**	**Cr_2O_3**	**Fe_2O_3**	**SiO_2**	**MgO**	**Al_2O_3**	**CaO**	**NiO**	**Na_2O**	**V_2O_5**	**SO_3**
		79.60	18.80	0.67	---	---	---	0.19	---	0.24	---
	Elementary Analysis	**Cr**	**Fe**	**Si**	**Mg**	**Al**	**Ca**	**Ni**	**Na**	**V**	
		78.36	20.34	0.40	---	---	---	0.23	---	0.19	
Sample 5	**Oxide Analysis**	**Cr_2O_3**	**Fe_2O_3**	**SiO_2**	**MgO**	**Al_2O_3**	**CaO**	**NiO**	**Na_2O**	**V_2O_5**	**SO_3**
		65.23	20.15	6.46	3.43	2.40	1.25	0.30	0.16	0.18	0.12
	Elementary Analysis	**Cr**	**Fe**	**Si**	**Mg**	**Al**	**Ca**	**Ni**	**Na**	**V**	
		66.61	22.74	3.98	2.67	1.66	1.22	0.38	0.15	0.15	
Sample 6	**Oxide Analysis**	**Cr_2O_3**	**Fe_2O_3**	**SiO_2**	**MgO**	**Al_2O_3**	**CaO**	**NiO**	**Na_2O**	**V_2O_5**	**SO_3**
		79.17	18.97	0.68	---	0.14	0.19	0.18	---	0.24	---
	Elementary Analysis	**Cr**	**Fe**	**Si**	**Mg**	**Al**	**Ca**	**Ni**	**Na**	**V**	
		77.95	20.52	0.41	---	---	0.18	0.22	---	0.19	

SEM and EDX analyses of the samples are given in Fig. 2, Fig. 3 and Fig. 4, respectively. It is seen in Fig. 2-4 that similar structures are formed in the SEM and EDX analyses of the samples. Only in the EDX analysis of sample 5 (by-pass metal powder) Mn (manganese) peaks were observed. It is known that it gives a black color when it is in the form of manganese dioxide or manganese lignite. In addition, the color change depends on the oxidation and grain size of the iron minerals, the firing temperature, the furnace atmosphere, the vitrification degree and the iron, calcium oxide (CaO) and manganese oxide (MnO) it contains, etc. depending on their quantity [21-23]. Therefore, it can be said that bypass powder metal is darker than ferrochrome powder metal.

XRD analyses of the samples is given in Fig. 5. Similar characteristic peaks were observed in all samples. However, the characteristic Mn_3O_4 peak was observed in sample 5 (by-pass metal powder). This result supports the SEM/EDX analysis.

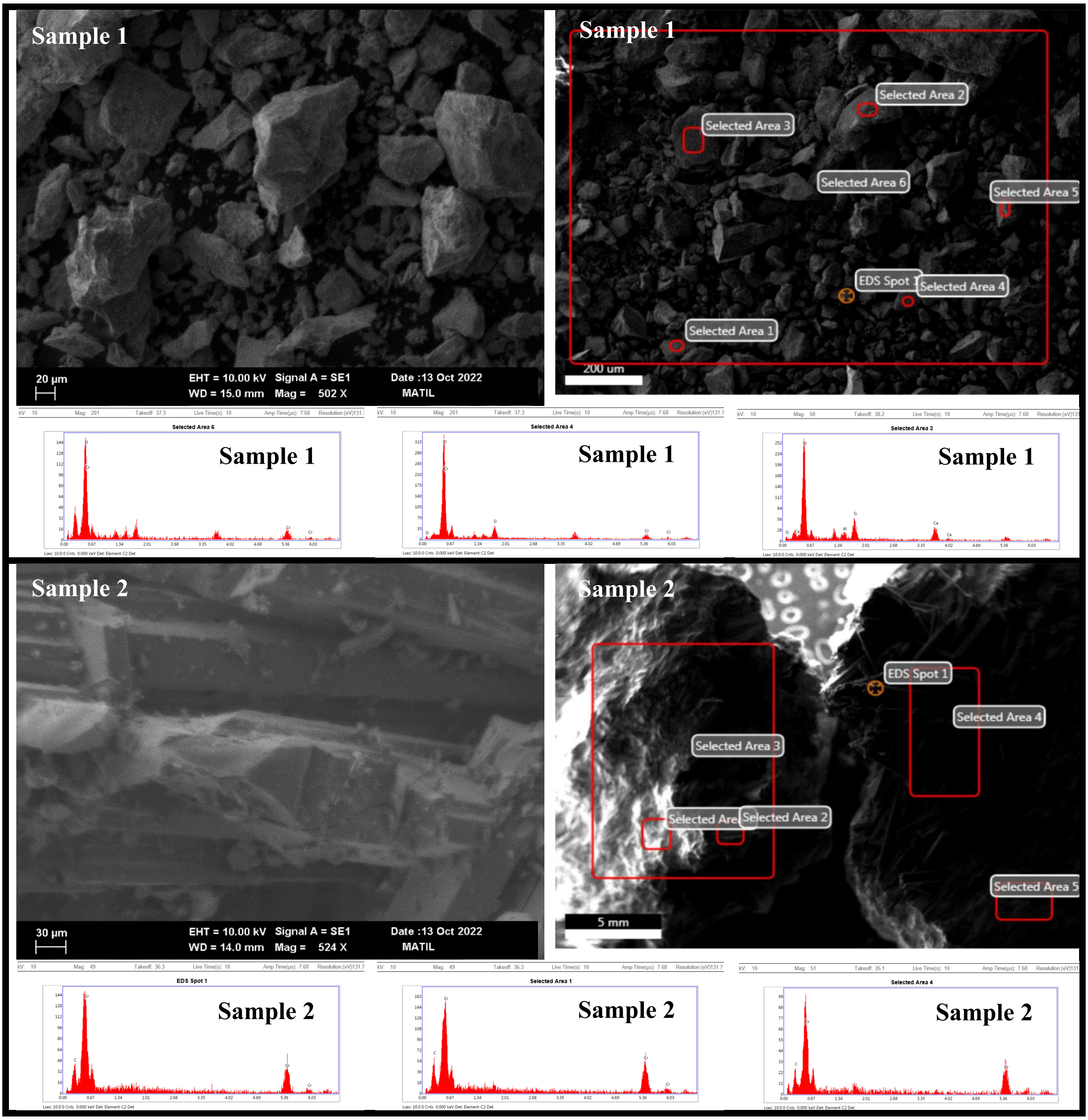

Figure 2. SEM/EDX analysis for sample 1 (by-pass powder laid in the metal pool no.356) and sample 2 (first metal poured into metal pool)

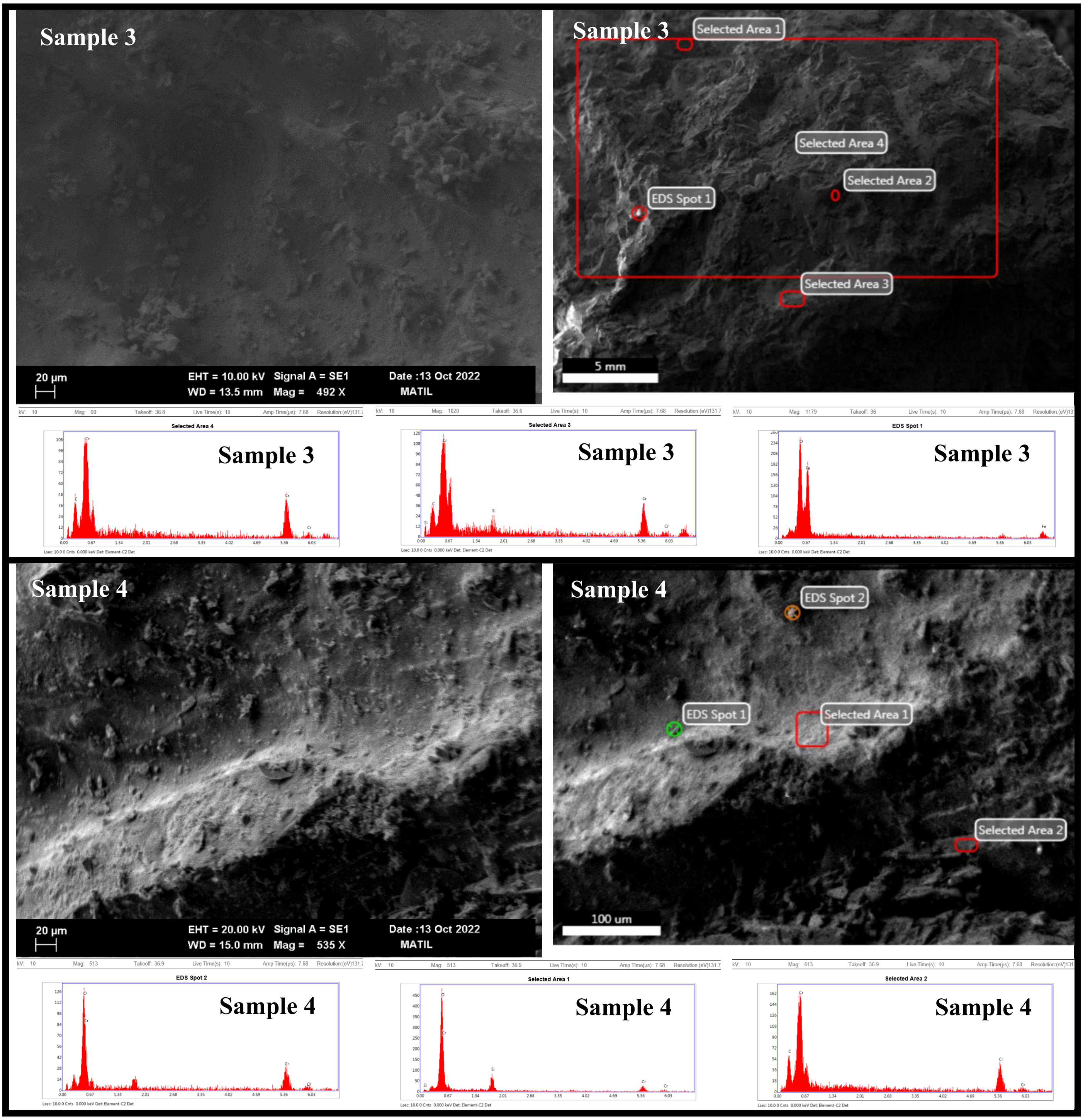

Figure 3. SEM/EDX analysis for sample 3 (second metal poured into metal pool) and sample 4 (by-pass metal obtained in the crushing-screening plant)

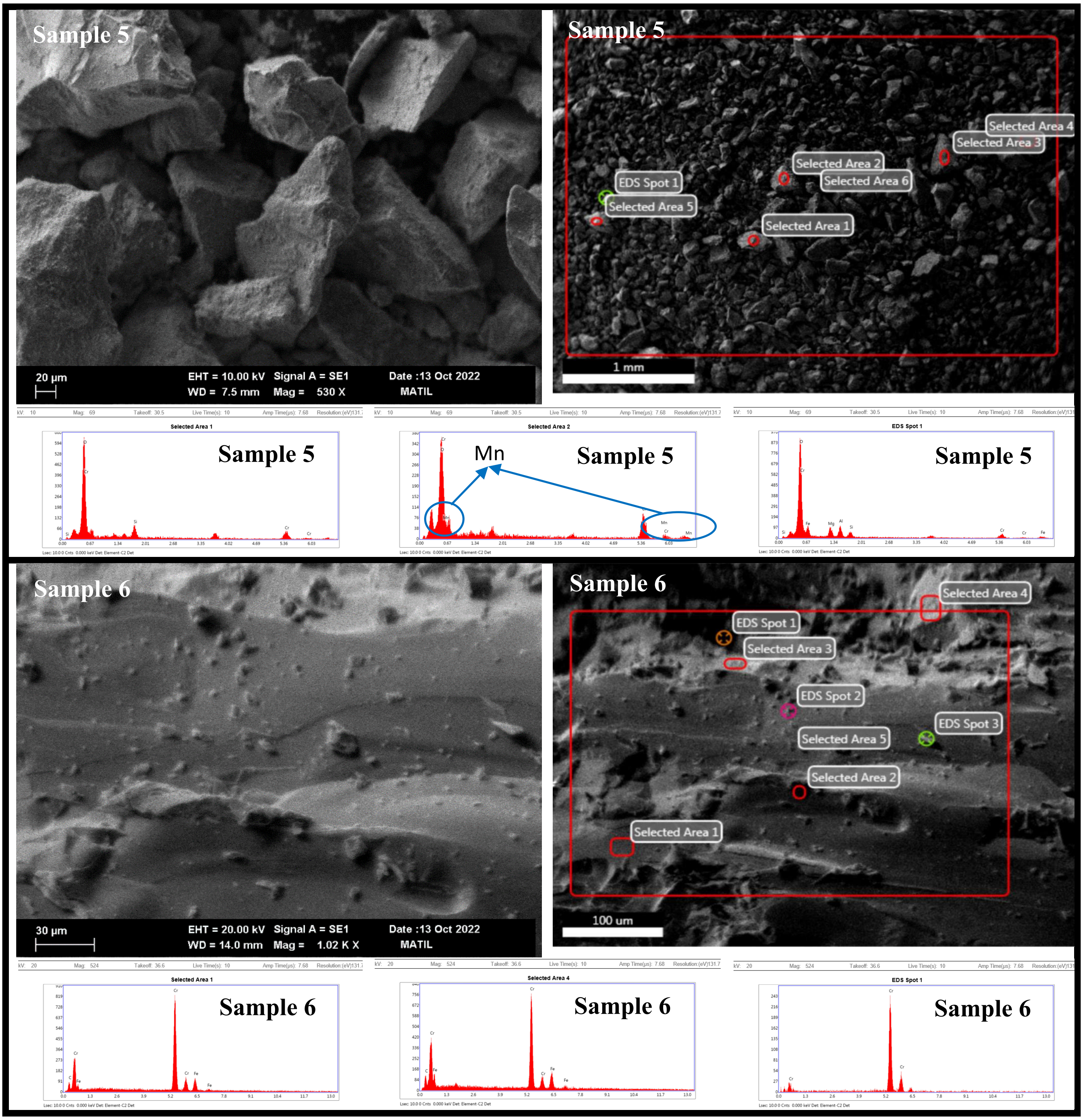

Figure 4. SEM/EDX analysis for sample 5(by-pass powder obtained in the crushing-screening plant) and sample 6 (Ferrochrome metal (10-50 mm) obtained in the crushing-screening plant)

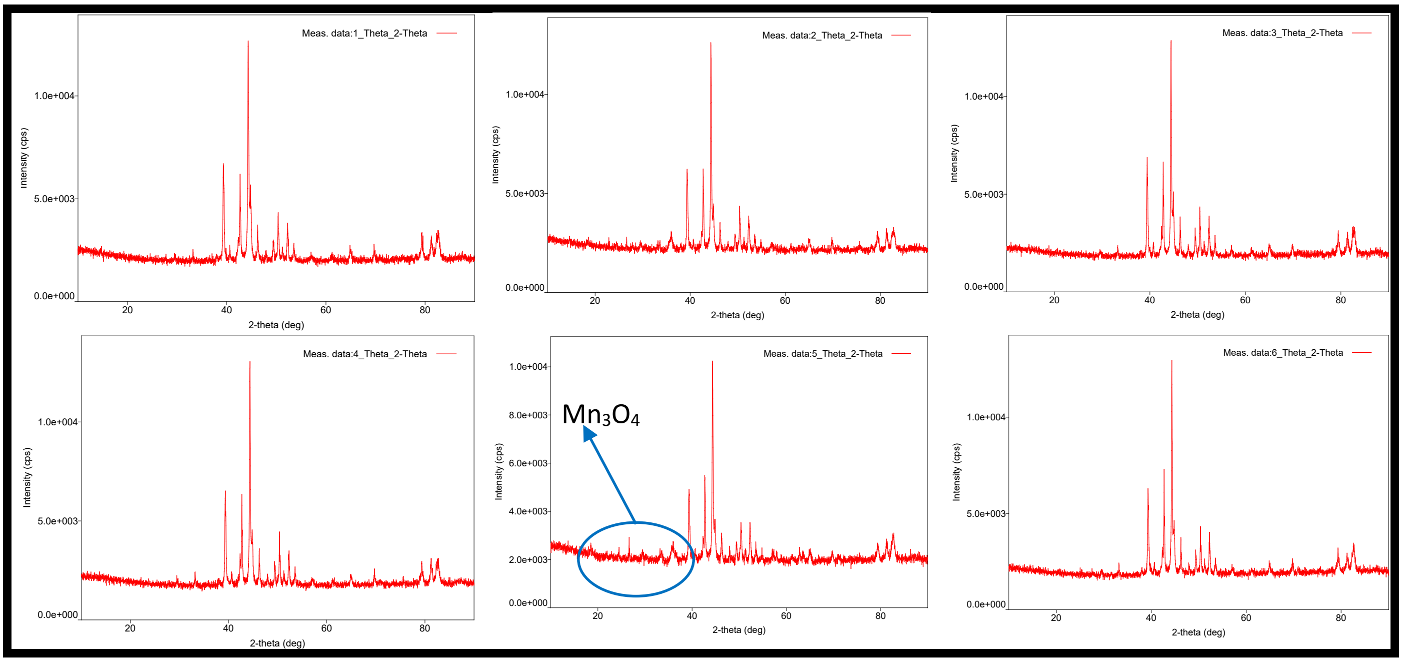

Figure 5. XRD analysis of samples

4. CONCLUSION

This study was carried out for operational process improvement. The color change between ferrochrome metal powder and by-pass metal powder was investigated by XRD, XRF and SEM/EDX analysis.

- ✓ XRF analyses confirmed the presence of oxides affecting the color change (Cr_2O_3, Fe_2O_3, Al_2O_3, CaO, MnO and Mn_3O_4 etc.),
- ✓ SEM/EDX analyses showed that similar structures were formed. But Mn peaks were observed in sample 5 (by-pass metal powder),
- ✓ Mn_3O_4 phase was detected in XRD analyses of sample 5 (by-pass metal powder). This phase causes color darkness.

The dissemination of these and similar studies will contribute to the development of projects based on industry-university cooperation.

ACKNOWLEDGMENTS

This study was supported by Eti Krom Inc./R&D Center under project number: ETİ-BYPASS-01.

REFERENCES

[1] Vapur, H., Top, S., Teymen, A., Türkmenoğlu, M., Elazığ Ferrokrom Tesisi Cüruflarının Agrega Özelliklerinin Araştırılması, Çukurova Üniversitesi Mühendislik Mimarlık Fakültesi Dergisi, 28(1), ss.77-88, 2013.

[2] Niemela, P. ve Kauppi, M., Production, Characteristics and Use of Ferrochromium Slags, Innovations in Ferro Alloy Industry, 2007.

[3] Özkaya, E., Yeşilay, S., Using of Chromite and Magnetite Ores in Artistic Glasses, Journal of Social Sciences of Mus Alparslan University, 6 (3), pp. 359-363, 2018.

[4] R. Hopper, "The Ceramic Spectrum", Chilton Book Company, Radnor Pennslvania, pp. 124–125, 1984

[5] R.A. Eppler, D.R. Eppler, "Glazes and Glass Coatings", The American Ceramic Society, Westerville, Ohio, pp. 113–130, 1998

[7] Ay, N., Çakı, M., Uluslararası Seramik Kongresi Bildiriler Kitabı, 'Baca tozlarının sırların renklendirilmesinde kullanılabilirliğinin araştırılması', 241-249, Eskişehir, 19-23 Ekim 1992.

[8] F. Bondioli, L. Barbieri, T, Manfredini, "Grey Pigment (Fe,Zn)Cr2O4 Obtained from Industrial Fly-Ash", Tile&Brick Int., Vol. 16, 4(2000), 246

[9] Ay, N., Çakı, M., 'Utilization of pigments obtained from fly ash in Colobration of ceramic glaze', (Poster Presentation), Conference Exhibition of the European Ceramic Societies, Turkey,2003.

[10] S.A. Chronisher, W. Chen, "Using Lead-Free Glaze with Chrome-Tin Color Underglaze", The American Ceramic Society Bulletin, Vol. 73, 9(1994), 71

[11] Ay, N., Çakı, M., 4.Uluslararası Seramik Kongresi Bildiriler Kitabı, 'Fe2O3 ve Cr2O3'ün Renk Oluşumuna Etkisi', 137-142, Eskişehir, 22-25 Eylül 1998.

[12] F. Ren, S. Ishida, N. Takeuchi, K. Fujiyoshi, "Chromium-Based Ceramic Colors", The American Ceramic Society Bulletin, Vol. 71, 5(1992), 759

[13] C.J. Byrne, S.G. Kutney, R.A. Pipoly, "How Glaze Composition Affects Chrome-Tin Pinks", The American Ceramic Society Bulletin, Vol. 73, 9(1994), 46

[14]. Ay, N., Çakı, M., 5.Seramik kongresi Bildiriler Kitabı, 'Stoneware Sırlarında Kromitin Renklendirici Olarak Kullanımı',195-200, İstanbul, 3-5 Ekim 2001.

[15] N. Ay, M. Çakı, A. Kara, "Ferrrochromium Fly Ash Used As a Pigment in Ceramic Glaze", The American Ceramic Society Bulletin, Vol. 73, 12(1994).

[16] Richard A. Eppler, Douglas R.Eppler, "Which colors can and connot be produced in ceramic glazes", Ceram. Eng. Sci. Proc., 15[1], 281-288, 1994.

[17] Eppler, R., Eppler, A., 'The interaction Of Ceramic Pigments with Glazes', Ceramic Bulletin ,Vol. 68, No.1,1989.

[18] R.A. Eppler, D.R. Eppler, "Glazes and Glass Coatings", The American Ceramic Society, Westerville, Ohio, pp. 113–130, 1998.

[19] Norton, F.H., "Fine Ceramics Technology and Aplications", Robert E. Krieger

[20] Publishing Company, Malabar, Florida, 226–227, 1978.

[21] Karaman, S., Color Formation in Building Bricks, KSU. Journal of Science and Engineering 9(1), 2006.

[22] Murray, H.H., Common Clay. Industrial Minerals and Rocks, 6 Edition. (Senior editor carr,D.D), 247-248, 1996.

[23] Yıldırım, M., Toprak Sanayinde Ham Madde Sorunları, Üretimde ve Üretim Sonrası Kalite Kontrolleri. Tuğla ve Kiremit Endüstrisi Derg., Yıl 1, Sayı 2, İzmir, 20-27. 1996.

DESIGN AND MANUFACTURE OF A SOLAR PANEL CLEANER ROBOT: CHALLENGES AND LESSONS LEARNED FROM A CAPSTONE PROJECT

M. Diwan[1], M. Alhaj Mousa, M. Ahmad, M. Alaneme, T. Baalora, O. Shekoofa[2]

[1]Department of Mechanical Engineering, Faculty of Mechatronics Engineering, Eastern Mediterranean University, Famagusta, North Cyprus

E-mail: mohammaddiwan664@gmail.com, omid.shekoofa@emu.edu.tr

Abstract:

In this paper, we analysed the intricate challenges encountered in the development of a 12V Solar Panel Cleaner Robot, with a particular focus on three pivotal aspects: the acquisition of suitable robot components, the meticulous selection of efficient cleaning materials, and the utilization of 3D printing technology for precision part fabrication. Our investigation reveals the complexities associated with procuring appropriate robot components, exacerbated by delays, supply chain disruptions, and cost considerations. We examine how we choose the right materials and designs for important cleaning parts., emphasizing the imperative of performance optimization and durability. Moreover, our analysis closely examines the complexities of 3D printing, underscoring the need for precision and dependability during the manufacturing phase. Furthermore, we offer a visionary outlook by presenting a suite of innovative solutions poised to elevate the Solar Panel Cleaner Robot's capabilities, including the Autonomous Brush Case, Enhanced Autonomous Water Pump System, Self-Charging and Docking System, Machine Learning for Image Processing, Enhanced Obstacle Detection, and Smart Maintenance Alerts, underscoring our unwavering commitment to advancing the field of solar panel maintenance technology and ensuring a more efficient and sustainable solution. In sum, this paper not only elucidates main challenges but also charts a path for future advancements in this domain.

Keywrods: Photovoltaic, Solar Panel, Performance, Cleaning, Robot

1 Introduction

Solar panels generate their highest power output on sunny days, with reduced output on cloudy days and even less on rainy days. Sunlight conversion to usable electricity in solar panel systems faces various losses that affect their power output. The performance of these systems is assessed using a performance ratio (PR), calculated as the final yield (YF) divided by the reference yield (YR). The PR also compares AC and DC power to evaluate losses related to panel degradation, temperature, soiling, internal network, inverter, transformer, system availability, and grid connection network.

Soiling, a major factor in power loss, occurs as dirt accumulates on solar panels over time. The extent of power loss depends on the type of dirt, the influence of precipitation, and the tilt angle of the panels. Snowfall in winter also affects solar panel efficiency, as snow can limit radiation and disable cells. Researchers have studied the impact of snow on PV arrays.

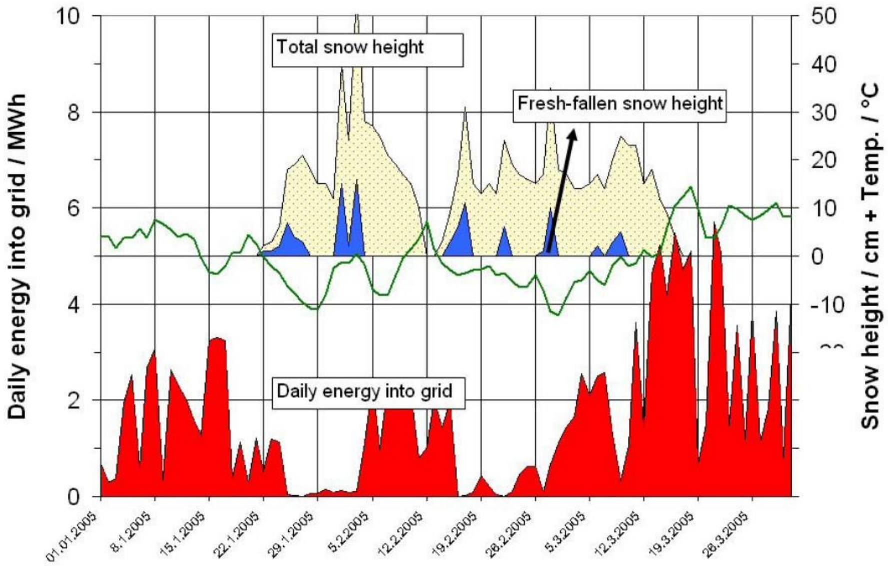

Figure 1: Influence of snowfall and total snow height on energy yield.[1]

Solar panel degradation refers to the loss of efficiency over time due to various factors, including exposure to the elements, wear and tear, and manufacturing defects. Degradation can be simple (slow and predictable) or permanent (irreversible damage). Contaminants like dirt and dust, when accumulated on panel surfaces, can reduce electricity production efficiency and cause physical damage. Therefore, maintaining clean solar panels is essential to minimize degradation, and robotic solar panel cleaners can be employed for this purpose. [1]

Cleaning Methods:

There are several methods for cleaning solar panels:

Robotics: Robotic technology is an efficient and time-saving approach to cleaning solar panels. It ensures effective cleaning while minimizing the risk of surface damage and reducing potential injuries to workers, especially in hazardous locations [2].

Waterless Vibration: This method involves using an industrial vibrator, sometimes referred to as "Vibra-clean," to shake the surface of solar panels. High-frequency vibrations break down dirt and oil without causing damage to the panels. However, excessive vibration can potentially harm the panels.

Nanoparticle Coating: Nanoparticle coatings designed for cleaning solar panels can be applied using an electrostatic spray gun or roller on both metal and glass surfaces. These coatings help remove dirt and grime from panels, even while they are in storage or shipping containers, making them ready for quick installation after cleaning [3].

To maintain optimal efficiency, various robotic solar panel cleaners have been developed, as shown and their specifications in Table 1. Other than these robotic systems, there is a robot called Ecoppia-E4 which is a fully autonomous robot uses microfiber brushes to remove dust from solar panels, making it well-suited for large installations in dry, sandy environments. This robot, employs the force of gravity to move its brushes downward while spinning, creating an airflow that helps dislodge dust. It has an onboard solar panel and battery system, allowing it to operate at night. The robot can move both horizontally and vertically along a guide rail, thanks to wheels, ensuring thorough cleaning and maximizing solar panel efficiency [4]. Furthermore, there is an automatic robotic cleaner that plays a pivotal role in the maintenance of floating solar panels, a task of immense complexity when attempted manually. This innovative robot is propelled by gear motors and a motor driver, featuring an additional motor fitted with a cleaning membrane specifically designed for efficient panel cleaning using water. Additionally, the robot is equipped with a camera system that provides continuous surveillance of the solar panel conditions, while simultaneously transmitting this data to cloud storage for both damage assessment and as a valuable reference for future cleaning procedures [5]. Another notable addition to our project research is the Cleaning Robot employing Omni Wheels. This robot has been equipped with sensors and encoders, enabling precise control of its movement as it skilfully traverses the gaps between panels and gracefully halts at the panel edges [6]. Moreover, we have developed a portable robotic cleaning device distinguished by its versatile platform, capable of traversing the entire length of a panel [7]. This table also shows the specifications of the robot that we have designed and manufactured in this project, called “Solar Shine” which will be discussed in the following section.

Table 1: Comparison with other standard robots [2].

	SolarCleano F1	SolarCleano M1	SolarCleano B1	Hy CLEANER SOLAR facelift	Solar Shine
					
Total weight (kg)	80	37	-	83	5.538
Dimensions (LxWxH) in (m)	1.45x1.3x0.35	0.80x0.86x0.35	5.95x1.74x3.51	1.2x0.9x0.5 (Without brush)	0.62x0.31x0.15 0.78x0.45x0.15
Brush size (m)	1.7	0.8	4.4	1.1x0.3x1.3	0.45x0.16x0.2
Remote control range (m)	200	200	-	-	30
Brush diameter (m)	0.17	0.17	0.38	0.3	0.18
Gradeability (°)	25	-	0 - 34	25	45

2 Materials and Methods

As we discussed above, the efficiency of solar panels can be hampered by the gradual accumulation of dirt, dust, and other pollutants. Traditional manual cleaning methods are laborious and time-consuming, prompting the need for an autonomous and efficient solution. In response to this demand, we have designed and manufactured an autonomous solar panel cleaner robot, as shown in Figure 2, empowered by edge detection sensor to identify and tackle heavily soiled regions on solar panels.

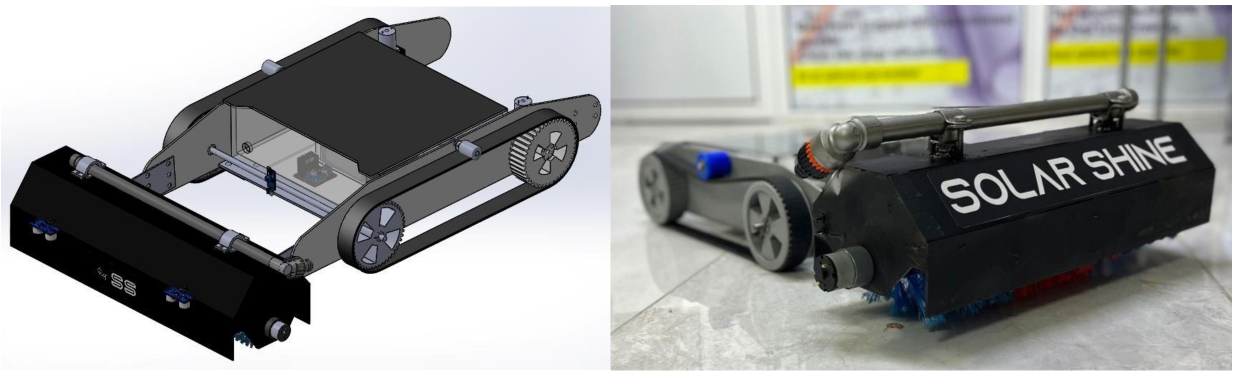

Figure 2. Left: the proposed design for solar panel cleaner robot (Solar Shine), Right: the manufactured robotic system [8]

The system breakdown structure of the robot is shown in figure 3. The detail of the design of this system can be found the capstone report which is available at the web address of [8]. In the following section we discuss the challenges and lessons learned from doing this project.

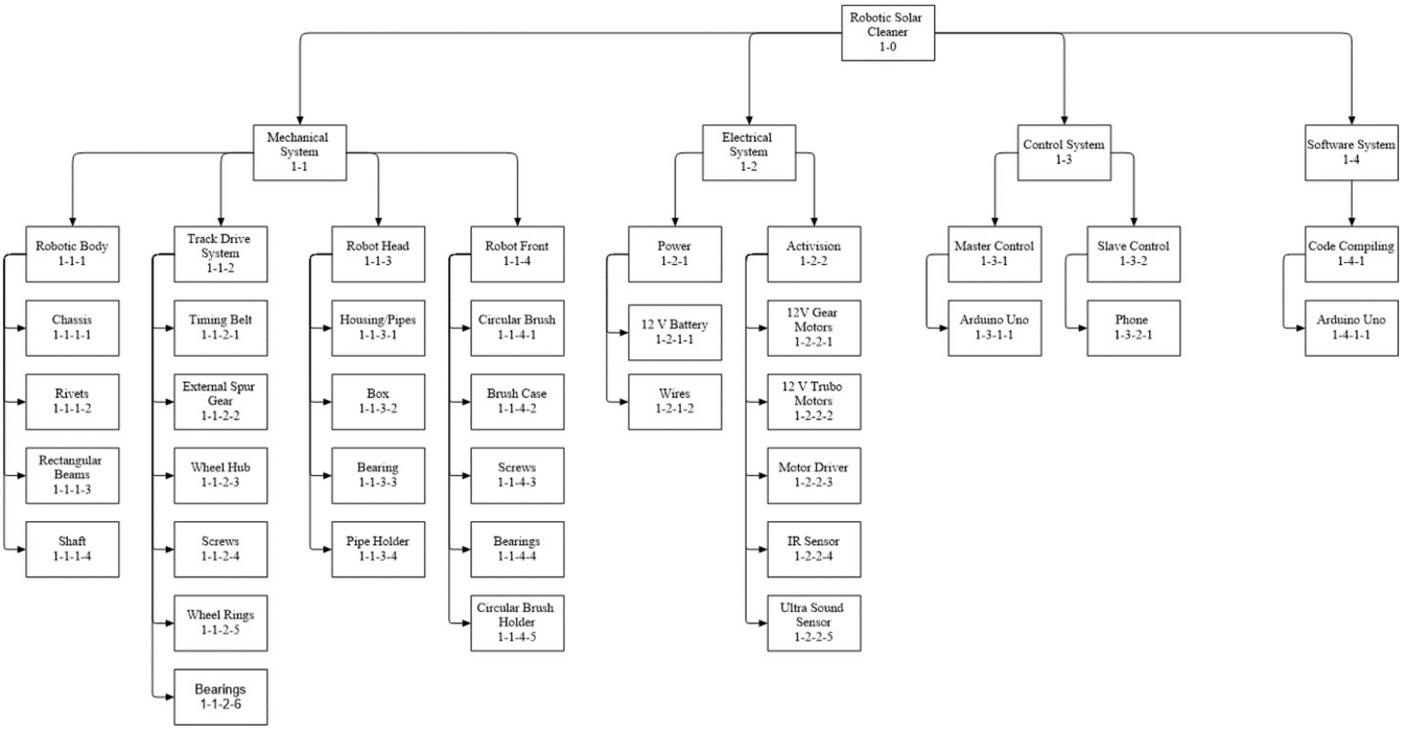

Figure 3: System Breakdown structure [8]

3. Results and Discussion

After we successfully designed and manufactured the Solar Shine robotic system, we reviewed the challenges and drawbacks of our work and documented it to help the future interested groups in such projects to avoid repeating such mistakes and help them to proceed in their project much easier than us. Therefore, in this section we discussed the challenges and lessons learned from this project. We also discussed some future works .

3.1 Component Procurement: The original design of the solar panel cleaner robot heavily depended on a specialized edge detection sensor that proved challenging to acquire due to limited availability and high costs. Additionally, sourcing certain actuators and processing units required for the edge detection system posed unexpected difficulties, further impeding progress on the initial design.

3.2 Belt and Gear Selection: The choice of an appropriate belt and gear combination was critical to achieving efficient traction and motion control on the solar panels' surface. We needed to consider factors such as durability, friction, load-bearing capacity, and compatibility with the robot's power source and motors. However, identifying a belt and gear combination that met all the required criteria proved to be more complex than anticipated.

3.3 3D Printing: Despite having a 3D printer, finding suitable settings and optimizing the printing process for robot components proved time-consuming and challenging. Complex parts required careful consideration of printing parameters, and iterative testing was necessary to achieve dimensionally accurate and structurally robust components.

Figure 4: 3D Printed Gear Wheels [8]

3.4 Image processing: While exploring image processing for dust detection held promise, challenges in component procurement and time constraints complicated its implementation. The research and development efforts required to fine-tune the image processing algorithms exceeded initial estimates, delaying progress.

3.5 Integrating the communication module: Integrating Bluetooth control via a smartphone application enhanced the robot's versatility. Users could remotely control the robot's movements, switch between autonomous and manual cleaning modes, and receive real-time performance feedback.

3.6 Battery and power source: The robot's 12V battery provided optimal power efficiency and portability. Charging and recharging mechanisms were designed for user convenience and safety. The choice of a 12V battery was driven by factors such as power requirements, weight considerations, and compatibility with the robot's motors and components. The battery's compact size and manageable weight allowed for easier integration within the robot's chassis while minimizing the overall weight to ensure safe operation on delicate solar panels. Safety was another concern when working with a rechargeable 12V battery. We implemented protective circuits and mechanisms to prevent overcharging and overcurrent, safeguarding both the battery's integrity and the robot's operation. Safety features were rigorously tested and integrated to ensure smooth and secure interactions with the battery during the robot's lifecycle.

3.7 Cleaning brush: The robot's cleaning brush featured adjustable speed control, allowing users to customize cleaning modes based on dirt accumulation levels and environmental conditions. The smartphone application provided an intuitive user interface, offering directional controls for precise movement, as well as cleaning mode options, allowing users to switch between gentle and vigorous cleaning modes. Additionally, the application provided recommendations based on real-time image processing data to guide users in choosing the most appropriate cleaning mode. The ability to adjust the brush speed proved particularly advantageous in accommodating various environmental conditions. For instance, during periods of heavy dust accumulation, users could increase the brush speed to tackle the added challenge effectively. Conversely, in delicate environments, such as residential solar installations, users could reduce the brush speed to ensure gentle cleaning without causing any potential damage.

4 Future Works

While the edge detection-enhanced solar panel cleaner robot presented in this paper showcases significant advancements in autonomous cleaning technology, there remain promising areas for future research and development. The following sections outline potential directions for further enhancing the robot's capabilities and exploring new features:

4.1. Autonomous Brush Case:

Currently, the robot's brush speed is adjustable through the smartphone application. However, to fully optimize the cleaning process and further reduce user intervention, future work could focus on developing an autonomous brush case. An autonomous brush case would incorporate AI-driven algorithms and environmental sensors to analyze the dirt accumulation levels and adjust the brush speed dynamically. This would enable the robot to adapt its cleaning strategy in real-time, ensuring efficient and effective cleaning without user input.

4.2. Enhanced Autonomous Water Pump System:

The current robot design incorporates a water pump system for wet cleaning, allowing it to spray water on solar panels to remove stubborn contaminants effectively. Future work could explore the development of an enhanced autonomous water pump system. By integrating environmental sensors and AI algorithms, the robot could intelligently regulate the water flow and adjust the spray patterns based on the level of soiling and environmental conditions. This would enable the robot to optimize water usage, minimize wastage, and improve the overall efficiency of the wet cleaning process.

4.3. Self-Charging and Docking System:

Autonomous operation is a key aspect of the solar panel cleaner robot. To further improve its autonomy, future work could explore the development of a self-charging and docking system. This would allow the robot to return to a designated charging station when the battery level is low, recharge automatically, and resume cleaning operations without human intervention. Integrating wireless charging technology would eliminate the need for physical connections, enhancing the robot's user-friendliness and reducing wear on charging ports.

4.4. Machine Learning for Image Processing:

Enhancing the robot's image processing capabilities with machine learning algorithms could enable it to recognize specific types of contaminants and adapt its cleaning approach accordingly. By training the robot with a diverse dataset of dust and debris types, it could learn to differentiate between harmless debris and harmful residues that could affect panel performance. This would enable the robot to prioritize cleaning tasks and focus on areas with the most significant impact on energy output.

4.5. Enhanced Obstacle Detection:

To ensure safe operation and minimize the risk of collisions with obstacles on the solar panel surface, future work could explore advanced obstacle detection and avoidance mechanisms. Incorporating 3D mapping and LiDAR technology could provide the robot with a comprehensive understanding of its surroundings, enabling it to navigate efficiently while avoiding potential hazards.

4.6. Smart Maintenance Alerts:

Implementing a smart maintenance alert system would further improve the robot's reliability and reduce downtime. By continuously monitoring its internal components and sensors, the robot could detect potential malfunctions or abnormalities and notify users proactively. This would allow users to address issues promptly, ensuring consistent and uninterrupted cleaning operations.

5 Conclusion

In summary, through an exhaustive study of prior designs and extensive research efforts, our team conceptualized and developed this robot. The challenges encountered on this journey not only honed our problem-solving skills but also taught us the value of adaptability and quick thinking, especially in formulating backup plans. The successful completion of this robot has not only fueled our enthusiasm but has also sparked a new wave of creativity, inspiring us to explore innovative ideas for future implementation.

References:

[1] KU Leuven, https://iiw.kuleuven.be/onderzoek/eavise/mastertheses/kegeleers.pdf(2006).

[2] SolarCleano, https://solarcleano.com/en (accessed Sep. 19, 2023).

[3] P. Dearing, “Top 5 Best Methods to Clean Your Solar Panels at Home,” Solar Energy World, https://www.solarenergyworld.com/5-best-methods-to-clean-your-solar-panels-at-home/ (accessed Sep. 19, 2023).

[4] “Robotic Solar Panel Cleaning Services for Utility-Scale PV Sites,” ECOPPIA, https://www.ecoppia.com/ (accessed Sep. 19, 2023).

[5] T. Sorndach, N. Pudchuen and P. Srisungsitthisunti, "Rooftop Solar Panel Cleaning Robot Using Omni Wheels," 2018 2nd International Conference on Engineering Innovation (ICEI), Bangkok, Thailand, 2018, pp. 7-12, doi: 10.1109/ICEI18.2018.8448530.

[6] T. Sorndach, N. Pudchuen and P. Srisungsitthisunti, "Rooftop Solar Panel Cleaning Robot Using Omni Wheels," 2018 2nd International Conference on Engineering Innovation (ICEI), Bangkok, Thailand, 2018, pp. 7-12, doi: 10.1109/ICEI18.2018.8448530.

[7] M. A. Jaradat et al., "A fully portable robot system for cleaning solar panels," 2015 10th International Symposium on Mechatronics and its Applications (ISMA), Sharjah, United Arab Emirates, 2015, pp. 1-6, doi: 10.1109/ISMA.2015.7373479.

[8] “Previous Capstone Projects,” EMU, https://me.emu.edu.tr/en/capstone-design-projects/previous-capstone-projects (accessed Sep. 19, 2023).